Control of power electronics of future smart grids for ancillary services

Hoang-Trung Ngo

MEMOIRE DE DOCTORAT DE

L'ECOLE CENTRALE DE NANTES

ECOLE DOCTORALE N° 602
Sciences de l'Ingénierie et des Systèmes
Spécialité : *Automatique*

Par

Hoang-Trung NGO

Control of power electronics of future smart grids for ancillary services

Projet de recherche doctoral présenté et soutenu à l'École Centrale de Nantes le 13 mars 2023
Unité de recherche : UMR 6004, Laboratoire des Sciences du Numérique de Nantes (LS2N)

Rapporteurs avant soutenance :

Rachid OUTBIB Professeur des universités, Aix-Marseille Université
Ioannis LESTAS Full professor, University of Cambridge, Royaume-Uni

Composition du Jury :

Président : Seddik BACHA Professeur des universités, Université Grenoble Alpes
Examinateurs : Rachid OUTBIB Professeur des universités, Aix-Marseille Université
Ioannis LESTAS Full professor, University of Cambridge, Royaume-Uni
Alessio IOVINE Chargé de recherche, CNRS - CentraleSupélec Campus Paris-Saclay, Gif-sur-Yvette
Ina TARALOVA Maître de conférences, École Centrale de Nantes
Directeur de recherches doctorales: Bogdan MARINESCU Professeur des universités, École Centrale de Nantes
Co-enc. de recherches doctorales: Elkhatib IBRAHIM Ingénieur de recherche, École Centrale de Nantes

Invitée
Marie-Sophie DEBRY Ingénieure de recherche, RTE France, La Défense

Acknowledgement

I would like to express my gratefulness to the persons and organizations listed below who helped me finish the thesis.

First and foremost, I would like to thank Prof. Bogdan Marinescu, University Professor at Ecole Centrale de Nantes (ECN), as well as my co-director, Mr. Elkhatib Kamal, researcher at ECN, and Mr. Florent Xavier from R&D Division, Réseau de Transport d'Electricité (RTE) France. In addition, I would like to thank other teams in POSYTYF project: prof. Oriol Gomis-Bellmunt from Polytechnic University of Catalonia and his team, prof. Horst Schulte from HTW Berlin - University of Applied Sciences and his team, as well as other teams. Prof. Bogdan Marinescu generated progress and overall direction for the thesis, Mr. Elkhatib Kamal engaged with me more regularly to work out all the specifics, and Mr. Florent Xavier gave me many beneficial opinions on my work and the publications published. The two aforementioned teams provided invaluable advise on my work, particularly on the POSYTYF project.

Since the beginning, due to the complicated and mixed fields of my thesis in power converter control, it was difficult for me to precisely determine the direction of PhD work. I would not be able to complete my thesis without the help of so many people. I would like to express my gratitude for the trust and inspiration you have given me.

In addition, I would like to express my gratitude to Laboratoire des Sciences du Numérique de Nantes (LS2N), RTE-ECN chair and European H2020 POSYTYF project, which gave me this opportunity to do my thesis in Nantes, France. I would also like to thank the members of the jury (rapporteurs and examiners), for your help, your patience, and your comments have helped me to improve my work.

Finally, I would like to thank my family and friends for their encouragement and support when I was having research difficulties, they are my main inspiration for moving forward with the thesis.

Table of Contents

List of Figures

List of Tables

List of Acronyms

ABB ASEA Brown Boveri 17

aFRR automatic Frequency Restoration Reserve 34

CCT Critical Clearing Time 34

CNRS Centre National de la Recherche Scientifique 1

CSC Current Sourced Converter 21

cVPP community-based Virtual Power Plant 20

DER Distributed Energy Resource 71

DERCAM Distributed Energy Resources Customer Adoption Model 20

DFIG Doubly - Fed Induction Generator 21

DRES Distributed Renewable Energy System 4

DSO Distribution System Operators 4

DSG Dynamics of Smart Grids 1

DVPP Dynamic Virtual Power Plant 2

ECN École Centrale de Nantes 1

EMT ElectroMagnetic Transient 42

ENTSO-E European Network of Transmission System Operators for Electricity 34

Introduction

The work described in this PhD thesis was carried out between October 2019 and December 2022 within the Dynamics of Smart Grids (DSG) team at Laboratoire des Sciences du Numérique de Nantes (LS2N) laboratory, Réseau de Transport d'Électricité (RTE) - École Centrale de Nantes (ECN) chair and The EU's research and innovation funding programme Horizon 2020 (H2020) POwering SYstem flexibiliTY in the Future through Renewable Energy Sources (POSYTYF) project at ECN.

Context of the PhD thesis

Introduction of the LS2N laboratory and DSG team

The LS2N (website: https://www.ls2n.fr/) is a joint research unit with the National Center for Scientific Research (Centre National de la Recherche Scientifique (CNRS)), ECN, the University of Nantes and IMT Atlantique. It is also a partner of the National Institute for Research in Computer Science and Automation (l'Institut National de Recherche en Informatique et en Automatique (INRIA)). It was created in January 2017 as a result of the merger of the Nantes Institute of Communication and Cyber Research (IRCCyN - UMR6597) and the Nantes Atlantique Computer Science Laboratory (LINA - UMR6241). A single objective of LS2N is to bring together Nantes's research expertise in computer science and cybernetics to develop digital sciences, inclusive of other disciplines and taking account of the social challenges involved.

Figure 1: Logo of LS2N

The DSG team of LS2N (website: https://www.ls2n.fr/equipe/dsg/) aims to develop a center of competence in the dynamic operation of electrical grids at national and international levels. With a fresh perspective, we tackle the electrical network difficulties of the energy transition. It is a system approach designed specifically for automation engineers and capable of taking into account the dynamic interactions between the various parts of an electrical production, transmission, and distribution system from the perspective of the system as a whole.

The research schemes are conducted by DSG team are cross-disciplinary and focuses on the following fields:

- Automatic: for stability analysis, managing the system's overall dynamics, and new control methodologies (robustness, managing interactions, aggregating/disaggregating specifications/orders). Large interconnected electrical system aspect: electrical systems/networks (power systems) (at the mesh of the European system)
- Renewable Energy Sources (RES): new technologies, such as marine renewables, dispatchable and non-dispatchable energy sources.

- Power electronics: modelling, analysis, and control of power converters inserted into an electrical network (to connect renewable energy sources or as a new mode of transportation like direct current lines, such as High-Voltage Direct Current (HVDC)).

Currently, the DSG team works on two important projects: RTE - ECN Chair (website: http://chairerte.ec-nantes.fr/) and European H2020 POSYTYF project (website: https://posytyf-h2020.eu/).

Introduction of the RTE - ECN chair

Electricity Transmission Network, usually known as RTE, is the electricity transmission system operator of France. It is responsible for the operation, maintenance and development of the French high-voltage transmission system, which at approximately 100,000 kilometres (62,000 mi), is Europe's largest.

In order to build the smart grids of the future, the RTE - ECN chair (website: http://chairerte.ec-nantes.fr/) seeks to bring together the best skills in several scientific disciplines. The unique alliance between automatic control and electrical engineering provides a tremendous opportunity to boost innovation and foster the necessary technological development. On 14 January 2015 in Nantes, RTE and Centrale Nantes officially inaugurated the international teaching and research Chair for the analysis and control of smart grids.

The RTE - ECN chair was established to address the wide ranging technological challenges faced in electricity today. Grids have to adapt in the context of energy transition. Bringing together automatic control and electrical engineering within the RTE - ECN chair paves the way for future breakthroughs. This pioneering approach is a key feature of the industrial development strategy for smart grids.

Figure 2: Logo of RTE (left) and of ECN (right)

Power grids today have to address new challenges within the context of energy transition, alongside developments in consumption and production and the large-scale integration renewable energies, which are both decentralized and random in nature. Within this more complex technological environment, on both a national and European scale, RTE is adapting its load centers and its network in order to continue to ensure the supply/demand balance, whilst allowing the whole power system to become more flexible. The integration of new technical components within the network and the factoring in of changes in the electricity production mix require large-scale simulations to be undertaken on the dynamic behavior of the European power system.

Introduction of the POSYTYF project

POSYTYF is an abbreviation of POwering SYstem flexibiliTY in the Future through RES (website: https://posytyf-h2020.eu/), which intends to support the further integration of RES into the power system by developing the Dynamic Virtual Power Plant (DVPP) concept. This DVPP aims to aggregate in a portfolio some renewable sources of both dispatchable and non-dispatchable natures, thus enabling an optimal internal redispatch of resources. Compared to other already proposed Virtual Power Plant (VPP), the DVPP concept jointly addresses:

- the static power dispatch at single VPP level.
- the dynamic coordination of several VPPs to provide ancillary services to the system.
- the attainment of an economic optimum.

A multidisciplinary approach combining expertise on power systems, power electronics, automatic control and RES allows to:

- cover both the transmission and distribution levels.

- investigate centralized vs decentralized control concepts for single device and VPP management.
- address the specific stability issues associated to low inertia systems.

The project explores two complementary routes: develop solutions directly implementable in today's power system to support network stability; and investigate future electricity networks with massive RES penetration to formulate technical and regulatory recommendations for tomorrow.

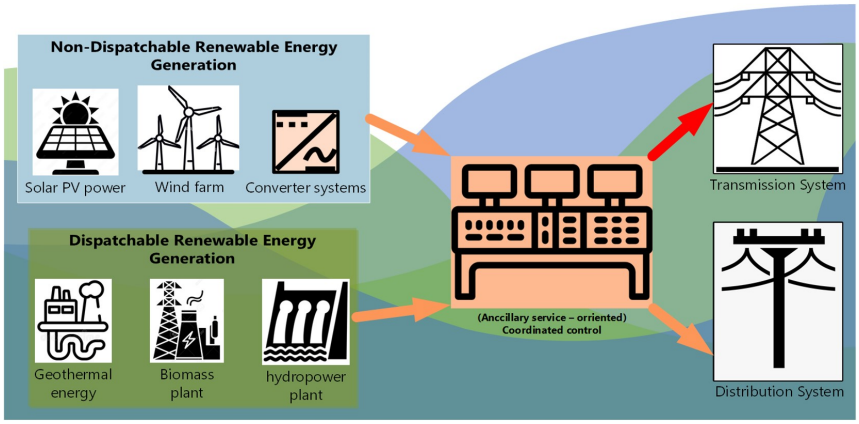

Figure 3: Concept and objectives of POSYTYF project

Project objectives of POSYTYF are to:

- determine optimality criteria to define the perimeter/portfolio of DVPP both for long term and real-time application.
- develop new controllers to allow RES to contribute to ancillary services ultimately enabling system stability.
- Test the developed solutions by simulation and Hardware in the Loop (HiL) on realistic scenarios to validate the feasibility of the concept.
- define new business cases for the optimal operation and configuration of DVPP.
- propose regulatory recommendations to enable DVPP development and operation in conjunction with the generators run in a classic way.
- assess economic competitiveness of the DVPP compared with solutions combining variable RES with electrochemical storage.
- propose new stability definitions and methodologies for stability analysis and assessment.

The expected impacts are to:

- enable the increase of the global (dispatchable + non dispatchable) RES share within the European energy system.
- ensure grid security thanks to real-time optimal redispatch of DVPP resources.
- open participation of RES to ancillary services.
- facilitate adoption of the multidisciplinary DVPP concept thanks to specific dissemination interfacing automatic control, power systems and power electronics disciplines.

Target of the PhD thesis

Power electronics is more and more used on the power transmission and generation grids. Indeed, all wind and photovoltaic generation is connected to the grid by converters. Also, the reinforcement of the grid is frequently done with HVDC lines which consist of power converters into a back-to-back connection and a DC cable. This tendency is extended in order to ensure the transition towards decarbonized energy systems as formulated, for example, in Europe. Converters' control is addressed in a grid context. More specifically, in this thesis, the following aspects have been studied:

- How to coordinate this control with the one of generators in case of RES and among several RESs.
- How to independently regulate each converter in a converter-based power system (e.g., HVDCs) while diminishing the interactions between two close converters (i.e., to damp the coupling modes put into evidence; for the case of RES and HVDCs).
- In general, how to provide grid ancillary services with power electronics RES connected.

Nowadays, with the energy crisis, the mixed sources of energy leads to requirements of reliably and affordably integrating the energy generated from Distributed Renewable Energy System (DRES) into the AC system, grid reinforcement as well as DC grids. To realize such a multi-objectives, HVDC is the preferred technology. In order to link offshore resources to continental grids and to strengthen ties between and within nations, a rapid development of HVDC transmission is already under way. The development of HVDC grids linked to the current AC power system, creating a hybrid AC/DC power system, will result from the acceleration of this trend [1]. By maximising the geographic smoothing of renewable energy sources and utilising flexible generation and loads to fill in the gaps, the future system will be used to transmit power over much greater distances, with different operating points. Thus, the decentralized and optimal control methods are desirable for HVDC systems.

With the domination of DRES in the shares of net annual additions in power generating capacity during the last decade (phenomenal 83% in 2020) [2], a new set of Grid Ancillary Services (GAS) for DRES are introduced and sharply demanded [3]. With the massive penetration of power converter-based sources for DRES(e.g. solar and wind power) grid connection, there is a significant decrease on global grid inertia constant [4]. As a consequence, active power RAMP rate control, which may cause a severe frequency drop and a significant increase in energy price if ignored [3], has to be addressed and provided for DRES. GAS inertia response or Rate of Change of Frequency (RoCoF) control is now required [3], with the two main approaches [5], [4]: hidden inertia control and fast power reserve. In addition, thanks to converter-based power sources dominating situation, fast-response capacity is brought to power system grid [5]. Besides, frequency response for DRES is possible through the mean of active power deload control [5], [4]. More importantly, some of DRES are non-dispatchable, i.e., there is a need of reserved power to be able to provide frequency support. Therefore, frequency support cannot be provided by sole optimization on frequency such as H_∞, but can only be done by incorporating power deload methods [5] into these optimization strategies. Also Fault-Ride Through (FRT) capability is demanded according to [3]. Consequently, the Local Services (LS) are expanding [5]: Maximum Power Point Tracking (MPPT) and active power deloading control, active/reactive powers control, DC voltage control and system stabilization.

Unlike the concentration of the classical synchronous generator power plants, the RES are often distributed on large regions (see [6]). On the one hand, centralized control may provide a better coordination between each generator/converter and with grid, leading to better performance and grid stability. In addition, with DRES penetrated into power systems, since the classical two-level loops vector control separately regulates each converter by one controller, the resulting controllers can not be fully optimized and integrated into the coordination in providing GAS utilizing the fast response capacity of power converter [5]. On the other hand, the adoption of centralized control structure inevitably faces many difficulties, e.g., cost of signal transmission economically and technically, political issues in transmission, lengthy negotiations between Transmission System Operator (TSO) and/or Distribution System Operators (DSO) and lack of resilience in case of failure of part of the actuators. In conclusion, a thorough re-investigation into more coordinated strategies should be conducted and a GAS-oriented control structure should be established, and both approaches of centralization and decentralization should be considered.

A large portion of renewable energy sources, especially renewable energy such as wind and solar energy systems, are non-dispatchable and intermittent, meaning that there are distortions in the generation systems. Thus, the bulk power transmission using HVDC technology, requires a more flexible control with a large range of operating points, i.e., need of nonlinear control. In addition, standing at the DRES position, the integration of DRES into grid brings interaction from grid into DRES systems and vice versa. Since they are converter-based, the DRES and HVDC systems are also highly nonlinear and their system parameter uncertainties are considerable. These problems require better control approaches on tackling disturbance, nonlinearities as well as uncertainties. As a result, there is a need in using nonlinear control to handle nonlinear system, disturbance rejection using optimal control (e.g., H_2/H_∞, fuzzy) and a more robust control approach in order to fulfill the needs of DRES and HVDC systems.

In conclusion, the handling of converter-based systems (e.g. DRES and HVDC) should be done by using a (nonlinear) robust optimal control in a coordinated control structure if possible (for better providing of GAS). On top of that, the control structure should be also implemented in both centralized and decentralized schemes. These requirements lead to the following questions: when and where should a converter-based system use a centralized control or a decentralized control? Which control techniques should be used to handle nonlinearities, uncertainties and disturbance rejection (e.g., fuzzy control, robust H_∞ control and related control techniques)? How to apply these control strategies into a converter-based control system (such as DRES control system) to provide GAS and/or diminish the interactions between two close converters (in case of HVDC for example), i.e., how they are implemented?

Publications

International journals

1. Robust H_2 Nonlinear Fuzzy Decentralized Control Design for a VSC-HVDC Link. (Submitted to Advanced Control for Applications)

International conferences

1. Ngo, H. T., Kamal, E., & Marinescu, B. (2022, October). EMT three-phase VSC grid-connected converter reactive power control using H_∞ LMI MIMO approach. In 2022 IEEE PES Innovative Smart Grid Technologies Conference Europe (ISGT-Europe) (pp. 1-6). IEEE.
2. Ngo, H. T., Kamal, E., & Marinescu, B. (2021, December). Fast Frequency Support at a Wind Energy System Using Time-Varying Inertia and Droop Controls based on Globally Optimal H_∞ Control Design. In 2021 22nd International Middle East Power Systems Conference (MEPCON) (pp. 32-37). IEEE.
3. Ngo, H. T., Kamal, E., Marinescu, B., & Xavier, F. (2020, November). Robust H_∞ Decentralized Control Design for HVDC Link Embedded in a Large-scale AC Grid. In 2020 Electrical Power and Energy Conference.

Organization of this thesis

The works of this thesis are presented as follows:

- The introduction about context of the PhD thesis, the LS2N lab, the RTE - ECN chair, the POSYTYF project and the target of this thesis in chapter Introduction.
- Next, the literature review about renewable energy system modeling and control is done in chapter 1 Literature review.
- The control objectives and proposed approaches are given in chapter 2 Grid-connected power converter system objectives and proposed approaches.
- The Voltage Source Converter (VSC) - based applications are presented in the following chapters: VSC-HVDC application in chapter 3, Permanent Magnet Synchronous Generator (PMSG) - based wind energy system in chapter 4 and STATic synchronous COMpensator (STATCOM) application in chapter 5.

- Finally, the conclusion and discussion about future works are given in chapter Conclusion and possible future works.

Bibliography

[1] TYNDP, Europe's Network Development Plan to 2025, 2030 and 2040, https://tyndp.entsoe.eu/.

[2] "Renewables 2021 global status report.", https://www.ren21.net/wp-content/uploads/2019/05/GSR2021_Full_Report.pdf.

[3] Oureilidis, K., Malamaki, K. N., Gallos, K., Tsitsimelis, A., Dikaiakos, C., Gkavanoudis, S., ... & Demoulias, C. (2020). Ancillary services market design in distribution networks: Review and identification of barriers. Energies, 13(4), 917.

[4] Fernández-Guillamón, A., Gómez-Lázaro, E., Muljadi, E., & Molina-García, Á. (2019). Power systems with high renewable energy sources: A review of inertia and frequency control strategies over time. Renewable and Sustainable Energy Reviews, 115, 109369.

[5] Dreidy, M., Mokhlis, H., & Mekhilef, S. (2017). Inertia response and frequency control techniques for renewable energy sources: A review. Renewable and sustainable energy reviews, 69, 144-155.

[6] "Worldwide wind farms maps.", https://www.thewindpower.net/media_maps_en.php. The Wind Power website.

Chapter 1

Literature review

As discussed in Introduction, there is a need in reinvestigating the modelling and control techniques for power converter-based applications. At the same time, a look into the current status, their popularity and how they are classified can provide a clearer picture and pave the way to develop suitable strategies for their control systems, technically and economically.

This chapter includes the current status of renewable energy and generators, the modelling and controlling methods for power converter systems, the overview of VSC-HVDC systems and finally the most popular wind energy systems at the time being.

1.1 Renewable energy sources overview

1.1.1 Renewable energy share

Nowadays, the energy generation is increasingly shifted from the classical fossil fuel to cleaner energy sources. The shift is not only due to climate change, but also the technologies are developed to a suitable degree for practical application with cost-effective satisfaction, at least in the field of power systems. This trend was reported as in Figs. 1.1, 1.2 and 1.3.

1.1.2 Generators classification

A wind turbine, or alternatively referred to as a wind energy generator, is a type of electric power generator that converts the wind's kinetic energy into electrical energy. There are many types of generators, as resumed in Fig. 1.4. There are several different differences between synchronous and asynchronous machines as shown in table 1.1.

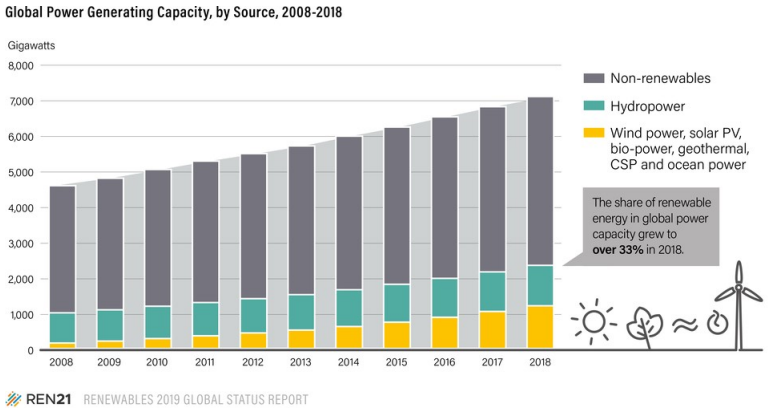

Figure 1.1: Global power generation capacity (2008 - 2018) [1]

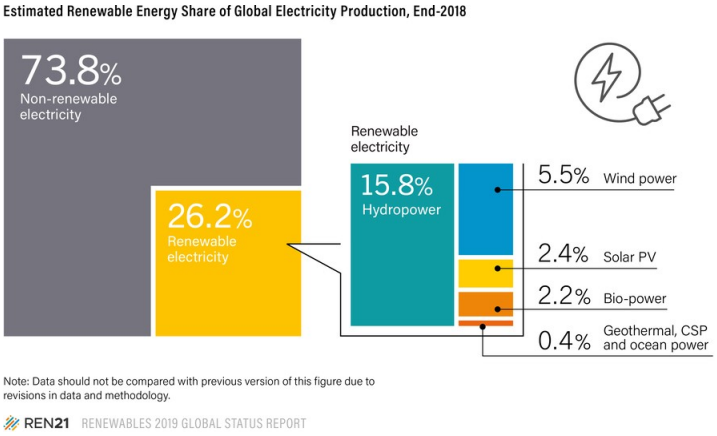

Figure 1.2: Global renewable energy share at the end of 2018 [1]

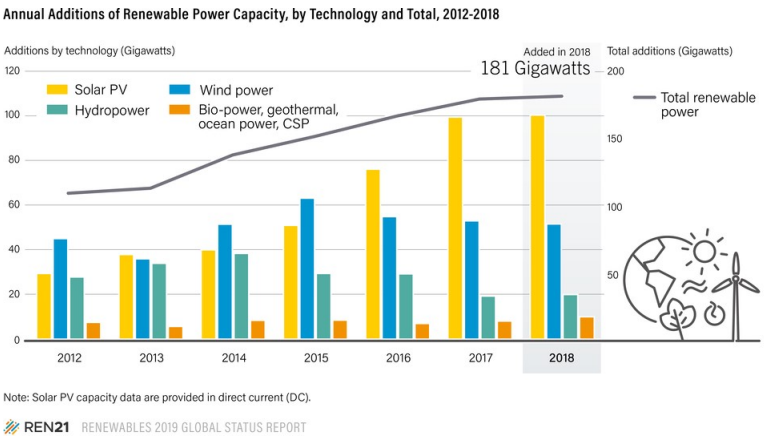

Figure 1.3: Annually additions of renewable power capacity (2012 - 2018) [1]

BASIS	SYNCHRONOUS MOTOR	ASYNCHRONOUS MOTOR
Definition	A synchronous motor is a device whose magnetic field speed NS and rotor speed N are equivalent: $N = NS$	A machine known as an asynchronous motor turns its rotor at a speed N lower than the synchronous speed NS: $N < NS$
Type	Synchronous motors include Brushless motor, Variable Reluctance Motor, Switched Reluctance Motor and Hysteresis motor.	Asynchronous Motor is another name for an AC induction motor.
Slip	There is no slip.	Because there is slip, the value of slip is not zero.
Additional power source	To initially rotate the rotor close to synchronous speed, an additional DC power source is needed.	There is no additional beginning source needed.
Slip ring and brushes	Brushes and a slip ring are needed.	There is no need for brushes or a slip ring.
Cost	More expensive	more affordable
Efficiency	More efficient.	Less efficient.
Power factor	Excitation can be altered to change the power factor from lagging to leading or unity.	Only can run at a lagging power factor.
Current supply	The synchronous motor's rotor receives current.	The rotor need no current supply.
Speed	Independent to the load's change. It is constant.	As the load increases, the asynchronous motor's speed lowers.
Self starting	Synchronous motors cannot start themselves.	It is self starting.
Affect in torque	The torque of the synchronous motor is unaffected by changes in the applied voltage.	The torque of the asynchronous motor is affected by changes in the applied voltage.
Operational speed	Below 300 rpm, they run smoothly and rather well.	Motor operation is great above 600 rpm.
Applications	Synchronous motors are utilized as voltage controllers and in power plants, manufacturing industries, etc.	used in elevators, compressors, blowers, centrifugal fans, paper and textile mills.

Table 1.1: Comparison between Synchronous and Asynchronous Motor [2]

Zooming in the wind turbine generator sector, there are some rapid developments in manufacture and controlling technology. A review is given in [3].

1.2 Power converter modelling and control

1.2.1 Power converter modelling

Power systems modelling is one of the most complicated modelling tasks for control. As power systems are highly nonlinear, the hardest part is to capture adequate information of the grid, power converters or machine both for analysis and control. There are two main methods of power converter modelling, the classical averaged model and the generalized averaged model. Both methods are based on Fourier series, the former deals with DC signal, the latter is used for more general AC signal to capture the sinewave. There are many researches into the so-call averaged modelling method, among which [4]. The more recent updates are presented in [5] - [11].

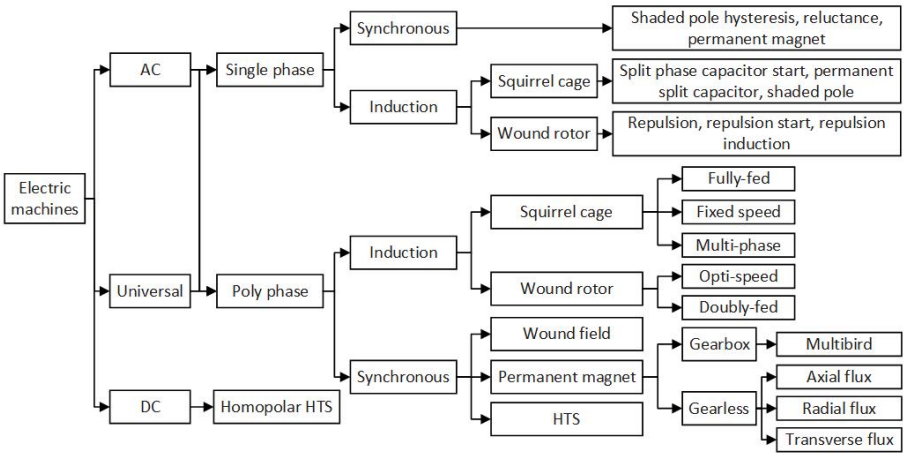

Figure 1.4: Electric machine classification diagram [3]

Factor	SCIG	DFIG	MPIG	SG	EESG	PMSG	HTSG
Torque density	P	−	+	−	P	+	E
Speed range	P	+	+	+	E	+	E
Cost	+	+	−	+	P	−	P
Size	+	−	+	+	P	+	E
Foot print	+	+	+	+	P	+	+
Gearbox requirement	−	−	E	−	E	+	E
Converter size	+	E	−	+	+	+	+
Efficiency	−	+	+	+	+	+	E
Reliability	+	+	+	−	+	+	+
Maintenance	−	−	+	−	+	+	+
Noise level	−	+	+	−	+	+	+
Fault detection	−	−	−	−	+	+	E
Power factor	−	+	+	+	+	+	E
Power quality	−	+	+	+	+	+	E
Power range	+	−	E	−	E	−	+
Simple structure	+	−	+	+	−	+	+
Reduced head-mass	−	−	+	+	P	+	E

E Excellent, + Good, − Fair, P Poor

Table 1.2: Performance comparison of different wind generator concepts [3]

1.2.1.1 Classical averaged model

In DC part of the electrical system or at the steady state, the state values are nearly equal to their averaged values in a time window. The classical averaged method is to find such an averaged value based on a time window of width T as in the definition 1 [4].

Definition 1 *If signal $f(t)$ is averaged on a time window of width T, which is moving along the time axis, one obtains the expression of the so-called sliding average (or local average):*

$$\langle f(t)\rangle_0(t) = \frac{1}{T}\int_{t-T}^{t} f(\tau)\,d\tau$$

Also, there are some properties which should be considered since they are related to the DC part of power system [4].

Property 1 *The property of sliding average includes:*

- *Average of a switch ($S = E$ when $u = 1$ and $S = 0$ when $u = 0$):*

$$\langle S\rangle_0 = \langle E\rangle_0\langle u\rangle_0$$

- *the time derivative of a signal sliding average is the sliding average of the signal time derivative:*

$$\frac{d}{dt}\langle f(t)\rangle_0(t) = \left\langle \frac{d}{dt}f(t)\right\rangle_0(t)$$

- *relations of average of passive circuit elements are as the same as relations of real values:*
  - *For an inductor L:* $\langle v\rangle_0(t) = L\frac{d}{dt}\langle i\rangle_0(t)$
  - *For a capacitor C:* $\langle i\rangle_0(t) = C\frac{d}{dt}\langle v\rangle_0(t)$
  - *For a resistor R:* $\langle v\rangle_0(t) = R\langle i\rangle_0(t)$

For the analytical approach, the mathematical basis and then averaged model are detailed in [4].

1.2.1.2 Generalized averaged model

For the AC signal, the sliding average value cannot fully illustrate the behaviour of the signal (e.g., if a signal is a sine wave, then the sliding average of the signal is equal to zero). This requires to have a more general approach for averaged value of any kind of signal. Definition 2 provides a new concept called generalized averaged model [4].

Definition 2 *The generalized averaged model is based on the waveform representation using the complex Fourier series. Thus, every periodic variable $x(t)$ can be expressed as:*

$$x(t) = \sum_{-\infty}^{+\infty} x_k(t)\,e^{jk\omega t}$$

where ω is the fundamental pulsation and x_k is the coefficient of the k^{th} harmonic

$$x_k = \frac{1}{T}\int_{t-T}^{t} x(\tau)\,e^{-jk\omega\tau}d\tau$$

Property 2 *The property of generalized average includes:*

- *Fundamentals:*

$$\begin{cases} \frac{d}{dt}\langle x\rangle_k(t) = \left\langle \frac{d}{dt}x\right\rangle_k(t) - jk\omega\langle x\rangle_k(t) \\ \langle x.y\rangle_k(t) = \sum_i \langle x\rangle_{k-i}(t)\langle y\rangle_i(t) \end{cases}$$

- *State variables:*

$$\begin{cases} x(t) = \langle x\rangle_0 + 2\left[\mathrm{Re}\left(\langle x\rangle_1\right)\cos(\omega t) - \mathrm{Im}\left(\langle x\rangle_1\right)\sin(\omega t)\right] \\ \langle G_C u\rangle_1 = \langle G_C\rangle_0\langle u\rangle_1 + \langle G_C\rangle_1\langle u\rangle_0 \\ \langle G_a u\rangle_0 = \langle G_a\rangle_0\langle u\rangle_0 + \langle G_a\rangle_1\langle u\rangle_{-1} + \langle G_a\rangle_{-1}\langle u\rangle_1 \end{cases}$$

- *relations of average of passive circuit elements are as the same as relations of real values:*
  - *For an inductor L:*

$$\begin{cases} v = L\frac{di}{dt} \\ \langle v\rangle_k = \left\langle L\frac{di}{dt}\right\rangle_k = jk\omega L\langle i\rangle_k + L\frac{d\langle i\rangle_k}{dt} \end{cases}$$

  - *For a capacitor C:*

$$\begin{cases} i = C\frac{dv}{dt} \\ \langle i\rangle_k = \left\langle C\frac{dv}{dt}\right\rangle_k = jk\omega L\langle v\rangle_k + L\frac{d\langle v\rangle_k}{dt} \end{cases}$$

  - *For a resistor R:*

$$\begin{cases} v = Ri \\ \langle v\rangle_k = R\langle i\rangle_k \end{cases}$$

Details for this method can be found in [4].

1.2.2 Power converter control

DRES are basically the DC sources or low frequency AC sources, which power cannot be injected directly to the AC grid. To deal with this problem, power converters were introduced. As a consequence, power converters brought some new problems for power systems, from frequency and power flow control to the new types of power system oscillations. And again, of course, new controlling methodologies were developed to handle such converter-related problems.

1.2.2.1 Power-angle control

Principle of power-angle control (or voltage-angle control), is based on the following well-known equations [12] - [15] in (1.1). This is a phase-locked loop Phase Locked Loop (PLL) based control, where a PLL is used to determine the frequency and the phase of grid voltage in Fig. 1.5.

$$\begin{cases} P = \dfrac{U_1 U_2 \sin\theta}{X} \\ Q = \dfrac{U_1^2 - U_1 U_2\cos\theta}{X} \end{cases} \tag{1.1}$$

where:

- P and Q are the active and reactive powers between two electrical nodes in AC systems with voltage magnitudes U_1 and U_2.

- The quantities θ and X are the phase-angle difference and line reactance between the two nodes.

Therefore:

- The active power P is mainly related to the phase angle θ.

- The reactive power Q is more related to the voltage-magnitude difference.

The power-angle control structure is shown in Fig. 1.5. The controller is rather easy to design and implement compared to other methodologies. However, it has two drawbacks:

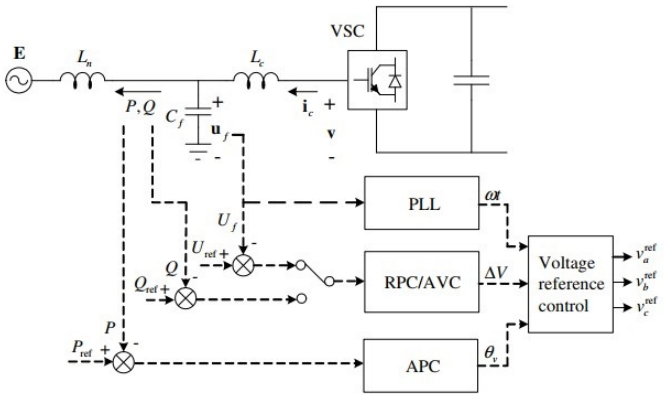

Figure 1.5: Power-angle control for grid-connected converter

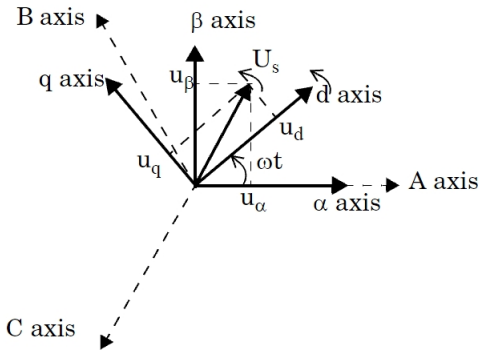

Figure 1.6: abc to dq transformations

- The control system has no general means to damp the various resonances in the AC system as its bandwidth is limited.

- The control system does not have the capability to limit the valve current of the converter (This is a serious problem, as the converters of a VSC - HVDC link usually do not have over-current capability).

Fortunately, these problems can be solved by PLL-based control techniques such as vector control or multi-model/ fuzzy and modern control techniques.

1.2.2.2 Vector current control

The vector control method [4],[16] - [18] is also a PLL - based control. This method is based on the transformations from abc frame to dq frame. It includes two transformations, the abc to $\alpha\beta$ transformation and the $\alpha\beta$ to dq transformation as in Fig. 1.6.

The voltage equations in dq synchronous reference frame are (1.2), where i_{dq} are components of the current flow to/from grid in dq frame corresponding to currents in abc frame. The same notations are for v_{dq} and v_{dqconv}.

The classical approach is to decouple the currents in dq frame and then establish the transfer function from the control signals m_d and m_q to the currents. This also mean that they are assuming grid frequency ω as a constant (i.e. $\dot{\theta} = \omega$, $\omega = \omega_0 = 100\pi$). As a result, the dq system equation in Fig. 1.7 becomes:

$$\begin{cases} \dfrac{di_d}{dt} = -\dfrac{R}{L}i_d + \omega_0 i_q + \dfrac{1}{L}\left(-V_d + \dfrac{m_d V_{DC}}{2}\right) \\ \dfrac{di_q}{dt} = -\dfrac{R}{L}i_q - \omega_0 i_d + \dfrac{1}{L}\left(-V_q + \dfrac{m_q V_{DC}}{2}\right) \end{cases} \tag{1.2}$$

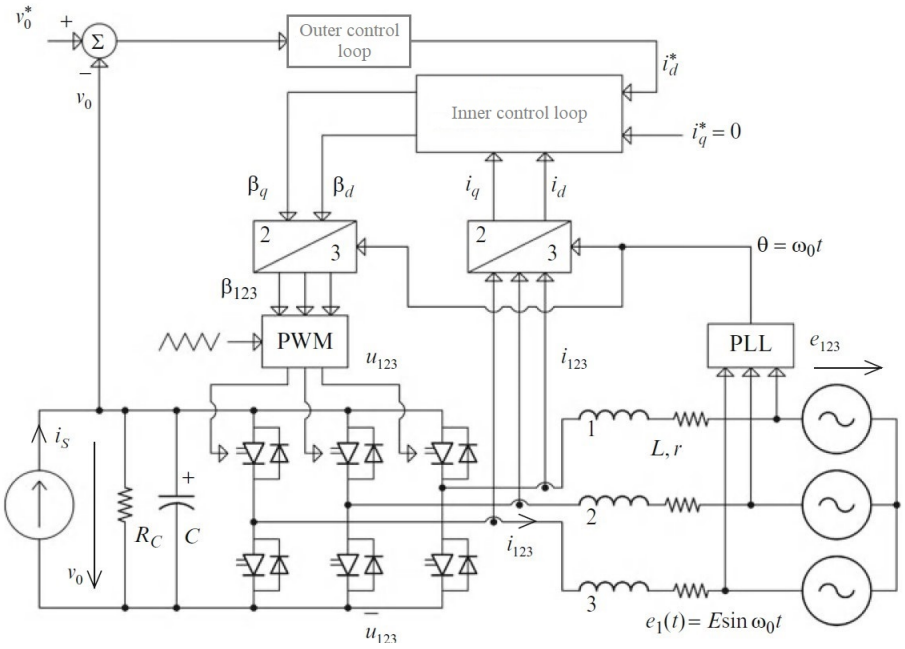

Figure 1.7: Vector current control structure

The classical vector control using two separated Proportional – Integral – Derivative (PID) control loops shown as in Fig. 1.7. Using the feed-forward terms $\{\omega L i_q, V_d\}$ (for i_d control) and $\{\omega L i_d, V_q\}$ (for i_q control), the control structure is able to decouple the currents i_d and i_q. These decoupled terms can provide some aid in smoothing the transient behavior, but may make it worse in case of grid fault happen, where grid voltage V_d, V_q and grid frequency ω vary greatly.

The two i_d and i_q dynamics are handled by identical PI control, with closed-loop transfer function (from i_{ref} to i for both of i_d and i_q dynamics) are:

$$\begin{cases} i(s) = i_{ref}(s)\dfrac{G(s)}{1+G(s)} \\ G(s) = \dfrac{K_P}{Ls}\dfrac{s+\dfrac{K_i}{K_p}}{s+\dfrac{R}{L}} \end{cases}$$

By using pole cancellation for the pole $s + \dfrac{R}{L}$, i.e.:

$$\frac{K_i}{K_p} = \frac{R}{L}$$

The transfer function of closed-loop is now:

$$i(s) = i_{ref}(s)\frac{1}{1+\dfrac{L}{K_P}s}$$

Choosing a time constant $\tau_i = \dfrac{L}{K_P}$, the PID controller gains are calculated as:

$$\begin{cases} K_P = \dfrac{L}{\tau_i} \\ K_i = K_p\dfrac{R}{L} = \dfrac{R}{\tau_i} \end{cases}$$

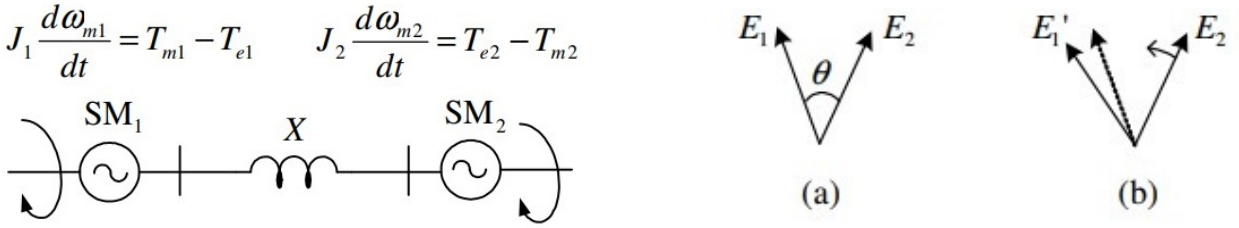

Figure 1.8: Internal power-synchronization mechanism for synchronous machines

The current, the DC voltage, the AC voltage or the power flow through the converter are regulated to reference values. For that, the vector control is structured in two layers, called the inner and outer loops as shown in Fig. 1.7. Design is given in detail in, e.g., [4] (Chapter 9) or in [18].

The vector control is easy to design and to implement. In addition, thanks to the two layers-structure, hard constraints on current can be easily taken into account to protect the converter. However, as a Single Input Single Output (SISO) based control method, performances can be limited, especially in case of connection to weak grids. This limitation can be compensated by using modern control using Multi Input Multi Output (MIMO) model-based advanced control methods (e.g., optimal H_2/H_∞ or fuzzy control).

1.2.2.3 Advanced control

MIMO control can provide more performance and stability margin for converter system since it can object to some characteristics of the power system while stabilizing the system. At the same time, it is relatively easy to take into account nonlinearities (e.g., using fuzzy based control [19]) and uncertainty (e.g., using robust control [21]). The overall control objectives can also be achieved by means of Linear Matrix Inequality (LMI) techniques [20], which makes the MIMO control become attractive to power converter systems.

The MIMO control can also be a PLL - based control, with the design process relatively similar to the one of classical cascade vector control.

1.2.2.4 Power-synchronization control

This method is an alternative of PLL-based converter control, and it is highly developed by ASEA Brown Boveri (ABB) recently in [12], [22] - [25]. For the PLL controller (which is a PID controller), in the transformation from abc to dq frame, there are always problems with stability and performance. To handle this, the Power - Synchronization Control (PSC) uses the internal synchronization mechanism in AC systems (that the VSC can utilize to synchronize with the AC system).

In Fig. 1.8 it is recalled the principle of PSC in case of Synchronous Generator (SG) [12]: from steady-state, T_{m1} is increased in a short time and brought back to its initial value. The advance of the mechanical angle of the rotor of SM_1 inevitably causes an advance of the phase of the electromotive force (emf) of SM_1 (figure a). This also translates into an increase of the electric power transmitted from SM_1 to SM_2. This increase in power is equivalent to an increase in the electromagnetic torque T_{e2} of SM_2. As the rotor of SM_2 starts to accelerate, the same thing occurs with the phase of E_2, as indicated by the arc-shaped arrow in (b). After a transient (which in reality involves a certain amount of damping), the phase difference between the emfs of the two SMs is brought back to its initial value, and the system is in steady-state again.

In case of grid connected VSC, the power-synchronization loop controls the active power output from the VSC directly, whereas the reactive power (or alternating voltage) is regulated by modifying the magnitude of the voltage. Theses relationships are shown as in (1.3) for active power, and in (1.1) for reactive power, similar to the case of power-angle control.

$$\frac{d\Delta\theta}{dt} = k_p \left(P_{ref} - P\right) \tag{1.3}$$

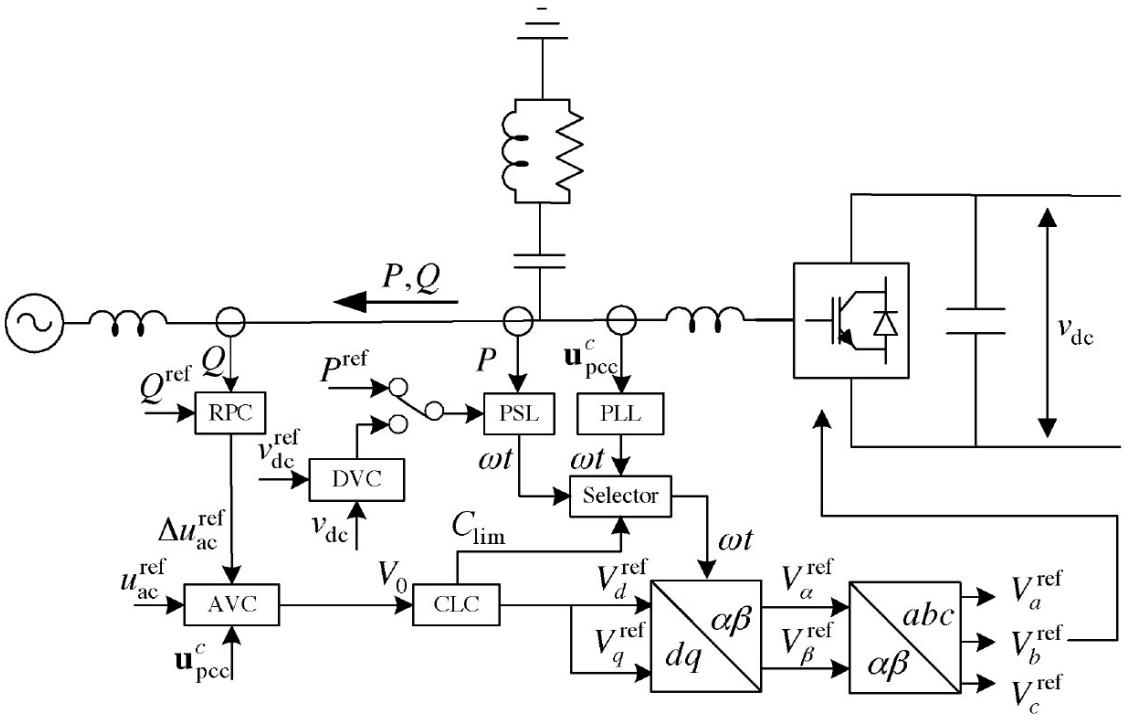

Figure 1.9: Power-synchronization control for grid connected VSC converter

The controller then can be designed by any suitable methods, e.g., as in Fig. 1.9 [23], where RPC is reactive power controller, AVC is alternating-voltage controller, DVC is direct-voltage controller, CLC is current-limitation controller, PSL is power-synchronization loop and PLL is the back-up PLL control in case of faulty events to limit the current in converter (e.g., grid short-circuit).

1.2.3 Anti-windup techniques

For improving the performance of converter control which contains many constraints, the anti-windup techniques can be utilized. Books from [26] - [28] are the state of the art in this field. Also, [27] provides a detailed process to obtain an anti-windup mechanism for any kind of system. In addition, [28] provides an intensive look into nonlinear constrained and saturated control of power electronics and related systems.

The anti-windup augmentation scheme is as in Fig. 1.10, where:

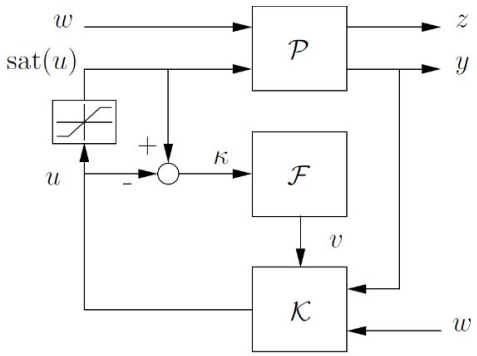

Figure 1.10: The anti-windup augmentation scheme

- F is the anti-windup augmentation

- K is the unconstrained controller

- P is the plant

- W is the vector of disturbance and reference

- y is the anti-windup augmented measured output response

- z is the anti-windup augmented performance output response

There anti-windup objectives are

- Unconstrained response recovery (model recovery anti-windup): recover the unconstrained closed-loop response asymptotically whenever this is possible.

- Small signal preservation: keep the same response between the anti-windup augmented closed-loop system and the unconstrained closed-loop system whenever this is possible.

- Internal stability: in the absence of exogenous inputs, a desired constant operating point asymptotically stable with a basin of attraction at least as large as the set of states over which the system is expected to operate (globally or regionally).

- Input-output stability: induce a bounded response for initial states and exogenous inputs that are expected during operation.

The anti-windup augmentation types are grouped by:

- Linear vs nonlinear: the augmentation F is a linear system or nonlinear system

- Continuous-time vs. sampled data: the augmentation F is a continuous or a discrete system

- Static vs. dynamic: the augmentation F is a static system or dynamic system

- External vs. full authority: the augmentation F is only affecting the input-output of the controller or it can directly affect the controller states

1.3 Virtual power plant

A VPP is a cloud-based distributed power plant that aggregates the capabilities of heterogeneous distributed energy resources to improve power generation and trade or sell power on the electricity market. Virtual power plants are already in use in the United States, Europe, and Australia. A virtual power plant is a system that combines many types of power sources to provide a stable overall power supply [29]. The sources often form a cluster of different types of dispatchable and non-dispatchable energies, controllable or flexible load distributed generation systems that are controlled by a central authority and can include micro combined heat and power, natural gas-fired reciprocating engines, small-scale wind power plants, Photovoltaics (PV), run-of-river hydroelectricity plants, small hydro, biomass, backup generators, and energy storage systems.

Benefits of this VPP system include the capacity to offer peak load electricity or load-following power generation on short notice. A VPP of this type can replace a traditional power plant while providing increased efficiency and flexibility, allowing the system to respond to load changes more effectively. The disadvantage is that the system is more sophisticated, necessitating complicated optimization, control, and secure communications [30].

1.3.1 Current researches on VPP and its structure in context of technology, economy and environment

[31] gives a full discussion of the microgrid and VPP ideas used in power systems, as well as distributed energy resource scheduling. The formulation type and objective function, solving technique, uncertainties, reliability, reactive power, control and automation, emission, stability, demand response, and multi-objective are all related with the scheduling issue. It also provides a thorough comparison of previous studies completed before 2016, giving us a comprehensive picture of VPP in terms of technology, economy, and environment. [32] [33] provide a comprehensive review on structure and operation of a virtual power plant in a power system, including the topology of the power system and the VPP integration and control methods (characteristics of VPP, renewable energy systems, conventional energy resources, framework of VPP and internal control of VPP). [32] also provides the business of market bidding strategy of VPP. The DRES management techniques and VPP applications are carefully investigated in [32].

[34] shows a novel and complete approach about goals, structure, and roles in VPP using community-based Virtual Power Plant (cVPP). It provides the structure (of five building blocks) that together form a cVPP: the community involved, the community-logic under which the project operates, the portfolio of distributed energy resources aggregated and controlled by an ICT control architecture (ICT Architecture comprises all static and dynamic aspects of the framework defining your company's information and telecommunication structures), and the roles that communities can collectively play in the energy system by means of cVPP.

[35] gives a techno-economic study of solar grid-based virtual powerplant (in Indian) power industry. The Distributed Energy Resources Customer Adoption Model (DERCAM), a mixed integer linear Programming based decision making tool, is used. A case study of Punjab State Power Corporation Limited, a state power provider, is explored to determine the potential of VPP and its repercussions. The paper's primary goals are cost reduction, peakload reduction, and reliability enhancement. The DERCAM model simulates various load profiles and determines the best investment option, ensuring monetary advantages for both the customer and the utility.

[38] describes an approach for multi-energy VPP control while accounting for multiple uncertainties: a robust stochastic optimum dispatching method for solving the scheduling issue while accounting for multiple uncertainties. The uncertain set of cardinalities with a resilient adjustable coefficient is used to represent the output of wind turbines and photovoltaics for the source side uncertainties. The Wasserstein generative adversarial network with gradient penalty is utilised to produce electric, thermal, cooling, and natural gas load scenarios, and K-medoids clustering is employed to generate typical scenes for the load side uncertainty. The min-max-min structure was represented by a two-stage robust stochastic optimum model. The original model was solved alternatively using the dual transformation theory and the column constraint generation approach.

[39] illustrates a capability-coordinated frequency control scheme of a VPP including adjustable-speed pumped storage hydropower, a wind power plant, and an energy storage system to support the frequency nadir and reduce the steady-state error of system frequency. This paper demonstrates the role of VPP on frequency nadir supported in a wide context.

1.3.2 Practices and existed projects on VPP

There are some well-known VPP projects, mostly started before 2012 [33]: 1. European Union 5th Framework Programme, 2. EDISON Project, 3. Konwers 2010, 4. FENIX Project European project FENIX—Northern and Southern Scenarios, and 5. 'Smart' Heat Pumps. There are also three practical cases in Ireland, Belgium and the Netherlands, which highlight the diversity of cVPPs [34], and one VPP application in India [35]. In [36] [37], an overview of ancillary services for VPP in Spain is given, including a detailed technical description of the services and the organization of the ancillary services markets. In addition, a comprehensive review of different optimization algorithms and tools used by the agents and system operator within the Spanish electricity business is presented.

1.4 VSC-based power energy applications

One of the VSC application is the VSC-HVDC, which is increasingly becoming popular in bulk power transmission thanks to its power efficiency and performance. Economically and technically, although HVDC is relatively expensive compared to High-Voltage Alternating Current (HVAC) transmission system, the former provide a more

robust and reliable transmission solution. In addition, compared to HVAC the applicability of HVDC in modern grid is much larger, and its functionalities are much more suitable to the DRES-dominant grid.

As for wind energy systems, there are two popular and overall cost-efficient types of wind energy generator, Doubly - Fed Induction Generator (DFIG) and PMSG. These two types of wind turbine energy system use VSC - based converter connected back to back to connect to the grid. However, DFIG wind systems require a gear-box system and with a power converter rating at around 30%, while PMSG systems are with full rate converters and gear-box are optional. Thus, in comparison with PMSG, DFIG has poorer output power quality but lower initial cost of power converters. At the same time, in order to maximize the produced powers from wind turbine energy system, an MPPT searching table has to be established [106]. In addition, not only the maximum produced power is desired, but also a deload level of produced power is needed to have suitable reserved power, which then is used for ancillary services [106]. The searching table, along with searching strategy, are reminded in this subsection [106].

1.4.1 VSC-HVDC system

HVAC is a classical and economical mean of power transmission [40] [41]. However, compared to traditional HVAC, HVDC technology is proven to have more performance and less losses, especially for long transmission lines [41], [42]. In addition, although HVDC requires more complicated control system, but with the recent development in HVDC control and protection [43], [44], the HVDC transmission systems are becoming more and more popular and affordable, technically and economically.

Traditional bulk-power line-commutated thyristors are the primary building blocks of the converters at the sending and receiving end stations in HVDC transmission systems [46]. This type of HVDC is known as a Current Sourced Converter (CSC)-HVDC. This HVDC solution is cheaper compared to Insulated-Gate Bipolar Transistor (IGBT)-based HVDC [46], [47]. However, IGBT-based HVDC, known as VSC-HVDC, has many advantages over traditional CSC-HVDC, including: rapid and separated reactive and active powers (i.e., support grid voltage and frequency fast/slow response), easily reversing active power flow by reversing the DC current without changing polarity of DC voltage, able to supply weak AC networks, hamonic mitigation and filter tunning are simpler, and finally VSC-HVDC supports black start [46], [44], [45].

A VSC-HVDC consists of two VSC converters connected back to back as in Fig. 1.11. Each side of the converter is connected to the AC grid, and the harmonic is filtered by an LCL filter. Depending on the situation, before connected to the grid, the converter may need a transformer to balance the voltage and even a smoothing reactor to further reduce the harmonics in the output powers of the converter.

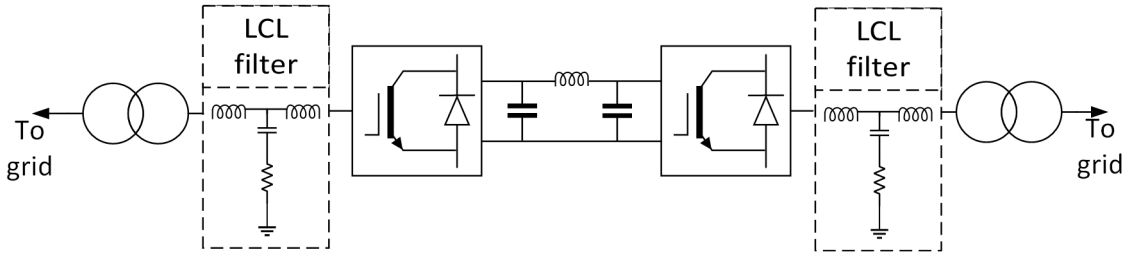

Figure 1.11: VSC-HVDC line with two back to back VSC converters

1.4.2 Doubly-fed induction generator

DFIG is a widely used technology [48] - [53], [55] - [61], [65] - [69],[71] - [72], [74] - [75]. As shown in Fig. 1.12 it consists of:

- Rotor Side Converter (RSC): control the generator output power.
- Grid Side Converter (GSC): ensures the stability of the DC-link voltage irrespective of the direction and magnitude of the rotor power.
- The equivalent electric circuit model of DFIG is as in Fig. 1.13.

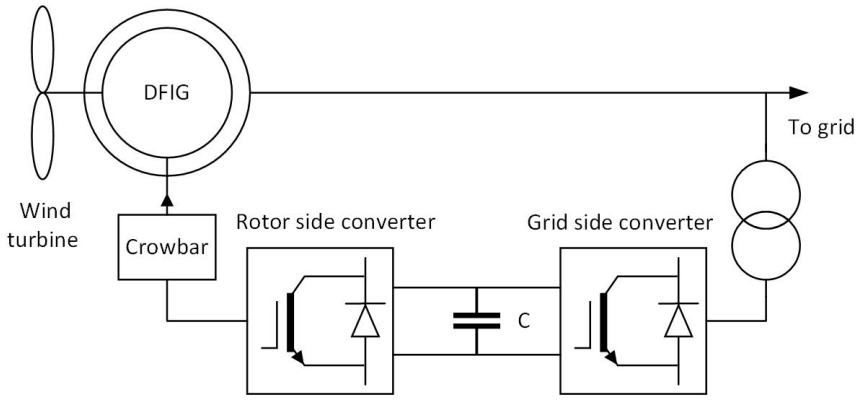

Figure 1.12: DFIG with back to back converter

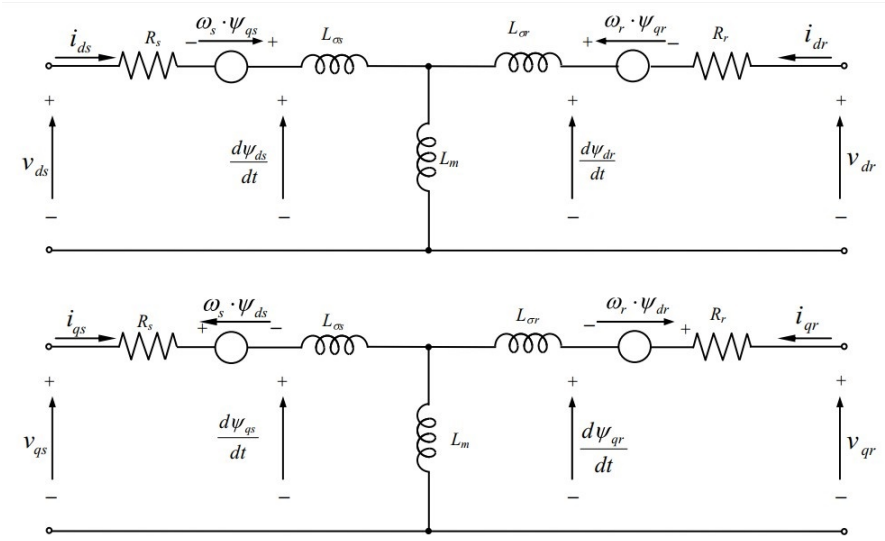

Figure 1.13: DFIG equivalent modelling

The current research status on DFIG modeling:

- For the full model, [51] and [77] shows a complete and detailed insight into DFIG: modelling, testing, voltage dips analysis and control (vector control and direct control), including torque control and power control. [77] also provides some knowledge on test bench for DFIG building in the lab.
- [48] and [73] can be used for additional information. [1] also introduces multi-machine modeling and inter-area oscillation damping.
- Most of the recent studies using classical averaged model [48] - [53], [55] - [61], [65] - [69], [71] - [72], [74] - [75].
- For enhancing the modelling task, some used multi-model/ Fuzzy [49][54][56].
- MATLAB/Simscape Specialized Power Systems has libraries for DFIG detailed model.

The current research status on DFIG controlling:

- For the control of DFIG, which the focus on RSC and GSC control, [1] provides clear methods (chapter 3) with an assumption of averaged model. However, [51] provides a more detailed technique in direct power control (chapter 8).

- For RSC control, many researches used MPPT [48], [50] - [51], [53], [58], [61], [66], [68], [76]. In addition, [76] provides a detailed description about MPPT and related techniques in photovoltaic energy generation systems.

1.4.3 Permanent magnet synchronous generator

A PMSG with two level converters AC/DC/AC is given in Fig. 1.14 [78] - [80], [82] - [84], [86] - [88], [91] - [93], [98].

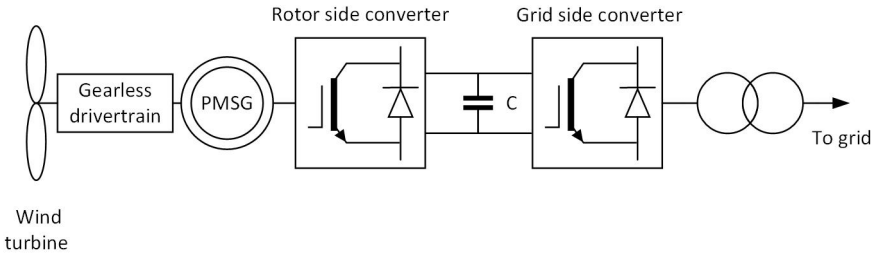

Figure 1.14: PMSG with full converter

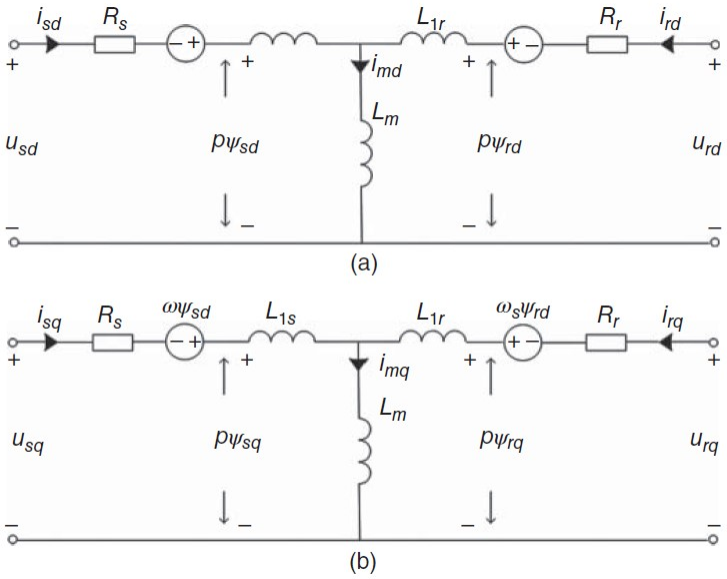

Figure 1.15: PMSG equivalent modelling

The current research status on modeling:

- For the full model, [95] and [104] shows a complete and detailed insight into PMSG.
- For the control task, one should use the dq equations provided by MATLAB's website, which is confirmed by [78], [82], [84], [95] - [96], [98], [104].
- MATLAB/ Specialized Power Systems has libraries for detailed model. The current research status on controlling:
- For the control of PMSG: the wind turbine control itself and the control of the full-scale converter [78] - [80], [82] - [84], [86] - [88],[91] - [93], [96], [98].
- [96] provides details in PMSG controlling.

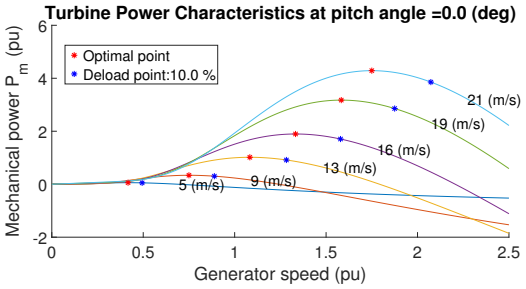

Figure 1.16: The output power at different wind speeds at MPPT and at 10% deload

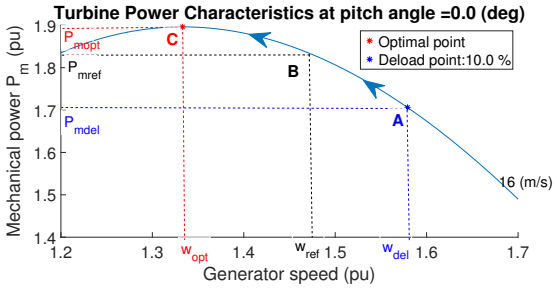

Figure 1.17: The generator speed deloading strategy at wind speed of 16 m/s

- MPPT is used for torque control [78], [82],[88], [91], [93], [96].

1.4.4 Maximum power point tracking data generation

MPPT is a well-known method to extract maximum power from renewable energy sources [106] (e.g., wind or solar energy). In the scope of this thesis, only MPPT for wind turbine is generated, but the MPPT for other sources (e.g., MPPT for solar energy) can be achieved with similar process. MPPT can also help to deload the system to keep an amount of reserved power in order to provide ancillary services. 10% is a typical value for the reserve of the deloading control using generator speed control. Higher reserve can be ensured if pitch angle control is used in addition.

Firstly, consider the pitch angle is kept at 0 (deg), the deloading relationship between wind speed, generator speed and wind turbine mechanical power is given in Fig. 1.16.

To understand the deloading strategy, consider the wind turbine is operating at wind speed of 16m/s. The wind turbine will produce power at 10% deloading point A of Fig. 1.17 to reserve 10% of its power capacity.

To utilize this reserved power for frequency support, a droop relationship is established [105]

$$\Delta P_{ref} = -\frac{1}{R}\Delta f, \tag{1.4}$$

where ΔP_{ref} is the required amount of change in power when there is a change in frequency Δf.

A consequence of a shortage in power of the the grid is a fall in grid frequency [105]. This fall will partly be compensated by the reserved power of wind turbine. At this moment, through the droop relationship (1.4), the wind turbine will have to move its operating point from A to B to increase its mechanical power. The operating point is now at

$$P_{mref} = P_{mdel} + \Delta P_{ref} = P_{mdel} - \frac{1}{R}\Delta f. \tag{1.5}$$

This P_{mref} will be used to determine desired generator speed Ω_{ref}, and through generator speed control to shift the operating point of wind turbine. This action can easily be achieved by a look-up table [106], but with a cost in delay due to the time for searching the equivalent value of Ω_{ref}. To overcome this, because the two points of optimal and deloading points are very close, it is possible to consider that the three points A, B and C are collinear. As a consequence, the relationship between P_{mref} and Ω_{ref} is [106]:

$$P_{mref} = P_{mdel} + (P_{mopt} - P_{mdel})\frac{\Omega_{del} - \Omega_{ref}}{\Omega_{del} - \Omega_{opt}} \tag{1.6}$$

Based on (1.6), the value of Ω_{ref} is

$$\Omega_{ref} = \Omega_{del} - (\Omega_{del} - \Omega_{opt})\left(-\frac{1}{R}\frac{\Delta f}{P_{mopt} - P_{mdel}}\right) \tag{1.7}$$

Secondly, consider all the deloading relationships between wind speed, generator speed, pitch angle and wind turbine mechanical power in the 3D scheme of Fig. 1.18. The program to generate this data is as in appendix section B.1 (Listing. B.1).

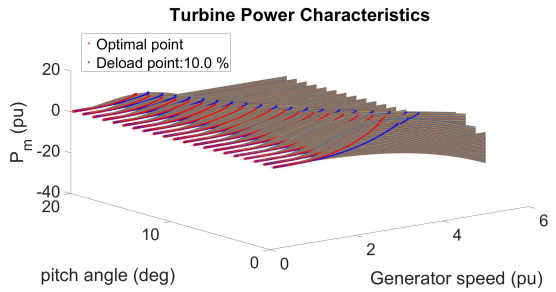

Figure 1.18: The output power at different wind speeds (1-30 m/s) at MPPT and at 10% deload

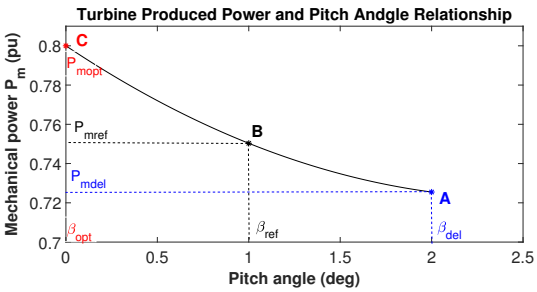

Figure 1.19: The pitch angle deloading strategy at wind speed of 12 m/s

Again, to deload the wind turbine using pitch angle control, the pitch angle will be kept at deloading point instead of optimal point (0 deg) [106]. To understand the deloading pitch angle strategy, consider the wind turbine is operating at constant wind speed 12 (m/s) for Fig. 1.19.

At steady-state, wind turbine will operate at point A with pitch angle β_{del} and produce power at P_{del}. Following a request to increase the power (1.5) via the droop control (1.4), the pitch angle will be changed from point A to point B.

Once again, a look-up table can be used, but this results in introducing significant delay into the control loop. This problem can be dealt with the same method as in (1.6). The relationship between desired produced power P_{mref} and desired pitch angle β_{ref} is then

$$P_{mref} = P_{mdel} + (P_{mopt} - P_{mdel}) \frac{\beta_{del} - \beta_{ref}}{\beta_{del} - \beta_{opt}} \tag{1.8}$$

From droop control relationship (1.5) and (1.8), the desired pitch angle β_{ref} is

$$\beta_{ref} = \beta_{del} - (\beta_{del} - \beta_{opt}) \left(-\frac{1}{R} \frac{\Delta f}{P_{mopt} - P_{mdel}} \right). \tag{1.9}$$

Bibliography

[1] Raturi, A. K. (2019). Renewables 2019 global status report.

[2] "Difference Between Synchronous and Asynchronous Motor". https://circuitglobe.com/difference-between-synchronous-and-asynchronous-motor.html

[3] Goudarzi, N., & Zhu, W. D. (2012, November). A review of the development of wind turbine generators across the world. In ASME International Mechanical Engineering Congress and Exposition (Vol. 45202, pp. 1257-1265). American Society of Mechanical Engineers.

[4] Bacha, S., Munteanu, I., & Bratcu, A. I. (2014). Power electronic converters modeling and control. Advanced textbooks in control and signal processing, 454(454).

[5] Aganza-Torres, A., Cárdenas, V., & Pacas, M. (2019). Generalized average model for a high-frequency link grid-connected DC/AC converter. International Journal of Electrical Power & Energy Systems, 107, 344-351.

[6] Che, Y., Xu, J., Yang, Y., Zhou, J., & Zhao, Y. (2018). Large signal modeling method for AC/DC independent power system in dq-coordinates. IEEE Access, 6, 32207-32215.

[7] Li, H., Ju, P., Yu, Y., Wu, F., & Liu, Y. (2015, June). Quasi generalized Hamiltonian model of power systems considering the reference node under stochastic excitations. In 2015 IEEE Eindhoven PowerTech (pp. 1-5). IEEE.

[8] Liu, X., Cramer, A. M., & Pan, F. (2016). Generalized average method for time-invariant modeling of inverters. IEEE Transactions on Circuits and Systems I: Regular Papers, 64(3), 740-751.

[9] An, F., Song, W., Yang, K., Hou, N., & Ma, J. (2018). Improved dynamic performance of dual active bridge dc–dc converters using MPC scheme. IET Power Electronics, 11(11), 1756-1765.

[10] Mueller, J. A., & Kimball, J. W. (2018). An improved generalized average model of DC–DC dual active bridge converters. IEEE Transactions on Power Electronics, 33(11), 9975-9988.

[11] Ebrahimi, H., & El-Kishky, H. (2015). A novel Generalized State-Space Averaging (GSSA) model for advanced aircraft electric power systems. Energy Conversion and Management, 89, 507-524.

[12] Zhang, L., Harnefors, L., & Nee, H. P. (2010). Modeling and control of VSC-HVDC links connected to island systems. IEEE Transactions on Power Systems, 26(2), 783-793.

[13] Joos, G., Moran, L., & Ziogas, P. (1991). Performance analysis of a PWM inverter VAR compensator. IEEE Transactions on Power Electronics, 6(3), 380-391.

[14] Svensson, J. (1995). Power angle control of grid-connected voltage source converter in a wind energy application.

[15] Ooi, B. T., & Wang, X. (1990). Voltage angle lock loop control of the boost type PWM converter for HVDC application. IEEE Transactions on Power Electronics, 5(2), 229-235.

[16] Irwin, J. D. (2002). Control in power electronics: selected problems. Elsevier.

[17] Bajracharya, C. (2008). Control of VSC-HVDC for wind power (Master's thesis, Institutt for elkraftteknikk).

[18] Bajracharya, C., Molinas, M., Suul, J. A., & Undeland, T. M. (2008). Understanding of tuning techniques of converter controllers for VSC-HVDC. In Nordic Workshop on Power and Industrial Electronics (NORPIE/2008), June 9-11, 2008, Espoo, Finland. Helsinki University of Technology.

[19] Tanaka, K., & Wang, H. O. (2001). Fuzzy control systems design and analysis. John Wiley & Sons Ltd.

[20] Duan, G. R., & Yu, H. H. (2013). LMIs in control systems: analysis, design and applications. CRC press.

[21] Zhou, K., & Doyle, J. C. (1998). Essentials of robust control (Vol. 104). Upper Saddle River, NJ: Prentice hall.

[22] Mitra, P., Zhang, L., & Harnefors, L. (2013). Offshore wind integration to a weak grid by VSC-HVDC links using power-synchronization control: A case study. IEEE Transactions on Power Delivery, 29(1), 453-461.

[23] Zhang, L., Harnefors, L., & Nee, H. P. (2010). Power-synchronization control of grid-connected voltage-source converters. IEEE Transactions on Power systems, 25(2), 809-820.

[24] Harnefors, L., Hinkkanen, M., Riaz, U., Rahman, F. M., & Zhang, L. (2018). Robust analytic design of power-synchronization control. IEEE Transactions on Industrial Electronics, 66(8), 5810-5819.

[25] Harnefors, L., & Zhang, L. (2019). U.S. Patent No. 10,389,129. Washington, DC: U.S. Patent and Trademark Office.

[26] Tarbouriech, S., Garcia, G., da Silva Jr, J. M. G., & Queinnec, I. (2011). Stability and stabilization of linear systems with saturating actuators. Springer Science & Business Media.

[27] Zaccarian, L., & Teel, A. R. (2011). Modern anti-windup synthesis. In Modern Anti-windup Synthesis. Princeton University Press.

[28] Conficoni, C. (2013). Nonlinear constrained and saturated control of power electronics and electromechanical systems.

[29] "Feasibility, beneficiality, and institutional compatibility of a micro-CHP virtual power plant in the Netherlands". http://repository.tudelft.nl/view/ir/uuid%3Aee01fc77-2d91-43bb-83d3-847e787494af/

[30] Fang, X., Misra, S., Xue, G., & Yang, D. (2011). Smart grid—The new and improved power grid: A survey. IEEE communications surveys & tutorials, 14(4), 944-980.

[31] Nosratabadi, S. M., Hooshmand, R. A., & Gholipour, E. (2017). A comprehensive review on microgrid and virtual power plant concepts employed for distributed energy resources scheduling in power systems. Renewable and Sustainable Energy Reviews, 67, 341-363.

[32] Zhang, G., Jiang, C., & Wang, X. (2019). Comprehensive review on structure and operation of virtual power plant in electrical system. IET Generation, Transmission & Distribution, 13(2), 145-156.

[33] Nikonowicz, Ł., & Milewski, J. (2012). Virtual power plants-general review: structure, application and optimization. Journal of power technologies, 92(3).

[34] van Summeren, L. F., Wieczorek, A. J., Bombaerts, G. J., & Verbong, G. P. (2020). Community energy meets smart grids: Reviewing goals, structure, and roles in Virtual Power Plants in Ireland, Belgium and the Netherlands. Energy Research & Social Science, 63, 101415.

[35] Sharma, H., & Mishra, S. (2020). Techno-economic analysis of solar grid-based virtual power plant in Indian power sector: A case study. International Transactions on Electrical Energy Systems, 30(1), e12177.

[36] Miguélez, E. L., Cortés, I. E., Rodríguez, L. R., & Camino, G. L. (2008). An overview of ancillary services in Spain. Electric Power Systems Research, 78(3), 515-523.

[37] Egido, I., Fernandez-Bernal, F., & Rouco, L. (2008). The Spanish AGC system: description and analysis. IEEE Transactions on Power Systems, 24(1), 271-278.

[38] Kong, X., Xiao, J., Liu, D., Wu, J., Wang, C., & Shen, Y. (2020). Robust stochastic optimal dispatching method of multi-energy virtual power plant considering multiple uncertainties. Applied Energy, 279, 115707.

[39] Kim, J., Muljadi, E., Gevorgian, V., Mohanpurkar, M., Luo, Y., Hovsapian, R., & Koritarov, V. (2019). Capability-coordinated frequency control scheme of a virtual power plant with renewable energy sources. IET Generation, Transmission & Distribution, 13(16), 3642-3648.

[40] Kalair, A., Abas, N., & Khan, N. (2016). Comparative study of HVAC and HVDC transmission systems. Renewable and Sustainable Energy Reviews, 59, 1653-1675.

[41] Meah, K., & Ula, S. (2007, June). Comparative evaluation of HVDC and HVAC transmission systems. In 2007 IEEE Power Engineering Society General Meeting (pp. 1-5). IEEE.

[42] May, T. W., Yeap, Y. M., & Ukil, A. (2016, November). Comparative evaluation of power loss in HVAC and HVDC transmission systems. In 2016 IEEE Region 10 Conference (TENCON) (pp. 637-641). IEEE.

[43] Wang, S. (2016). Control and protection of HVDC grids (Doctoral dissertation, Cardiff University).

[44] Sharifabadi, K., Harnefors, L., Nee, H. P., Norrga, S., & Teodorescu, R. (2016). Design, control, and application of modular multilevel converters for HVDC transmission systems. John Wiley & Sons.

[45] Jovcic, D. (2019). High voltage direct current transmission: converters, systems and DC grids. John Wiley & Sons.

[46] Abbas, A. M., & Lehn, P. W. (2009, July). PWM based VSC-HVDC systems—a review. In 2009 IEEE Power & Energy Society General Meeting (pp. 1-9). IEEE.

[47] Korompili, A., Wu, Q., & Zhao, H. (2016). Review of VSC HVDC connection for offshore wind power integration. Renewable and Sustainable Energy Reviews, 59, 1405-1414.

[48] Fan, L., & Miao, Z. (2015). Modeling and analysis of doubly fed induction generator wind energy systems. Academic Press.

[49] Khan, I., Zeb, K., Din, W. U., Islam, S. U., Ishfaq, M., Hussain, S., & Kim, H. J. (2019). Dynamic modeling and robust controllers design for doubly fed induction generator-based wind turbines under unbalanced grid fault conditions. Energies, 12(3), 454.

[50] Elghali, S. B., Benbouzid, M. E. H., Charpentier, J. F., Ahmed-Ali, T., Gahery, J. M., & Denis, A. (2008, September). Modeling and MPPT sensorless control of a DFIG-based marine current turbine. In 2008 18th International Conference on Electrical Machines (pp. 1-6). IEEE.

[51] Abad, G., Lopez, J., Rodriguez, M., Marroyo, L., & Iwanski, G. (2011). Doubly fed induction machine: modeling and control for wind energy generation. John Wiley & Sons.

[52] Mohammed, O. A., Liu, Z., & Liu, S. (2005). A novel sensorless control strategy of doubly fed induction motor and its examination with the physical modeling of machines. IEEE Transactions on Magnetics, 41(5), 1852-1855.

[53] Hallak, M., Hasni, M., & Menaa, M. (2018, October). Modeling and control of a doubly fed induction generator base wind turbine system. In 2018 International Conference on Electrical Sciences and Technologies in Maghreb (CISTEM) (pp. 1-5). IEEE.

[54] Aicha, A., Mouna, B. H., & Lassâad, S. (2015, March). Multi-model modeling methods based on novel clustering strategy and comparative study: Application to induction machines. In 2015 IEEE 12th International Multi-Conference on Systems, Signals & Devices (SSD15) (pp. 1-7). IEEE.

[55] Lei, Y., Mullane, A., Lightbody, G., & Yacamini, R. (2006). Modeling of the wind turbine with a doubly fed induction generator for grid integration studies. IEEE transactions on energy conversion, 21(1), 257-264.

[56] Abdelmalek, S., Gencer, A., & Rezazi, S. (2019, June). Multiple Models Representation for a Doubly-Fed Induction Generator based Wind Energy Conversion Systems. In 2019 1st Global Power, Energy and Communication Conference (GPECOM) (pp. 348-352). IEEE.

[57] Mei, F., & Pal, B. (2007). Modal analysis of grid-connected doubly fed induction generators. IEEE transactions on energy conversion, 22(3), 728-736.

[58] Yang, B., Jiang, L., Wang, L., Yao, W., & Wu, Q. H. (2016). Nonlinear maximum power point tracking control and modal analysis of DFIG based wind turbine. International Journal of Electrical Power & Energy Systems, 74, 429-436.

[59] Protsenko, K., & Xu, D. (2008). Modeling and control of brushless doubly-fed induction generators in wind energy applications. IEEE Transactions on power electronics, 23(3), 1191-1197.

[60] Tan, Z., Sun, L., Zhao, D., & Meliopoulos, A. P. (2013, July). Dynamic modeling of doubly fed induction machine during balanced voltage dips with control effects formulation. In 2013 IEEE Power & Energy Society General Meeting (pp. 1-5). IEEE.

[61] Ibrahim, A., Solomin, E., & Miroshnichenko, A. (2018, October). Control strategy for maximum power point tracking of doubly fed induction motor for wind turbine. In 2018 International Ural Conference on Green Energy (UralCon) (pp. 14-19). IEEE.

[62] Mehler, C., Tisborn, G., & Orlik, B. (2013, September). Advanced modeling of a doubly fed induction generator with open stator for soft grid synchronization. In 2013 15th European Conference on Power Electronics and Applications (EPE) (pp. 1-9). IEEE.

[63] Nos, O. V. (2016, June). The quaternion model of doubly-fed induction motor. In 2016 11th International Forum on Strategic Technology (IFOST) (pp. 32-36). IEEE.

[64] Han, P., Cheng, M., Wei, X., & Li, N. (2015). Modeling and performance analysis of a dual-stator brushless doubly fed induction machine based on spiral vector theory. IEEE Transactions on Industry Applications, 52(2), 1380-1389.

[65] Alamouti, M. K., Golkar, M. A., Kojoori, S. S., & Hosseini, S. A. (2011, May). Modeling and control of reactive power in a microgrid using doubly fed induction generator. In 2011 10th International Conference on Environment and Electrical Engineering (pp. 1-4). IEEE.

[66] Sun, Z., Wang, H., & Li, Y. (2012). Modelling and simulation of doubly-fed induction wind power system based on Matlab/Simulink.

[67] Bakouri, A., Mahmoudi, H., & Abbou, A. (2016, November). Modelling and optimal control of the doubly fed induction generator wind turbine system connected to utility grid. In 2016 International Renewable and Sustainable Energy Conference (IRSEC) (pp. 807-812). IEEE.

[68] Spahic, E., Morren, J., Balzer, G., & Michalke, G. (2007, April). Mathematical model of the double fed induction generator for wind turbines and its control quality. In 2007 International Conference on Power Engineering, Energy and Electrical Drives (pp. 642-647). IEEE.

[69] Maciejewski, P., & Iwanski, G. (2015, March). Modeling of six-phase double fed induction machine for autonomous dc voltage generation. In 2015 Tenth International Conference on Ecological Vehicles and Renewable Energies (EVER) (pp. 1-6). IEEE.

[70] Pena, R., Clare, J. C., & Asher, G. M. (1996). Doubly fed induction generator using back-to-back PWM converters and its application to variable-speed wind-energy generation. IEE Proceedings-Electric power applications, 143(3), 231-241.

[71] Rouco, L., & Zamora, J. L. (2006, June). Dynamic patterns and model order reduction in small-signal models of doubly fed induction generators for wind power applications. In 2006 IEEE Power Engineering Society General Meeting (pp. 8-pp). IEEE.

[72] Krause, P. C., Wasynczuk, O., Sudhoff, S. D., & Pekarek, S. D. (2013). Analysis of electric machinery and drive systems (Vol. 75). John Wiley & Sons.

[73] Xia, S. W., Bu, S. Q., Zhang, X., Xu, Y., Zhou, B., & Zhu, J. B. (2018). Model reduction strategy of doubly-fed induction generator-based wind farms for power system small-signal rotor angle stability analysis. Applied energy, 222, 608-620.

[74] Chen, Z., Guerrero, J. M., & Blaabjerg, F. (2009). A review of the state of the art of power electronics for wind turbines. IEEE Transactions on power electronics, 24(8), 1859-1875.

[75] Miller, N. W., Sanchez-Gasca, J. J., Price, W. W., & Delmerico, R. W. (2003, July). Dynamic modeling of GE 1.5 and 3.6 MW wind turbine-generators for stability simulations. In 2003 IEEE Power Engineering Society General Meeting (IEEE Cat. No. 03CH37491) (Vol. 3, pp. 1977-1983). IEEE.

[76] Akhmatov, V. (2002). Variable-speed wind turbines with doubly-fed induction generators: Part i: Modelling in dynamic simulation tools. Wind engineering, 26(2), 85-108.

[77] Xu, D., Blaabjerg, F., Chen, W., & Zhu, N. (2018). Advanced control of doubly fed induction generator for wind power systems. John Wiley & Sons.

[78] Hansen, A. D., & Michalke, G. (2008). Modelling and control of variable-speed multi-pole permanent magnet synchronous generator wind turbine. Wind Energy: An International Journal for Progress and Applications in Wind Power Conversion Technology, 11(5), 537-554.

[79] Hansen, A. D., & Michalke, G. (2009). Multi-pole permanent magnet synchronous generator wind turbines' grid support capability in uninterrupted operation during grid faults. IET Renewable Power Generation, 3(3), 333-348.

[80] Miao, Z., & Fan, L. (2012, July). Modeling and small signal analysis of a PMSG-based wind generator with sensorless maximum power extraction. In 2012 IEEE Power and Energy Society General Meeting (pp. 1-8). IEEE.

[81] Morimoto, S., Kawamoto, K., Sanada, M., & Takeda, Y. (2002). Sensorless control strategy for salient-pole PMSM based on extended EMF in rotating reference frame. IEEE transactions on industry applications, 38(4), 1054-1061.

[82] Haque, M. E., Negnevitsky, M., & Muttaqi, K. M. (2008, October). A novel control strategy for a variable speed wind turbine with a permanent magnet synchronous generator. In 2008 IEEE industry applications society annual meeting (pp. 1-8). IEEE.

[83] Yin, M., Li, G., Zhou, M., & Zhao, C. (2007, June). Modeling of the wind turbine with a permanent magnet synchronous generator for integration. In 2007 IEEE Power Engineering Society General Meeting (pp. 1-6). IEEE.

[84] Melício, R., Mendes, V. M., & Catalão, J. P. (2011). Wind turbines with permanent magnet synchronous generator and full-power converters: modelling, control and simulation. Wind turbines, 465-470.

[85] Lai, L. L., & Chan, T. F. (2008). Distributed generation: Induction and permanent magnet generators. John Wiley & Sons.

[86] Colak, I., Bulbul, H. I., Sagiroglu, S., & Sahin, M. (2012, November). Modeling a permanent magnet synchronous generator used in wind turbine and the realization of voltage control on the model with artificial neural networks. In 2012 International Conference on Renewable Energy Research and Applications (ICRERA) (pp. 1-6). IEEE.

[87] Rolan, A., Luna, A., Vazquez, G., Aguilar, D., & Azevedo, G. (2009, July). Modeling of a variable speed wind turbine with a permanent magnet synchronous generator. In 2009 IEEE international symposium on industrial electronics (pp. 734-739). IEEE.

[88] Vijayalakshmi, S., Saikumar, S., Saravanan, S., Sandip, R. V., & Sridhar, V. (2011). Modelling and control of a wind turbine using permanent magnet synchronous generator. International Journal of Engineering Science and Technology (IJEST), 3(3), 2377-2384.

[89] Fateh, L., Ahmed, O., Amar, O., Abdelhak, D., & Lakhdar, B. (2016). Modeling and control of a permanent magnet synchronous generator dedicated to standalone wind energy conversion system. Frontiers in Energy, 10(2), 155-163.

[90] Von Meier, A. (2006). Electric power systems: a conceptual introduction. John Wiley & Sons.

[91] Fateh, L., Ahmed, O., Amar, O., Abdelhak, D., & Lakhdar, B. (2016). Modeling and control of a permanent magnet synchronous generator dedicated to standalone wind energy conversion system. Frontiers in Energy, 10(2), 155-163.

[92] Djellad, A., Logerais, P. O., Omeiri, A., Riou, O., Durastanti, J. F., & Khelfi, A. (2013). Modeling of wind energy conversion system and power quality analysis. In International conference on renewable energy. Sousse, Tunisie.

[93] Messaoud, M., & Abdessamed, R. (2011). Modeling and optimization of wind turbine driving permanent magnet synchronous generator. EDITORIAL BOARD, 5(6), 489.

[94] Boldea, I. (2005). Synchronous generators. CRC press.

[95] Krause, P. C., Wasynczuk, O., Sudhoff, S. D., & Pekarek, S. D. (2013). Analysis of electric machinery and drive systems (Vol. 75). John Wiley & Sons.

[96] Wu, Q., & Sun, Y. (Eds.). (2018). Modeling and modern control of wind power. John Wiley & Sons.

[97] Gieras, J. F., Wang, R. J., & Kamper, M. J. (2008). Axial flux permanent magnet brushless machines. Springer Science & Business Media.

[98] Kim, H. W., Kim, S. S., & Ko, H. S. (2010). Modeling and control of PMSG-based variable-speed wind turbine. Electric Power Systems Research, 80(1), 46-52.

[99] Dom, S., Kucukcoskun, K., Illa, K., & De Langhe, K. (2019). Permanent Magnet Synchronous Machine for Electrical Vehicles: Optimized Electromagnetic Loads for Better Vibro-Acoustics Performance (No. 2019-26-0207). SAE Technical Paper.

[100] Grenier, D., Dessaint, L. A., Akhrif, O., Bonnassieux, Y., & Le Pioufle, B. (1997). Experimental nonlinear torque control of a permanent-magnet synchronous motor using saliency. IEEE Transactions on Industrial Electronics, 44(5), 680-687.

[101] Toliyat, H. A. (1998). Analysis and simulation of five-phase variable-speed induction motor drives under asymmetrical connections. IEEE transactions on power electronics, 13(4), 748-756.

[102] Baudart, F., Labrique, F., Matagne, E., Telteu, D., & Alexandre, P. (2009, March). Control under normal and fault tolerant operation of multiphase SMPM synchronous machines with mechanically and magnetically decoupled phases. In 2009 International Conference on Power Engineering, Energy and Electrical Drives (pp. 461-466). IEEE.

[103] MATLAB/Simulink model library (2006). Permanent Magnet Synchronous Machine.

[104] Kundur, P., Balu, N. J., & Lauby, M. G. (1994). Power system stability and control (Vol. 7, p. 623). New York: McGraw-hill.

[105] Kundur, P. S., & Malik, O. P. (2022). Power system stability and control. McGraw-Hill Education.

[106] Dreidy, M., Mokhlis, H., & Mekhilef, S. (2017). Inertia response and frequency control techniques for renewable energy sources: A review. Renewable and sustainable energy reviews, 69, 144-155.

Chapter 2

Grid-connected power converter system objectives and proposed approaches

To address and handle the problem of grid-connected renewable energy systems, especially in providing ancillary services, the power system electrical objectives must be established. To be able to achieve these electrical objectives by the mean of control systems, corresponding control objectives should be derived.

In addition, there is a need of introducing some relevant concepts and propose suitable approaches, in terms of control structures and control strategies. The control problem is generally defined and control structures as well as corresponding control strategies can be applied for any grid-connected converter-based application. The first and foremost concept is the time and space separation control structure. In real life applications, the system is controlled using Real Time Operating System (RTOS), which only achieves its best performance and stability when same time constant outputs are grouped together. For this purpose, time and space separation control structure will classify the system dynamics into suitable groups.

At the same time, the generalized coordinated RES control (with both centralized and decentralized implementations) and control system design procedure are formulated in this chapter. The processes are generally established, and act as a guideline for designing a controller satisfying the multi-objective goals of grid-connected power converter applications, which are presented in chapters 3, 4 and 5.

2.1 Power converter system objectives for grid-connected RES

A grid-connected generator/converter control specifications are normally divided into two categories: local (machine) specifications and global (grid) specifications.

The local ones are to ensure the machine's proper operation and to manage its produced active power P and reactive power Q. Other variables, such as blade pitch/position and shaft speed, may be managed depending on technology if a wind turbine is used in the DRES.

Grid specifications are aimed towards ancillary services. This includes regulation of produced P and Q as well, but with distinct requirements. Indeed, the DRES should adjust its voltage not only for the safe and efficient operation of the generator, but also for the neighboring AC grid. This means that the voltage at various (far) nodes of the grid should respond differently in the event of many (specified by TSOs) grid-level faulty incidents. In addition, the grid frequency should also be constantly monitored and regulated. Large DRESs should, to the greatest extent practicable, completely engage in voltage V and frequency f control, with the same duties and rights as traditional SGs. Also, large DRESs should participate in market mechanisms.

Similarly, HVDC can be viewed as a special case of DRES where the power converter system doesn't have generators. However, HVDC systems, especially VSC-HVDC, can participate in regulating active and reactive powers in large amount, thus they can also participate in grid voltage support/regulation and active power redispatch. As a result, all of power system objectives for HVDC are included in those of DRES. However, depending on the circumstances, some of the requirements in power converter objectives can be omitted when applying for HVDC system.

2.1.1 Power converter system electrical objectives

Overall, providing GAS for converter-based applications (DRES and VSC-HVDC) is more complicated than for classical SGs. From power system point of view, the primary GAS electrical objectives (e.g. forDRES) in this thesis include grid voltage and frequency support. These regulations are equivalent to active and reactive powers control. At the same time, these regulations have to be compliant with the local generation plant control. Therefore, the power system electrical objectives are defined as following.

Firstly, grid voltage V_{grid} support, i.e. regulation of reactive power Q to a desired value Q_{ref} (or directly control V_{grid}), based on local request and the whole grid requirement (e.g., secondary/tertiary control), in order to provide Voltage Service Provider (VSP) services. The regulation of V_{grid} by the mean of reactive power control, can be done through the Q-V characteristics [1].

The ability to regulate active power P to control or support frequency, is also one of the main Frequency Containment Reserve (FCR) services. This capability is not only important for local plant stabilization but also crucial for frequency-related services. Without this ability, DRES will fail to comply to grid code [2], thus it cannot operate independently.

Fast frequency response (part of FCR), i.e., inertia response or inertia emulation, which is similar to those of conventional high inertia constant SGs. Using the fast-regulation capacity of power converter, the low inertia of DRES can be partly compensated. For large DRESs, this capability can even be sufficient to fully emulate the grid inertia, thus achieve a high inertia constant grid.

Next, the ability to maintain stable output power when there is a distortion in power source in a short time (e.g. a drop in wind speed for wind systems, or sunset for solar systems), i.e., active power RAMP control (FCR), should also be provided. This is to ensure that the change on produced power is not too fast. Otherwise, due to the sudden shortage of energy, the market-based energy price may increase vastly in case the source of energy instantly drop, e.g., sunset for PV systems.

Another important feature is the ability to endure a grid distortion (e.g., short-circuit) and recover its operating status before the faulty event, i.e., FRT capability and fault-clearing, with a required Critical Clearing Time (CCT) according to European Network of Transmission System Operators for Electricity (ENTSO-E) grid code for grid connection applicable to all generators [2].

Finally, the coordinated control structure should also be easy to integrate secondary/tertiary services, including automatic Frequency Restoration Reserve (aFRR), manual Frequency Restoration Reserve (mFRR) and the aforementioned VSP. The control structure should be established in both of centralization and decentralization approaches, then tested and finally compared to each other.

2.1.2 Power converter system control objectives

The power system electrical objectives defined in subsection 2.1.1 are now converted into equivalent power system control objectives. The resulting control objectives are next utilized for power control system design.

Firstly, reactive power Q is regulated at suitable Q_{ref}, including operating point value Q_{OP}, voltage support reactive power ΔQ_{Q-V} (using Q-V characteristic [1]) and grid-requirement secondary reactive power $Q_{secondary}$. All of these signals are combined into Q_{ref}, which is then used for control reference signal at local level control, ensuring not only local plant stability but also GAS:

$$Q_{ref} = Q_{OP} + \Delta Q_{Q-V} + Q_{secondary} \tag{2.1}$$

Secondly, active power P is controlled at desired value P_{ref}, includes operating point P_{OP}, inertia response active power ΔP_{RoCoF} (H is grid inertia time constant), frequency response active power ΔP_{FrDe} and secondary request $P_{secondary}$. Similar to reactive power control this reference signal P_{ref} is used at local plant regulation, satisfying both of local stability and grid-level ancillary services:

$$\begin{cases} P_{ref} = P_{OP} + \Delta P_{RoCoF} + \Delta P_{FrDe} + P_{secondary} \\ \min \leq RAMP\_rate\,(P_{ref}) \leq \max \end{cases} \tag{2.2}$$

At the same time, the DC voltage is regulated at suitable operating point, depending on the request from grid and/or the local services. In case of PV systems, DC voltage reference signal can also be influenced by the MPPT

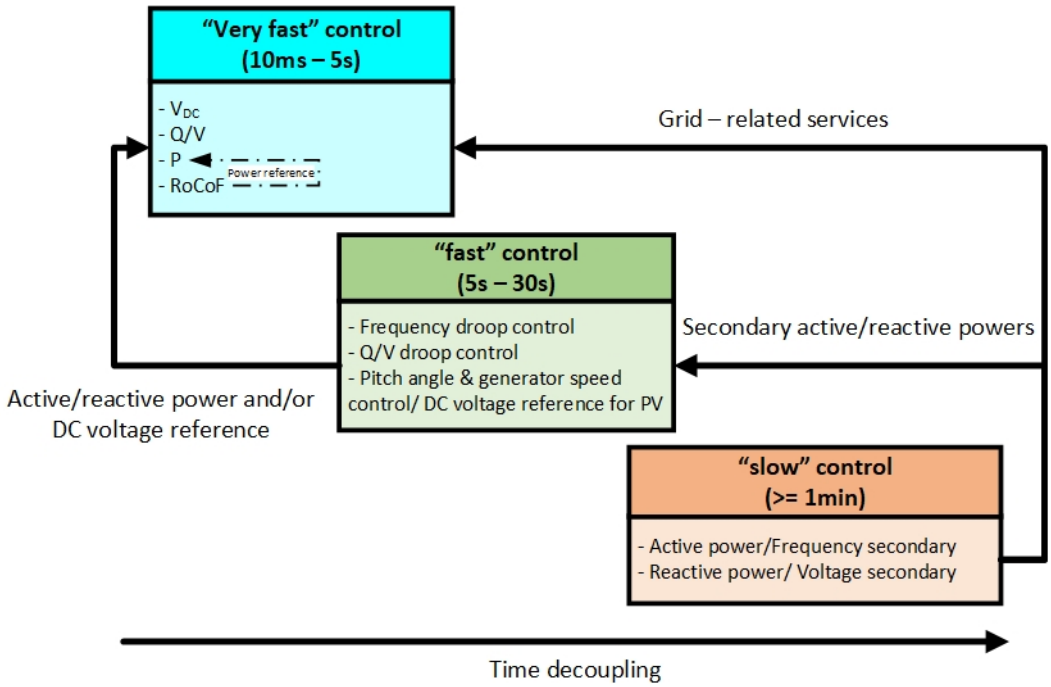

Figure 2.1: Time separation for renewable generation systems

searching table.

Finally, the control system is settled in both centralized and decentralized structures, along with other necessary objectives (robust/ nonlinear/ optimal control). Thanks to these carefully defined control objectives, the control structure can be implemented with GAS-oriented mindset.

2.2 Time and space separation control structures

As discussed in section 2.1, in power converter system, there are different control outputs in different dynamics with different time constants. Since the real power converter applications are controlled using RTOS [3], controlling these dynamics with the same control level will reduce the performance of faster dynamics in the group as well as stability of the whole system. For this, there is a need to classify and group these dynamics into suitable groups, which then can be controlled in different control levels, resulting in a better performance and stability.

2.2.1 Time decouple for renewable generation systems

The DRES system dynamics are classified into 3 groups, "very fast" - "fast" and "slow" whith time constant of 10ms - 5s, 5s - 30s and more that 1min, respectively. This is illustrated in Fig. 2.1.

The first group, "very fast", consists of DC voltage V_{DC}, reactive power Q (for AC voltage control/support), active power P and grid inertia support $RoCoF$. These dynamics should be controlled at local generation plants. The second group, "fast", includes frequency - active power droop relationship, AC voltage - reactive power droop relationship, MPPT table (for wind energy are pitch angle and generator speed, for solar energy is desired DC voltage). The last group, "slow", consists of secondary reactive power Q and active power P dynamics. It means that the renewable power plant will be controlled to provide also secondary voltage and frequency support.

Each group in this control structure is generating corresponding reference signals for the lower level groups (faster dynamics), which ensure the integration and participation of DRES system in AC grid. In order to clarify

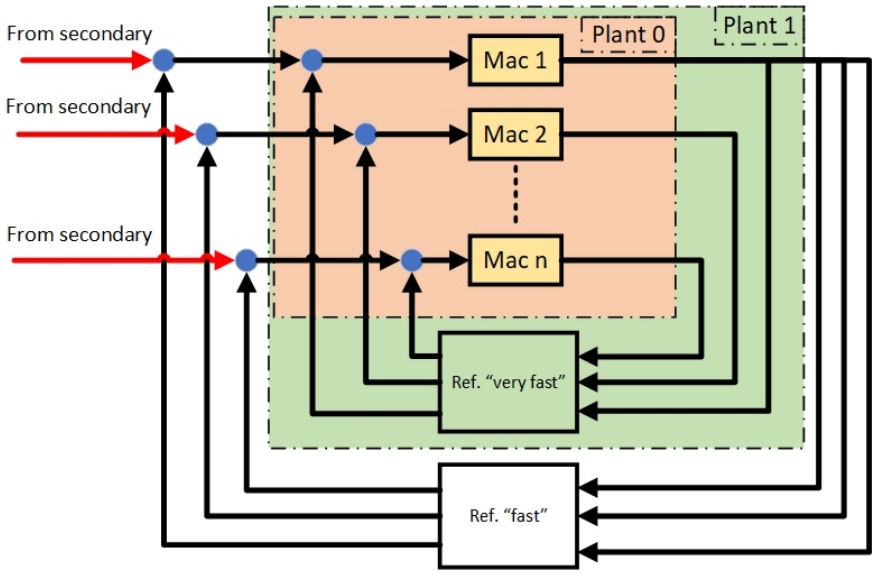

Figure 2.2: DRES centralized control structure

this structure as well as to pave the way for control system design, the two centralized and decentralized approaches will be presented in the next subsections.

2.2.2 Time separation using centralized approach

Consider there are n machines in the AC grid needed to be controlled. In the centralized approach, all these machines are considered as a unique plant (plant 0), illustrated in Fig. 2.2.

The aforementioned plant 0 is directly controlled by the first level control - the "very fast" control (i.e., Ref. "very fast"). It means that DC voltage V_{DC}, reactive power Q (for AC voltage control/support), active power P and grid inertia $RoCoF$ are controlled at this level at all machines at the same time using the same controller. These regulating tasks are to ensure that the local/lowest level control is able to integrate the GAS-related control services as discussed in subsection 2.2.1.

The next level control - "fast" control (i.e., Ref "fast"), provides references for the "very fast" control of plant 0. In other words, the ("very fast" control + plant 0) is directly controlled by the "fast" control. The ("very fast" control + plant 0) is now called plant 1. In this level, the primary frequency services and primary AC voltage services are handled using a single controller for all machines. These services are the required functions for renewable power plant control in providing GAS.

The highest level control - the reference control signal from secondary, is used to control the whole (plant 1 + "fast" control). Again, the secondary control signal will control all machines at the same time using a single controller. This slow control helps to provide GAS using DRES, but at grid level, i.e., this to ensure that the grid voltage and frequency are stable on the grid-scale.

The centralized control, as its name indicates, tends to provide more performance and stability since the controllers have all necessary information about the system. However, the cost of signal exchanging and signal delay handling are huge, economically and technically. Therefore, decentralized control should also be investigated.

2.2.3 Time separation using decentralized approach

Consider the same n machines as in subsection 2.2.2, but now each machine is controlled independently, as shown in Fig. 2.3.

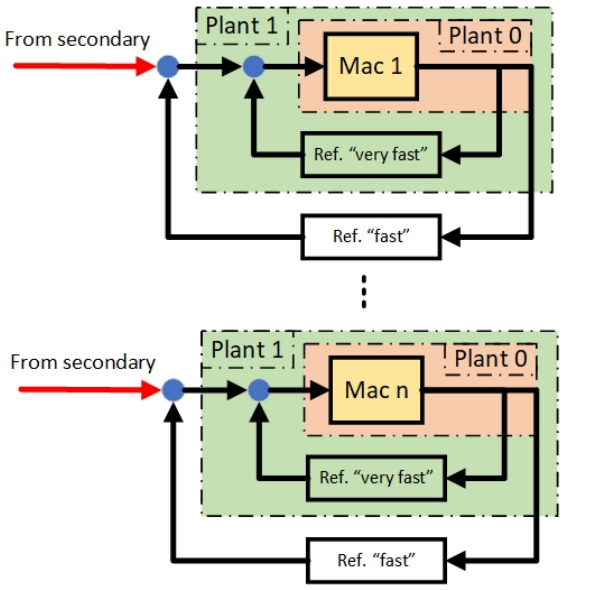

Figure 2.3: DRES decentralized control structure

The same as in previous approach, but now plant 0 is just one machine, which is directly regulated by the "very fast" control (i.e., Ref. "very fast"). Thus, for a DRES with considered n machines, there are n plant 0. Similar to the case of centralized control, output of each plant 0 are DC voltage V_{DC}, reactive power Q (for AC voltage control/support), active power P and grid inertia $RoCoF$. These output are controlled at this level at each machine using the its first level controller.

Each machine now has their own "fast" control (i.e., Ref "fast"), and each is indirectly controlled by "fast" control. The ("very fast" control + plant 0) of each machine is now called plant 1, and thus there are also n plant 1. Same as in centralized approach, in this level, the primary frequency services and primary AC voltage services are regulated using each controller for each machine. This means that each machine is participating into the grid voltage and frequency support/regulation independently, compared to the joint participation of all machines in case of centralized control.

The highest level control - the reference control signal from secondary, is applied to regulate the each (plant 1 + "fast" control). Again, this regulating action is done at each machine independently. Thus, each machine is integrated into the grid independently, and also each is participating in GAS - providing services on its own.

The decentralized control may bring the benefits of being independent in term of controlling and requires less information from other machines. However, the performance and stability of the whole system may be worsened due to the lack of necessary information from neighbor grid, especially in case of faulty events.

2.2.4 Control structure with frequency and voltage support

To make it clear for the establishment and implementation of proposed control approaches, the general time - space structure for renewable energy system is detailed and illustrated as in Fig. 2.4. In addition, the structure can be modified to adapt to the need of the control objectives in specific cases. In case of centralized control, there is only 1 control structure as in Fig. 2.4. In case of decentralized control, each machine has its own independent control structure as in the aforementioned figure, i.e., Fig. 2.4.

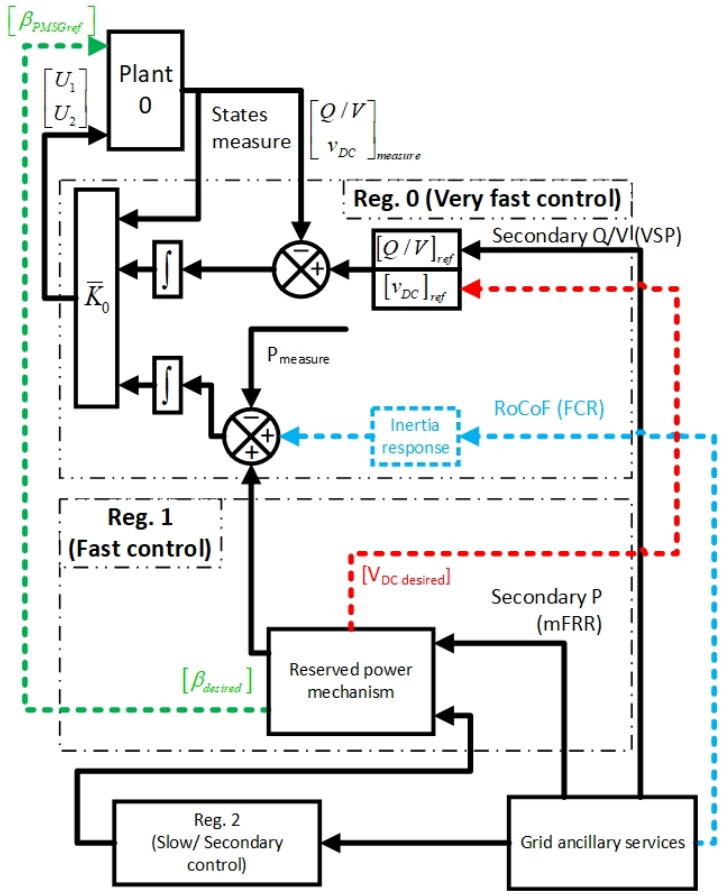

Figure 2.4: General time - space structure for renewable energy system

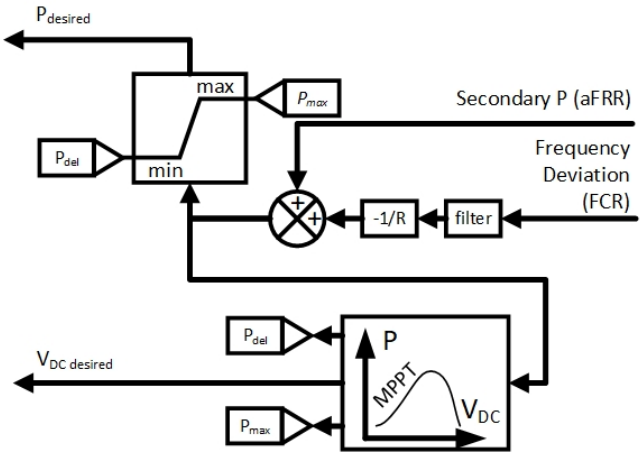

Figure 2.5: Reserved power mechanism for solar energy system

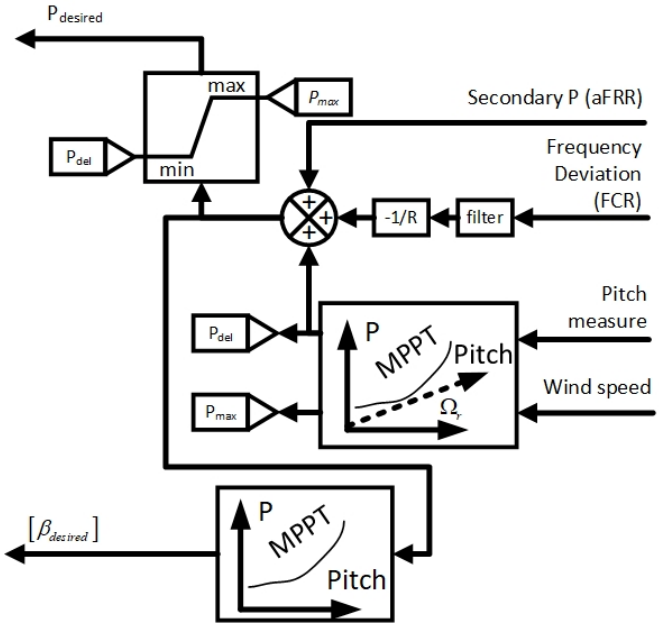

Figure 2.6: Reserved power mechanism for wind energy system

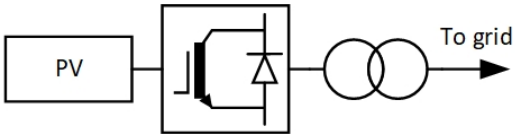

Figure 2.7: PV solar energy system

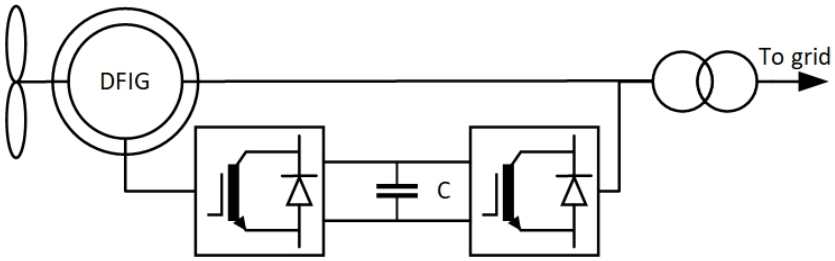

Figure 2.8: DFIG wind energy system

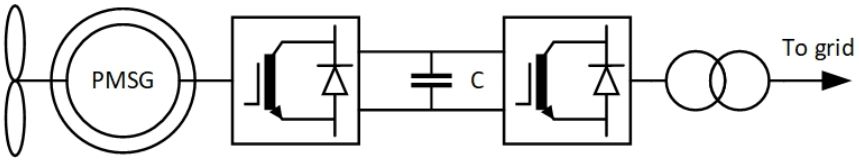

Figure 2.9: PMSG wind energy system

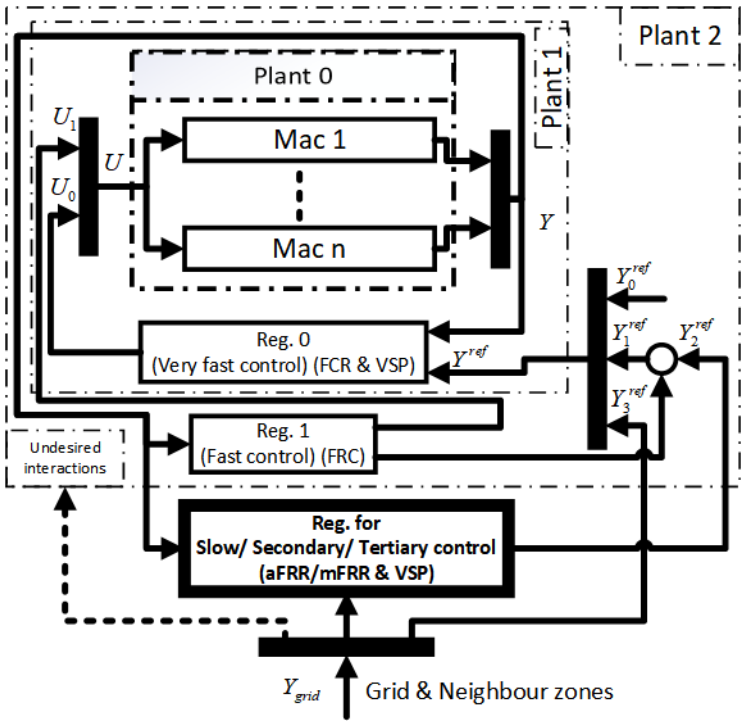

Figure 2.10: Time and space separation of the DRES centralized control

Plant 0 can be a PMSG wind energy system with full back to back two converters which connect the generator to the grid (Fig. 2.9). It can also be a DFIG wind energy system with two converters (Fig. 2.8). The plant 0 can also be a PV solar energy system consists of only 1 converter, which is illustrated in Fig. 2.7.

The plant 0 is directly controlled by Reg. 0, i.e., "very fast" control. This includes DC voltage V_{DC}, active power P, reactive power Q and inertia response (i.e., RoCoF control) if needed. As discussed before, this is to pave the way for integration of GAS-related control function into this local/lowest level control. The detailed strategy will be explained later on.

To be able to participate in active power P regulation, it is required that the DRES system has some reserved active/reactive energy in order to be able to increase its output if needed. This is done at the higher control level, i.e., at the "fast" control by a reserved power mechanism in a slower control loop - Reg. 1. For wind energy system, the reserved power mechanism are illustrated in Fig. 2.6, including the MPPT for pitch angle and generator speed Ω to deload the generator to a suitable level (e.g., 10 $\%$), which is then used for GAS. For the case of solar energy system, this mechanism is described in Fig. 2.5 which gives the MPPT relationship between the DC voltage and the output active power. A similar deload function is implemented to reserve some share of the output power which can then be used for GAS.

The details of the strategies using these time and space separation structure for renewable energy system will be discussed more in the next section.

2.3 Optimal coordinated approaches

2.3.1 Optimal coordinated centralized approach

As in Fig. 2.10 for centralized control approach, the considered system consists of n machines, all of them are treated as a single unit called plant 0. In addition, all the subsystems are controlled by a coordinated centralized controller with control input U.

Firstly, all of n machines are directly controlled by "very fast" control (i.e., Reg. 0), including FCR (RoCoF

and active power control) and VSP (reactive power control) services, through signal U_0. This Reg. 0 also receives the request from grid side (e.g., for inertia response) as well as from the higher level control. The reference signals Y^{ref}, shown in Fig. 2.10, include reference signals for reactive power Q_{ref}, active power P_{ref} and DC voltage V_{ref}. The inertia response, i.e., RoCoF control, is also achieved in this control level, through an additional part of active power control.

Secondly, the plant 0 and Reg. 0 are combined into plant 1, which is regulated by "fast" control, i.e., Reg. 1. This Reg. 1 is to provide FCR services, including frequency response, MPPT and deloading power functions. This is done to guarantee that the power produced is at a reasonable deloaded level, with a reserve quantity of power available for use when needed. A Q-V characteristic function is also used for AC voltage support, which generates the enhanced reactive power reference to support the grid voltage.

Next, the plant 1 and Reg. 1 are now considered as a single unit, and controlled by a higher level regulator, namely slow control (or secondary/tertiary control). For frequency support, the primary and secondary power references are combined and used in the "very fast" loop. The same procedure is followed for voltage support, which results in the generation of the reactive power reference for the "very fast" loop.

The vector Y_{grid} contains the grid ancillary service reference signals, which are used to build secondary and main signal references. Y_3^{ref} are grid-side direct requests (e.g., inertia response), which are routed directly to the very fast control loop. Y_2^{ref} are the secondary reference signals for $Q_{secondary}$ and $P_{secondary}$, respectively (as in (2.1) and (2.2)). All requests from the secondary level Y_2^{ref} and from the "fast" control loop are packed into Y_1^{ref}. Y_0^{ref} denotes the operational point reference signals or the system's desired beginning values. Y^{ref} represents all secondary and main primary service requests, which are the lowest level control references.

All of control signals are packed together through the control structure. The resulting control signals U then regulates all of n machines in a centralized structure.

The control gain is also synthesized using optimization to minimize the undesired interactions between machines and grid side. This can be achieved by the means of optimized control, such as disturbance rejection using H_2/H_∞ control.

2.3.2 Optimal coordinated decentralized approach

As in Fig. 2.11 for decentralized control approach, the considered system is divided into n subsystems (depending on their functions and their locations for example). Each subsystem consists of a single machine. In decentralized approach, an overlapping decentralized coordinated control is used to regulate each subsystem, in the form of an independent decentralized controller. The decentralized control structure has the following characteristics.

The control structure of the whole system is pretty much the same as in case of centralized control, but each subsystem is now independently controlled by 2 layers of control, namely Reg. 0 and Reg. 1. The secondary/tertiary control level is still a single unit, which sends reference signal to lower control levels.

The reference signals Y_{grid}, Y_3^{ref}, Y_2^{ref}, Y_1^{ref} and Y_0^{ref} are comparable to those used in the centralized approach. However, each subsystem now has its own combined reference signal $Yref$, which is formed from the combination of Y_{grid}, Y_3^{ref}, Y_2^{ref} and Y_1^{ref}.

Compared to centralized control, another difference is the need that the machine-to-machine interaction is minimized as part of the disturbance rejection process. As shown in Fig. 2.11, interactions with other subsystems and/or the grid are deemed disturbances for each specific subsystem, and the control is synthesized to reject them based on H_2/H_∞ optimal control.

The decentralized approach can also be used in a larger set, such as in a large-scale power system. For example, if there is undesired coupling between subsystems and/or the grid, disturbance rejection is used. If there is no interaction, the rejection mechanism can be skipped, and the control effort is then concentrated on the performance and stability of each subsystem as well as the overall considered power system.

2.4 Control system design procedure

To be able to design and implement the control approaches in section 2.3 with the control objectives in section 2.1, the following considerations are important: a guideline for power system control design, asymptotically tracking for output reference signals Y^{ref} and depending on different controlling purposes, suitable advanced MIMO control techniques should be employed and implemented by using a single control structure.

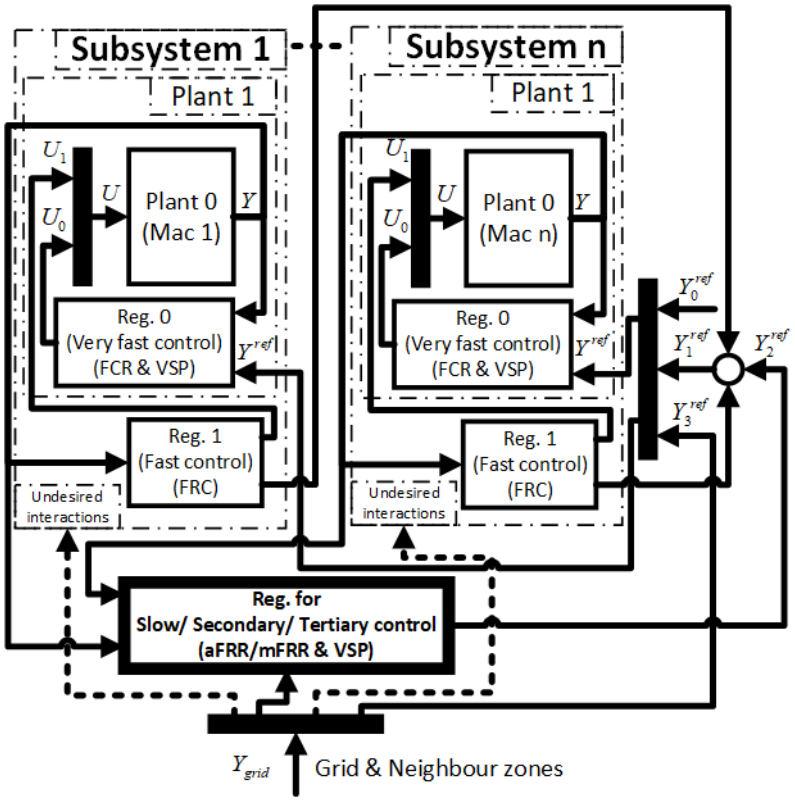

Figure 2.11: Time and space separation of the DRES overlapping decentralized control

A power system control design process is crucial both to identify and ensurr control objectives. In addition, this process guarantees the resulting controller to be optimal, by carefully selecting suitable modelling and controlling techniques.

To ensure asymptotic tracking of output references Y^{ref} (see Fig. 2.10 for centralized control and Fig. 2.11 for decentralized control), in the presence of disturbances and model uncertainties, the internal model principle [4] has to be utilized. At the same time, the power converter systems are MIMO systems, thus state-space model is employed to achieve optimal performance and stability.

Various advanced control strategies are applied depending on the situation. To be able to utilize several control strategies at the same time in a single control structure, LMI techniques are suitable and sufficient. For each control technique a group of LMI conditions is deduced and, all of these LMI conditions are combined and solved together. For example, optimal H_2/H_∞ control (for disturbance rejecting), mixed sensibility loop shaping (for cutting high frequency oscillation in LCL filter) and internal model principle (for reference tracking) can be combined easily using LMI techniques. In addition, because DRES are very nonlinear and uncertain, nonlinear fuzzy control may be considered. Another important technique to consider is the MIMO pole-placement technique, which helps to achieve suitable time constants and damping of targeted responses. These techniques will be presented accordingly in each application chapter, including chapters 3, 4 and 5.

2.4.1 Power system control design process

The power system control design process is described in Fig. 2.12, including the following steps:

1. Define the original model: first step is to define which is the original model we want to control, using Root Mean Square (RMS) or ElectroMagnetic Transient (EMT) simulation modes. This step is very important, because it may directly affect not only control objectives but also the chosen control techniques (e.g., if the original model has too many states and is highly nonlinear, the control objectives may not include a stable operation in large range of state values, thus fuzzy control technique is inapplicable and not useful in this

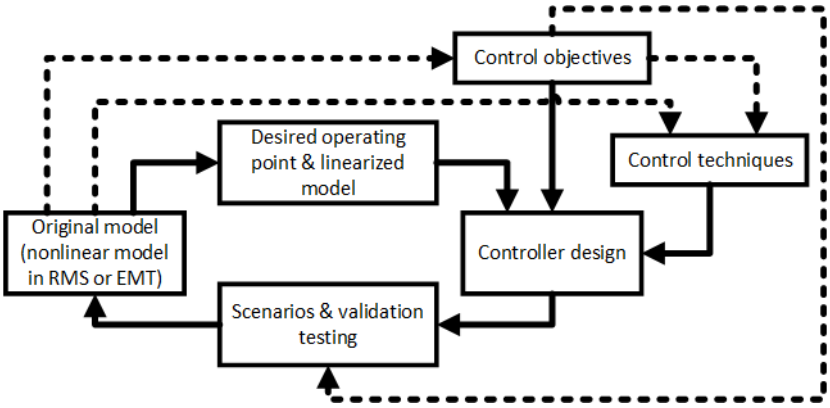

Figure 2.12: Global control system design process

case), and then indirectly affect controller design step.

2. Define desired operating point & linearized model: this is also a crucial step, since a good stable equilibrium point is necessary to obtain in order to achieve a reliable linearized system as well as optimal controller. Linearized model is useful in many cases, such as in rapid (linear) controller design and power system modal analysis. The operating point and linearized model can also help to start the system smoothly, avoid exhausting the actuator and its capacity (e.g., a bad starting point may saturate the controller capacity, thus greatly reducing the operating range of the system).

3. Define control objectives: according to the requirements from different sources, a group of control objectives should be formed. This step is the key step before choosing control techniques to be used to design the controller. A group of control objectives is the compass for selecting a control strategy. The control objectives are also influencing the scenarios for control validation (e.g., if frequency support is in the list of control objectives, then a scenario when there is a need for frequency support is required).

4. Select control techniques: based on personal preferences and control objectives, one or a group of control techniques (e.g., optimal H_2/H_∞ control and/or LMI) are chosen and applied for the controller design step.

5. Synthesize the controller gains: based on control objectives, chosen control techniques and the desired operating point (along with its linearized model, if necessary), the controller will be designed using the selected control techniques.

6. Defining scenarios and validation tests: this step is to validate the controller, using defined scenarios to ensure the controller satisfy all of the control objectives. The validation is done on the original model.

2.4.2 Control structure for reference asymptotic tracking

Consider a MIMO state-space model with state X, input U and output Y:

$$\begin{cases} \dot{X} = AX + BU \\ Y = CX + DU \\ Y(s) = G(s)U(s) \end{cases} \tag{2.3}$$

The general problem of power system control is to design a controller such that outputs Y of system (2.3) track the step references Y_{ref} in (2.4):

$$\begin{cases} \dot{X}_r = 0 \\ Y_{ref} = C_r X_r \end{cases} \tag{2.4}$$

Hence, the tracking error is $e = \mathrm{Y}_{ref} - Y$.

The internal model principle [4] states that the outputs of system are able to robustly track the step references Y_{ref} iff the two following conditions are satisfied:

- All eigenvalues of the closed-loop system are stable.
- The open-loop of the controlled system ,i.e., the system includes the original system (2.3) and its controller U, contains the reference model (2.4).

For the case of step references Y_{ref} in (2.4), the model of each reference will be $1/s$. In many cases, the original model doesn't contain $1/s$. Thus, to ensure asymptotic tracking, the controller has to contain $1/s$ in its model. To do this, an augmented system is introduced, with augmented state $\bar{X}$ is in (2.5):

$$\bar{X} = \begin{bmatrix} \dot{X} & e \end{bmatrix}^T \tag{2.5}$$

We have:

$$\begin{cases} \ddot{X} = A\dot{X} + B\dot{U} \\ \dot{e} = -C\dot{X} - D\dot{U} \end{cases}$$

Therefore, the augmented system is:

$$\begin{cases} \dot{\bar{X}} = \bar{A}\bar{X} + \bar{B}\bar{U} \\ \bar{Y} = \bar{C}\bar{X} \end{cases} \tag{2.6}$$

where:

$$\begin{cases} \bar{A} = \begin{bmatrix} 0 & A \\ 0 & -C \end{bmatrix}; \bar{B} = \begin{bmatrix} B \\ -D \end{bmatrix}; \bar{C} = \begin{bmatrix} 0 & I \end{bmatrix} \\ \bar{U} = \dot{U} \end{cases}$$

The controller is now a MIMO PID controller (2.7), having the integral action $1/s$ inside its form:

$$U = K \begin{bmatrix} X \\ \int e dt \end{bmatrix} \tag{2.7}$$

Generally, this control design process can be the same for larger classes of control system compared to system (2.3), e.g., including but not limiting to, the system with disturbance W in (2.8), and with uncertainties Δ in (2.10). It also can be the nonlinear system with state-space matrices are nonlinear (i.e, they are time-varying matrices) as in (2.9). Of course, the controller should be designed differently to meet the need of each situation, but the general process is almost the same as in this subsection.

$$\begin{cases} \dot{X} = AX + B_1U + B_2W \\ Y = CX + D_1U + D_2W \end{cases} \tag{2.8}$$

$$\begin{cases} \dot{X} = A_{nl}X + B_{1nl}U + B_{2nl}W \\ Y = C_{nl}X + D_{1nl}U + D_{2nl}W \end{cases} \tag{2.9}$$

$$\begin{cases} \dot{X} = (A + \Delta A)X + (B_1 + \Delta B_1)U + (B_2 + \Delta B_2)W \\ Y = (C + \Delta C)X + (D_1 + \Delta D_1)U + (D_2 + \Delta D_2)W \end{cases} \tag{2.10}$$

In case the reference signal is not a step but a higher order signal (e.g., RAMP), the controller itself has to contain the aforementioned higher order dynamic to satisfy the internal model principle, i.e., to ensure asymptotic tracking.

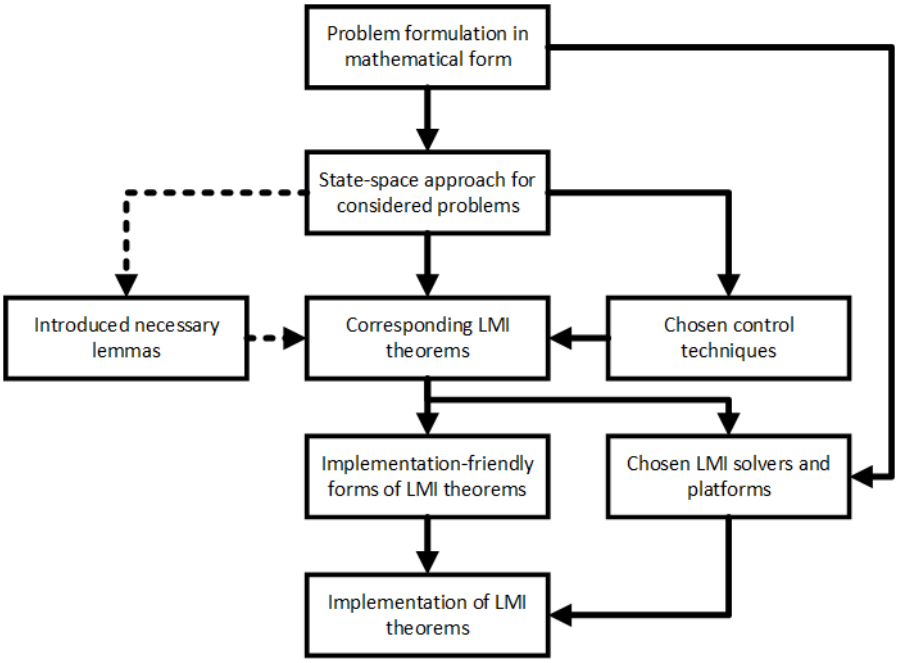

Figure 2.13: Generalized LMI-based control system design process

2.4.3 LMI-based control system design process

The LMI techniques, in general, are a particular way of translating the control problems (or even observation problems) into one or a group of LMI conditions, which next can be solved by a suitable LMI solver (e.g., MOSEK [5]). In addition, there are so many LMI theorems and lemmas so that they can cover entire classical frequency-domain approaches (e.g., loop-shaping technique) as well as time-domain approaches (MIMO control or fuzzy control). However, regardless the chosen approaches and conditions, as in Fig. 2.13, there are a common LMI-based process to solve the control problems, including:

1. Firstly, the control problems have to be formulated in mathematical forms. If there are other requirements in the forms of other fields, such as power systems or physics, these requirements have to be firstly transformed into mathematical forms.

2. Next, the considered model and the control problems, both of them have to be transformed into state-space model forms. As in the case of subsection 2.4.2 Control structure for reference asymptotic tracking, the model of the system and its outputs tracking problem are formulated using state-space approach.

3. Then, the control techniques have to be selected, based on the control designer's preferences and applications.

4. After that, the corresponding LMI theorems are formulated. If necessary, some lemmas will be introduced to alleviate the process of LMI theorems construction as well as their proofs.

5. The LMI theorems are generally formulated, but sometimes there are overlapping parts between LMI theorems or some unnecessary conditions. To maximize the probability of solving the formulated LMI conditions, corresponding implementation-friendly LMI conditions are established. This step is done just right before the implementation of the LMIs, i.e., just before the coding process, e.g., using MATLAB coding.

6. To be able to solve the LMI theorems, the platforms (e.g., MATLAB coding or python) and LMI solvers are selected. These selections are based on the problem formulations at the first step and the LMI theorems themselves. It is necessary to consider other constraints such as prices and the performance of platforms and LMI solvers.

7. Finally, the LMI theorems are implemented using the chosen LMI solvers and platforms. The resulting controller is tested and validated as in Fig. 2.12 of subsection 2.4.1.

In practice, the control design process using LMI-based techniques may seems to be very different from each other, especially in case the designers are using different platforms and solvers. These differences come from the way the problems are formulated, as well as the way each platform and/or solver works. However, following this process (i.e., Fig. 2.12), the control designer can manage to form and solve the considered control system problem. The platforms and LMI solvers will be discussed and presented in the next chapter in Appendix A.

Bibliography

[1] Jahangiri, P., & Aliprantis, D. C. (2013). Distributed Volt/VAr control by PV inverters. IEEE Transactions on power systems, 28(3), 3429-3439.

[2] "ENTSO-E Network Code for Requirements for Grid Connection Applicable to all Generators (2013)", https://eepublicdownloads.entsoe.eu/clean-documents/pre2015/resources/RfG/130308_Final_Version_NC_RfG.pdf.

[3] Gerstlauer, A., Yu, H., & Gajski, D. D. (2003). RTOS modeling for system level design. In Embedded Software for SoC (pp. 55-68). Springer, Boston, MA.

[4] Richard C.. Dorf, & Bishop, R. H. (2008). Modern control systems. Pearson Prentice Hall.

[5] ApS, M. (2019). Mosek optimization toolbox for matlab. User's Guide and Reference Manual, Version, 4.

Chapter 3

VSC-HVDC application

This chapter is focusing on the grid connected VSC-HVDC application, and the implementation of the decentralized control approach for its control. Due to the rapid growth in the size of power grids, the need for status and/or output information in remote areas has made traditional centralized control strategy solutions increasingly impractical. Moreover, it is much more difficult to obtain the necessary information when the supply signal source is very remote, such as when large-scale integration of distributed renewable energy sources in distribution systems. On the one hand, we need to decentralize our controllers because we have a lot of generators to deal with. In fact, it is necessary to increase the flexibility of modern energy systems so that the system can operate close to its limits. On the other hand, the strong and optimal decentralized management can satisfy the need for redundant information management and maintain the same performance as the previous method. Also, with the gradual development of decentralized control [1], [2] from the 1980s to the 2010s, and robust optimal controls [3]-[5] from the 1990s to the 2010s, now it is much more relevant to develop decentralization strategy in power system control, especially for grid-connected VSC application.

There are many studies on VSC-HVDC including feedback linearization [7], small-signal stability [8], and decoupling control of converter stations using LMI-based control [5], [6]. In addition, in recent years, not only DC networks, but also multi-terminal DC power networks, which have many advantages over AC networks [9], [10], [11], [12], have been rapidly developed and intensively studied. However, these works hardly cover the uncertainties of HVDC systems, and none of them have satisfied the need for decentralized methods.

This chapter includes: the VSC-HVDC system modeling in both of nonlinear and linearized models, the LMI-based linear robust H_∞ decentralized control in small-signal simulation and finally the LMI-based robust H_2 fuzzy decentralized control in nonlinear simulation.

3.1 VSC-HVDC system modeling in dq frame

3.1.1 VSC-HVDC nonlinear model in dq frame

Consider a VSC-HVDC link connecting two AC domains as in Fig. 3.1. If an average model [13], [14] is used for the converters, the resulting nonlinear model for the overall system is

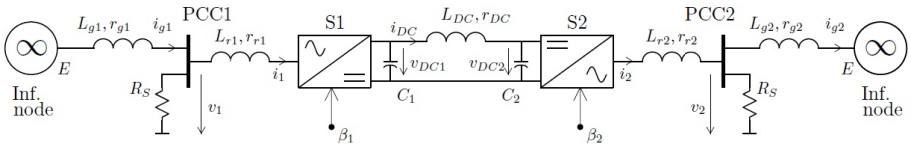

Figure 3.1: VSC-HVDC power structure

S.N	Variable Names	Constants	Values
1	AC grid inductance	$L_{g1} = L_{g2}$	$0.11H$
2	AC grid resistance	$r_{g1} = r_{g2}$	0.01Ω
3	Filter inductance	$L_{r1} = L_{r2}$	$0.025H$
4	Filter resistance	$r_{r1} = r_{r2}$	0.01Ω
5	AC filter resistance	R_s	2Ω
6	DC capacitor filter	$C_1 = C_2$	$220{*}10^{-6}F$
7	DC line resistance	r_{DC}	1.39Ω
8	DC line inductance	L_{DC}	$1.59{*}10^{-2}H$
9	Grid voltage	E	$187{*}10^{3}V$
10	Grid frequency	ω	$314rad/sec$

Table 3.1: VSC-HVDC system parameters

$$\begin{cases} \frac{dx_1}{dt} = \left(-\frac{R_s}{L_{g1}} - \frac{r_{g1}}{L_{g1}}\right)x_1 + \omega x_2 + \frac{R_s}{L_{g1}}x_3 + \frac{E}{L_{g1}} \\ \frac{dx_2}{dt} = \left(-\frac{R_s}{L_{g1}} - \frac{r_{g1}}{L_{g1}}\right)x_2 - \omega x_1 + \frac{R_s}{L_{g1}}x_4 \\ \frac{dx_3}{dt} = \left(-\frac{R_s}{L_{r1}} - \frac{r_{r1}}{L_{r1}}\right)x_3 + \frac{R_s}{L_{r1}}x_1 + \omega x_4 - \frac{x_5}{2L_{r1}}u_1 \\ \frac{dx_4}{dt} = \left(-\frac{R_s}{L_{r1}} - \frac{r_{r1}}{L_{r1}}\right)x_4 + \frac{R_s}{L_{r1}}x_2 - \omega x_3 - \frac{x_5}{2L_{r1}}u_2 \\ \frac{dx_5}{dt} = \frac{3}{2C_1}x_3u_1 + \frac{3}{2C_1}x_4u_2 - \frac{2}{C_1}x_6 \\ \frac{dx_6}{dt} = \frac{1}{2L_{DC}}x_5 - \frac{r_{DC}}{L_{DC}}x_6 - \frac{1}{2L_{DC}}x_7 \\ \frac{dx_7}{dt} = \frac{2}{C_2}x_6 + \frac{3}{2C_2}x_{10}u_3 + \frac{3}{2C_2}x_{11}u_4 \\ \frac{dx_8}{dt} = \left(-\frac{R_s}{L_{g2}} - \frac{r_{g2}}{L_{g2}}\right)x_8 + \omega x_9 + \frac{R_s}{L_{g2}}x_{10} + \frac{E}{L_{g2}} \\ \frac{dx_9}{dt} = \left(-\frac{R_s}{L_{g2}} - \frac{r_{g2}}{L_{g2}}\right)x_9 - \omega x_8 + \frac{R_s}{L_{g2}}x_{11} \\ \frac{dx_{10}}{dt} = \left(-\frac{R_s}{L_{r2}} - \frac{r_{r2}}{L_{r2}}\right)x_{10} + \frac{R_s}{L_{r2}}x_8 + \omega x_{11} - \frac{x_7}{2L_{r2}}u_3 \\ \frac{dx_{11}}{dt} = \left(-\frac{R_s}{L_{r2}} - \frac{r_{r2}}{L_{r2}}\right)x_{11} + \frac{R_s}{L_{r2}}x_9 - \omega x_{10} - \frac{x_7}{2L_{r2}}u_4 \end{cases} \tag{3.1}$$

with

$$\begin{cases} x_1 = i_{g1d}, \quad x_2 = i_{g1q} \\ x_3 = i_{1d}^{\infty}, \quad x_4 = i_{1q}^{\infty} \\ x_5 = v_{DC1}, \quad x_6 = i_{DC} \\ x_7 = v_{DC2}, \quad x_8 = i_{g2d} \\ x_9 = i_{g2q}, \quad x_{10} = i_{2d}^{\infty} \\ x_{11} = i_{2q}^{\infty} \end{cases} \quad \begin{cases} u_1 = \beta_{1d} \\ u_2 = \beta_{1q} \\ u_3 = \beta_{2d} \\ u_4 = \beta_{2q} \end{cases} \tag{3.2}$$

The outputs of the system are

$$\begin{cases} y_1 = v_{DC1} = x_5 \\ y_2 = Q_1 = \frac{3}{2}R_s x_2 x_3 - \frac{3}{2}R_s x_1 x_4 \\ y_3 = P_2 = \frac{3}{2}R_s x_8 x_{10} - \frac{3}{2}R_s x_{10}^2 + \frac{3}{2}R_s x_9 x_{11} - \frac{3}{2}R_s x_{11}^2 \\ y_4 = Q_2 = \frac{3}{2}R_s x_9 x_{10} - \frac{3}{2}R_s x_8 x_{11} \end{cases} \tag{3.3}$$

The system parameters are given in table 3.1.

3.1.2 Linearization of VSC-HVDC nonlinear model

To control the nonlinear system (3.1) using a linear control, a linearized system must be derived. The nonlinear system (3.1) is of the general form

$$\dot{X} = f(X,U), \quad Y = g(X) \tag{3.4}$$

The resulting linear approximation of this system around an equilibrium point (X^*, U^*) is

$$\Delta\dot{X} = A\Delta X + B\Delta U, \quad \Delta Y = C\Delta X \tag{3.5}$$

where

$$\Delta X = X - X^*, \Delta U = U - U^*, A = \left.\frac{\partial f(X,U)}{\partial X}\right|_{(X^*,U^*)}$$
$$B = \left.\frac{\partial f(X,U)}{\partial U}\right|_{(X^*,U^*)}, C = \left.\frac{\partial g(X,U)}{\partial X}\right|_{(X^*,U^*)}$$
$$X^* = \begin{bmatrix} x_1^* & x_2^* & x_3^* & x_4^* & x_5^* & x_6^* & x_7^* & x_8^* & x_9^* & x_{10}^* & x_{11}^* \end{bmatrix}^T$$
$$U^* = \begin{bmatrix} u_1^* & u_2^* & u_3^* & u_4^* \end{bmatrix}^T$$
$$A = \begin{bmatrix} A_{11} & A_{12} & 0 \\ A_{21} & A_{22} & A_{23} \\ 0 & A_{32} & A_{33} \end{bmatrix}, B = \begin{bmatrix} B_{11} & 0 \\ B_{21} & B_{22} \\ 0 & B_{32} \end{bmatrix}, C = \begin{bmatrix} C_{11} & 0 \\ C_{12} & C_{22} \\ 0 & C_{23} \end{bmatrix}^T$$

with

$$A_{12} = \begin{bmatrix} 0 & 0 & 0 & 0 & -\frac{2}{C_1} \end{bmatrix}^T, A_{21} = \begin{bmatrix} 0 & 0 & 0 & 0 & \frac{1}{2L_{DC}} \end{bmatrix};$$
$$A_{22} = \begin{bmatrix} -\frac{r_{DC}}{L_{DC}} \end{bmatrix}$$
$$A_{23} = \begin{bmatrix} \frac{-1}{2L_{DC}} & 0 & 0 & 0 & 0 \end{bmatrix}, A_{32} = \begin{bmatrix} \frac{2}{C_2} & 0 & 0 & 0 & 0 \end{bmatrix}^T$$
$$A_{11} = \begin{bmatrix} \frac{-R_s}{L_{g1}} - \frac{r_{g1}}{L_{g1}} & \omega & \frac{R_s}{L_{g1}} & 0 & 0 \\ -\omega & \frac{-R_s}{L_{g1}} - \frac{r_{g1}}{L_{g1}} & 0 & \frac{R_s}{L_{g1}} & 0 \\ \frac{R_s}{L_{r1}} & 0 & \frac{-R_s}{L_{r1}} - \frac{r_{r1}}{L_{r1}} & \omega & \frac{-u_1^*}{2L_{r1}} \\ 0 & \frac{R_s}{L_{r1}} & -\omega & \frac{-R_s}{L_{r1}} - \frac{r_{r1}}{L_{r1}} & \frac{-u_2^*}{2L_{r1}} \\ 0 & 0 & \frac{3u_1^*}{2C_1} & \frac{3u_2^*}{2C_1} & 0 \end{bmatrix}$$
$$A_{33} = \begin{bmatrix} 0 & 0 & 0 & \frac{3u_3^*}{2C_2} & \frac{3u_4^*}{2C_2} \\ 0 & \frac{-R_s}{L_{g2}} - \frac{r_{g2}}{L_{g2}} & \omega & \frac{R_s}{L_{g2}} & 0 \\ 0 & -\omega & \frac{-R_s}{L_{g2}} - \frac{r_{g2}}{L_{g2}} & 0 & \frac{R_s}{L_{g2}} \\ \frac{-u_3^*}{2L_{r2}} & \frac{R_s}{L_{r2}} & 0 & \frac{-R_s}{L_{r2}} - \frac{r_{r2}}{L_{r2}} & \omega \\ \frac{-u_4^*}{2L_{r2}} & 0 & \frac{R_s}{L_{r2}} & -\omega & \frac{-R_s}{L_{r2}} - \frac{r_{r2}}{L_{r2}} \end{bmatrix}$$

$$B_{11} = \begin{bmatrix} 0 & 0 \\ 0 & 0 \\ -\frac{x_5^*}{2L_{r1}} & 0 \\ 0 & -\frac{x_5^*}{2L_{r1}} \\ \frac{3x_3^*}{2C_1} & \frac{3x_4^*}{2C_1} \end{bmatrix}; B_{32} = \begin{bmatrix} \frac{3x_{10}^*}{2C_2} & \frac{3x_{11}^*}{2C_2} \\ 0 & 0 \\ 0 & 0 \\ -\frac{x_7^*}{2L_{r2}} & 0 \\ 0 & -\frac{x_7^*}{2L_{r2}} \end{bmatrix}$$
$$B_{21} = \begin{bmatrix} 0 & 0 \end{bmatrix}; B_{22} = \begin{bmatrix} 0 & 0 \end{bmatrix}$$
$$C_{11} = \begin{bmatrix} 0 & 0 & 0 & 0 & 1 \\ -\frac{3R_s x_4^*}{2} & \frac{3R_s x_3^*}{2} & \frac{3R_s x_2^*}{2} & -\frac{3R_s x_1^*}{2} & 0 \end{bmatrix}$$
$$C_{12} = \begin{bmatrix} 0 \\ 0 \end{bmatrix}; C_{22} = \begin{bmatrix} 0 \\ 0 \end{bmatrix}$$
$$C_{23} = \begin{bmatrix} 0 & \frac{3R_s x_{10}^*}{2} & \frac{3R_s x_{11}^*}{2} & \frac{3R_s x_8^*}{2} - 3R_s x_{10}^* & \frac{3R_s x_9^*}{2} - 3R_s x_{11}^* \\ 0 & -\frac{3R_s x_{11}^*}{2} & \frac{3R_s x_{10}^*}{2} & \frac{3R_s x_9^*}{2} & -\frac{3R_s x_9^*}{2} \end{bmatrix}$$

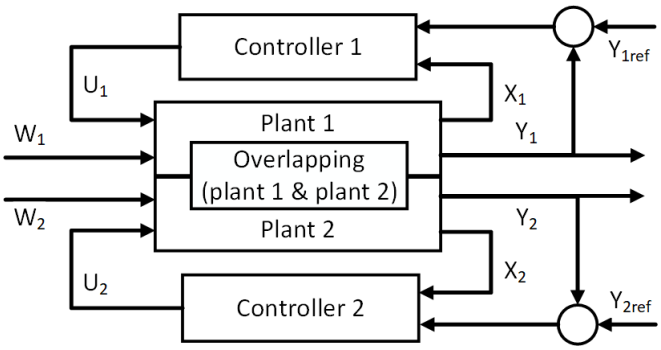

Figure 3.2: The decentralized overlapping system

Notice that the linearization process can also be done using MATLAB linear analysis tool as mentioned in Appendix A.1 Linearization with MATLAB/Simulink. In this case, the result is numerical only.

3.2 Linear robust H_∞ decentralized control in linear model simulation

This section is dedicated to the linear optimal H_∞ decentralized control approach base on overlapping control technique [1] and applied for the mentioned VSC-HVDC model, with the performance verification is done in the linearized model (3.5) (i.e., small-signal simulation).

3.2.1 Overlapping decentralized VSC-HVDC linear model

The general principle of the decentralized control is given in Fig. 2.11 (section 2.1, chapter Grid-connected power converter system objectives and proposed approaches). Here it is achieved via a overlapping decentralized control structure [1] which is schematized in Fig. 3.2 for the case of two subsystems/plants. In case of HVDC system as in Fig. 3.1, each plant is a converter, where plant 1 is converter S1 and plant 2 is converter S2. This structure uses state feedback control with integral action [15] to ensure the asymptotic tracking to a step in reference signals.

One can notice that from the linearized system equation (3.5), or again on the VSC-HVDC physical model in Fig. 3.1, the system (3.5) can be divided into the two overlapping subsystems:

$$\begin{array}{l} (I)\left\{\begin{array}{l} \dot{X}_1 = A_1X_1 + B_1^1U_1 + B_2^1W_1 \\ Y_1 = C_1X_1 \end{array}\right. \\ (II)\left\{\begin{array}{l} \dot{X}_2 = A_2X_2 + B_1^2U_2 + B_2^2W_2 \\ Y_2 = C_2X_2 \end{array}\right. \end{array} \tag{3.6}$$

where $W_1 = x_7$ for system (I), $W_1 = x_5$ for system (II), the common states is x_6, and:

$$\begin{array}{l} X_1 = \left[\begin{array}{cccccc} x_1 & x_2 & x_3 & x_4 & x_5 & x_6 \end{array}\right]^T \\ X_2 = \left[\begin{array}{cccccc} x_6 & x_7 & x_8 & x_9 & x_{10} & x_{11} \end{array}\right]^T \\ A_1 = \left[\begin{array}{cc} A_{11} & A_{12} \\ A_{21} & A_{22} \end{array}\right]; A_2 = \left[\begin{array}{cc} A_{22} & A_{23} \\ A_{32} & A_{33} \end{array}\right] \\ B_1^1 = \left[\begin{array}{c} B_{11} \\ B_{21} \end{array}\right]; B_1^2 = \left[\begin{array}{c} B_{22} \\ B_{32} \end{array}\right] \\ C_1 = \left[\begin{array}{cc} C_{11} & C_{12} \end{array}\right]; C_2 = \left[\begin{array}{cc} C_{22} & C_{23} \end{array}\right] \\ B_2^1 = \left[\begin{array}{cccccc} 0 & 0 & 0 & 0 & 0 & \frac{-1}{2L_{DC}} \end{array}\right]^T \\ B_2^2 = \left[\begin{array}{cccccc} \frac{1}{2L_{DC}} & 0 & 0 & 0 & 0 & 0 \end{array}\right]^T \end{array}$$

3.2.2 Augmented System for Reference Tracking

Each subsytem in the linearized HVDC system (equation (3.6)) is in the form of a state-space linear system with disturbance:

$$\dot{X} = AX + B_1U + B_2W, \quad Y = CX \tag{3.7}$$

Consider the tracking error between the reference and output:

$$e = -CX + Y_{ref}. \tag{3.8}$$

To be able to ensure asymptotic tracking, an augmented system should be constructed. Using internal model principle [15], respectively, the considered augmented state, output, input and disturbance are:

$$\bar{X} = \begin{bmatrix} \dot{X} \\ e \end{bmatrix}; \bar{Y} = e; \bar{U} = \dot{U}; \bar{W} = \dot{W} \tag{3.9}$$

The resulting augmented system is:

$$\begin{cases} \dot{\bar{X}} = \bar{A}\bar{X} + \bar{B}_1\bar{U} + \bar{B}_2\bar{W} \\ \bar{Y} = \bar{C}\bar{X} \end{cases} \tag{3.10}$$

where the augmented matrices are:

$$\bar{A} = \begin{bmatrix} A & 0 \\ -C & 0 \end{bmatrix}; \bar{B}_1 = \begin{bmatrix} B_1 \\ 0 \end{bmatrix}; \bar{B}_2 = \begin{bmatrix} B_2 \\ 0 \end{bmatrix}; \bar{C} = \begin{bmatrix} 0 & I \end{bmatrix}$$

3.2.3 Robust H_∞ Decentralized State Feedback Control

Now, to control the mentioned VSC-HVDC system, H_∞ decentralized control approaches are introduced. Firstly, the approach ignores the uncertainties for simplicity. The control gain is produced using LMI technique [5], [6]. Next, a the control gain will be generated again but we will take into account of the norm-bounded parametric uncertainties.

Consider a state-feedback controller $\bar{U}$ of the augmented system (3.10) (i.e., the controller U with integral action for the original system (3.7)):

$$\bar{U} = \dot{U} = \bar{K}\bar{X} \Rightarrow U = \bar{K}\begin{bmatrix} X \\ \int edt \end{bmatrix} \tag{3.11}$$

3.2.3.1 Uncertainty-Free H_∞ Decentralized State Feedback Control

For the uncertainty-free case, the considered augmented system (3.10) can be generalized in a full form of state-space model with disturbance

$$\begin{cases} \dot{\bar{X}} = \bar{A}\bar{X} + \bar{B}_1\bar{U} + \bar{B}_2\bar{W} \\ \bar{Y} = \bar{C}\bar{X} + \bar{D}_1\bar{U} + \bar{D}_2\bar{W} \end{cases} \tag{3.12}$$

The transfer function $G(s)$ from the disturbance $\bar{W}$ to the output $\bar{Y}$ is:

$$\begin{cases} \bar{Y}(s) = G(s)\bar{W}(s) \\ G(s) = (\bar{C} + \bar{D}_1\bar{K})\big(sI - \big(\bar{A} + \bar{B}_1\bar{K}\big)\big)^{-1}\bar{B}_2 + \bar{D}_2 \end{cases} \tag{3.13}$$

To minimize the undesired interaction of the overlapping state between the two converters one has to minimize the norm of the transfer function $G(s)$

$$\left\|\bar{Y}\right\|_2 \leq \|G\|_\infty \left\|\bar{W}\right\|_2 \tag{3.14}$$

Problem 1 *The H_∞ problem for the linear system* (3.12) *is to formulate the control law such that*

$$\sup_{\|\bar{W}\|_2 \neq 0} \frac{\|\bar{Y}\|_2}{\|\bar{W}\|_2} \leq \gamma \tag{3.15}$$

for a given positive scalar γ.

Analysis of stability and reliability in the uncertainty-free case (i.e., problem 1) is summarized in Theorem 1 below.

Theorem 1 *Problem 1 (i.e., H_∞ problem) has a solution iff there exists a matrix W_p and a symmetric positive definite matrix X_p , satisfying:*

$$\begin{array}{c} \underset{X_P, W_P}{min} \quad \gamma \\ \left\{ \begin{array}{l} \left[\begin{array}{ccc} \Psi & \bar{B}_2 & \left(\bar{C}X_p + \bar{D}_1 W_p\right)^T \\ \bar{B}_2^T & -\gamma I & \bar{D}_2^T \\ \bar{C}X_p + \bar{D}_1 W_p & \bar{D}_2 & -\gamma I \end{array} \right] < 0 \\ \Psi = \left(\bar{A}X_p + \bar{B}_1 W_p\right)^T + \bar{A}X_p + \bar{B}_1 W_p \end{array} \right. \end{array} \tag{3.16}$$

The control gain $\bar{K}$ is

$$\bar{K} = W_p X_p^{-1} \tag{3.17}$$

Proof 1 *Consider the linear system without disturbance*

$$\left\{ \begin{array}{l} \dot{X} = AX + BU \\ Y = CX + DU \end{array} \right. \tag{3.18}$$

The transfer function $G(s)$ of this system from input U to output Y is:

$$\left\{ \begin{array}{l} Y = G(s)\, U \\ G(s) = C(sI - A)^{-1} B + D \end{array} \right. \tag{3.19}$$

The H_∞ problem of this system, i.e., problem 1, is solved, iff there exist a positive definite symmetric matrix X_p , such that [5], [6]

$$\left[\begin{array}{ccc} X_P A^T + A X_P & B & X_P C^T \\ B^T & -\gamma I & D^T \\ C X_P & D & -\gamma I \end{array} \right] < 0 \tag{3.20}$$

This result applied for the linear system with disturbance (equation (3.12)*), along with defining $W_P = K X_P$, proves Theorem 1.*

3.2.3.2 Robust H_∞ Decentralized State Feedback Control

Consider now also the bounded uncertainties via the version (3.12) of the system

$$\left\{ \begin{array}{l} \dot{\bar{X}} = (\bar{A} + \Delta\bar{A})X + \left(\bar{B}_1 + \Delta\bar{B}_1\right)\bar{U} + \bar{B}_2\bar{W} \\ \bar{Y} = \bar{C}\bar{X} + \bar{D}_1\bar{U} + \bar{D}_2\bar{W} \end{array} \right. \tag{3.21}$$

where

$$\left\{ \begin{array}{l} \left[\begin{array}{cc} \Delta\bar{A} & \Delta\bar{B}_1 \end{array} \right] = HF \left[\begin{array}{cc} E_1 & E_2 \end{array} \right] \\ E_1 = \delta_1 \bar{A}; |\delta_1| < r_1; r_1 \in R^+ \\ E_2 = \delta_2 \bar{B}_1; |\delta_2| < r_2; r_2 \in R^+ \\ F^T F \leq I \end{array} \right. \tag{3.22}$$

The transfer function $G(s)$ from disturbance $\bar{W}$ to the output $\bar{Y}$ is

$$\left\{ \begin{array}{l} \bar{Y}(s) = G(s)\, \bar{W}(s) \\ G(s) = (\bar{C} + \bar{D}_1\bar{K})\left(sI - \left((\bar{A} + \Delta\bar{A}) + \left(\bar{B}_1 + \Delta\bar{B}_1\right)\bar{K}\right)\right)^{-1}\bar{B}_2 + \bar{D}_2 \end{array} \right. \tag{3.23}$$

Problem 2 *For the linear system with uncertainties (3.23), the robust H_∞ problem is to design a state feedback regulator such that*

$$\sup_{\|\bar{W}\|_2 \neq 0} \frac{\|\bar{Y}\|_2}{\|\bar{W}\|_2} \leq \gamma \tag{3.24}$$

holds for a given positive scalar γ.

Stability conditions in terms of LMI are given for the system (3.21) in Theorem 2 below.

Theorem 2 *The robust H_∞ problem, that is, Problem 2, has a solution iff there exist a positive scalar α, a matrix W_p and a symmetric positive definite matrix X_p , satisfying:*

$$\underset{X_P, W_P}{min} \quad \gamma$$

$$\begin{bmatrix} \Psi & \bar{B}_2 & \left(\bar{C}X_p + \bar{D}_1 W_p\right)^T & \left(E_1 X_p + E_2 W_p\right)^T \\ \bar{B}_2^T & -\gamma I & \bar{D}_2^T & 0 \\ \bar{C}X_p + \bar{D}_1 W_p & \bar{D}_2 & -\gamma I & 0 \\ E_1 X_p + E_2 W_p & 0 & 0 & -\alpha I \end{bmatrix} < 0 \tag{3.25}$$

where, $\Psi = \left(\bar{A}X_p + \bar{B}_1 W_p\right)^T + \bar{A}X_p + \bar{B}_1 W_p + \alpha H H^T$
The control gain $\bar{K}$ is

$$\bar{K} = W_p X_p^{-1} \tag{3.26}$$

Proof 2 *To prove this theorem, a well-known lemma [5], [6] is needed:*

Lemma 1 *The following inequality*

$$Q + MFN + N^T F^T M^T < 0 \ , \forall F^T F < I \tag{3.27}$$

holds iff there exist $\alpha > 0$ satisfying

$$Q + \alpha M M^T + \alpha^{-1} N^T N < 0 \tag{3.28}$$

Next, use Theorem 1 with $G(s)$ given by equation (3.23)*:*

$$\begin{array}{l} \begin{bmatrix} \left\langle \bar{A}X_p + \bar{B}_1 W_p \right\rangle_s & \bar{B}_2 & \left(\bar{C}X_p + \bar{D}_1 W_p\right)^T \\ \bar{B}_2^T & -\gamma I & \bar{D}_2^T \\ \bar{C}X_p + \bar{D}_1 W_p & \bar{D}_2 & -\gamma I \end{bmatrix} \\ + \left\langle \begin{bmatrix} H \\ 0 \\ 0 \end{bmatrix} F \begin{bmatrix} E_1 X_p + E_2 W_p & 0 & 0 \end{bmatrix} \right\rangle_s < 0 \end{array} \tag{3.29}$$

Using lemma 1 with

$$\begin{cases} Q = \begin{bmatrix} \left\langle \bar{A}X_p + \bar{B}_1 W_p \right\rangle_s & \bar{B}_2 & \left(\bar{C}X_p + \bar{D}_1 W_p\right)^T \\ \bar{B}_2^T & -\gamma I & \bar{D}_2^T \\ \bar{C}X_p + \bar{D}_1 W_p & \bar{D}_2 & -\gamma I \end{bmatrix} \\ M = \begin{bmatrix} H \\ 0 \\ 0 \end{bmatrix}; N = \begin{bmatrix} E_1 X_p + E_2 W_p & 0 & 0 \end{bmatrix} \end{cases}$$

inequality (3.29) is written as

$$\begin{bmatrix} \Psi & \bar{B}_2 & \left(\bar{C}X_p + \bar{D}_1 W_p\right)^T \\ \bar{B}_2^T & -\gamma I & \bar{D}_2^T \\ \bar{C}X_p + \bar{D}_1 W_p & \bar{D}_2 & -\gamma I \end{bmatrix} + \alpha^{-1} \begin{bmatrix} E_1 X_p + E_2 W_p \\ 0 \\ 0 \end{bmatrix} \begin{bmatrix} E_1 X_p + E_2 W_p & 0 & 0 \end{bmatrix} < 0 \tag{3.30}$$

where

$$\Psi = \left\langle \bar{A}X_p + \bar{B}_1 W_p \right\rangle_s + \alpha H H^T \tag{3.31}$$

The latter inequality can be equivalently written to the LMI form of Theorem 2 using Schur complement lemma [5], [6].

3.2.4 Simulations and results

The proposed control strategies are verified in this section with the linearized model (3.6), in different HVDC line lengths (110 Km, 750 Km, 1400 Km), with the consideration of parameter uncertainties in system equations (3.6). The HVDC system using proposed overlapping decentralized controls are tested and validated through 3 different scenarios:

- Scenario 1: the H_∞ Robust Decentralized Control ($H_{inf}RDC$) and H_∞ Decentralized Control ($H_{inf}DC$) are tested for the 110Km HVDC link with 20% uncertainty in matrices $\bar{A}$ and $\bar{B}_1$ of system (3.12) ($\Delta\bar{A} = 0.2\bar{A}$ and $\Delta\bar{B}_1 = 0.2\bar{B}_1$, i.e. an increase of 20% of $R_s, r_{g1}, r_{r1}, r_{g2}, r_{r2}$, and a decrease of 17.3% of $L_{DC}, L_{r1}, L_{g1}, C_1, L_{r2}, L_{g2}$). As shown in Figs. 3.3 and 3.4 (for v_{DC}, Q_1, P_2, Q_2 respectively), the robust control version $H_{inf}RDC$ provides a much better damped outputs and shorter transient time.

- Scenario 2: the $H_{inf}RDC$ is tested for different lengths of the DC line (110 Km, 750 Km, 1400 Km), and also with 20% uncertainty as in scenario 1. As can be seen in Figs. 3.5 and 3.5, there is a clear relationship between the length of the line and the control performance. The longer the length, the better performance. This can be explained by carefully examining the system of equations HVDC where there is a strong coupling between v_{DC1} and v_{DC2}. The coupling between these voltages is inverse proportional with the length of the line (i.e., with r_{DC} and L_{DC}). For short HVDC line (110 km) the performance is acceptable with sufficient damping, while on longer lines the oscillations due to the undesired interaction are completely damped.

- Scenario 3: If one converter loses control (that converter's input control is now 0), the other converter will still operate correctly. This scenario is validated using 2 tests. For the first test converter 1 losses its control (i.e., converter $S1$ in Fig. 3.1 (illustrated in Figs. 3.7 and 3.8)) and for the second one, same situation is studied for converter 2 (i.e., converter $S2$ in Fig. 3.1) (illustrated in Figs. 3.9 and 3.10). In the first test (Figs. 3.7 and 3.8)), the outputs of converter 1, i.e., v_{DC}, Q_1, are not tracking the reference since the control input of this converter are equal to zero. However, the second converter is still able to control its outputs P_2, Q_2 to track the desired references. The same behavior is found in the second test, where the second converter S2 lost its control (i.e., P_2, Q_2 are not tracking the references), the first converter S1 is still able to regulate its output v_{DC}, Q_1 to track the references as in Figs. 3.9 and 3.10.

3.2.5 Conclusion

This section provides *decentralized regulation* of HVDC links. It has the advantage of providing two independent controls for each inverter. Independence at all levels: aggregation, action and use of measurement. This is an advantage over traditional vector control, which has a separate synthesis but uses feedback from different transducers to isolate the dynamics. Our proposed control provides *resilience*. In the event of a control fault in 1 converter (loss of measurement or control), control of the other converter is not severely affected. Communication between the two terminals is not required. The natural interaction between the dynamics of the two converters is considered as undesired disturbance and is handled by the advanced control. In order to analytically ensure the stability of the entire closed loop (ie, for the entire grid-connected HVDC), the gains are synthesized by solving

the LMI. The coupling between inverters is quantified by the length of the HVDC link. The aforementioned H_∞ LMI-based synthesis improves parameter robustness and interference suppression. As a result, coupling effects are well tolerated and good results can be obtained even with short HVDC lines (and thus strong undesired interactions between the two converters).

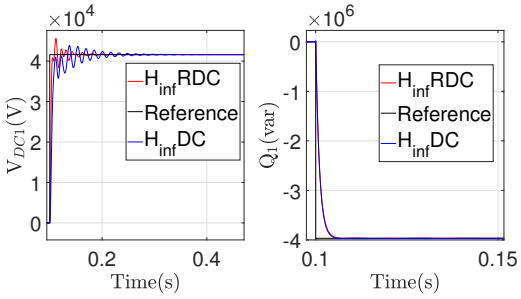

Figure 3.3: DC voltage v_{DC1} & reactive power Q_1 in 110 Km line

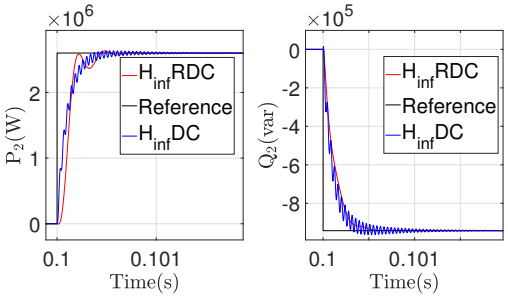

Figure 3.4: Active power P_2 & reactive power Q_2 in 110 Km line

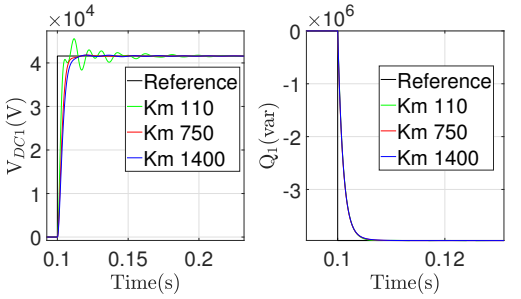

Figure 3.5: DC voltage v_{DC1} & reactive power Q_1 in 110 , 750, 1400 Km line

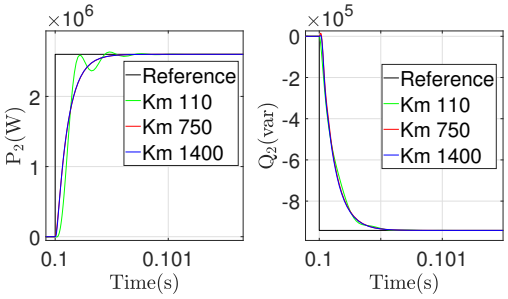

Figure 3.6: Active & reactive power P_2, Q_2 in 110 , 750, 1400 Km line

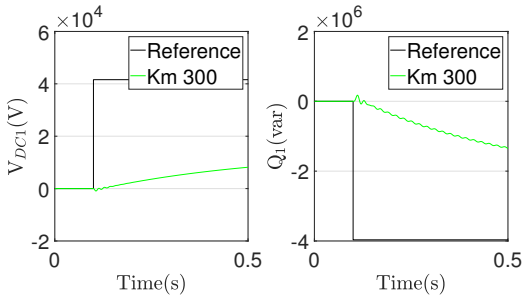

Figure 3.7: DC voltage v_{DC1} & reactive power Q_1 (control loss in converter 1)

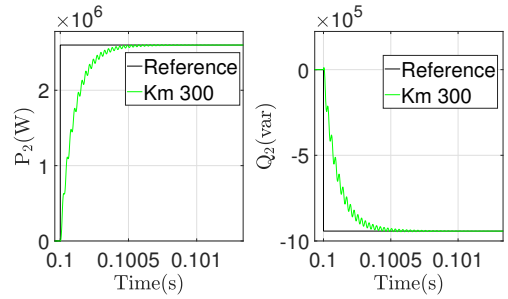

Figure 3.8: Active & reactive power P_2, Q_2 (control loss in converter 1)

3.3 Robust H_2 fuzzy decentralized control in nonlinear simulation

As discussed in chapter Introduction and in chapter Grid-connected power converter system objectives and proposed approaches, a grid connected power converter system in general, as well as a VSC-HVDC system in particular, not only has parameter uncertainties but also has many nonlinear dynamics. Also, VSC-HVDC can be required to operate at different operating points. To handle such a nonlinear system, a H_2 Robust Nonlinear Fuzzy

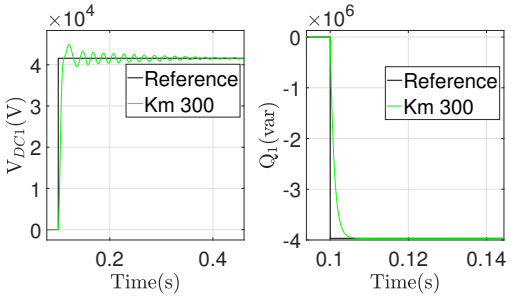

Figure 3.9: DC voltage v_{DC1} & reactive power Q_1 (control loss in converter 2)

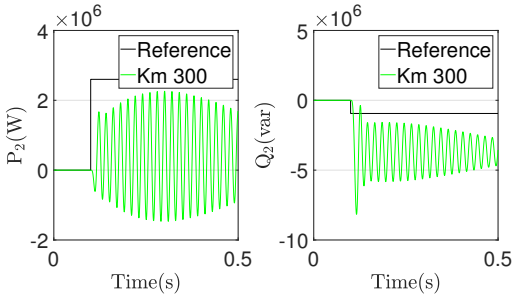

Figure 3.10: Active & reactive power P_2, Q_2 (control loss in converter 2)

Decentralized Control (H_2RNFDC) was proposed. Similar to the decentralized approach in section 3.2, the VSC-HVDC consists of two nonlinear subsystems, each subsystem is 1 converter. The nonlinear interactions between the two subsystems are treated as disturbance rejection using fuzzy optimal control methods. First, the Takagi Sugeno (TS) fuzzy model is used for fuzzy modeling of nominal nonlinear system. Next, new stability conditions for VSC-HVDC control system taking into account of parameter uncertainties. The control method is based on the LMI techniques.

3.3.1 Overlapping decentralized VSC-HVDC nonlinear model

(3.1) is a nonlinear model, and its nonlinear state-space representation can be put in the form of (3.32):

$$\begin{cases} \dot{X} = AX + BU + B_d W \\ Y = CX \end{cases} \tag{3.32}$$

where

$$A = \begin{bmatrix} A_{11} & A_{12} & 0 \\ A_{21} & A_{22} & A_{23} \\ 0 & A_{32} & A_{33} \end{bmatrix} B = \begin{bmatrix} B_{11} & 0 \\ B_{21} & B_{22} \\ 0 & B_{32} \end{bmatrix}; C = \begin{bmatrix} C_{11} & C_{12} & 0 \\ 0 & C_{22} & C_{23} \end{bmatrix}$$
$$B_d = \begin{bmatrix} \frac{1}{L_{g1}} & 0 & 0 & 0 & 0 & 0 & 0 & \frac{1}{L_{g2}} & 0 & 0 & 0 \end{bmatrix}^T$$

with:

$$A_{11} = \begin{bmatrix} \frac{-R_s}{L_{g1}} - \frac{r_{g1}}{L_{g1}} & \omega & \frac{R_s}{L_{g1}} & 0 & 0 \\ -\omega & \frac{-R_s}{L_{g1}} - \frac{r_{g1}}{L_{g1}} & 0 & \frac{R_s}{L_{g1}} & 0 \\ \frac{R_s}{L_{r1}} & 0 & \frac{-R_s}{L_{r1}} - \frac{r_{r1}}{L_{r1}} & \omega & 0 \\ 0 & \frac{R_s}{L_{r1}} & -\omega & \frac{-R_s}{L_{r1}} - \frac{r_{r1}}{L_{r1}} & 0 \\ 0 & 0 & 0 & 0 & 0 \end{bmatrix}; A_{12} = \begin{bmatrix} 0 & 0 & 0 & 0 & -\frac{2}{C_1} \end{bmatrix}^T;$$
$$A_{21} = \begin{bmatrix} 0 & 0 & 0 & 0 & \frac{1}{2L_{DC}} \end{bmatrix}; A_{22} = \begin{bmatrix} -\frac{r_{DC}}{L_{DC}} \end{bmatrix}; A_{23} = \begin{bmatrix} \frac{-1}{2L_{DC}} & 0 & 0 & 0 & 0 \end{bmatrix};$$
$$A_{32} = \begin{bmatrix} \frac{2}{C_2} & 0 & 0 & 0 & 0 \end{bmatrix}^T; A_{33} = \begin{bmatrix} 0 & 0 & 0 & 0 & 0 \\ 0 & \frac{-R_s}{L_{g2}} - \frac{r_{g2}}{L_{g2}} & \omega & \frac{R_s}{L_{g2}} & 0 \\ 0 & -\omega & \frac{-R_s}{L_{g2}} - \frac{r_{g2}}{L_{g2}} & 0 & \frac{R_s}{L_{g2}} \\ 0 & \frac{R_s}{L_{r2}} & 0 & \frac{-R_s}{L_{r2}} - \frac{r_{r2}}{L_{r2}} & \omega \\ 0 & 0 & \frac{R_s}{L_{r2}} & -\omega & \frac{-R_s}{L_{r2}} - \frac{r_{r2}}{L_{r2}} \end{bmatrix}$$

$$B_{11} = \begin{bmatrix} 0 & 0 \\ 0 & 0 \\ -\frac{x_5}{2L_{r1}} & 0 \\ 0 & -\frac{x_5}{2L_{r1}} \\ \frac{3x_3}{2C_1} & \frac{3x_4}{2C_1} \end{bmatrix}; B_{32} = \begin{bmatrix} \frac{3x_{10}}{2C_2} & \frac{3x_{11}}{2C_2} \\ 0 & 0 \\ 0 & 0 \\ -\frac{x_7}{2L_{r2}} & 0 \\ 0 & -\frac{x_7}{2L_{r2}} \end{bmatrix};$$
$$B_{21} = \begin{bmatrix} 0 & 0 \end{bmatrix}; B_{22} = \begin{bmatrix} 0 & 0 \end{bmatrix}; C_{12} = \begin{bmatrix} 0 & 0 \end{bmatrix}^T; C_{22} = \begin{bmatrix} 0 & 0 \end{bmatrix}^T;$$
$$C_{11} = \begin{bmatrix} 0 & 0 & 0 & 0 & 1 \\ -\frac{3R_s x_4}{2} & \frac{3R_s x_3}{2} & 0 & 0 & 0 \end{bmatrix};$$
$$C_{23} = \begin{bmatrix} 0 & \frac{3R_s x_{10}}{2} & \frac{3R_s x_{11}}{2} & -\frac{3R_s x_{10}}{2} & -\frac{3R_s x_{11}}{2} \\ 0 & -\frac{3R_s x_{11}}{2} & \frac{3R_s x_{10}}{2} & 0 & 0 \end{bmatrix}$$

Here, as in the case of linear decentralized control, the nonlinear HVDC system also consists of two strongly coupled inverters. Each part of the converter is treated as a subsystem (or block) and then controlled independently.

The nonlinear HVDC system (3.32) can be divided into 2 overlapping subsystems:

$$(I) \begin{cases} \dot{X}_1 = A_1 X_1 + B_1^1 U_1 + B_2^1 W_1 \\ Y_1 = C_1 X_1 \end{cases} \quad (II) \begin{cases} \dot{X}_2 = A_2 X_2 + B_1^2 U_2 + B_2^2 W_2 \\ Y_2 = C_2 X_2 \end{cases} \tag{3.33}$$

where:

$$W_1 = \begin{bmatrix} x_7 & E \end{bmatrix}^T; W_1 = \begin{bmatrix} x_5 & E \end{bmatrix}^T$$

and:

$$X_1 = \begin{bmatrix} x_1 & x_2 & x_3 & x_4 & x_5 & x_6 \end{bmatrix}^T; X_2 = \begin{bmatrix} x_6 & x_7 & x_8 & x_9 & x_{10} & x_{11} \end{bmatrix}^T;$$
$$A_1 = \begin{bmatrix} A_{11} & A_{12} \\ A_{21} & A_{22} \end{bmatrix}; A_2 = \begin{bmatrix} A_{22} & A_{23} \\ A_{32} & A_{33} \end{bmatrix}; B_1^1 = \begin{bmatrix} B_{11} \\ B_{21} \end{bmatrix}; B_1^2 = \begin{bmatrix} B_{22} \\ B_{32} \end{bmatrix}; C_1 = \begin{bmatrix} C_{11} & C_{12} \end{bmatrix};$$
$$C_2 = \begin{bmatrix} C_{22} & C_{23} \end{bmatrix}; B_2^1 = \begin{bmatrix} 0 & 0 & 0 & 0 & 0 & \frac{-1}{2L_{DC}} \\ \frac{1}{L_{g1}} & 0 & 0 & 0 & 0 & 0 \end{bmatrix}^T; B_2^2 = \begin{bmatrix} \frac{1}{2L_{DC}} & 0 & 0 & 0 & 0 & 0 \\ 0 & 0 & \frac{1}{L_{g2}} & 0 & 0 & 0 \end{bmatrix}^T$$

By using Kirchoffs law, the d-q voltages at PCC1 and PCC2 in Fig. 3.1 can be written respectively as:

$$\begin{cases} v_{1d}^{\infty} = R_s \left(i_{g1d} - i_{1d}^{\infty} \right) = R_s \left(x_1 - x_3 \right) \\ v_{1q}^{\infty} = R_s \left(i_{g1q} - i_{1q}^{\infty} \right) = R_s \left(x_2 - x_4 \right) \end{cases} \tag{3.34}$$

$$\begin{cases} v_{2d}^{\infty} = R_s \left(i_{g2d} - i_{2d}^{\infty} \right) = R_s \left(x_8 - x_{10} \right) \\ v_{2q}^{\infty} = R_s \left(i_{g2q} - i_{2q}^{\infty} \right) = R_s \left(x_9 - x_{11} \right) \end{cases} \tag{3.35}$$

To simplify the controllers, the voltage on the q-axis is also assumed to be zero. So to indirectly control active and reactive power we can directly control currents. So the result of the system is:

$$y = \begin{bmatrix} x_4 & x_5 & x_{10} & x_{11} \end{bmatrix}^T \tag{3.36}$$

The nonlinear system (3.33) is now written as:

$$\begin{cases} \frac{dx_3}{dt} = \left(-\frac{r_{r1}}{L_{r1}} \right) x_3 + \omega x_4 - \frac{x_5}{2L_{r1}} u_1 + \frac{1}{L_{r1}} v_{1d}^{\infty} \\ \frac{dx_4}{dt} = -\omega x_3 + \left(-\frac{r_{r1}}{L_{r1}} \right) x_4 - \frac{x_5}{2L_{r1}} u_2 + \frac{1}{L_{r1}} v_{1q}^{\infty} \\ \frac{dx_5}{dt} = \frac{3}{2C_1} x_3 u_1 + \frac{3}{2C_1} x_4 u_2 - \frac{2}{C_1} x_6 \\ \frac{dx_6}{dt} = \frac{1}{2L_{DC}} x_5 - \frac{r_{DC}}{L_{DC}} x_6 - \frac{1}{2L_{DC}} x_7 \\ \frac{dx_7}{dt} = \frac{2}{C_2} x_6 + \frac{3}{2C_2} x_{10} u_3 + \frac{3}{2C_2} x_{11} u_4 \\ \frac{dx_{10}}{dt} = \left(-\frac{r_{r2}}{L_{r2}} \right) x_{10} + \omega x_{11} - \frac{x_7}{2L_{r2}} u_3 + \frac{1}{L_{r2}} v_{2d}^{\infty} \\ \frac{dx_{11}}{dt} = \left(-\frac{r_{r2}}{L_{r2}} \right) x_{11} - \omega x_{10} - \frac{x_7}{2L_{r2}} u_4 + \frac{1}{L_{r2}} v_{2q}^{\infty} \end{cases} \tag{3.37}$$

Thus, the nonlinear decentralized system (3.33) now has disturbances W_1, W_2 and states X_1, X_2 as:

$$W_1 = \begin{bmatrix} x_7 & v_{1d}^{\infty} & v_{1q}^{\infty} \end{bmatrix}^T; W_2 = \begin{bmatrix} x_5 & v_{2d}^{\infty} & v_{2q}^{\infty} \end{bmatrix}^T;$$
$$X_1 = \begin{bmatrix} x_3 & x_4 & x_5 & x_6 \end{bmatrix}^T; X_2 = \begin{bmatrix} x_6 & x_7 & x_{10} & x_{11} \end{bmatrix}^T$$

and its state-space matrices are

$$A_1 = \begin{bmatrix} -\frac{r_{r1}}{L_{r1}} & \omega & 0 & 0 \\ -\omega & -\frac{r_{r1}}{L_{r1}} & 0 & 0 \\ 0 & 0 & 0 & -\frac{2}{C_1} \\ 0 & 0 & \frac{1}{2L_{DC}} & -\frac{r_{DC}}{L_{DC}} \end{bmatrix}; A_2 = \begin{bmatrix} -\frac{r_{DC}}{L_{DC}} & \frac{-1}{2L_{DC}} & 0 & 0 \\ -\frac{2}{C_2} & 0 & 0 & 0 \\ 0 & 0 & -\frac{r_{r2}}{L_{r2}} & \omega \\ 0 & 0 & -\omega & -\frac{r_{r2}}{L_{r2}} \end{bmatrix};$$
$$B_1 = \begin{bmatrix} -\frac{x_5}{2L_{r1}} & 0 \\ 0 & -\frac{x_5}{2L_{r1}} \\ \frac{3x_3}{2C_1} & \frac{3x_4}{2C_1} \\ 0 & 0 \end{bmatrix}; B_2 = \begin{bmatrix} 0 & 0 \\ \frac{3x_{10}}{2C_2} & \frac{3x_{11}}{2C_2} \\ -\frac{x_7}{2L_{r2}} & 0 \\ 0 & -\frac{x_7}{2L_{r2}} \end{bmatrix}; C_1 = \begin{bmatrix} 0 & 1 & 0 & 0 \\ 0 & 0 & 1 & 0 \end{bmatrix}; C_2 = \begin{bmatrix} 0 & 0 & 1 & 0 \\ 0 & 0 & 0 & 1 \end{bmatrix}$$

The control system structure is still similar to those of linear control presented in section 3.2. The overlapping nonlinear strategy structure using fuzzy technique is exactly the same as in Fig. 3.2, just the controller itself is different.

3.3.2 Fuzzification of decentralized HVDC nonlinear model

To be able to control each subsystem in the overlapping HVDC nonlinear system (3.33) using fuzzy technique, firstly we have to define the nonlinear sectors [16]. These nonlinear sectors are the time-varying state-dependent elements in the converter state-space matrices, which is actually a bi-linear system:

$$\dot{X} = AX + B_1U + B_2W; B_1 = B_1'X$$

where A, B_1' and B_2 are time-invariant matrices.

Obviously, these nonlinear sectors come from the $B_1 = B_1'X$ matrix of the converter, which is a linear function of the X state. To capture the dynamics of a nonlinear system, the control design must account for the variations of these nonlinear sectors. The fuzification process is the process of transforming these nonlinear sectors into a convex combination of time-invariant linear elements, which can then be handled by linear controllers using a global Lyapunov function.

In the subsystem (I) of system (3.33), the nonlinear sectors are: $-\frac{x_5}{2L_{r1}}, \frac{3x_3}{2C_1}, \frac{3x_4}{2C_1}$
In the subsystem (II) of system (3.33), the nonlinear sectors are:$-\frac{x_7}{2L_{r2}}, \frac{3x_{10}}{2C_2}, \frac{3x_{11}}{2C_2}$

These nonlinear sectors share the same membership function with the states $x_3, x_4, x_5, x_7, x_{10}, x_{11}$ because they are the linear functions of those states. Thus, there are three nonlinear sectors for subsystem (I): x_3, x_4, x_5, and three nonlinear sectors for subsystem (II): x_7, x_{10}, x_{11}.

The ranges of these states for the considered VSC-HVDC are given in table 3.2. They were carefully selected to closely match the actual state's range of value in VSC-HVDC system and cover the system operations such as power flow inversion, and parameter uncertainty.

Therefore, each subsystem in the decentralized system (3.33) can be put in the fuzzy system (3.38):

$$\begin{cases} \dot{X} = \dfrac{\sum_{i=1}^{r} w_i(z)\left(A_iX + B_{1i}U\right)}{\sum_{i=1}^{r} w_i(z)} + B_2W \\ \quad = \sum_{i=1}^{r} h_i(z)\left(A_iX + B_{1i}U\right) + B_2W \\ Y = CX \end{cases} \tag{3.38}$$

S.N	Variable Names	Signal	Ranges of Value
1	x_3	i_{1d}^{∞}	[-3000, 3000] (A)
2	x_4	i_{1q}^{∞}	[-3000, 3000] (A)
3	x_5	v_{DC1}	[300e3, 400e3] (V)
4	x_7	v_{DC2}	[300e3, 400e3] (V)
5	x_{10}	i_{2d}^{∞}	[-5400, 5400] (A)
6	x_{11}	i_{2q}^{∞}	[-5400, 5400] (A)

Table 3.2: Ranges of the states of VSC-HVDC system

where

$$z = \left[\begin{array}{cccc} z_1 & z_2 & \dots & z_p \end{array} \right]; w_i(z) = \prod_{j=1}^{p} M_{ij}(z_j); h_i(z) = \frac{w_i(z)}{\sum_{i=1}^{r} w_i(z)}$$

and z_i are the nonlinear sectors and $M_{ij}(z_j)$ is the grade of membership of z_j in M_{ij}. In the considered decentralized HVDC system (3.33), subsystem (I) has 3 nonlinear sectors: $z_1 = x_3, z_2 = x_4, z_3 = x_5$, and subsystem (II) has 3 nonlinear sectors: $z_1{}' = x_7, z_2{}' = x_{10}, z_3{}' = x_{11}$.

3.3.3 Augmented System for Reference Tracking

Consider the nonlinear fuzzy system (3.38). The error between the vector of the output signals and the one of reference signals is:

$$e = -CX + Y_{ref} \tag{3.39}$$

As in the linear case, the states and the output of the augmented system are

$$\bar{X} = \left[\begin{array}{c} \dot{X} \\ e \end{array} \right]; \bar{Y} = e \tag{3.40}$$

Thus, the augmented system is as in (3.42):

$$\left\{ \begin{array}{l} \dot{\bar{X}} = \sum_{i=1}^{r} h_i(z) \left(\left[\begin{array}{cc} A_i & 0 \\ -C & 0 \end{array} \right] \bar{X} + \left[\begin{array}{c} B_{1i} \\ 0 \end{array} \right] \dot{U} \right) + \left[\begin{array}{c} B_2 \\ 0 \end{array} \right] \dot{W} \\ \bar{Y} = \left[\begin{array}{cc} 0 & I \end{array} \right] \bar{X} \end{array} \right. \tag{3.41}$$

or, in a concise form:

$$\left\{ \begin{array}{l} \dot{\bar{X}} = \bar{A}\bar{X} + \bar{B}_1\bar{U} + \bar{B}_2\bar{W} \\ \bar{Y} = \bar{C}\bar{X} \end{array} \right. \tag{3.42}$$

where:

$$\begin{array}{l} \bar{U} = \dot{U}; \bar{W} = \dot{W} \\ \bar{A} = \sum_{i=1}^{r} h_i(z) \bar{A}_i = \sum_{i=1}^{r} h_i(z) \left[\begin{array}{cc} A_i & 0 \\ -C & 0 \end{array} \right]; \bar{B}_2 = \left[\begin{array}{c} B_2 \\ 0 \end{array} \right]; \\ \bar{B}_1 = \sum_{i=1}^{r} h_i(z) \bar{B}_{1i} = \sum_{i=1}^{r} h_i(z) \left[\begin{array}{c} B_{1i} \\ 0 \end{array} \right]; \bar{C} = \left[\begin{array}{cc} 0 & I \end{array} \right] \end{array}$$

3.3.4 Robust H_2 Nonlinear Fuzzy Decentralized Controller

As in the linear control, the system (3.42) can be controlled using state-feedback fuzzy control technique:

$$\bar{U} = \dot{U} = \bar{K}\bar{X} \Rightarrow U = \bar{K}\begin{bmatrix} X \\ \int edt \end{bmatrix} \tag{3.43}$$

The fuzzy control for the fuzzy system (3.42) is constructed using the Parallel Distributed Compensation (PDC):

Control Rule j:
IF z_1 is M_{j1} and z_2 is M_{j2} and ... and z_p is M_{jp},
THEN $\bar{U}_j = \bar{K}_j\bar{X}, j = 1, 2, ..., r$

Thus, the general fuzzy controller is:

$$\begin{cases} \bar{U} = \dfrac{\sum\limits_{j=1}^{r} w_j(z)\bar{K}_j\bar{X}}{\sum\limits_{j=1}^{r} w_j(z)} = \sum\limits_{j=1}^{r} h_j(z)\bar{K}_j\bar{X} = \bar{K}\bar{X} \\ \bar{K} = \sum\limits_{j=1}^{r} h_j(z)\bar{K}_j \end{cases} \tag{3.44}$$

3.3.4.1 Uncertainty-free fuzzy H_2 decentralized state feedback control

Problem 3 *For the fuzzy system* (3.42)*, the H_2 problem is to find minimal value of γ such that:*

$$\|G(s)\|_2 \leq \gamma, \tag{3.45}$$

where $G(s)$ is the transfer function from disturbance $\bar{W}$ to output $\bar{Y}$: $\bar{Y}(s) = G(s)\bar{W}(s)$.

Theorem 3 *The H_2 problem 3 can be solved through LMI mean by minimizing γ:*

$$\min_{X_P, W_{P1}, ..., W_{Pr}} \gamma$$

subject to

$$\begin{cases} X_p > 0, \gamma > 0 \\ \bar{A}_i X_P + \bar{B}_{1i} W_{Pj} + \left(\bar{A}_i X_P + \bar{B}_{1i} W_{Pj}\right)^T + \bar{B}_2\bar{B}_2^T < 0 \\ \begin{bmatrix} -Z & \bar{C}X_P \\ \left(\bar{C}X_P\right)^T & -X_P \end{bmatrix} < 0 \\ trace(Z) < \gamma^2 \end{cases}$$

where the matrices Z and X_p are symmetric. The controller gains K_i are then calculated as:

$$K_j = W_{Pj}X_P^{-1}. \tag{3.46}$$

Proof 3 *At first, we investigate a simple state-space system:*

$$\begin{cases} \dot{X} = AX + BW \\ Z = CX \\ Z(s) = G(s)W(s) \end{cases} \tag{3.47}$$

The condition using LMI mean for H_2 problem of this system is:

$$\left\| C(sI - A)^{-1}B \right\|_2 < \gamma. \tag{3.48}$$

The problem (3.48) has a solution if $\exists X > 0$ satisfying [5], [6]:

$$\begin{cases} AX + XA^T + BB^T < 0 \\ trace\left(CXC^T\right) < \gamma^2. \end{cases} \tag{3.49}$$

Now, the closed-loop of system (3.42) *with the regulator* (3.43)*:*

$$\begin{cases} \dot{\bar{X}} = \left(\bar{A} + \bar{B}_1\bar{K}\right)\bar{X} + \bar{B}_2\bar{W} \\ Y = \bar{C}\bar{X} \end{cases} \tag{3.50}$$

Using the solution from problem (3.49) *for this closed-loop system, the H_2 problem becomes finding $X > 0$ satisfying:*

$$\begin{cases} \left(\bar{A} + \bar{B}_1\bar{K}\right)X_P + X_P\left(\bar{A} + \bar{B}_1\bar{K}\right)^T + \bar{B}_2\bar{B}_2^T < 0 \\ trace\left(\bar{C}X_P\bar{C}^T\right) < \gamma^2. \end{cases} \tag{3.51}$$

Now, consider the following lemma:

Lemma 2 *Let $A(x)$ is a symmetric matrix, $x \in R^n$, and $\gamma \in R, \gamma > 0$. The following statements are equivalent:*

(i) $\exists x \in R^n$ *such that* $trace\left(A(x)\right) < \gamma$

(ii) $\exists x \in R^n, Z \in R^{m\times m}, Z = Z^T$ *such that* $A(x) < Z$ *while* $trace(Z) < \gamma$

The proof for this lemma 2 can be retrieved in, e.g., [5], section 2.4.1 Trace of an LMI, Lemma 2.13.
Next, from the Lemma 2, LMI (3.51) *can be rewritten as the following LMI:*

$$\begin{cases} \left(\bar{A} + \bar{B}_1\bar{K}\right)X_P + X_P\left(\bar{A} + \bar{B}_1\bar{K}\right)^T + \bar{B}_2\bar{B}_2^T < 0 \\ \bar{C}X_P\bar{C}^T < Z \\ trace(Z) < \gamma^2. \end{cases}$$

Finally, by applying Schur complement lemma [5] [6], this LMI becomes:

$$\begin{cases} X_p > 0, \gamma > 0 \\ \bar{A}X_P + \bar{B}_1W_P + \left(\bar{A}X_P + \bar{B}_1W_P\right)^T + \bar{B}_2\bar{B}_2^T < 0 \\ \begin{bmatrix} -Z & \bar{C}X_P \\ \left(\bar{C}X_P\right)^T & -X_P \end{bmatrix} < 0 \\ trace(Z) < \gamma^2. \end{cases}$$

Replace the matrices with the ones of the augmented fuzzy system (3.42)*, we obtain the LMI condition in Theorem 3.*

3.3.4.2 Robust fuzzy H_2 decentralized state feedback control

Now, we will investigate the fuzzy system (3.42), but with uncertainties in their state-space matrices $\bar{A}_i$ and $\bar{B}_{1i}$:

$$\begin{cases} \dot{\bar{X}} = \left(\bar{A} + \Delta\bar{A}\right)\bar{X} + \left(\bar{B}_1 + \Delta\bar{B}_1\right)\bar{U} + \bar{B}_2\bar{W} \\ \bar{Y} = \bar{C}\bar{X} \end{cases} \tag{3.52}$$

where:

$$\bar{A} = \sum_{i=1}^{r} h_i(z)\,\bar{A}_i = \sum_{i=1}^{r} h_i(z)\begin{bmatrix} A_i & 0 \\ -C & 0 \end{bmatrix}; \bar{B}_2 = \begin{bmatrix} B_2 \\ 0 \end{bmatrix};$$
$$\bar{B}_1 = \sum_{i=1}^{r} h_i(z)\,\bar{B}_{1i} = \sum_{i=1}^{r} h_i(z)\begin{bmatrix} B_{1i} \\ 0 \end{bmatrix}; \bar{C} = \begin{bmatrix} 0 & I \end{bmatrix};$$
$$\Delta\bar{A} = \sum_{i=1}^{r} h_i(z)\,\Delta\bar{A}_i; \Delta\bar{B}_1 = \sum_{i=1}^{r} h_i(z)\,\Delta\bar{B}_{1i}$$

and:

$$\begin{cases} \left[\begin{array}{cc} \Delta\bar{A}_i & \Delta\bar{B}_{1i} \end{array}\right] = H_i F_i \left[\begin{array}{cc} E_{1i} & E_{2i} \end{array}\right] \\ E_{1i} = \delta_{1i}\bar{A}_i; |\delta_{1i}| < r_{1i}; r_{1i} \in R^+ \\ E_{2i} = \delta_{2i}\bar{B}_{1i}; |\delta_{2i}| < r_{2i}; r_{2i} \in R^+ \\ F_i^T F_i \leq I \end{cases} \tag{3.53}$$

Problem 4 *Consider the fuzzy system with uncertainties in equation* (3.52)*, the H_2 problem can be solved by minimizing γ such that:*

$$\begin{cases} \bar{Y}(s) = G(s)\bar{W}(s) \\ \|G(s)\|_2 \leq \gamma \end{cases} \tag{3.54}$$

Theorem 4 *Problem 2, i.e., the H_2 problem, is to minimize value of γ and ensure the stability of fuzzy system with uncertainties* (3.52)*, at the same time satisfying:*

$$\min_{X_P, W_{P1}, \ldots, W_{Pr}} \quad \gamma$$

subject to:

$$\begin{cases} X_p > 0, \gamma > 0, \beta > 0 \\ \Psi = \bar{A}_i X_P + \bar{B}_{1i} W_{Pj} + \left(\bar{A}_i X_P + \bar{B}_{1i} W_{Pj}\right)^T + \bar{B}_2 \bar{B}_2^T + \beta H_i H_i^T \\ \left[\begin{array}{cc} \Psi & \left(E_{1i} X_P + E_{2i} W_{Pj}\right)^T \\ E_{1i} X_P + E_{2i} W_{Pj} & -\beta I \end{array}\right] < 0 \\ \left[\begin{array}{cc} -Z & \bar{C} X_P \\ \left(\bar{C} X_P\right)^T & -X_P \end{array}\right] < 0 \\ trace(Z) < \gamma^2 \end{cases}$$

where $Z = Z'$ and X_p is a symmetric positive definite matrix. The controller's gain K_j is then calculated by:

$$\bar{K}_j = W_{Pj} X_P^{-1}. \tag{3.55}$$

Proof 4 *To prove this theorem, i.e., Theorem 4, one can start by applying Theorem 3 for fuzzy system with uncertainties (system* (3.52)*): the H_2 problem of system* (3.52) *can be solved by finding controller's gains K_i to stabilize the fuzzy system, and finding the minimum value of γ. This action can be done through LMI mean:*

$$\min_{X_P, W_{P1}, \ldots, W_{Pr}} \quad \gamma$$

subject to:

$$\begin{cases} X_p > 0, \gamma > 0 \\ \left(\bar{A}_i + \Delta\bar{A}_i\right) X_P + \left(\bar{B}_{1i} + \Delta\bar{B}_{1i}\right) W_{Pj} \\ + \left(\left(\bar{A}_i + \Delta\bar{A}_i\right) X_P + \left(\bar{B}_{1i} + \Delta\bar{B}_{1i}\right) W_{Pj}\right)^T + \bar{B}_2 \bar{B}_2^T < 0 \\ \left[\begin{array}{cc} -Z & \bar{C} X_P \\ \left(\bar{C} X_P\right)^T & -X_P \end{array}\right] < 0 \\ trace(Z) < \gamma^2 \end{cases} \tag{3.56}$$

where $Z = Z'$ and X_p is a symmetric positive definite matrix.
To have a concise proof, defining the following term: $\langle M \rangle_S = M + M^T$. Based on this, one can have:

$$\begin{aligned} &\left\langle \left(\bar{A}_i + \Delta\bar{A}_i\right) X_P + \left(\bar{B}_{1i} + \Delta\bar{B}_{1i}\right) W_{Pj} \right\rangle_S + \bar{B}_2 \bar{B}_2^T \\ &= \left\langle \bar{A}_i X_P + \bar{B}_{1i} W_{Pj} \right\rangle_S + \bar{B}_2 \bar{B}_2^T + \left\langle \Delta\bar{A}_i X_{Pj} + \Delta\bar{B}_{1i} W_{Pj} \right\rangle_S \end{aligned}$$

From the considered system with uncertainties (3.52)*:*

$$\left\langle \Delta\bar{A}_i X_P + \Delta\bar{B}_{1i} W_{Pj} \right\rangle_S = \left\langle H_i F_i \left(E_{1i} X_P + E_{2i} W_{Pj}\right) \right\rangle_S$$

Thus, first LMI condition in (3.56) *can be rewritten as:*

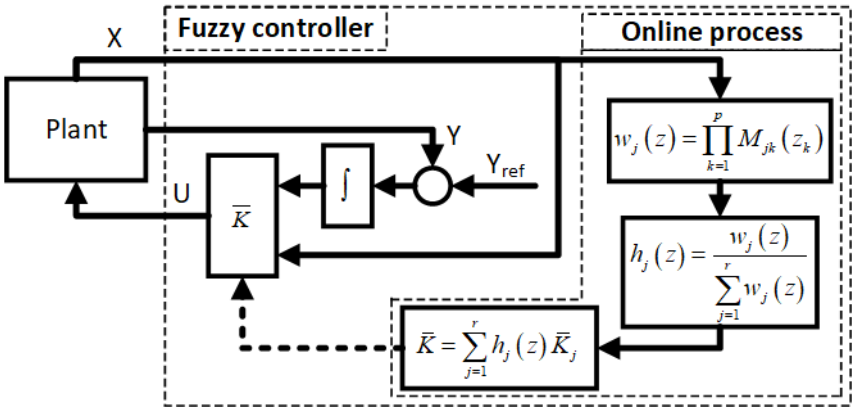

Figure 3.11: Implementation of the state feedback fuzzy controller

$$\begin{aligned}&\left\langle \bar{A}_i X_P + \bar{B}_{1i} W_{Pj} \right\rangle_S + \bar{B}_2 \bar{B}_2^T \\ &+\langle H_i F_i \left(E_{1i} X_P + E_{2i} W_{Pj}\right)\rangle_S < 0.\end{aligned} \tag{3.57}$$

From this, one can reuse Lemma 1, the LMI (3.57) *equivalently becomes:*

$$\begin{aligned}&\left\langle \bar{A}_i X_P + \bar{B}_{1i} W_{Pj} \right\rangle_S + \bar{B}_2 \bar{B}_2^T + \beta H_i H_i^T \\ &+\beta^{-1} (E_{1i} X_P + E_{2i} W_{Pj})^T (E_{1i} X_P + E_{2i} W_{Pj}) < 0\end{aligned}$$

Finally, applying Schur complement lemma [5], [6], this LMI can be converted into Theorem 4.

3.3.4.3 Implementation

As time-varying control, fuzzy control implementation is more specific.

After obtaining the local constant gain K_j offline (using Theorem 3 for uncertainty-free case or Theorem 4 for robust control depending on the control designer's choice), the controller can be implemented as shown in Fig. 3.11. The control system is running by updating in real-time the dynamic gain $\bar{K}$ as in the fuzzy controller (3.44) and according to the blocs in the right part of the Fig. 3.11. The fuzzy controller is thus a MIMO controller with the gain $\bar{K}$ time-varying, different from the static gain of the linear case presented in section 3.2.

3.3.5 Simulations and results

Simulations were done with a dual purpose in mind: they test the approach from a specifications standpoint and they also provide an idea about the decoupling limits of the approach in general. The length of the DC line is modified for the latter to measure the approach's limits of decoupling. Indeed, the HVDC is a closely coupled system due to the connection of the two converters. It is usual that the decoupling control approach presented here works only for DC line lengths greater than a threshold put into evidence in this subsection.

To cover the specifications to be tested, four scenarios were defined: variation of the DC line length, variation of the operation point (variation of the quantity and direction of active power transited through the DC line), parametric robustness, and fault ride-through capability. They are all robustness tests. The regulators are particularly built for a normal circumstance (800km for the DC line and 20MW transmission), while the majority of the simulations are done with other grid conditions. It is worth noting that the gains $\bar{K}_i$ of the regulators are unchanged (the ones obtained from the synthesis on the nominal operation point are always used):

- Scenario 1 - Changes of operating point: This is designed to test the response of the output (V_{DC1}, Q_1, P_2, Q_2) to a change in the reference signal to the HVDC control system. Initially at t = 1(s), the active power reference P_1 is set from 20 (MW) to -20 (MW), and this is a major test since the power flow is reverted, which can not be handled by linear control such as $H_{inf}RDC$ in section 3.2. Then, at t = 3(s), the reactive power reference Q_2 changes from -7.248 (MW) to -10.872 (MW). At t = 5(s), the reference V_{DC1} changes from 319.89 (kV) to 323.09 (kV). Finally, at t = 7(s), the reactive power reference Q_1 changes from -30.518

(MW) to -45.777 (MW). The test is also done for different HVDC line lengths (600Km, 800Km, 1000Km, 1200Km). This scenario is illustrated for DC voltage v_{DC1}, Q_1, P_2, Q_2 from Fig. 3.12 to Fig. 3.15, respectively. From 600Km to 1200Km, the performance is increasing, because the coupling between two converters is reduced.

- Scenario 2 - Resilience in case of failure of one converter control (i.e., open-loop): we investigate the case of loss of the control (i.e., open-loop) of converter 1 in situation of Scenario 1 where transited power is reversed to demonstrate the robustness of this decentralized control. The regulator of converter 2 continues to function independently (as it uses no information from converter 1). It can be viewed from Fig. 3.16 to Fig. 3.19, that the H_2 Nonlinear Fuzzy Decentralized Control (H_2NFDC) control stabilizes the HVDC system even after significant changes of the operating point at t=1s. The responses to the loss of control of converter 1 (loss of control for v_{DC1} and Q_1) are shown in Figs. 3.16 and 3.17, where the v_{DC1} and Q_1 outputs can no longer follow the reference signals as in normal operation. However, the stability and performance of converter 2 (including the reverted active power flow action) are maintained as shown in Figs. 3.18 and 3.19.

- Scenario 3 - comparison between linear control $H_{inf}RDC$ (section 3.2), proposed H_2NFDC and proposed H_2RNFDC: The purpose of this scenario is to demonstrate the advantages of robust fuzzy control over uncertainty-free fuzzy control, as well as the capability of fuzzy nonlinear control over linear control. The two fuzzy control strategies (H_2NFDC and H_2RNFDC) are tested in the presence of operating point changes (P_2 varying from 20(MW) to -20(MW), Q_2 varying from -7.248 (MW) to -10.872 (MW)) and with the presence of uncertainty in HVDC system parameters. As explained in scenario 1, linear control (e.g., $H_{inf}RDC$) cannot tolerate such a variance. As a result, the $H_{inf}RDC$ is tested by a significantly smaller reference variation of P_2 (from 20(MW) to 21(MW)) and Q_2 (from -7.248 (MW) to -7.6104 (MW)). The length of the HVDC link is nominal (800 km). For the case of fuzzy controls, the uncertainties are up to 40% for state-space matrices A, B and C of system (3.32). From Figs. 3.20 and 3.21, it is obvious that fuzzy control strategies (H_2NFDC and H_2RNFDC) are superior to linear control strategy ($H_{inf}RDC$), even the fuzzy controllers are dealing with 40% uncertainties while linear controller is working with nominal value of system parameters. The overshoot/undershoot of fuzzy controllers is under 5% with smooth transient while linear control has over 30% overshoot, not less than 80% undershoot and a worse transient behavior.

- Scenario 4 - Fault ride through capability: the FRT capacity is demonstrated with 800Km HVDC link through a faulty event, i.e., a short-circuit of 150ms at the equivalent grid side of converter $S2$ (see Fig. 3.1). The Figs. 3.22, 3.23, 3.24 and 3.25 prove that the fuzzy controllers can recover the normal behavior of HVDC system after the event.

3.3.6 Conclusion

For a nonlinear VSC-HVDC link, a Robust H_2 Nonlinear Fuzzy Decentralized Control technique in the presence of parameter uncertainty and disturbances has been developed. In an LMI formalism, sufficient requirements for robust stabilization of the TS fuzzy model were derived. To validate the proposed technique, the proposed method was developed in MATLAB software and tested against alternative frameworks in various simulations.

These tests demonstrated that decoupling is successful for a wide range of variations in the length of the DC line, which is a direct measure of dynamic coupling. Aside from HVDC links, this hints at the method's application to other power system difficult topics, such as decentralized control of renewable sources in a zone or a VPP.

From the control point of view, the proposed approaches are applicable for real-world applications since their control structures are quite simple, even for nonlinear fuzzy control (see Fig. 3.11). The strategies are also providing robustness and FRT capacity for converter systems. In addition, because of its decentralized implementation, the controller become resilient to even a severe fault of neighbor subsystem (i.e., loss of control in the other converter). All in all, the proposed fuzzy control approaches are showing their potential for industrial level application in an interconnected power systems, especially for power converter systems.

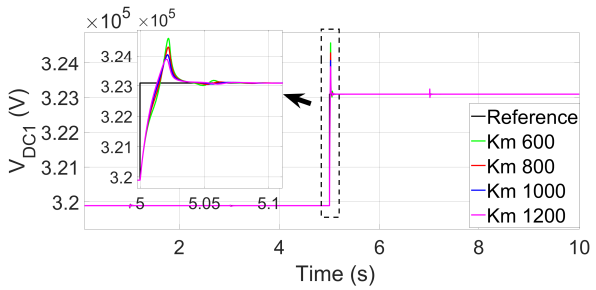

Figure 3.12: Voltage v_{DC1} using decentralized H_2 fuzzy control

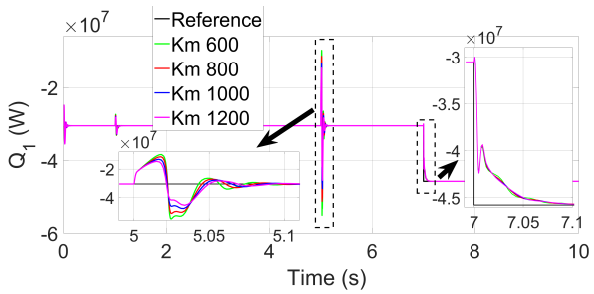

Figure 3.13: Reactive power Q_1 using decentralized H_2 fuzzy control

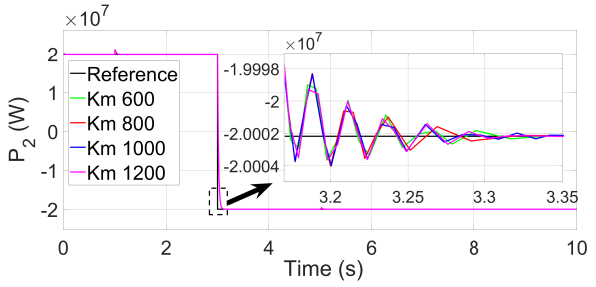

Figure 3.14: Active power P_2 using decentralized H_2 fuzzy control

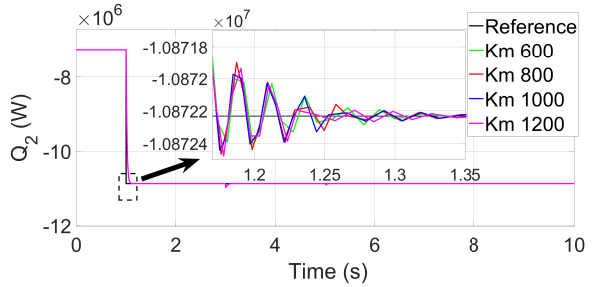

Figure 3.15: Reactive power Q_2 using decentralized H_2 fuzzy control

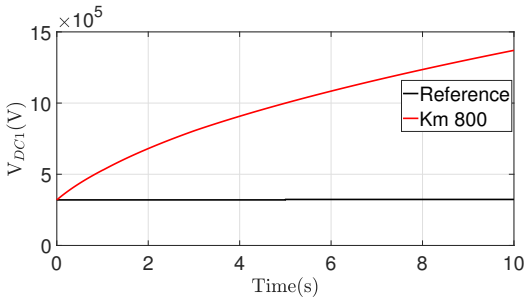

Figure 3.16: Voltage v_{DC1} in 800 Km line (loss of control in converter 1)

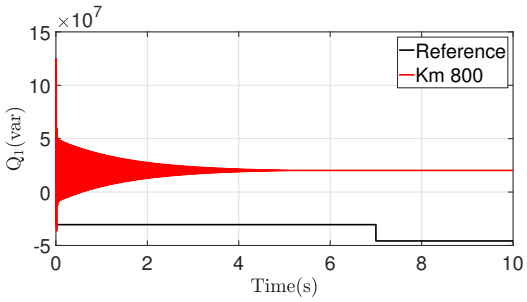

Figure 3.17: Reactive power Q_1 in 800 Km line (loss of control in converter 1)

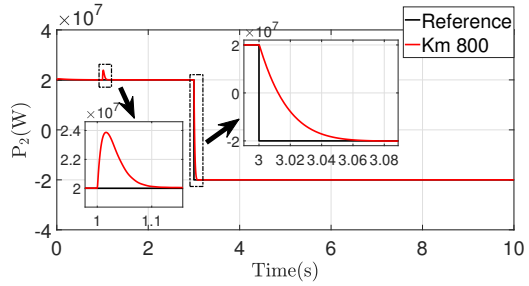

Figure 3.18: Active power P_2 in 800 Km line (loss of control in converter 1)

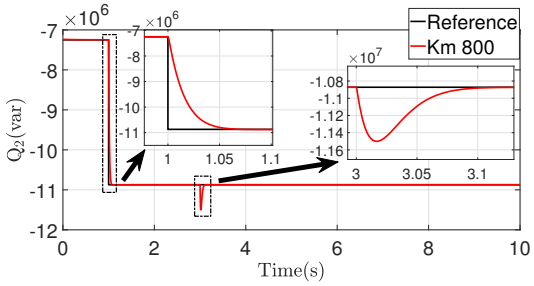

Figure 3.19: Reactive power Q_2 in 800 Km line (loss of control in converter 1)

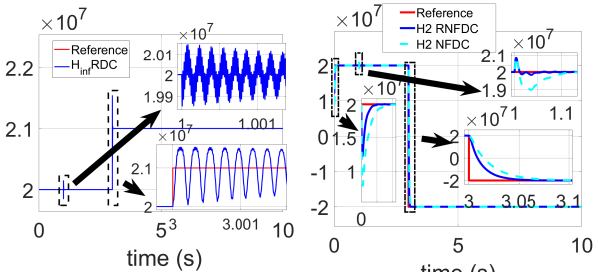

Figure 3.20: Active power $P_2(W)$: $H_{inf}RDC$, H_2NFDC and H_2RNFDC

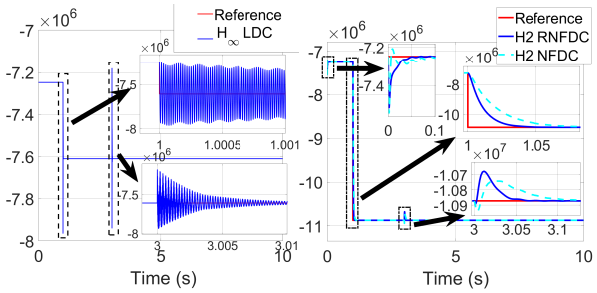

Figure 3.21: Reactive power $Q_2(W)$: $H_{inf}RDC$, H_2NFDC and H_2RNFDC

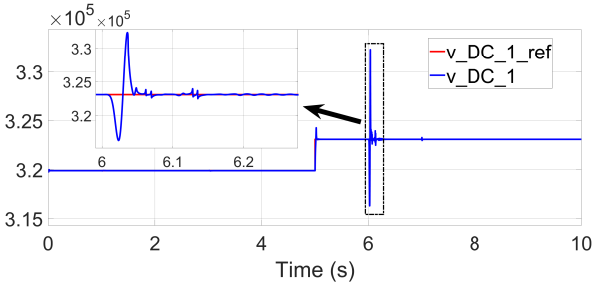

Figure 3.22: Voltage v_{DC1} in 800 Km line

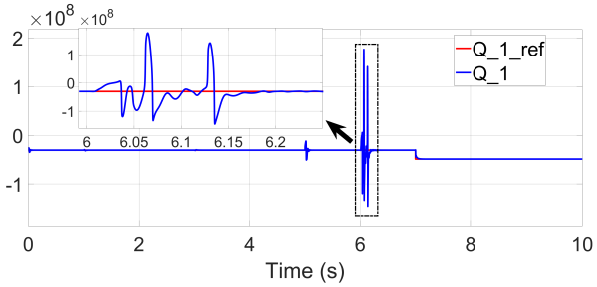

Figure 3.23: Reactive power Q_1 in 800 Km line

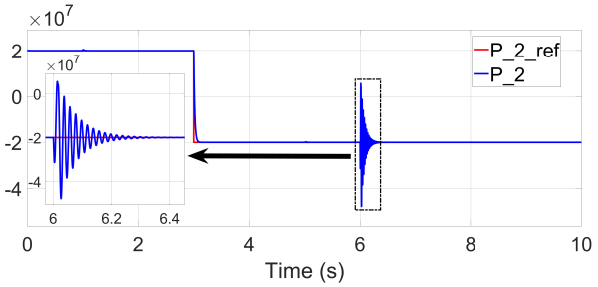

Figure 3.24: Active power P_2 in 800 Km line

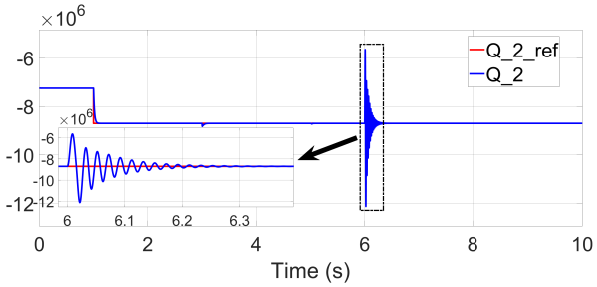

Figure 3.25: Reactive power Q_2 in 800 Km line

Bibliography

[1] Siljak, D. D. (2011). Decentralized control of complex systems. Courier Corporation.

[2] LEONDES, C. T. (1986). Control and dynamic systems: Decentralized/distributed control and dynamic systems. Part 3((Book)). Orlando, FL, Academic Press, Inc.(Advances in Theory and Applications., 24.

[3] Zhou, K., & Doyle, J. C. (1998). Essentials of robust control (Vol. 104). Upper Saddle River, NJ: Prentice hall.

[4] Khalil, I. S., Doyle, J. C., & Glover, K. (1996). Robust and optimal control. Prentice hall.

[5] Duan, G. R., & Yu, H. H. (2013). LMIs in control systems: analysis, design and applications. CRC press.

[6] Boyd, S., El Ghaoui, L., Feron, E., & Balakrishnan, V. (1994). Linear matrix inequalities in system and control theory. Society for industrial and applied mathematics.

[7] G. Zhang and Z. Xu, Steady-state model for VSC based HVDC system and its controller design, IEEE Power Engineering Society Winter Meeting, vol.3, pp.1085-1090, 2001.

[8] G. Asplund, Application of HVDC Light to power system enhancement, IEEE Power Engineering Society Winter Meeting, Vol.4, Jan 2000,pp.2498-2503.

[9] Van Hertem, Dirk, and Mehrdad Ghandhari. "Multi-terminal VSC HVDC for the European supergrid: Obstacles." Renewable and sustainable energy reviews 14.9 (2010): 3156-3163.

[10] Rahimi, Ebrahim, et al. "Commutation failure analysis in multi-infeed HVDC systems." IEEE Transactions on power delivery 26.1 (2010): 378-384.

[11] Robinson, Jonathan, Dragan Jovcic, and Géza Joós. "Analysis and design of an offshore wind farm using a MV DC grid." IEEE Transactions on Power Delivery 25.4 (2010): 2164-2173.

[12] Jovcic, Dragan. High voltage direct current transmission: converters, systems and DC grids. John Wiley & Sons, 2019.

[13] E. Kamal, and B. Marinescu. "Robust Control of VSC-HVDC System with Input and States Constraints." 14th International Workshop on Advanced Control and Diagnosis. No. 16-17. 2017.

[14] L. Arioua and B. Marinescu, Robust grid-oriented control of high voltage DC links embedded in an AC transmission system, Int. J. Robust Nonlinear Control, vol. 26, pp.1944-1961, 2016.

[15] Richard C.. Dorf, & Bishop, R. H. (2008). Modern control systems. Pearson Prentice Hall.

[16] Wang, H. O., & Tanaka, K. (2004). Fuzzy control systems design and analysis: A linear matrix inequality approach. John Wiley & Sons.

[17] Kamal, E., & Marinescu, B. (2017, November). Robust Control of VSC-HVDC System with Input and States Constraints. In 14th International Workshop on Advanced Control and Diagnosis (No. 16-17, p. 6).

Chapter 4

Wind system application

This chapter is dedicated to enhance the wind control system performance and stability, mainly its active and reactive power, using coordinated control structure with both centralized and decentralized approaches. The control approaches are partly inherited from chapter 3 for the overlapping decentralized control. At the same time, a centralized control approach is also investigated and implemented for the same wind system. Both approaches are compared, and also using coordinated control structures to provide GAS as introduced in chapter Grid-connected power converter system objectives and proposed approaches, i.e., overlapping decentralized control and centralized control structures in Figs. 2.11 and 2.10, respectively. In addition, a distributed nonlinear control using fuzzy technique is also developed and implemented for the wind system in order to enhance further the performance and stability of the system. All of these approaches are also based on the general time - space structure for renewable energy system in Fig. 2.4 of chapter 2.

To be able to achieve a better understanding and thus better constructed control strategies, some new concepts are introduced in this chapter, related to VPP and DVPP. These concepts are parts of POSYTYF project, with the purpose of renewable energy integrating into AC grid as well as enhancing the renewable energy - dominated grid using centralized approach.

The content of this chapter includes: the DRES PMSG-based wind system application (with the definition of DVPP, IEEE 14-bus benchmark and nonlinear model of PMSG), the linear optimal H_∞ mixed-sensitivity loop shaping control applied for the considered PMSG-based wind system (RMS simulation), and finally the robust distributed fuzzy optimal H_∞ control (RMS simulation).

4.1 DRES wind system application

Modern AC grid, as discussed in chapter Introduction, with a large portion of DRES, would require a better coordinated treatment in order to provide GAS. In this section, a DVPP concept is introduced as part of the POSYTYF project. A test case is build along with a control model. The proposed control approach will be established and tested on the proposed case.

4.1.1 Dynamic Virtual Power Plant

A VPP is a distributed power plant that runs on the cloud and combines the capabilities of various Distributed Energy Resource (DER) in order to increase power generation and trade or sell power on the market for electricity. There are many VPPs in the US, Europe, and Australia.

The DVPP is the concept developed in the POSYTYF project to deal with the dynamic aspects of the VPP and to provide the best internal resource redispatch. The DVPP group together in a portfolio those renewable sources that are both dispatchable and non-dispatchable in nature. On top of a VPP functionalities, a DVPP jointly addresses [7]: the static power dispatch at single VPP level, the dynamic coordination of several VPPs to provide ancillary services to the system, and the attainment of an economic optimal.

4.1.1.1 Dynamic Virtual Power Plant Structure

Components A DVPP is a set of RES, including numerous geographically distributed generators owned or operated by the same company or entity that are primarily joined together for economic purposes with the aim of ensuring ancillary services.

The following dynamic generators are considered as possible components of the studied DVPP (e.g., the components in red in Fig. 4.1):

- Wind generators
- Hydro generators
- Solar thermal generators
- Photovoltaic generators
- Biomass generators

Optionally, the other devices can be considered as components of the DVPP:

- Hydrogen generation (in the distribution part)
- Synchronous condensers (in the transmission part)
- Flywheels (in the transmission part)
- Flexible demand

The following devices are not considered as components of DVPP:

- Electrochemical storage
- Classic thermal generators

Perimeter As seen in Fig. 4.1, one DVPP may contain dynamic components from the transmission and distribution grid levels. 1 (devices in red). As a result, DVPP components are not always neighbors. Additionally, some nearby generators can choose not to participate in the DVPP (devices in black in Fig.). In the synthesis of the DVPP controls, they should be taken into account as disturbances or dynamic interactions.

Several DVPPs (two for the studies) need also be taken into account. As a result, neighborhood generators could be from different DVPPs (components in red in Fig. 4.1).

A DVPP's perimeter is initially considered of as fixed. In a subsequent stage, it is possible to look into perimeters with time-varying properties.

Data availability Accessibility of signal measurements is capital for controls. This is crucial, particularly for second level controls (to guarantee ancillary services) and for general control activity coordination (as DVPP actuators are geographically distant). At a common control point known as DVPP dispatching in the sequel, voltage and frequency measurements from both the transmission and distribution sides are supposed to be available. In the DVPP dispatching, controls is calculated and transmitted back to the DVPP actuators.

4.1.1.2 Dynamic Virtual Power Plant Ancillary services: voltage and frequency

A DVPP needs to deliver the same voltage support as the traditional generation. This entails achieving the same goals and being able to take part in the same regulatory frameworks [7]. The precise goals are:

- For transmission:
  - Control voltage at generator connection points.

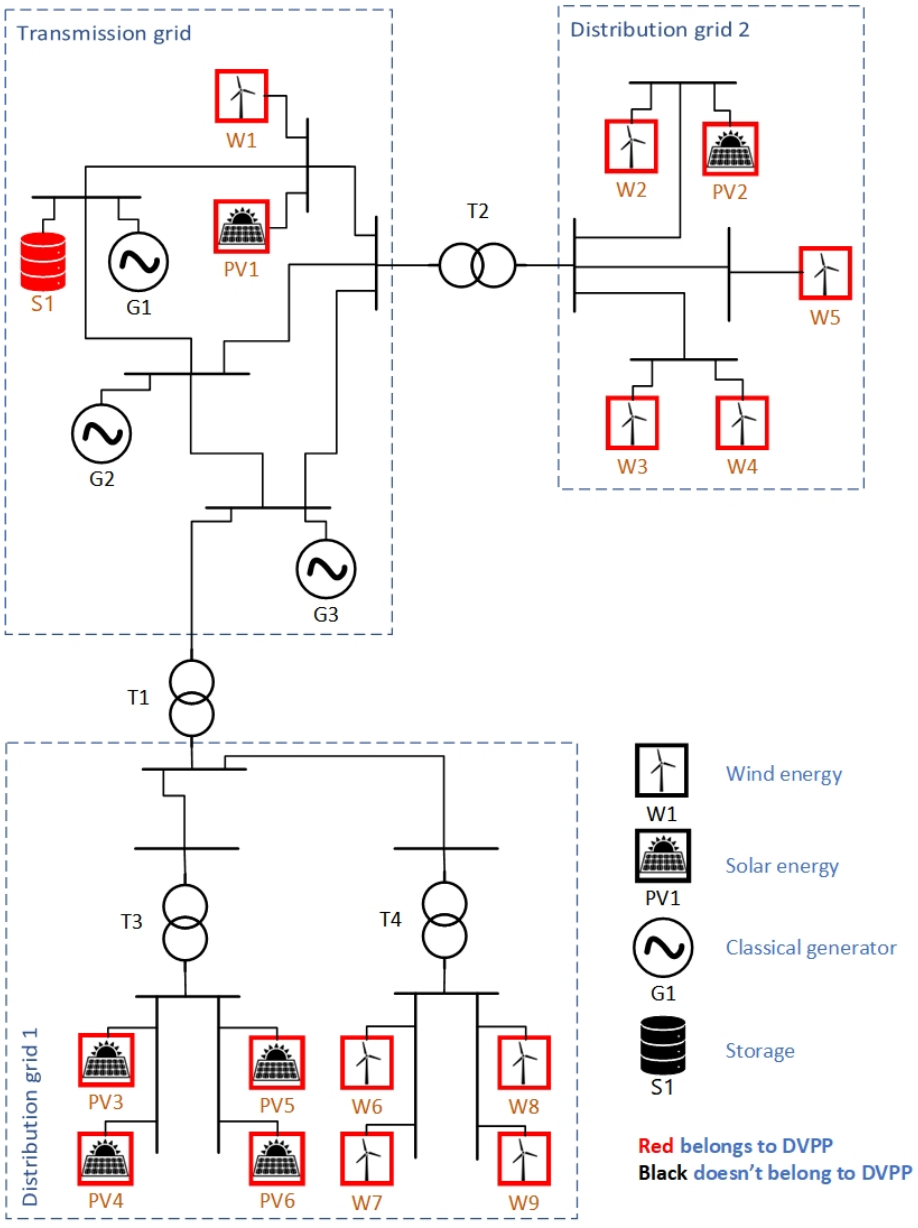

Figure 4.1: DVPP Components and Structure

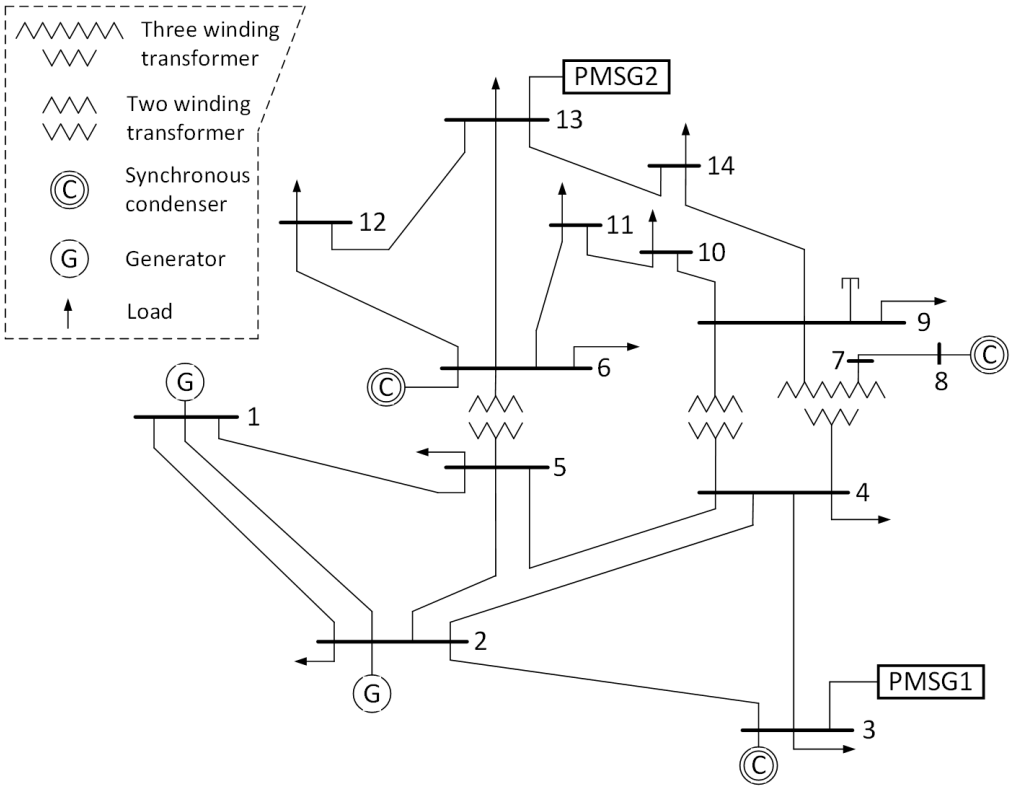

Figure 4.2: The modified IEEE 14 bus test case with 2 PMSGs

- Control each generator's reactive power reserve (Q regulation/alignment).
- Control voltage at a few key grid locations, such as pilot points.

- For distribution:
  - Manage reactive power exchange at the point of connection with the transmission grid.
  - Keep terminal voltage within limits of Vmax/min.
  - Another possibility is to damp grid oscillations (inter-area or coupling modes).

- For actual regulatory and control framework:
  - Participation at the secondary voltage control level in addition to local regulation.
  - Coordination of the management of the DVPP RES generators on the transmission and distribution grid sides is crucial.
  - The primary and secondary frequency control levels should be included in DVPP regulation.

4.1.2 Modified IEEE 14-bus benchmark

The original IEEE 14 bus grid includes a part of the American Electric Power System (in the Midwest of the United States) in February 1962 [1], including 14 buses, 2 generators, 3 synchronous condensers, and eleven loads.

We qdded to this benchmark two PMSGs in bus 3 (PMSG1) and bus 13 (PMSG2), as shown in Fig. 4.2. The benchmark is established using MATLAB/Simulink/Simscape, as shown in Fig. 4.3. In order to validate the GAS and LS of the proposed control strategy, several scenarios to verify the effectiveness of each proposed control were considered.

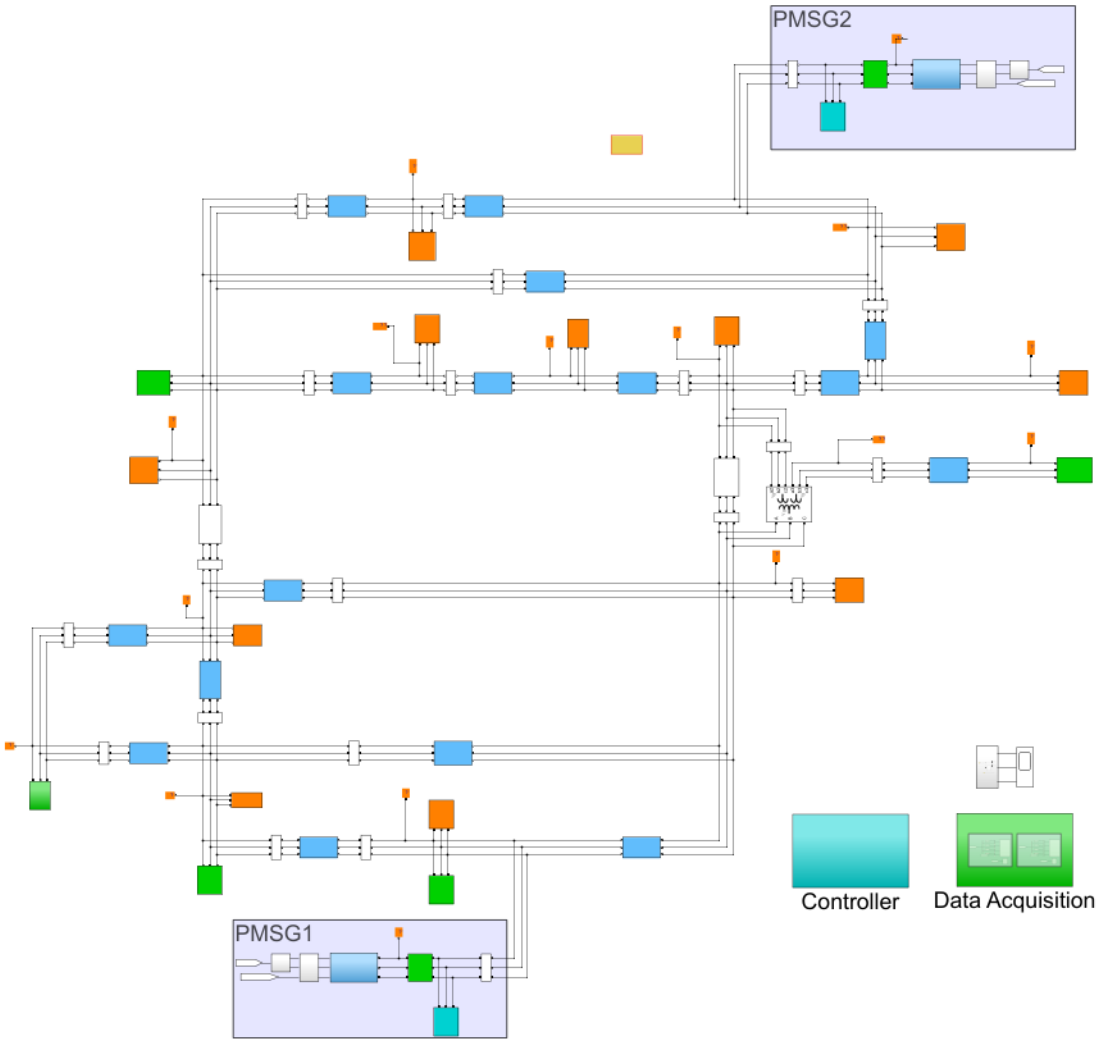

Figure 4.3: The modified IEEE 14 bus test case with 2 PMSGs in Simulink Simscape

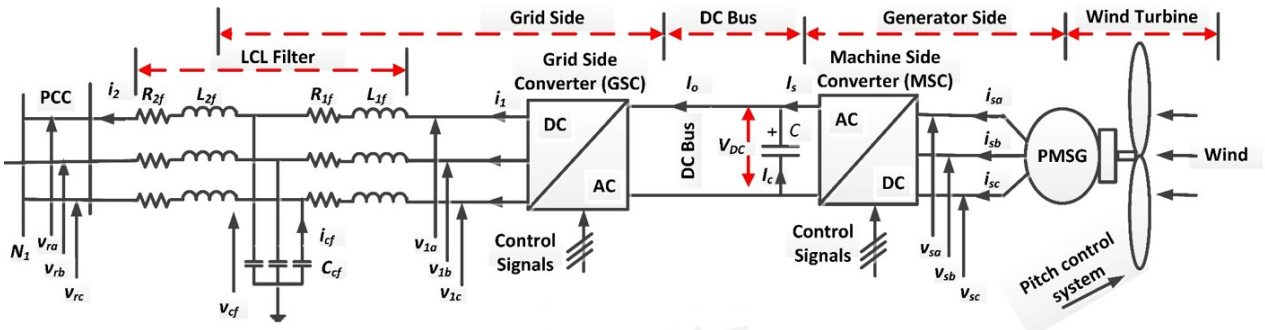

Figure 4.4: Physical model of PMSG in the IEEE 14 bus benchmark

4.1.3 Nonlinear model of PMSGs and grid system

The two PMSGs in Fig. 4.2, have the detailed dq model shown in Fig. 4.4 [2]. The model of each PMSG is represented using average model of the converters [3] as in equations (4.1) and (4.2) for PMSG1 and PMSG2, respectively. Phasor, i.e., RMS simulation was done.

$$\begin{cases} \frac{di_{11d}}{dt} = -\omega_{fb}\frac{R_{11f}i_{11d}}{L_{11f}} + \omega_{fb}\omega_f i_{11q} - \omega_{fb}\frac{v_{cf1d}}{L_{11f}} + \frac{1}{2}\omega_{fb}\frac{\beta_{11d}v_{DC1}}{L_{11f}} \\ \frac{di_{11q}}{dt} = -\omega_{fb}\frac{R_{11f}i_{11q}}{L_{11f}} - \omega_{fb}\omega_f i_{11d} - \omega_{fb}\frac{v_{cf1q}}{L_{11f}} + \frac{1}{2}\omega_{fb}\frac{\beta_{11q}v_{DC1}}{L_{11f}} \\ \frac{di_{21d}}{dt} = -\omega_{fb}\frac{R_{21f}i_{21d}}{L_{21f}} + \omega_{fb}\omega_f i_{21q} + \omega_{fb}\frac{v_{cf1d}}{L_{21f}} - \omega_{fb}\frac{1}{L_{21f}}\frac{1}{n_1}V_{r1d} \\ \frac{di_{21q}}{dt} = -\omega_{fb}\frac{R_{21f}i_{21q}}{L_{21f}} - \omega_{fb}\omega_f i_{21d} + \omega_{fb}\frac{v_{cf1q}}{L_{21f}} - \omega_{fb}\frac{1}{L_{21f}}\frac{1}{n_1}V_{r1q} \\ \frac{dv_{cf1d}}{dt} = \omega_{fb}\frac{i_{11d}}{C_{f1}} - \omega_{fb}\frac{i_{21d}}{C_{f1}} + \omega_{fb}\omega_f v_{cf1q} \\ \frac{dv_{cf1q}}{dt} = \omega_{fb}\frac{i_{11q}}{C_{f1}} - \omega_{fb}\frac{i_{21q}}{C_{f1}} - \omega_{fb}\omega_f v_{cf1d} \\ \frac{di_{s1d}}{dt} = -\omega_{fb}\frac{R_{s1}i_{s1d}}{L_{s1}} + \Omega_b p_1\Omega_1 i_{s1q} - \frac{1}{2}\omega_{fb}\frac{\beta_{s1d}v_{DC1}}{L_{s1}} \\ \frac{di_{s1q}}{dt} = -\omega_{fb}\frac{R_{s1}i_{s1q}}{L_{s1}} - \Omega_b p_1\Omega_1 i_{s1d} + \Omega_b\frac{p_1\Psi_{f1}\Omega_1}{L_{s1}} - \frac{1}{2}\omega_{fb}\frac{\beta_{s1q}v_{DC1}}{L_{s1}} \\ \frac{dv_{DC1}}{dt} = -\omega_{fb}\frac{3}{4C_1}\beta_{11d}i_{11d} - \omega_{fb}\frac{3}{4C_1}\beta_{11q}i_{11q} + \omega_{fb}\frac{3}{4C_1}\beta_{s1d}i_{s1d} \\ +\omega_{fb}\frac{3}{4C_1}\beta_{s1q}i_{s1q} \\ \frac{d\Omega_1}{dt} = \frac{1}{2H_1}\frac{P_{m1}}{\Omega_1} - \frac{1}{2H_1}\frac{\Omega_b}{\omega_{fb}}\frac{3}{2}p_1\Psi_{f1}i_{s1q} - \frac{1}{2H_1}D_{L1}\Omega_1; D_{L1} = \frac{\Omega_b^2 f_1}{S_b} \end{cases} \tag{4.1}$$

$$\begin{cases} \frac{di_{12d}}{dt} = -\omega_{fb}\frac{R_{12f}i_{12d}}{L_{12f}} + \omega_{fb}\omega_f i_{12q} - \omega_{fb}\frac{v_{cf2d}}{L_{12f}} + \frac{1}{2}\omega_{fb}\frac{\beta_{12d}v_{DC2}}{L_{12f}} \\ \frac{di_{12q}}{dt} = -\omega_{fb}\frac{R_{12f}i_{12q}}{L_{12f}} - \omega_{fb}\omega_f i_{12d} - \omega_{fb}\frac{v_{cf2q}}{L_{12f}} + \frac{1}{2}\omega_{fb}\frac{\beta_{12q}v_{DC2}}{L_{12f}} \\ \frac{di_{22d}}{dt} = -\omega_{fb}\frac{R_{22f}i_{22d}}{L_{22f}} + \omega_{fb}\omega_f i_{22q} + \omega_{fb}\frac{v_{cf2d}}{L_{22f}} - \omega_{fb}\frac{1}{L_{22f}}\frac{1}{n_2}V_{r2d} \\ \frac{di_{22q}}{dt} = -\omega_{fb}\frac{R_{22f}i_{22q}}{L_{22f}} - \omega_{fb}\omega_f i_{22d} + \omega_{fb}\frac{v_{cf2q}}{L_{22f}} - \omega_{fb}\frac{1}{L_{22f}}\frac{1}{n_2}V_{r2q} \\ \frac{dv_{cf2d}}{dt} = \omega_{fb}\frac{i_{12d}}{C_{f2}} - \omega_{fb}\frac{i_{22d}}{C_{f2}} + \omega_{fb}\omega_f v_{cf2q} \\ \frac{dv_{cf2q}}{dt} = \omega_{fb}\frac{i_{12q}}{C_{f2}} - \omega_{fb}\frac{i_{22q}}{C_{f2}} - \omega_{fb}\omega_f v_{cf2d} \\ \frac{di_{s2d}}{dt} = -\omega_{fb}\frac{R_{s2}i_{s2d}}{L_{s2}} + \Omega_b p_2\Omega_2 i_{s2q} - \frac{1}{2}\omega_{fb}\frac{\beta_{s2d}v_{DC2}}{L_{s2}} \\ \frac{di_{s2q}}{dt} = -\omega_{fb}\frac{R_{s2}i_{s2q}}{L_{s2}} - \Omega_b p_2\Omega_2 i_{s2d} + \Omega_b\frac{p_2\Psi_{f2}\Omega_2}{L_{s2}} - \frac{1}{2}\omega_{fb}\frac{\beta_{s2q}v_{DC2}}{L_{s2}} \\ \frac{dv_{DC2}}{dt} = -\omega_{fb}\frac{3}{4C_2}\beta_{12d}i_{12d} - \omega_{fb}\frac{3}{4C_2}\beta_{12q}i_{12q} + \omega_{fb}\frac{3}{4C_2}\beta_{s2d}i_{s2d} \\ +\omega_{fb}\frac{3}{4C_2}\beta_{s2q}i_{s2q} \\ \frac{d\Omega_2}{dt} = \frac{1}{2H_2}\frac{P_{m2}}{\Omega_2} - \frac{1}{2H_2}\frac{\Omega_b}{\omega_{fb}}\frac{3}{2}p_2\Psi_{f2}i_{s2q} - \frac{1}{2H_2}D_{L2}\Omega_2; D_{L2} = \frac{\Omega_b^2 f_2}{S_b} \end{cases} \tag{4.2}$$

where (V_{r1d}, V_{r1q}) are PMSG1's terminal voltages in dq frame and (V_{r2d}, V_{r2q}) are PMSG2's terminal voltages. These voltages are directly affected by the interaction between the PMSGs and grid as in Fig. 4.2.

The PMSG pitch angle dynamics are separated from the converter's dynamic [4], [5]:

$$\begin{cases} \frac{d\beta_{PMSG1}}{dt} = -\frac{1}{\tau_{C1}}\beta_{PMSG1} + \frac{1}{\tau_{C1}}\beta_{PMSG1ref} \\ \frac{d\beta_{PMSG2}}{dt} = -\frac{1}{\tau_{C2}}\beta_{PMSG2} + \frac{1}{\tau_{C2}}\beta_{PMSG2ref} \end{cases} \tag{4.3}$$

where

$$\begin{cases} \beta_{\min} \le \beta_{PMSG1}, \beta_{PMSG2} \le \beta_{\max} \\ \left(\frac{d\beta}{dt}\right)_{\min} \le \frac{d\beta_{PMSG1}}{dt}, \frac{d\beta_{PMSG2}}{dt} \le \left(\frac{d\beta}{dt}\right)_{\max} \end{cases}$$

and the physical ranges of the servo motors [4], [5]:

$$\begin{cases} \tau_{C1} = 0.2\,(s)\,; \tau_{C2} = 0.2\,(s) \\ \beta_{\min} = 0\,(\deg)\,; \beta_{\max} = 20\,(\deg) \\ \left(\frac{d\beta}{dt}\right)_{\min} = -10\,(\deg)\,; \left(\frac{d\beta}{dt}\right)_{\max} = 10\,(\deg) \end{cases}$$

Discussed and considered in [6], the mismatch in generator speed reference generation can be avoided by calculating active powers at the generators:

$$\begin{cases} P_1 = \dfrac{3}{2}\dfrac{\Omega_b}{\omega_{fb}} p\psi_{f1} i_{s1q} \Omega_1 \\ P_2 = \dfrac{3}{2}\dfrac{\Omega_b}{\omega_{fb}} p\psi_{f2} i_{s2q} \Omega_2. \end{cases} \tag{4.4}$$

Reactive power can be calculated from the voltages of capacitor in the LCL filter:

$$\begin{cases} Q_1 = \dfrac{3}{2}\left(i_{11d} v_{cf1q} - i_{11q} v_{cf1d}\right) \\ Q_2 = \dfrac{3}{2}\left(i_{12d} v_{cf2q} - i_{12q} v_{cf2d}\right). \end{cases} \tag{4.5}$$

The neighbor grid equivalent dynamic, as introduced in [6], is in the form of:

$$\frac{d\omega_f}{dt} = \frac{1}{2H}\left(P_m - P_L + P_e\right) - \frac{1}{2H} D_u \Delta\omega_f; D_u = \frac{\omega_b^2 D}{S_b} \tag{4.6}$$

where P_m is the generated power of AC grid, P_L is the equivalent grid load, P_e is the power from two PMSGs, H is the grid inertia constant, and ω_f is the grid frequency.

4.2 Linear optimal H_∞ mixed-sensitivity loop shaping control

The coordinated control structures regardless of using overlapping decentralized strategy developed in chapter 3 (Fig. 2.11) or centralized control (as for DVPP, with control structure as in Fig. 2.10), using MIMO state-space model method, are always containing:

- Input control U: each subsystem will be controlled separately (for decentralized control) or all subsystems will be controlled by a single regulator, depending on the strategy (for centralized control).
- System or subsystem states X: In the case of centralized approach, the states of all subsystems are grouped into a single system state vector. Instead, each subsystem has its own state vector for centralized control method.
- System or subsystem outputs Y: Each technique, like the case of state vector, will have a system/subsystem output vector.
- Considered disturbances W: In the case of centralized approach, the disturbances are the undesired interactions of the whole system with the neighbor grid (Fig. 2.10). For decentralized approach (Fig. 2.11), W includes not only these undesired interactions but also the interactions between subsystems, that are, overlapping states in each subsystem (e.g., in [8]).

Thus, whatever approach is used, the control model can be represented using state-space model, and by linearization, can be put into linear model as:

$$\begin{cases} \dot{X} = AX + B_1 U + B_2 W \\ Y = CX + D_1 U \end{cases} \tag{4.7}$$

4.2.1 Control system synthesis

Each approach (centralized and decentralized) is explored and has its own control design process to optimally design a control system. However, since both are coordinated controls focusing on GAS delivery, the control structures for both approaches are similar and are illustrated in Fig. 4.5, and includes:

- two controllers (i.e., Reg. 0 and Reg. 1) for each loop (Reg. 0 for Plant 0, Reg. 1 for Plant 1).
- Reg. 0 will control Plant 0, which is providing FCR (grid inertia control, i.e., RoCoF control), VSP (reactive Q control) and LS (here is V_{DC} control).

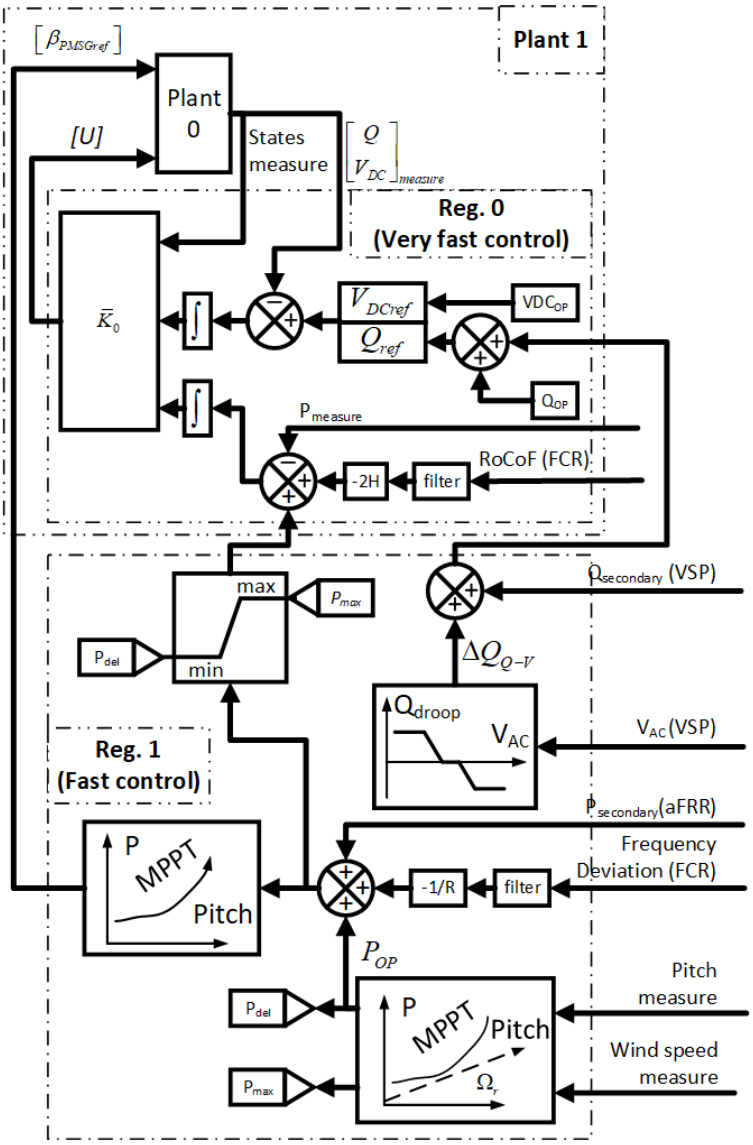

Figure 4.5: Coordinated control for PMSG with LS and GAS

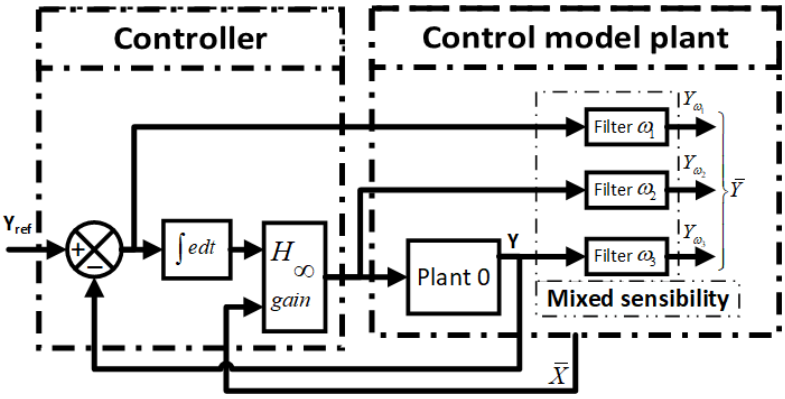

Figure 4.6: Optimal H_∞ control structure with mixed sensitivity loop shaping technique

- In Reg. 0, optimal control method are used to reject disturbance (e.g., optimal H_∞ control) and oscillation/pole placement (e.g., mixed sensitivity loop shaping for reduce the oscillation in LCL filter [9]).
- Reg. 1 controls Plant 1, which is participating in FCR (here is frequency response [10]) and VSP (Q-V characteristic [11]) services. Reg. 1 also receives requests from secondary/tertiary control loop (that are, aFRR/mFRR and AC voltage control loop) to be sure that the system/subsystem is participating in GAS.

Therefore, the general control strategy for Reg. 0 (in both centralized and decentralized approaches) is proposed as in Fig. 4.6, including:

- The control model plant includes plant 0 (Fig. 2.10 in case of centralized control or in Fig. 2.11 in case of decentralized control) along with the mixed sensitivity filters ω_1, ω_3, ω_3.
- The controller is designed using the integral action for asymptotic tracking and H_∞ optimization for disturbance rejection.
- Filter ω_1 is typically for enhancing reference tracking and reducing disturbance influence. The proposed control, however, is using integral action for asymptotic reference tracking as in Fig. 4.6. The H_∞ optimization is also used for rejecting disturbance. Therefore, filter ω_1 should be a unit gain: $\omega_1 = 1$.
- Filter ω_2 is for control effort limiting in a specific frequency band, but in this case, there is no need for that, therefore this filter can be ignored: $\omega_2 = 0$.
- Filter ω_3 is used to enhance the poor damped oscillation (e.g., LCL filter oscillation). By using modal analysis, the oscillation is verified that it comes capacitor voltage of the LCL filter, which is recoverable using the output reactive powers. Transform matrix C_Q is used to extract reactive power signal from system output. The resulting state-space model of the dynamic ω_3 is:

$$\begin{cases} \dot{X}_{\omega_3} = A_{\omega_3} X_{\omega_3} + B_{\omega_3} C_Q C X \\ Y_{\omega_3} = C_{\omega_3} X_{\omega_3} + D_{\omega_3} C_Q C X \end{cases} \tag{4.8}$$

The error between system output and reference are:

$$e = Y_{ref} - CX - D_1 U \tag{4.9}$$

The resulting augmented output $\bar{Y}$ and augmented state $\bar{X}$:

$$\begin{cases} \bar{X} = \begin{bmatrix} X & X_{\omega_3} & Int\_e \end{bmatrix}^T; Int\_e = \int e dt \\ \bar{Y} = \begin{bmatrix} e & Y_{\omega_3} \end{bmatrix}^T; \bar{W} = \begin{bmatrix} W^T & Y_{ref} \end{bmatrix}^T \end{cases} \tag{4.10}$$

Therefore, the augmented model for the control system (Fig. 4.6):

$$\begin{cases} \dot{\bar{X}} = \bar{A}\bar{X} + \bar{B}_1 U + \bar{B}_2 \bar{W} \\ \bar{Y} = \bar{C}\bar{X} + \bar{D}_1 U + \bar{D}_2 \bar{W} \end{cases} \tag{4.11}$$

where:

$$\bar{D}_1 = \begin{bmatrix} -D_1 \\ 0 \end{bmatrix}; \bar{D}_2 = \begin{bmatrix} 0 & I \\ 0 & 0 \end{bmatrix}; \bar{A} = \begin{bmatrix} A & 0 & 0 \\ B_{\omega_3} C_Q C & A_{\omega_3} & 0 \\ -C & 0 & 0 \end{bmatrix};$$
$$\bar{B}_1 = \begin{bmatrix} B_1 \\ 0 \\ 0 \end{bmatrix}; \bar{B}_2 = \begin{bmatrix} B_1 & 0 \\ 0 & 0 \\ 0 & I \end{bmatrix}; \bar{C} = \begin{bmatrix} -C & 0 & 0 \\ D_{\omega_3} C_Q C & C_{\omega_3} & 0 \end{bmatrix}$$

The state - feedback controller is:

$$U = \bar{K}_0 \bar{X} \tag{4.12}$$

The relationship between augmented disturbance $\bar{W}$ and augmented output $\bar{Y}$ of closed-loop:

$$\begin{cases} \bar{Y}(s) = G(s)\bar{W}(s) \\ G(s) = (\bar{C} + \bar{D}_1\bar{K}_0)\big(sI - \big(\bar{A} + \bar{B}_1\bar{K}_0\big)\big)^{-1}\bar{B}_2 + \bar{D}_2 \end{cases} \tag{4.13}$$

Problem 5 *The H_∞ problem for the linear system* (4.11) *is to find a controller* (4.12) *such that:*

$$\|G\|_\infty < \gamma \tag{4.14}$$

At the same time, an effort is made to minimize the positive scalar γ.

4.2.2 Augmented system for centralized approach

In case of centralized approach, there is only 1 augmented system for the whole system. The linearized state-space system is obtained from its nonlinear model in subsection 4.1.3, and is in the form of system equation (4.7).

The output Y of this system:

$$\begin{cases} Y = \begin{bmatrix} Y_1 \\ Y_2 \end{bmatrix} \\ Y_1 = \begin{bmatrix} Q_1 & P_1 & v_{DC1} \end{bmatrix}^T \\ Y_2 = \begin{bmatrix} Q_2 & P_2 & v_{DC2} \end{bmatrix}^T \end{cases}$$

Considered disturbance W is:

$$W = \begin{bmatrix} P_{m1} & P_{m2} & P_L \end{bmatrix}^T$$

The state X is:

$$\begin{cases} X = \begin{bmatrix} X_1^T & X_2^T & \omega_f \end{bmatrix}^T \\ X_1 = [i_{11d}, i_{11q}, i_{21d}, i_{21q}, v_{cf1d}, v_{cf1q}, i_{s1d}, i_{s1q}, v_{DC1}, \Omega_1]^T \\ X_2 = [i_{12d}, i_{12q}, i_{22d}, i_{22q}, v_{cf2d}, v_{cf2q}, i_{s2d}, i_{s2q}, v_{DC2}, \Omega_2]^T \end{cases}$$

The augmented system is then constructed and the control gain is generated by following the procedure given in subsection 4.2.4.

4.2.3 Augmented system for overlapping decentralized approach

In case of overlapping decentralized approach, similar to our previous work for HVDC decentralized control in chapter 3, there should be two augmented systems, each one for each PMSG, along with their overlapping state. The considered decentralized system is

$$\begin{array}{l} (I) \begin{cases} \dot{X}_1 = A_1X_1 + B_1^1U_1 + B_2^1W_1 \\ Y_1 = C_1X_1 \end{cases} \\ (II) \begin{cases} \dot{X}_2 = A_2X_2 + B_1^2U_2 + B_2^2W_2 \\ Y_2 = C_2X_2 \end{cases} \end{array} \tag{4.15}$$

The considered output Y_1, Y_2 (for PMSG1 and PMSG2, respectively):

$$\begin{cases} Y_1 = \begin{bmatrix} Q_1 & P_1 & v_{DC1} \end{bmatrix}^T \\ Y_2 = \begin{bmatrix} Q_2 & P_2 & v_{DC2} \end{bmatrix}^T \end{cases}$$

The disturbance (including overlapping states and grid dynamic) W_1, W_2 for PMSG1, PMSG2 are:

$$\begin{cases} W_1 = \begin{bmatrix} i_{22d} & i_{22d} & P_{m1} \end{bmatrix}^T \\ W_2 = \begin{bmatrix} i_{21d} & i_{21d} & P_{m2} \end{bmatrix}^T \end{cases}$$

The states X_1 of PMSG1 and X_2 of PMSG2 are:

$$\begin{cases} X_1 = [i_{11d}, i_{11q}, i_{21d}, i_{21q}, v_{cf1d}, v_{cf1q}, i_{s1d}, i_{s1q}, v_{DC1}, \Omega_1, \omega_f]^T \\ X_2 = [i_{12d}, i_{12q}, i_{22d}, i_{22q}, v_{cf2d}, v_{cf2q}, i_{s2d}, i_{s2q}, v_{DC2}, \Omega_2, \omega_f]^T \end{cases}$$

As for the case of the centralized approach, each subsystem in (4.15) is used to create the corresponding augmented subsystem for PMSG1 and PMSG2 as explained in the next subsection.

4.2.4 Linear LMI-based optimal H_∞ control theorem

Theorem 5 *The problem 5, i.e, H_∞ problem, has a solution iff there exists a matrix W_P and a positive definite symmetric matrix $X_P = {X_P}^T$, satisfying:*

$$\underset{W_P, X_P}{minimize} \;\; \gamma$$

such that:

$$\begin{bmatrix} \Psi & \bar{B}_2 & \left(\bar{C}X_P + \bar{D}_1 W_P\right)^T \\ \bar{B}_2^T & -\gamma I & \bar{D}_2^T \\ \bar{C}X_P + \bar{D}_1 W_P & \bar{D}_2 & -\gamma I \end{bmatrix} < 0$$

where

$$\Psi = \left(\bar{A}X_P + \bar{B}_1 W_P\right)^T + \bar{A}X_P + \bar{B}_1 W_P \tag{4.16}$$

The controller's gain $\bar{K}_0$ for Reg. 0 is

$$\bar{K}_0 = W_P X_P^{-1} \tag{4.17}$$

Proof 5 *Consider a linear system in the state-space form*

$$\begin{cases} \dot{X} = AX + BU \\ Y = CX + DU \end{cases} \tag{4.18}$$

The relationship of input U to output Y is:

$$\begin{cases} Y = G(s)\, U \\ G(s) = C(sI - A)^{-1} B + D \end{cases} \tag{4.19}$$

The H_∞ problem, i.e., problem 5, is considered for the aforementioned linear system. The solution of this problem exists iff there exist a definite positive symmetric matrix X_p , such that the following LMI condition hold [12], [13]:

$$\begin{bmatrix} X_P A^T + A X_P & B & X_P C^T \\ B^T & -\gamma I & D^T \\ C X_P & D & -\gamma I \end{bmatrix} < 0 \tag{4.20}$$

Now, consider this solution, but for our augmented linear system with disturbance, i.e., system (4.11)*, the relevant LMI condition is:*

$$\begin{cases} \begin{bmatrix} \Psi & \bar{B}_2 & \left(\bar{C}X_P + \bar{D}_1 \bar{K}_0 X_P\right)^T \\ \bar{B}_2^T & -\gamma I & \bar{D}_2^T \\ \bar{C}X_P + \bar{D}_1 \bar{K}_0 X_P & \bar{D}_2 & -\gamma I \end{bmatrix} < 0 \\ \Psi = X_P\left(\bar{A} + \bar{B}_1 \bar{K}_0\right)^T + \left(\bar{A} + \bar{B}_1 \bar{K}_0\right) X_P \end{cases} \tag{4.21}$$

Then, theorem 5 can be derived from this LMI by setting $W_P = \bar{K}_0 X_P$.

4.2.5 Simulations and results

To verify the effectiveness of the two proposed approaches, the both controllers, i.e., decentralized and centralized controllers, are tested on the modified IEEE 14-bus benchmark. LMI MOSEK solver is used to compute the control gains [14]. The two PMSGs have the same 7.5 MW nominal capacity and all the tests are started with active power $P_e = 0.6527pu$ for both PMSGs. The two decentralized and centralized are tuned with the same same averaged time constant $\tau = 3.75$s for their outputs P, Q and v_{DC} in order to be able to compare robustness. A set of test scenario for GAS is shown in Fig. 4.7:

- Scenario 1 - Local services: To evaluate DC voltage, active power (FCR), and reactive power regulation (VSP), step responses to references of the control signals are simulated. This will only be tested on PMSG1 because PMSG2 behaves similarly to PMSG1. As shown from Fig. 4.8 to Fig. 4.10 for active/reactive powers and DC voltage of PMSG1, the two centralized and decentralized controllers provide pretty much the same performance as they are synthesized for nearly the same closed-loop time constant, around 3-4s.

- Scenario 2 - FRT and CCT capability: a three-phase short-circuit at bus 6 at t = 30s as in the IEEE 14-bus benchmark, far from PMSG1 and close to PMSG2, is used to compare the FRT capacity and CCT of the two approaches. With the same controller's gains as in scenario 1, the CCT for centralized control is 720ms (Figs. 4.11 and Fig. 4.13 for PMSG1 and PMSG2 terminal voltages, respectively) and for decentralized control is 540ms (Figs. 4.12 and Fig. 4.14 for PMSG1 and PMSG2 terminal voltages, respectively). Since the short-circuit event happened close to the PMSG2, the terminal voltage dip of PMSG2 is higher compared to the one of the PMSG1 terminal voltage.

- Scenario 3 - Frequency services (FCR): At t = 30s, load at bus 1 is increased by 2MW. As shown in Figs. 4.18 and 4.19, the active powers of two PMSGs using both approaches are increased to cope with the droop on frequency (Fig. 4.17) and RoCoF (Fig. 4.20). Also as illustrated in Fig. 4.17 and 4.20, the behaviors of frequency and RoCoF are considerable improved using both approaches, compared to the result of the strategy without frequency supports.

- Scenario 4 - Voltage services (VSP): load at bus 14 is increased by 10MVar at time t = 30s in order to test the voltage service. Through the Q-V characteristic, the two control structures offer reactive power [15]. As seen in Figs. 4.21 and 4.23, the reactive power was increased for both of PMSGs, with a slightly larger portion of PMSG2 reactive power since the injected load is close to its location (i.e., its terminal voltage dip is larger). Thanks to these supports, shown in Figs. 4.22 and 4.24, the terminal voltages of two PMSGs are improved greatly compared to the case when there is no support in reactive power.

- Scenario 5 - Wind speed change: This scenario evaluates the two control strategies at PMSG1 with a changing wind profile over a 400-second period. The wind profile in Km/h is shown in Fig. 4.25. As shown in Fig. 4.26, both of the approaches provide an asymptotic tracking for the active power to the reference, with a time constant at around 3s.

4.2.6 Conclusion

For a PMSG-based wind energy system, coordinated control approaches using both centralization and decentralization were developed. The controllers are formulated using LMI techniques, reference tracking internal model principle and mixed sensibility loop-shaping. For validation, the proposed methods are implemented in MATLAB and validated using a modified IEEE 14-bus benchmark using Simscape and tested in various simulations.

These tests demonstrated that the proposed controls can potentially be generalized for any DRES. In comparison to decentralized approach, the centralized approach is more effective in terms of performance and robustness. Decentralized control provides resilence.

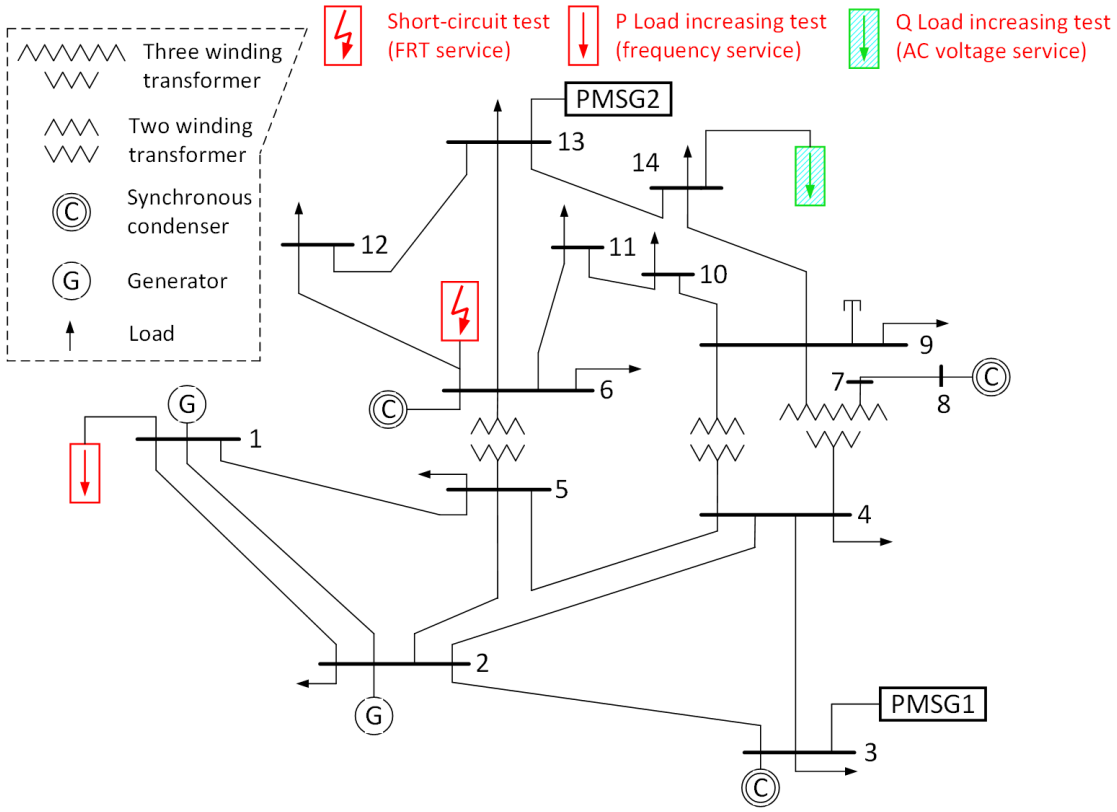

Figure 4.7: The modified IEEE 14 bus test case with 2 PMSGs for testing scenarios

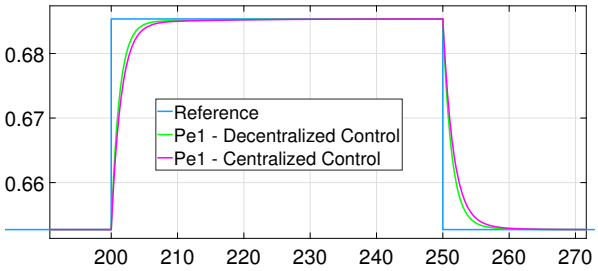

Figure 4.8: Senario 1: Step response for active power (p.u.) of PMSG1

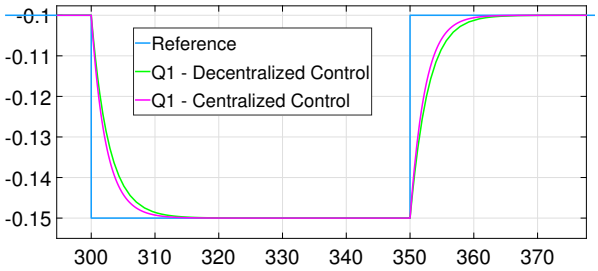

Figure 4.9: Senario 1: Step response for reactive power (p.u.) of PMSG1

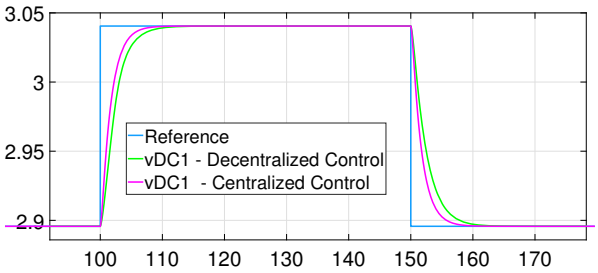

Figure 4.10: Senario 1: Step response for DC voltage (p.u.) of PMSG1

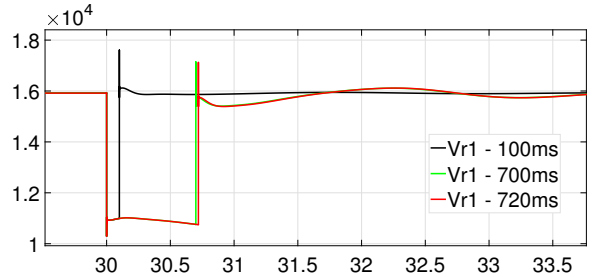

Figure 4.11: Senario 2: The terminal voltages (V) of PMSG1 (Centralized control)

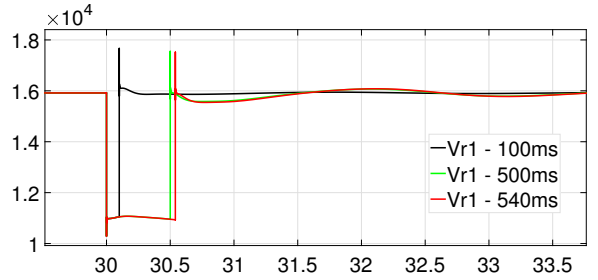

Figure 4.12: Senario 2: The terminal voltages (V) of PMSG1 (Decentralized control)

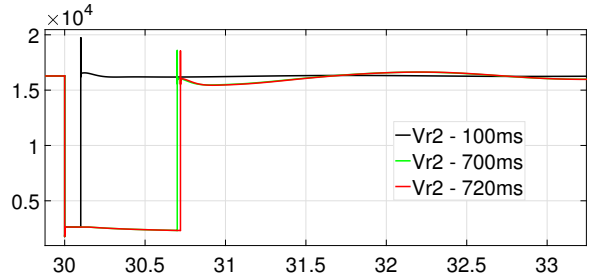

Figure 4.13: Senario 2: The terminal voltages (V) of PMSG2 (Centralized control)

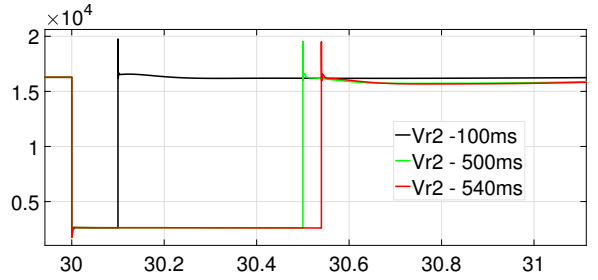

Figure 4.14: Senario 2: The terminal voltages (V) of PMSG2 (Decentralized control)

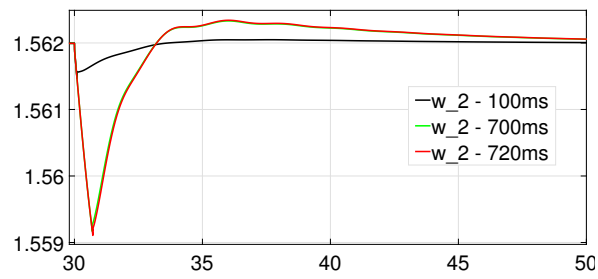

Figure 4.15: Senario 2: The generator speed (p.u.) of PMSG2 (Centralized control)

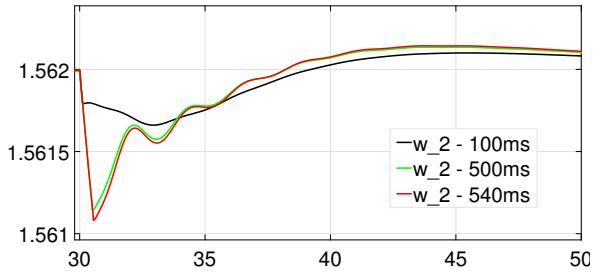

Figure 4.16: Senario 2: The generator speed (p.u.) of PMSG2 (Decentralized control)

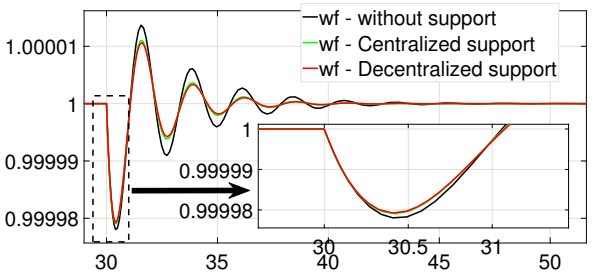

Figure 4.17: Senario 3: grid frequency (p.u)

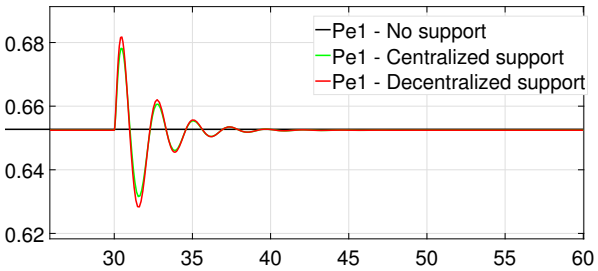

Figure 4.18: Senario 3: active power (p.u.) of PMSG1

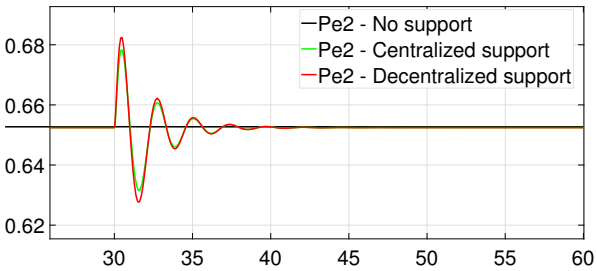

Figure 4.19: Senario 3: active power (p.u.) of PMSG2

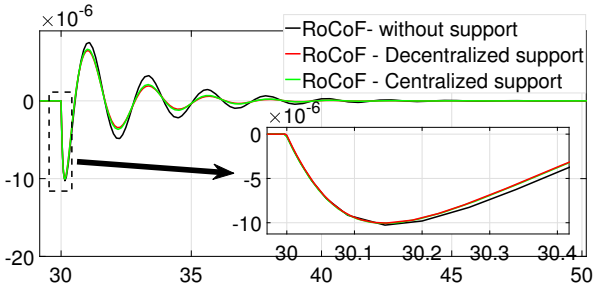

Figure 4.20: Senario 3: Grid RoCoF (p.u.)

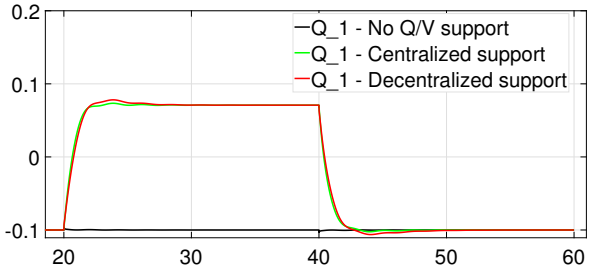

Figure 4.21: Senario 4: reactive power (p.u.) of PMSG1

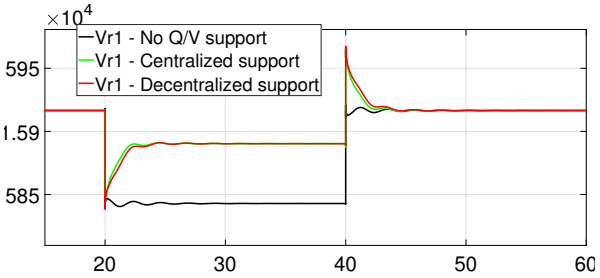

Figure 4.22: Senario 4: The terminal voltages (V) of PMSG1

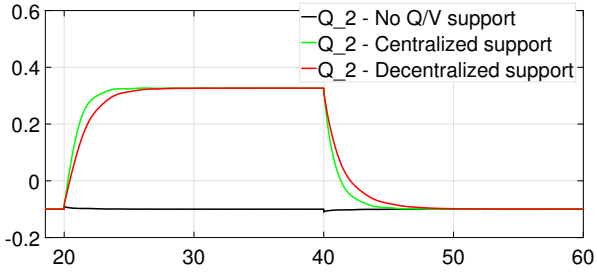

Figure 4.23: Senario 4: reactive power (p.u.) of PMSG2

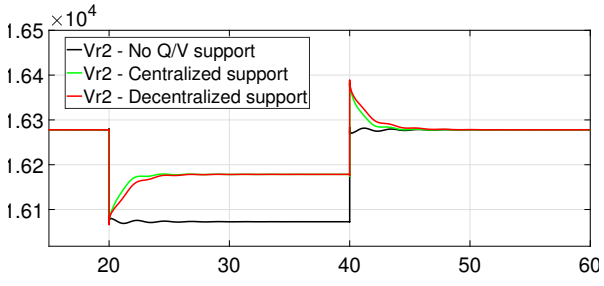

Figure 4.24: Senario 4: The terminal voltages (V) of PMSG2

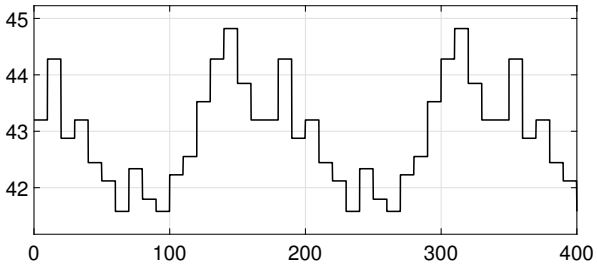

Figure 4.25: Senario 5: Wind speed profile (Km/h)

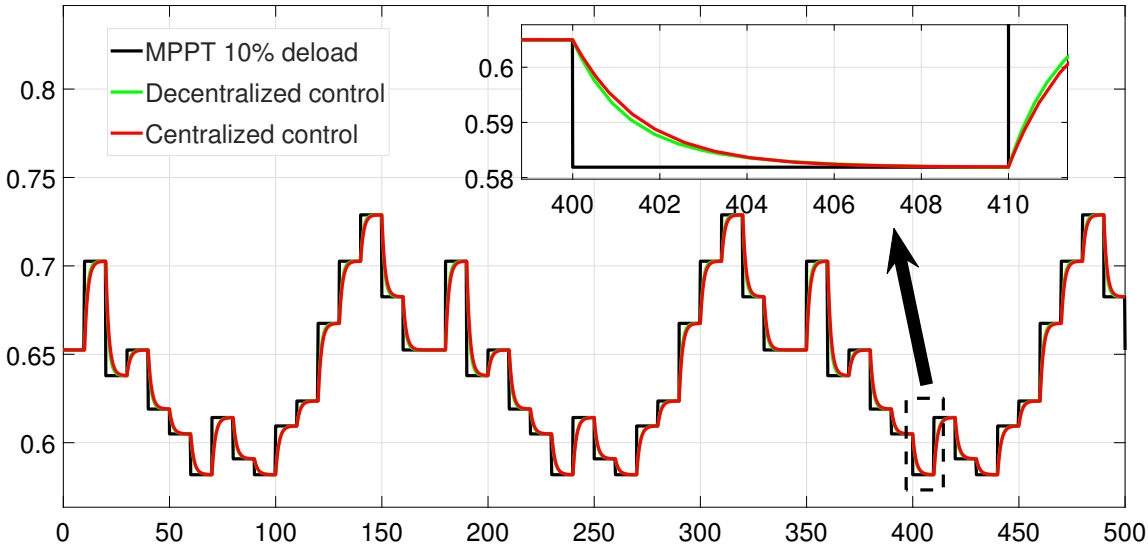

Figure 4.26: The active power of PMSG1 with wind speed profile in Fig. 4.25

4.3 Robust distributed fuzzy optimal H_∞ control

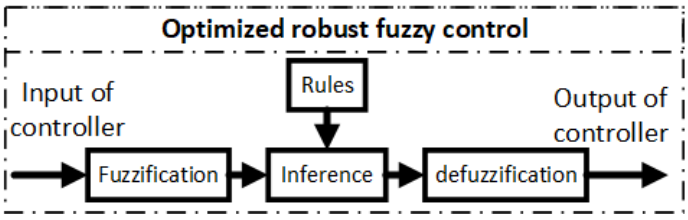

Figure 4.27: The optimized robust fuzzy control structure of Reg. 0

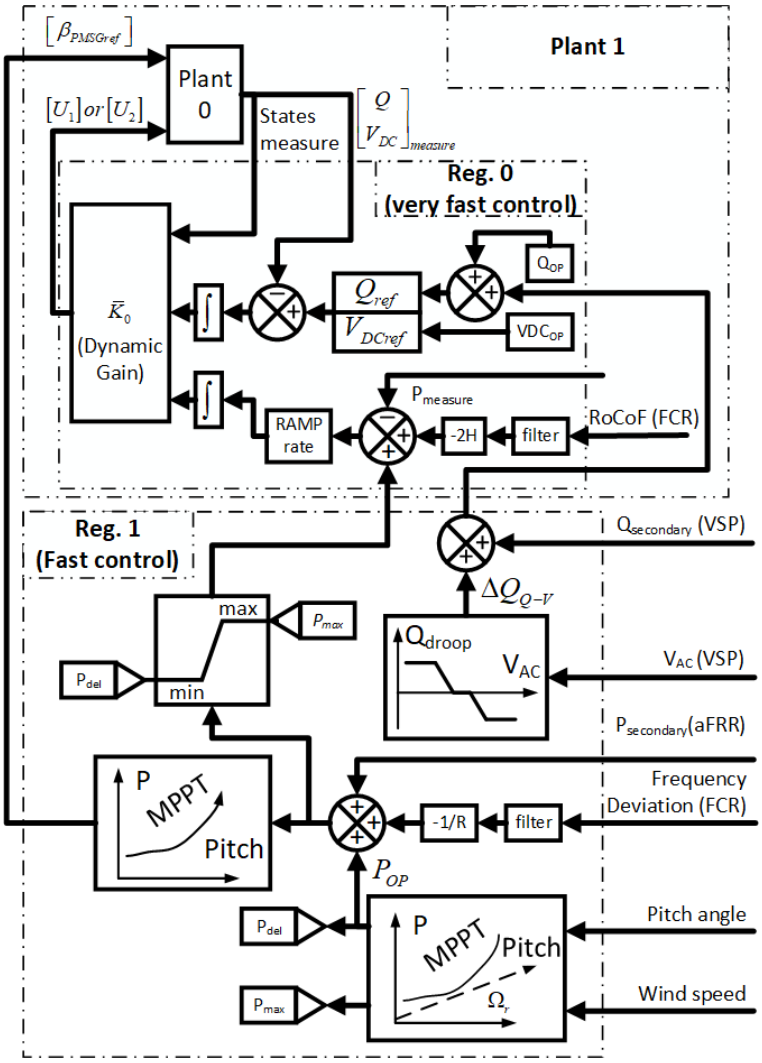

Figure 4.28: Coordinated control for PMSG with LS and GAS

4.3.1 Control system synthesis

Similar to the linear control approaches in subsection 4.2.1, the detailed control structure for fuzzy distributed control, based on the decentralized control structure in Fig. 2.11, is described as in Fig. 4.28. The two PMSGs and grid are now considered as two independent susbsystem, each PMSG is a subsystem and is treated independently

by a fuzzy control structure.

In this nonlinear fuzzy distributed approach, the control fulfills all the specifications considered in subsection Power converter system control objectives of chapter Grid-connected power converter system objectives and proposed approaches, including robustness and nonlinearity handling. Thus, the general control strategy described in Fig. 4.28, consist of:

- Same as in linear approaches, there are two control loops, Reg. 0 for plant O and Reg. 1 for plant 1.
- The gain $\bar{K}_0$ of Reg. 0 is now updated online using fuzzy technique as in Fig. 4.27.
- Similar to linear controls, in Reg. 0, optimal control method are used to reject disturbance (e.g., optimal H_∞ control).
- Reg. 0 and Reg. 1 are also ensuring the participation of each subsystem (each PMSG) in providing GAS.

Each PMSG nonlinear subsystem is modeled by a nonlinear state-space model in equation (4.22):

$$\begin{cases} \dot{X} = A_{nl}X + B_{nl1}U + B_{nl2}W \\ Y = C_{nl}X \end{cases} \tag{4.22}$$

where:

- The system output Y includes DC voltage of the DC line between two converters and their active/reactive powers.
- The system state X are the PMSG states, including currents and voltages.
- The disturbance W, as discussed in case of decentralized control, consists of the undesired interaction between subsystems and neighbor environment influences.

Similar to the fuzzification process [16] in subsection 3.3.2 of chapter 3, the nonlinear state-space model (4.22) is converted into fuzzy model in equation (4.23):

$$\begin{cases} \dot{X} = \sum_{i=1}^{r} h_i(z)\left(A_iX + B_{1i}U\right) + B_2W \\ \quad = AX + B_1U + B_2W \\ Y = CX \end{cases} \tag{4.23}$$

The value of the fuzzy membership functions $M_{ij}(z_j)$, based on each fuzzy rule, are calculated as [16]:

$$\begin{cases} M_{ij}^1(z_j) = \frac{z_j - \min(z_j)}{\max(z_j) - \min(z_j)} \\ M_{ij}^2(z_j) = \frac{\max(z_j) - z_j}{\max(z_j) - \min(z_j)} \end{cases} \tag{4.24}$$

These membership function values correspond to each nonlinear sector's behavior as described in [16]. Based on these, a collection of linear systems (i.e., matrices set $\{A_i, B_{1i}, B_2, C\}$) will be used to characterize the system's nonlinear dynamics. As a result, the stability of the nonlinear system is assured if it is possible to have a set of static control gains, such as when the Lyapunov function of the fuzzy system is negative. Additional capacities can be provided, such as robustness and disturbance rejection, for example, by utilizing LMI techniques.

The output and reference signals of the two PMSGs are:

$$\begin{cases} Y = [Q, P, V_{DC}]^T \\ Y_{ref} = [Q_{ref}, P_{ref}, V_{DCref}]^T \end{cases} \tag{4.25}$$

The error between output and reference:

$$e = -CX + Y_{ref} \tag{4.26}$$

The extended augmented state:

$$\bar{X} = \begin{bmatrix} \dot{X} \\ e \end{bmatrix}; \bar{Y} = e \tag{4.27}$$

The fuzzy augmented system is:

$$\begin{cases} \dot{\bar{X}} = \bar{A}\bar{X} + \bar{B}_1\bar{U} + \bar{B}_2\bar{W} \\ \bar{Y} = \bar{C}\bar{X} \\ \bar{U} = \dot{U}, \bar{W} = \dot{W} \end{cases} \tag{4.28}$$

The state-space matrices are:

$$\bar{A} = \sum_{i=1}^{r} h_i(z)\,\bar{A}_i; \bar{A}_i = \begin{bmatrix} A_i & 0 \\ -C & 0 \end{bmatrix}; \bar{B}_2 = \begin{bmatrix} B_2 \\ 0 \end{bmatrix};$$
$$\bar{B}_1 = \sum_{i=1}^{r} h_i(z)\,\bar{B}_{1i}; \bar{B}_{1i} = \begin{bmatrix} B_{1i} \\ 0 \end{bmatrix}; \bar{C} = \begin{bmatrix} 0 & I \end{bmatrix}$$

and $r = 2^p$ is the number of fuzzy rule.

The state-feedback fuzzy controller using the PDC [16]:

Control Rule j:

IF z_1 is with M_{j1} and z_2 is with M_{j2} and ... and z_p is with M_{jp},
THEN $\dot{U}_j = \bar{K}_j\bar{X}, i = 1, 2, ..., r$

where p is the number of nonlinear sector.

The fuzzy control dynamic gain $\bar{K}_0$ for augmented system (4.28) is:

$$\bar{U} = \frac{\sum_{j=1}^{r} w_j(z)\,\bar{K}_j\bar{X}}{\sum_{j=1}^{r} w_j(z)} = \sum_{j=1}^{r} h_j(z)\,\bar{K}_j\bar{X} = \bar{K}_0\bar{X} \tag{4.29}$$

The controller for the original nonlinear system (4.22) is a MIMO controller:

$$\begin{cases} U = \bar{K}_0 \begin{bmatrix} X \\ \int e dt \end{bmatrix} \\ \bar{K}_0 = \sum_{j=1}^{r} h_j(z)\,\bar{K}_j \end{cases} \tag{4.30}$$

To implement the fuzzy controller, the controller's dynamic gain are calculated using a set of static gains, which is an online process. The static gains are precalculated through an offline process. These two processes are described as in Fig. 4.29. The implementation of the fuzzy control (here is the Reg. 0 in Fig. 4.28) is then as in Fig. 4.30.

The unified nonlinear sector is introduced and discussed in the next subusection, that is, subsection 4.3.2. The two theorems, i.e., uncertainty-free and robust fuzzy theorems, are introduced in subsection 4.3.3 and 4.3.4, respectively.

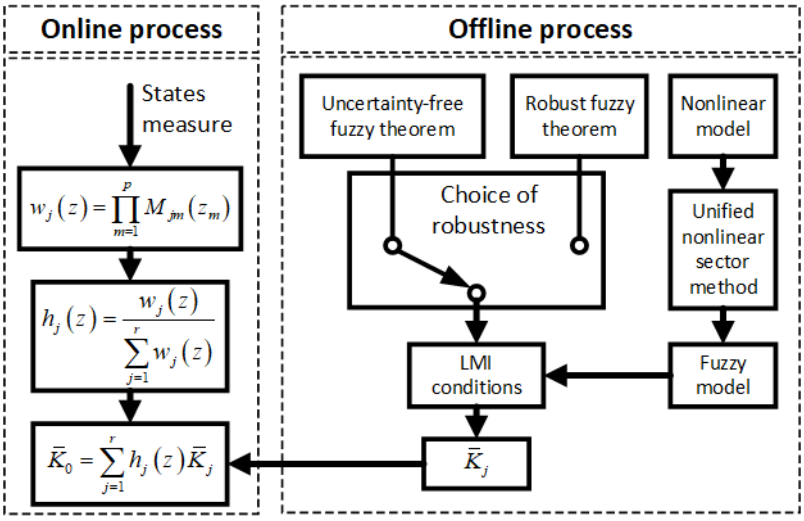

Figure 4.29: Fuzzy-based control: online and offline processes

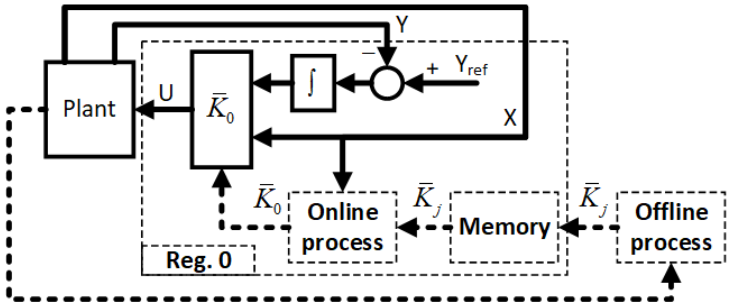

Figure 4.30: Fuzzy-based control: Implementation of (robust) H_∞ fuzzy control

4.3.2 Unified nonlinear sector in fuzzy system

In many cases, especially in power system, there are too many nonlinear sectors, i.e., to many fuzzy rules, which is impossible to find a common Lyapunov function, so there will be no solution, no suitable controller. Fortunately, the DRES, or nonlinear converter-based systems in general, are actually bi-linear systems with disturbance (as in (4.23)):

$$\dot{X} = AX + B_1U + B_2W; B_1 = B_1'X \tag{4.31}$$

where A, B_1' and B_2 are time-invariant matrices.

The then arisen nonlinear sectors, from $B_1 = B_1'X$, are linear functions of one or some of the states $X = \begin{bmatrix} x_1 & \cdots & x_n \end{bmatrix}^T$. The physical converter-based system's outputs are $Y = CX$. These outputs, such as active/reactive powers, voltages, or currents, are genuinely physical. This indicates that, in the worst scenario, the outputs of the system under consideration are the products, or sums of the products, of a maximum of two states. The resulting linear functions of one of the states will be the eventual nonlinear sectors. This nonlinear characteristic of converter-based systems is exploited to further reduce the number of fuzzy rules by stacking them with the minimized rules utilizing nonlinear sectors, as shown by the following fuzzy-based treatment.

Notice that the system (4.31) has p number of nonlinear sectors as considered in system equation (4.23). According to [16], the number of resulting fuzzy rules is 2^p. Since nonlinear sectors are linear functions of one or some of the states, the arbitrary two same state-dependent nonlinear sectors in the investigated system can be put in forms of:

As seen in the system equation (4.23), the system (4.31) has p number of nonlinear sectors. As discussed in [16], there are 2^p fuzzy rules as a result. Since nonlinear sectors are linear functions of one or more of the states, the randomly chosen two identical state-dependent nonlinear sectors in the system under investigation can be expressed as follows:

$$\begin{cases} z_1 = f_1 x_i \\ z_2 = f_2 x_i \end{cases} \tag{4.32}$$

where f_1, f_2 are known constants.

The physical state x_i is bounded: $x_i \in [x_{\min}, x_{\max}]$. As a result, the two x_i-dependent nonlinear sectors are naturally bounded:

$$\begin{cases} z_1 \in [f_1 x_{\min}, f_1 x_{\max}] \\ z_2 \in [f_2 x_{\min}, f_2 x_{\max}] \end{cases} \tag{4.33}$$

The membership functions of the nonlinear sector z_1 is:

$$\begin{cases} M^1(z_1) = \dfrac{z_1 - f_1 x_{\min}}{f_1 x_{\max} - f_1 x_{\min}} = \dfrac{x_i - x_{\min}}{x_{\max} - x_{\min}} \\ M^2(z_1) = \dfrac{f_1 x_{\max} - z_1}{f_1 x_{\max} - f_1 x_{\min}} = \dfrac{x_{\max} - x_i}{x_{\max} - x_{\min}} \end{cases} \tag{4.34}$$

The membership functions of the nonlinear sector z_2 is:

$$\begin{cases} M^1(z_2) = \dfrac{z_2 - f_2 x_{\min}}{f_2 x_{\max} - f_2 x_{\min}} = \dfrac{x_i - x_{\min}}{x_{\max} - x_{\min}} \\ M^2(z_2) = \dfrac{f_2 x_{\max} - z_2}{f_2 x_{\max} - f_2 x_{\min}} = \dfrac{x_{\max} - x_i}{x_{\max} - x_{\min}} \end{cases} \tag{4.35}$$

It goes without saying that the membership functions of z_1 and z_2, as well as those of a nonlinear sector $z' = x_i$, are identical. This indicates that all of the nonlinear sectors in the system under consideration, whether it be a converter-based system, or a bi-linear system in general, can be characterized by just the involved states in the nonlinear sectors of the system. In other words, the total number of states involved now equals the total number of nonlinear sectors. In essence, there are now 2^k rules, where k is the number of involved states. It's important to note that $k \leq p$, and normally k is significantly smaller than p. From now, this nonlinear sector method will be called unified nonlinear sector, since many nonlinear sectors can be represented by a state, i.e., a unified nonlinear sector.

4.3.3 Uncertainty-free H-infinity Nonlinear Fuzzy Distributed Control

Firstly, we focus on the case where system (4.28) has no parameter uncertainty. In this case, the controller gain is generated by using the norminal value of the system matrices. The resulting controller is called H_∞ Nonlinear Fuzzy Distributed Control ($H_{inf}NFDC$).

The transfer function $G(s)$ from the disturbance $\bar{W}$ to the output $\bar{Y}$ is:

$$\begin{cases} G(s) = \bar{C}\left(sI - \left(\bar{A} + \bar{B}_1 \bar{K}_0\right)\right)^{-1} \bar{B}_2 \\ \bar{Y}(s) = G(s)\,\bar{W}(s) \end{cases} \tag{4.36}$$

By using the definition of the H_∞ norm [12], [13], we have:

$$\left\|\bar{Y}\right\|_2 \leq \|G\|_\infty \left\|\bar{W}\right\|_2 \tag{4.37}$$

Problem 6 *For the fuzzy system* (4.28)*, with the transfer function* $G(s)$ *from the disturbance* $\bar{W}$ *to the output* $\bar{Y}$ *as in* (4.36)*, the* H_∞ *nonlinear problem is to stabilize the dynamics using a fuzzy control law* (4.29) *which satisfies*

$$\|G\|_\infty < \gamma \tag{4.38}$$

and, at the same time, minimizing the positive scalar γ*.*

Theorem 6 *The H_∞ nonlinear problem 6 has a solution iff there exists matrices a positive symmetric definite matrix X_P and W_{Pj}, satisfying:*

$$\underset{X_P, W_P}{minimize} \ \ \gamma$$

such that

$$\begin{cases} X_p > 0, \gamma > 0 \\ \begin{bmatrix} \Psi_{ij} & \bar{B}_2 & \left(\bar{C}X_P\right)^T \\ \bar{B}_2^T & -\gamma I & 0 \\ \bar{C}X_P & 0 & -\gamma I \end{bmatrix} < 0 \\ \Psi_{ij} = \left(\bar{A}_i X_P + \bar{B}_{1i} W_{Pj}\right)^T + \bar{A}_i X_P + \bar{B}_{1i} W_{Pj} \\ i, j = \overline{1, r} \end{cases}$$

Similar to linear approaches, static gains $\bar{K}_j$ are calculated using:

$$\bar{K}_j = W_{Pj} X_P^{-1}. \tag{4.39}$$

Proof 6 *Similar to the proof of theorem 5, apply the solution of H_∞ problem of the state-space system* (4.18) *for system* (4.28)*, the LMI solution is now:*

$$\begin{cases} \begin{bmatrix} \Psi & \bar{B}_2 & \left(\bar{C}X_P\right)^T \\ \bar{B}_2^T & -\gamma I & 0 \\ \bar{C}X_P & 0 & -\gamma I \end{bmatrix} < 0 \\ \Psi = \left(\bar{A}X_P + \bar{B}_1 \bar{K}_0 X_P\right)^T + \bar{A}X_P + \bar{B}_1 \bar{K}_0 X_P \end{cases} \tag{4.40}$$

From the matrices of system (4.28) *and its controller* (4.29)*, Ψ can be rewritten as:*

$$\begin{cases} \Psi = \sum_{i=1}^{r} \sum_{j=1}^{r} h_i(z) h_j(z) \Psi_{ij} \\ \Psi_{ij} = \left(\bar{A}_i X_P + \bar{B}_{1i} \bar{K}_j X_P\right)^T + \bar{A}_i X_P + \bar{B}_{1i} \bar{K}_j X_P \end{cases} \tag{4.41}$$

Thus, the condition (4.40) *is now:*

$$\begin{cases} \sum_{i=1}^{r} \sum_{j=1}^{r} h_i(z) h_j(z) \begin{bmatrix} \Psi_{ij} & \bar{B}_2 & \left(\bar{C}X_P\right)^T \\ \bar{B}_2^T & -\gamma I & 0 \\ \bar{C}X_P & 0 & -\gamma I \end{bmatrix} < 0 \\ \Psi_{ij} = \left(\bar{A}_i X_P + \bar{B}_{1i} \bar{K}_j X_P\right)^T + \bar{A}_i X_P + \bar{B}_{1i} \bar{K}_j X_P \end{cases} \tag{4.42}$$

Now, consider:

$$\begin{cases} a_1(z) = h_1(z) h_1(z) \\ a_2(z) = h_1(z) h_2(z) \\ \vdots \\ a_r(z) = h_1(z) h_r(z) \\ a_{r+1}(z) = h_2(z) h_1(z) \\ \vdots \\ a_{r^2}(z) = h_r(z) h_r(z) \end{cases} \tag{4.43}$$

According to the fuzzy rule [16]:

$$\begin{cases} h_i(z) \geq 0; \sum_{i=1}^{r} h_i(z) = 1 \\ h_j(z) \geq 0; \sum_{j=1}^{r} h_j(z) = 1 \end{cases} \tag{4.44}$$

As a result, the value ranges of $a_i(z)$ are:

$$\begin{cases} 1 \geq a_i(z) \geq 0, \forall i = \overline{1, r^2} \\ \sum_{i=1}^{r^2} a_i(z) = 1 \end{cases} \tag{4.45}$$

The closed-loop system is stabilized iff (4.42) *holds for all* $h_i(z), h_j(z)$ *so that:*

$$\begin{cases} 0 \leq h_i(z) \leq 1 \\ 0 \leq h_j(z) \leq 1 \end{cases}$$

Equivalently, the closed-loop system is stabilized iff (4.42) *holds for all* $a_i(z)$ *with the condition* (4.45)*.*
By using lemma for convex problem (i.e. lemma C.1 in Appendices), the condition (4.42) *can be written as:*

$$\begin{cases} \begin{bmatrix} \Psi_{ij} & \bar{B}_2 & \left(\bar{C}X_P\right)^T \\ \bar{B}_2^T & -\gamma I & 0 \\ \bar{C}X_P & 0 & -\gamma I \end{bmatrix} < 0 \\ \Psi_{ij} = \left(\bar{A}_i X_P + \bar{B}_{1i}\bar{K}_j X_P\right)^T + \bar{A}_i X_P + \bar{B}_{1i}\bar{K}_j X_P \\ i, j = \overline{1, r} \end{cases} \tag{4.46}$$

and, set $W_{Pj} = \bar{K}_j X_P$*, the theorem 6 is proven.*

4.3.4 H-infinity Robust Nonlinear Fuzzy Distributed Control

Now, we consider the uncertainty in system parameter. The resulting controller is named H_∞ Robust Nonlinear Fuzzy Distributed Control ($H_{inf}RNFDC$). The augmented system (4.28) is in the form:

$$\begin{cases} \dot{\bar{X}} = \sum_{i=1}^{r} h_i(z)\left(\bar{A}_i + \Delta\bar{A}_i\right)\bar{X} + \sum_{i=1}^{r} h_i(z)\left(\bar{B}_{1i} + \Delta\bar{B}_{1i}\right)\dot{U} + \bar{B}_2\dot{W} \\ Y = \bar{C}\bar{X} \end{cases} \tag{4.47}$$

where:

$$\begin{cases} \begin{bmatrix} \Delta\bar{A}_i & \Delta\bar{B}_{1i} \end{bmatrix} = H_i F_i \begin{bmatrix} E_{1i} & E_{2i} \end{bmatrix} \\ E_{1i} = \delta_{1i}\bar{A}_i; |\delta_{1i}| < r_{1i}; r_{1i} \in R^+ \\ E_{2i} = \delta_{2i}\bar{B}_{1i}; |\delta_{2i}| < r_{2i}; r_{2i} \in R^+ \\ F_i^T F_i \leq I \end{cases}$$

Problem 7 *The* H_∞ *nonlinear problem of system* (4.47) *is to stabilize the system with a control law* (4.29)*, satisfying:*

$$\|G\|_\infty < \gamma \tag{4.48}$$

and, at the same time, minimizing the positive scalar γ*.*

Theorem 7 *There is a solution to the* H_∞ *problem 7 iff there exists matrices* W_{Pj} *and a symmetric positive definite matrix* X_P*, satisfying:*

$$\underset{X_P, W_P}{minimize} \quad \gamma$$

so that

$$\begin{cases} X_p > 0, \gamma > 0, \alpha > 0 \\ \begin{bmatrix} \Psi_{ij} & \bar{B}_2 & \left(\bar{C}X_P\right)^T & \left(E_{1i}X_P + E_{2i}W_{Pj}\right)^T \\ \bar{B}_2^T & -\gamma I & 0 & 0 \\ \bar{C}X_P & 0 & -\gamma I & 0 \\ E_{1i}X_P + E_{2i}W_{Pj} & 0 & 0 & -\alpha I \end{bmatrix} < 0 \\ \Psi_{ij} = \left(\bar{A}_i X_P + \bar{B}_{1i}W_{Pj}\right)^T + \bar{A}_i X_P + \bar{B}_{1i}W_{Pj} + \alpha H H^T \\ i, j = \overline{1, r} \end{cases}$$

The gains $\bar{K}_j$ are calculated from W_{Pj} and X_P:

$$\bar{K}_j = W_{Pj} X_P^{-1}. \tag{4.49}$$

Proof 7 *To prove theorem 7, we can take advantage of the proven theorem 6, i.e., apply theorem 6 for system* (4.47)*, problem 7 has a solution iff:*

$$\begin{cases} X_p > 0, \gamma > 0 \\ \begin{bmatrix} \Psi_{ij} & \bar{B}_2 & \left(\bar{C}X_P\right)^T \\ \bar{B}_2^T & -\gamma I & 0 \\ \bar{C}X_P & 0 & -\gamma I \end{bmatrix} < 0 \\ \Psi_{ij} = \left(\left(\bar{A}_i + \Delta\bar{A}_i\right) X_P + \left(\bar{B}_{1i} + \Delta\bar{B}_{1i}\right) W_{Pj}\right)^T \\ \quad + \left(\bar{A}_i + \Delta\bar{A}_i\right) X_P + \left(\bar{B}_{1i} + \Delta\bar{B}_{1i}\right) W_{Pj} \\ i, j = \overline{1, r} \end{cases} \tag{4.50}$$

Expand the matrix in the LMI:

$$\begin{bmatrix} \Psi_{ij} & \bar{B}_2 & \left(\bar{C}X_P\right)^T \\ \bar{B}_2^T & -\gamma I & 0 \\ \bar{C}X_P & 0 & -\gamma I \end{bmatrix}$$
$$= \begin{bmatrix} \left(\bar{A}_i X_P + \bar{B}_{1i} W_{Pj}\right)^T & \bar{B}_2 & \left(\bar{C}X_P\right)^T \\ + \left(\bar{A}_i X_P + \bar{B}_{1i} W_{Pj}\right) & & \\ \bar{B}_2^T & -\gamma I & 0 \\ \bar{C}X_P & 0 & -\gamma I \end{bmatrix} + \begin{bmatrix} \left(\Delta\bar{A}_i X_P + \Delta\bar{B}_{1i} W_{Pj}\right)^T & 0 & 0 \\ + \left(\Delta\bar{A}_i X_P + \Delta\bar{B}_{1i} W_{Pj}\right) & & \\ 0 & 0 & 0 \\ 0 & 0 & 0 \end{bmatrix}$$

We have the following expansion from the definition of system (4.47)*:*

$$\begin{bmatrix} \left(\Delta\bar{A}_i X_P + \Delta\bar{B}_{1i} W_{Pj}\right)^T & 0 & 0 \\ + \left(\Delta\bar{A}_i X_P + \Delta\bar{B}_{1i} W_{Pj}\right) & & \\ 0 & 0 & 0 \\ 0 & 0 & 0 \end{bmatrix} = \begin{bmatrix} \left(HF\left(E_{1i} X_P + E_{2i} W_{Pj}\right)\right)^T & 0 & 0 \\ + HF\left(E_{1i} X_P + E_{2i} W_{Pj}\right) & & \\ 0 & 0 & 0 \\ 0 & 0 & 0 \end{bmatrix}$$
$$= \begin{bmatrix} H \\ 0 \\ 0 \end{bmatrix} F \begin{bmatrix} E_{1i} X_P + E_{2i} W_{Pj} & 0 & 0 \end{bmatrix} + \begin{bmatrix} \left(E_{1i} X_P + E_{2i} W_{Pj}\right)^T \\ 0 \\ 0 \end{bmatrix} F^T \begin{bmatrix} H^T & 0 & 0 \end{bmatrix}$$

Thus, the LMI condition (4.50) *can be written as:*

$$\begin{bmatrix} \left(\bar{A}_i X_P + \bar{B}_{1i} W_{Pj}\right)^T & \bar{B}_2 & \left(\bar{C}X_P\right)^T \\ + \left(\bar{A}_i X_P + \bar{B}_{1i} W_{Pj}\right) & & \\ \bar{B}_2^T & -\gamma I & 0 \\ \bar{C}X_P & 0 & -\gamma I \end{bmatrix} + \begin{bmatrix} H \\ 0 \\ 0 \end{bmatrix} F \begin{bmatrix} E_{1i} X_P + E_{2i} W_{Pj} & 0 & 0 \end{bmatrix}$$
$$+ \begin{bmatrix} \left(E_{1i} X_P + E_{2i} W_{Pj}\right)^T \\ 0 \\ 0 \end{bmatrix} F^T \begin{bmatrix} H^T & 0 & 0 \end{bmatrix} < 0 \tag{4.51}$$

Using lemma 4 (see Appendices), the condition (4.51) *holds iff there exists $\alpha > 0$ satisfying:*

$$\begin{bmatrix} \left(\bar{A}_i X_P + \bar{B}_{1i} W_{Pj}\right)^T & & \\ + \left(\bar{A}_i X_P + \bar{B}_{1i} W_{Pj}\right) + \alpha H H^T & \bar{B}_2 & \left(\bar{C}X_P\right)^T \\ \bar{B}_2^T & -\gamma I & 0 \\ \bar{C}X_P & 0 & -\gamma I \end{bmatrix}$$
$$+ \alpha^{-1} \begin{bmatrix} \left(E_{1i} X_P + E_{2i} W_{Pj}\right)^T \\ 0 \\ 0 \end{bmatrix} \begin{bmatrix} E_{1i} X_P + E_{2i} W_{Pj} & 0 & 0 \end{bmatrix} < 0$$

Using Schur complement lemma [12], [13], the theorem 7 is proven.

4.3.5 Augmented fuzzy system for wind energy system

Similar to subsection 4.1.3, but now we consider all of the interaction between 1 subsystem to other subsystem and neighborhood grid as one, i.e., the terminal voltages of the PMSGs. The nonlinear models of PMSG1 is as in (4.52) and of PMSG2 is as in (4.53), in per unit.

$$\begin{cases}
\frac{di_{11d}}{dt} = -\omega_{fb}\frac{R_{11f}i_{11d}}{L_{11f}} + \omega_{fb}\omega_f i_{11q} - \omega_{fb}\frac{v_{cf1d}}{L_{11f}} + \frac{1}{2}\omega_{fb}\frac{\beta_{11d}v_{DC1}}{L_{11f}} \\
\frac{di_{11q}}{dt} = -\omega_{fb}\frac{R_{11f}i_{11q}}{L_{11f}} - \omega_{fb}\omega_f i_{11d} - \omega_{fb}\frac{v_{cf1q}}{L_{11f}} + \frac{1}{2}\omega_{fb}\frac{\beta_{11q}v_{DC1}}{L_{11f}} \\
\frac{di_{21d}}{dt} = -\omega_{fb}\frac{R_{21f}i_{21d}}{L_{21f}} + \omega_{fb}\omega_f i_{21q} + \omega_{fb}\frac{v_{cf1d}}{L_{21f}} - \omega_{fb}\frac{1}{L_{21f}}\frac{1}{n_1}V_{r1d} \\
\frac{di_{21q}}{dt} = -\omega_{fb}\frac{R_{21f}i_{21q}}{L_{21f}} - \omega_{fb}\omega_f i_{21d} + \omega_{fb}\frac{v_{cf1q}}{L_{21f}} - \omega_{fb}\frac{1}{L_{21f}}\frac{1}{n_1}V_{r1q} \\
\frac{dv_{cf1d}}{dt} = \omega_{fb}\frac{i_{11d}}{C_{f1}} - \omega_{fb}\frac{i_{21d}}{C_{f1}} + \omega_{fb}\omega_f v_{cf1q} \\
\frac{dv_{cf1q}}{dt} = \omega_{fb}\frac{i_{11q}}{C_{f1}} - \omega_{fb}\frac{i_{21q}}{C_{f1}} - \omega_{fb}\omega_f v_{cf1d} \\
\frac{di_{s1d}}{dt} = -\omega_{fb}\frac{R_{s1}i_{s1d}}{L_{s1}} + \Omega_b p_1\Omega_1 i_{s1q} - \frac{1}{2}\omega_{fb}\frac{\beta_{s1d}v_{DC1}}{L_{s1}} \\
\frac{di_{s1q}}{dt} = -\omega_{fb}\frac{R_{s1}i_{s1q}}{L_{s1}} - \Omega_b p_1\Omega_1 i_{s1d} + \Omega_b\frac{p_1\Psi_{f1}\Omega_1}{L_{s1}} - \frac{1}{2}\omega_{fb}\frac{\beta_{s1q}v_{DC1}}{L_{s1}} \\
\frac{dv_{DC1}}{dt} = -\omega_{fb}\frac{3}{4C_1}\beta_{11d}i_{11d} - \omega_{fb}\frac{3}{4C_1}\beta_{11q}i_{11q} + \omega_{fb}\frac{3}{4C_1}\beta_{s1d}i_{s1d} \\
+\omega_{fb}\frac{3}{4C_1}\beta_{s1q}i_{s1q} \\
\frac{d\Omega_1}{dt} = \frac{1}{2H_1}\frac{P_{m1}}{\Omega_1} - \frac{1}{2H_1}\frac{\Omega_b}{\omega_{fb}}\frac{3}{2}p_1\Psi_{f1}i_{s1q} - \frac{1}{2H_1}D_{L1}\Omega_1; D_{L1} = \frac{\Omega_b^2 f_1}{S_b}
\end{cases} \tag{4.52}$$

$$\begin{cases}
\frac{di_{12d}}{dt} = -\omega_{fb}\frac{R_{12f}i_{12d}}{L_{12f}} + \omega_{fb}\omega_f i_{12q} - \omega_{fb}\frac{v_{cf2d}}{L_{12f}} + \frac{1}{2}\omega_{fb}\frac{\beta_{12d}v_{DC2}}{L_{12f}} \\
\frac{di_{12q}}{dt} = -\omega_{fb}\frac{R_{12f}i_{12q}}{L_{12f}} - \omega_{fb}\omega_f i_{12d} - \omega_{fb}\frac{v_{cf2q}}{L_{12f}} + \frac{1}{2}\omega_{fb}\frac{\beta_{12q}v_{DC2}}{L_{12f}} \\
\frac{di_{22d}}{dt} = -\omega_{fb}\frac{R_{22f}i_{22d}}{L_{22f}} + \omega_{fb}\omega_f i_{22q} + \omega_{fb}\frac{v_{cf2d}}{L_{22f}} - \omega_{fb}\frac{1}{L_{22f}}\frac{1}{n_2}V_{r2d} \\
\frac{di_{22q}}{dt} = -\omega_{fb}\frac{R_{22f}i_{22q}}{L_{22f}} - \omega_{fb}\omega_f i_{22d} + \omega_{fb}\frac{v_{cf2q}}{L_{22f}} - \omega_{fb}\frac{1}{L_{22f}}\frac{1}{n_2}V_{r2q} \\
\frac{dv_{cf2d}}{dt} = \omega_{fb}\frac{i_{12d}}{C_{f2}} - \omega_{fb}\frac{i_{22d}}{C_{f2}} + \omega_{fb}\omega_f v_{cf2q} \\
\frac{dv_{cf2q}}{dt} = \omega_{fb}\frac{i_{12q}}{C_{f2}} - \omega_{fb}\frac{i_{22q}}{C_{f2}} - \omega_{fb}\omega_f v_{cf2d} \\
\frac{di_{s2d}}{dt} = -\omega_{fb}\frac{R_{s2}i_{s2d}}{L_{s2}} + \Omega_b p_2\Omega_2 i_{s2q} - \frac{1}{2}\omega_{fb}\frac{\beta_{s2d}v_{DC2}}{L_{s2}} \\
\frac{di_{s2q}}{dt} = -\omega_{fb}\frac{R_{s2}i_{s2q}}{L_{s2}} - \Omega_b p_2\Omega_2 i_{s2d} + \Omega_b\frac{p_2\Psi_{f2}\Omega_2}{L_{s2}} - \frac{1}{2}\omega_{fb}\frac{\beta_{s2q}v_{DC2}}{L_{s2}} \\
\frac{dv_{DC2}}{dt} = -\omega_{fb}\frac{3}{4C_2}\beta_{12d}i_{12d} - \omega_{fb}\frac{3}{4C_2}\beta_{12q}i_{12q} + \omega_{fb}\frac{3}{4C_2}\beta_{s2d}i_{s2d} \\
+\omega_{fb}\frac{3}{4C_2}\beta_{s2q}i_{s2q} \\
\frac{d\Omega_2}{dt} = \frac{1}{2H_2}\frac{P_{m2}}{\Omega_2} - \frac{1}{2H_2}\frac{\Omega_b}{\omega_{fb}}\frac{3}{2}p_2\Psi_{f2}i_{s2q} - \frac{1}{2H_2}D_{L2}\Omega_2; D_{L2} = \frac{\Omega_b^2 f_2}{S_b}
\end{cases} \tag{4.53}$$

The terminal voltages of the two PMSGs, (V_{r1d}, V_{r1q}) for PMSG1 and (V_{r2d}, V_{r2q}) for PMSG2, depend on the interactions between the PMSGs and the AC grid.

The pitch angle dynamic, grid dynamic and system output are as in subsection 4.1.3.

The unified nonlinear sector fuzzy technique is now applied for the two subsystems (i.e., two PMSGs). The two subsystems can be expressed in a form of decentralized system:

$$\begin{array}{l}
(I)\begin{cases} \dot{X}_1 = A^1X_1 + B_1^1U_1 + B_2^1W_1 \\ Y_1 = C^1X_1 \end{cases} \\
(II)\begin{cases} \dot{X}_2 = A^2X_2 + B_1^2U_2 + B_2^2W_2 \\ Y_2 = C^2X_2 \end{cases}
\end{array} \tag{4.54}$$

where the output (Y_1, Y_2), states (X_1, X_2), input (U_1, U_2) and disturbance (W_1, W_2) are:

$$\begin{array}{l}
X_1 = [i_{11d}, i_{11q}, i_{21d}, i_{21q}, v_{cf1d}, v_{cf1q}, i_{s1d}, i_{s1q}, v_{DC1}, \Omega_1]^T \\
X_2 = [i_{12d}, i_{12q}, i_{22d}, i_{22q}, v_{cf2d}, v_{cf2q}, i_{s2d}, i_{s2q}, v_{DC2}, \Omega_2]^T \\
U_1 = [\beta_{11d}, \beta_{11q}, \beta_{21d}, \beta_{21q}]^T; U_2 = [\beta_{12d}, \beta_{12q}, \beta_{22d}, \beta_{22q}]^T \\
Y_1 = \left[\begin{array}{ccc} Q_1 & P_1 & v_{DC1} \end{array}\right]^T; Y_2 = \left[\begin{array}{ccc} Q_2 & P_2 & v_{DC2} \end{array}\right]^T \\
W_1 = \left[\begin{array}{ccc} V_{r1d} & V_{r1q} & T_{m1} \end{array}\right]^T; T_{m1} = \frac{P_{m1}}{\Omega_1} \\
W_2 = \left[\begin{array}{ccc} V_{r2d} & V_{r2q} & T_{m2} \end{array}\right]^T; T_{m2} = \frac{P_{m2}}{\Omega_2}
\end{array}$$

NS1	IS1	NS2	IS2	NS1	IS1	NS2	IS2
$\Omega_b p_1 \Omega_1$	Ω_1	$\Omega_b p_2 \Omega_2$	Ω_2	$-\Omega_b p_1 \Omega_1$	Ω_1	$-\Omega_b p_2 \Omega_2$	Ω_2
$\frac{\omega_{fb} v_{DC1}}{2L_{11f}}$	v_{DC1}	$\frac{\omega_{fb} v_{DC2}}{2L_{12f}}$	v_{DC2}	$\frac{-\omega_{fb} v_{DC1}}{2L_{s1}}$	v_{DC1}	$\frac{-\omega_{fb} v_{DC2}}{2L_{s2}}$	v_{DC2}
$\frac{-3\omega_{fb} i_{11d}}{4C_1}$	i_{11d}	$\frac{-3\omega_{fb} i_{12d}}{4C_2}$	i_{12d}	$\frac{-3\omega_{fb} i_{11q}}{4C_1}$	i_{11q}	$\frac{-3\omega_{fb} i_{12q}}{4C_2}$	i_{12q}
$\frac{3\omega_{fb} i_{s1d}}{4C_1}$	i_{s1d}	$\frac{3\omega_{fb} i_{s2d}}{4C_2}$	i_{s2d}	$\frac{3\omega_{fb} i_{s1q}}{4C_1}$	i_{s1q}	$\frac{3\omega_{fb} i_{s2q}}{4C_2}$	i_{s2q}
$-i_{11q}$	i_{11q}	$-i_{12q}$	i_{12q}	i_{11d}	i_{11d}	i_{12d}	i_{12d}
$\frac{3}{2}\frac{\Omega_b p \psi_{f1} i_{s1q}}{\omega_{fb}}$	i_{s1q}	$\frac{3}{2}\frac{\Omega_b p \psi_{f2} i_{s2q}}{\omega_{fb}}$	i_{s2q}				

Table 4.1: The nonlinear sectors (NS1, NS2) and involved states (IS1, IS2) of the two subsystems PMSGs

The time-varying nonlinear matrices of the two subsystems in (4.54) are as in (4.55) for PMSG1 (subsystem (I)) and in (4.56) for PMSG2 (subsystem (II)).

Next, the nonlinear sectors and involved states are defined based on the nonlinear matrices in (4.55) and in (4.56). These variables are as in table 4.1, including:

- Subsystem (I) (PMSG1) has 11 nonlinear sectors (NS1) and 6 involved states (IS1).

- Subsystem (II) (PMSG2) has 11 nonlinear sectors (NS2) and 6 involved states (IS2).

As in table 4.1, there should be $2^{11} = 2048$ fuzzy rules for each subsystem if using the conventional fuzzy technique as in [16]. However, with the unified nonlinear sectors as discussed and proven in subsection 4.3.2, there are only $2^6 = 64$ fuzzy rules for each subsystem.

$$
\begin{cases}
A^1 = \\
\begin{bmatrix}
\frac{-\omega_{fb}R_{11f}}{L_{11f}} & \omega_{fb}\omega_f & 0 & 0 & \frac{-\omega_{fb}}{L_{11f}} & 0 & 0 & 0 & 0 & 0 \\
-\omega_{fb}\omega_f & \frac{-\omega_{fb}R_{11f}}{L_{11f}} & 0 & 0 & 0 & \frac{-\omega_{fb}}{L_{11f}} & 0 & 0 & 0 & 0 \\
0 & 0 & \frac{-\omega_{fb}R_{21f}}{L_{21f}} & \omega_{fb}\omega_f & \frac{\omega_{fb}}{L_{21f}} & 0 & 0 & 0 & 0 & 0 \\
0 & 0 & -\omega_{fb}\omega_f & \frac{-\omega_{fb}R_{21f}}{L_{21f}} & 0 & \frac{\omega_{fb}}{L_{21f}} & 0 & 0 & 0 & 0 \\
\frac{\omega_{fb}}{C_{f1}} & 0 & \frac{-\omega_{fb}}{C_{f1}} & 0 & 0 & \omega_{fb}\omega_f & 0 & 0 & 0 & 0 \\
0 & \frac{\omega_{fb}}{C_{f1}} & 0 & \frac{-\omega_{fb}}{C_{f1}} & -\omega_{fb}\omega_f & 0 & 0 & 0 & 0 & 0 \\
0 & 0 & 0 & 0 & 0 & 0 & \frac{-\omega_{fb}R_{s1}}{L_{s1}} & \Omega_b p_1 \Omega_1 & 0 & 0 \\
0 & 0 & 0 & 0 & 0 & 0 & -\Omega_b p_1 \Omega_1 & \frac{-\omega_{fb}R_{s1}}{L_{s1}} & 0 & \frac{\Omega_b p_1 \Psi_{f1}}{L_{s1}} \\
0 & 0 & 0 & 0 & 0 & 0 & 0 & 0 & 0 & 0 \\
0 & 0 & 0 & 0 & 0 & 0 & \frac{-3\Omega_b p_1 \Psi_{f1}}{4H_1 \omega_{fb}} & 0 & 0 & \frac{-D_{L1}}{2H_1}
\end{bmatrix} \\
B_1^1 = \begin{bmatrix}
\frac{\omega_{fb}v_{DC1}}{2L_{11f}} & 0 & 0 & 0 \\
0 & \frac{\omega_{fb}v_{DC1}}{2L_{11f}} & 0 & 0 \\
0 & 0 & 0 & 0 \\
0 & 0 & 0 & 0 \\
0 & 0 & 0 & 0 \\
0 & 0 & 0 & 0 \\
0 & 0 & \frac{-\omega_{fb}v_{DC1}}{2L_{s1}} & 0 \\
0 & 0 & 0 & \frac{-\omega_{fb}v_{DC1}}{2L_{s1}} \\
\frac{-3\omega_{fb}i_{11d}}{4C_1} & \frac{-3\omega_{fb}i_{11q}}{4C_1} & \frac{3\omega_{fb}i_{s1d}}{4C_1} & \frac{3\omega_{fb}i_{s1q}}{4C_1} \\
0 & 0 & 0 & 0
\end{bmatrix} \quad
B_2^1 = \begin{bmatrix}
0 & 0 & 0 \\
0 & 0 & 0 \\
\frac{-\omega_{fb}}{L_{21f}n_1} & 0 & 0 \\
0 & \frac{-\omega_{fb}}{L_{21f}n_1} & 0 \\
0 & 0 & 0 \\
0 & 0 & 0 \\
0 & 0 & 0 \\
0 & 0 & 0 \\
0 & 0 & 0 \\
0 & 0 & \frac{1}{2H_1}
\end{bmatrix} \\
C^1 = \begin{bmatrix}
0 & 0 & 0 & 0 & -i_{11q} & i_{11d} & 0 & 0 & 0 & 0 \\
0 & 0 & 0 & 0 & 0 & 0 & 0 & \frac{3}{2}\frac{\Omega_b p \psi_{f1} i_{s1q}}{\omega_{fb}} & 0 & 0 \\
0 & 0 & 0 & 0 & 0 & 0 & 0 & 0 & 1 & 0
\end{bmatrix}
\end{cases}
\tag{4.55}
$$

$$
\begin{cases}
A^2 = \\
\begin{bmatrix}
\frac{-\omega_{fb}R_{12f}}{L_{12f}} & \omega_{fb}\omega_f & 0 & 0 & \frac{-\omega_{fb}}{L_{12f}} & 0 & 0 & 0 & 0 & 0 \\
-\omega_{fb}\omega_f & \frac{-\omega_{fb}R_{12f}}{L_{12f}} & 0 & 0 & 0 & \frac{-\omega_{fb}}{L_{12f}} & 0 & 0 & 0 & 0 \\
0 & 0 & \frac{-\omega_{fb}R_{22f}}{L_{22f}} & \omega_{fb}\omega_f & \frac{\omega_{fb}}{L_{22f}} & 0 & 0 & 0 & 0 & 0 \\
0 & 0 & -\omega_{fb}\omega_f & \frac{-\omega_{fb}R_{22f}}{L_{22f}} & 0 & \frac{\omega_{fb}}{L_{22f}} & 0 & 0 & 0 & 0 \\
\frac{\omega_{fb}}{C_{f2}} & 0 & \frac{-\omega_{fb}}{C_{f2}} & 0 & 0 & \omega_{fb}\omega_f & 0 & 0 & 0 & 0 \\
0 & \frac{\omega_{fb}}{C_{f2}} & 0 & \frac{-\omega_{fb}}{C_{f2}} & -\omega_{fb}\omega_f & 0 & 0 & 0 & 0 & 0 \\
0 & 0 & 0 & 0 & 0 & 0 & \frac{-\omega_{fb}R_{s2}}{L_{s2}} & \Omega_b p_2 \Omega_2 & 0 & 0 \\
0 & 0 & 0 & 0 & 0 & 0 & -\Omega_b p_2 \Omega_2 & \frac{-\omega_{fb}R_{s2}}{L_{s2}} & 0 & \frac{\Omega_b p_2 \Psi_{f2}}{L_{s2}} \\
0 & 0 & 0 & 0 & 0 & 0 & 0 & 0 & 0 & 0 \\
0 & 0 & 0 & 0 & 0 & 0 & \frac{-3\Omega_b p_2 \Psi_{f2}}{4H_2\omega_{fb}} & 0 & 0 & \frac{-D_{L2}}{2H_2}
\end{bmatrix} \\
B_1^2 = \begin{bmatrix}
\frac{\omega_{fb}v_{DC2}}{2L_{12f}} & 0 & 0 & 0 \\
0 & \frac{\omega_{fb}v_{DC2}}{2L_{12f}} & 0 & 0 \\
0 & 0 & 0 & 0 \\
0 & 0 & 0 & 0 \\
0 & 0 & 0 & 0 \\
0 & 0 & 0 & 0 \\
0 & 0 & \frac{-\omega_{fb}v_{DC2}}{2L_{s2}} & 0 \\
0 & 0 & 0 & \frac{-\omega_{fb}v_{DC2}}{2L_{s2}} \\
\frac{-3\omega_{fb}i_{12d}}{4C_2} & \frac{-3\omega_{fb}i_{12q}}{4C_2} & \frac{3\omega_{fb}i_{s2d}}{4C_2} & \frac{3\omega_{fb}i_{s2q}}{4C_2} \\
0 & 0 & 0 & 0
\end{bmatrix}
B_2^2 = \begin{bmatrix}
0 & 0 & 0 \\
0 & 0 & 0 \\
\frac{-\omega_{fb}}{L_{22f}n_2} & 0 & 0 \\
0 & \frac{-\omega_{fb}}{L_{22f}n_2} & 0 \\
0 & 0 & 0 \\
0 & 0 & 0 \\
0 & 0 & 0 \\
0 & 0 & 0 \\
0 & 0 & 0 \\
0 & 0 & \frac{1}{2H_2}
\end{bmatrix} \\
C^1 = \begin{bmatrix}
0 & 0 & 0 & 0 & -i_{12q} & i_{12d} & 0 & 0 & 0 & 0 \\
0 & 0 & 0 & 0 & 0 & 0 & 0 & \frac{3}{2}\frac{\Omega_b p \psi_{f2} i_{s2q}}{\omega_{fb}} & 0 & 0 \\
0 & 0 & 0 & 0 & 0 & 0 & 0 & 0 & 1 & 0
\end{bmatrix}
\end{cases}
\tag{4.56}
$$

Now, for each subsystem, choose the augmented state $\bar{X}$ and output $\bar{Y}$ as:

$$
\bar{X} = \begin{bmatrix} \dot{X} \\ e \end{bmatrix}; \bar{Y} = e = Y_{ref} - CX \tag{4.57}
$$

The augmented system is now:

$$
\begin{cases} \dot{\bar{X}} = \bar{A}\bar{X} + \bar{B}_1\bar{U} + \bar{B}_2\bar{W} \\ \bar{Y} = \bar{C}\bar{X} \end{cases} \tag{4.58}
$$

where input $\bar{U} = \dot{U}$, disturbance $\bar{W} = \dot{W}$, and the state-space matrices are:

$$
\begin{gathered}
\bar{A} = \sum_{i=1}^{r} h_i(z)\,\bar{A}_i; \bar{A}_i = \begin{bmatrix} A_i & 0 \\ -C & 0 \end{bmatrix}; \bar{B}_2 = \begin{bmatrix} B_2 \\ 0 \end{bmatrix}; \\
\bar{B}_1 = \sum_{i=1}^{r} h_i(z)\,\bar{B}_{1i}; \bar{B}_{1i} = \begin{bmatrix} B_{1i} \\ 0 \end{bmatrix}; \bar{C} = \begin{bmatrix} 0 & I \end{bmatrix}
\end{gathered}
$$

with the number of fuzzy rule is $r = 2^p$, p is the number of involved states ($p = 3$ for each subsystem). The fuzzy controller is now:

$$
\bar{U} = \dot{U} = \bar{K}_0\bar{X} \Rightarrow U = \bar{K}_0 \begin{bmatrix} X \\ \int e dt \end{bmatrix} \tag{4.59}
$$

The controller gain $\bar{K}_0$ is a dynamic gain as in (4.29), and depends on the consideration of parameter uncertainties, the local gains $\bar{K}_j$ can be generated by Theorem 6 or Theorem 7.

4.3.6 Simulations and results

In this subsection, the fuzzy control approaches are tested and validated using the IEEE 14-bus benchmark in subsection 4.1. The test scenarios for GAS are as in Fig. 4.31, and the operating point for all test scenarios corresponds to the generated active power $P_e = 0.6527pu$ for both PMSGs. The results are also compared with classical cascade vector control to prove the effectiveness of fuzzy control approaches. In total, six scenarios were investigated:

- Scenario 0 - Wind speed variation with a wind profile: the wind speed profile in the site of PMSG1 is given in Fig. 4.32 (the wind speed is varied from 8 m/s (28.8 Km/h) to 12.5 m/s (45 Km/h)). The output active power is regulated at P_{del} deload at 10%, as shown in Fig. 4.33. One can notice a nominal/smooth step reference tracking with time constant at around 3s.

- Scenario 1 - Local services: Step responses on reference control signals will be used to assess DC voltage, active power (FCR), and reactive power control (VSP). As shown in Figs. 4.34, 4.35 and 4.36 for PMSG1 active power, reactive power and DC voltage respectively, the proposed control strategy provides a smooth transient for a step response, with time constants between 3s-4s. The overshoot/undershoot is relatively small, under 10% for DC voltage, under 5% for active power and insignificantly small for reactive power. The same trend is observed at the PMSG2, as shown in Figs. 4.37, 4.38 and 4.39.

- Scenario 2 - FRT and CCT services: A three-phase metallic short-circuit is applied at bus 6 in the IEEE 14-bus benchmark (Fig. 4.31), which is close to PMSG2, in order to assess the FRT and CCT capacity of the proposed fuzzy control ($H_{inf}NFDC$). The short-circuit begins at t = 30 s, and its duration is progressively increased in order to determine the CCT. The efficiency of the proposed control will then be further clarified by comparing the findings to those of classical vector control. The FRT for proposed control is around 900ms, and for classical vector control is around 200ms. The behavior of the current in d frame, active power, generator speed and terminal voltage are shown in Figs. 4.40, 4.42, 4.44, 4.46 for the proposed control. For classical vector control, the responses are in Figs. 4.41, 4.43, 4.45, 4.47. Obviously, the proposed control provides a better transient, with a lower overshoot/undershoot of active power and generator speed.

- Scenario 3 - Frequency services (FCR): At t = 30s, the load of bus 1 is increased by 2MW. As shown in Figs. 4.48 and 4.50, the proposed control helps to increase the amount of active powers at both of PMSG1 and PMSG2, which in turn alleviate the frequency deviation and inertia response (i.e., RoCoF), as shown in Figs. 4.52 and 4.53, respectively. In addition, due to the change on output active power, the generator speeds are changed accordingly, as shown in Figs. 4.49 and 4.51 for PMSG1 and PMSG2, respectively.

- Scenario 4 - Voltage service (VSP): Grid voltages at the terminals of the two PMSGs will be lowered to test the voltage service and determine whether the proposed control can support AC voltage. The same scenario used for the FRT test is carried out; it begins at time t = 30 and ends at t = 30.1s. Due to the short-circuit, the terminal voltages of the two PMSGs fall as shown in Figs. 4.56 and 4.59, the proposed coordinated control helps to increase reactive powers of the two machine to a higher level compared to those of classical vector control, as demonstrated in Figs. 4.55 and 4.58. At the same time, thanks to the coordination effect, the active powers using proposed control are less varying compared to the results of classical vector control, clearly shown in Figs. 4.54 and 4.57.

- Scenario 5 - Active power RAMP rate control (FCR): The sources of power (i.e., wind speed) will be varied in order to test the RAMP rate service and the power RAMP rate control. In the first test, the wind speed in PMSG1 is reduced from 12 m/s to 8 m/s at t = 30s, and the reduced source of power is maintained throughout the test. Shown in Fig. 4.60, thanks to the RAMP rate limitation, the active power only gradually falls in contrast to sudden drop in case without the rate limitation. As a result, shown in Figs. 4.61 and 4.62 for frequency and RoCoF behavior, with RAMP rate control, the frequency deviation is 4 times smaller and the RoCoF variation is 6 times smaller that the ones obtained without RAMP rate control. In the second test, the wind speed is reduced by the same amount (in PMSG1, from 12 m/s to 8 m/s), but the event lasted just one second before returning to its regular value of 12 m/s. PMSG2 is not a subject to these two tests. Similar to the first test, the active power with RAMP rate control is only decreased

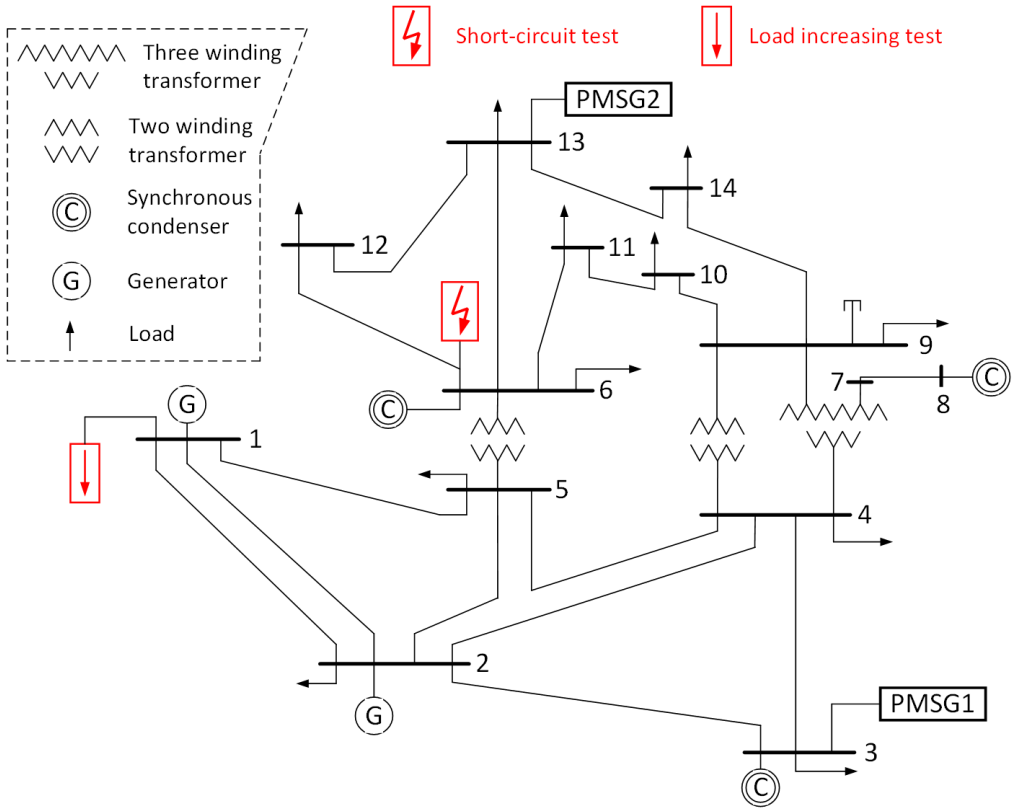

Figure 4.31: The modified IEEE 14 bus test case with 2 PMSGs for fuzzy control validation

from 0.65pu to 0.52pu, with without RAMP rate, it falls to nearly 0.2pu, shown in Fig. 4.63. The resulting frequency and RoCoF behavior are the same, as observed in Figs. 4.64 and 4.65.

- Scenario 6 - Robustness: This test compares the performance of the proposed nonlinear fuzzy distributed control's robust control version ($H_{inf}RNFDC$) and uncertainty-free control version ($H_{inf}NFDC$) in the presence of uncertainties. For that, a 40% increase in the parameters of the two synchronous generator (in the values of R_s1, R_s2, and L_s1 and L_s2) has been considered. As shown from Fig. 4.66 to Fig. 4.68, with robust control version, the overshoot/undershoot are clearly smaller, around 25%, 15% and 10% for active power, reactive power and DC voltage of PMSG1, respectively. The same trend can be observed for PMSG2 outputs, as shown in Figs. 4.69, 4.70 and 4.71.

4.3.7 Conclusion

For a PMSG-based wind energy system, coordinated robust nonlinear fuzzy control approaches were established and validated. The controllers are formulated using LMI technique, reference tracking internal model principle and robust fuzzy nonlinear sector method. The proposed methods are implemented in MATLAB and evaluated using IEEE 14-bus benchmark using Simscape and tested in various simulation scenarios.

These tests showed a better robustness and performance compared to classical vector control. These controls can be generalized for any DRES. Potentially, the centralized approach using fuzzy technique for wind energy system can be scaled up for a group of DRES, and each system can act as plug-and-play generation plant.

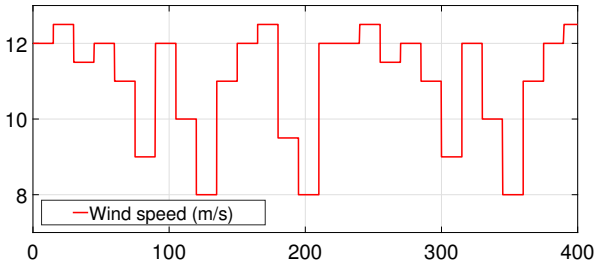

Figure 4.32: Wind speed profile in 400 second at PMSG1 site

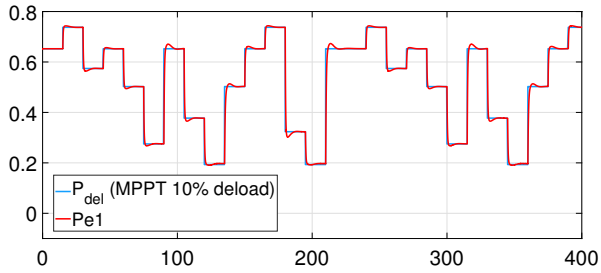

Figure 4.33: Output active power Pe1 of PMSG1 with the wind speed profile in Fig. 4.32

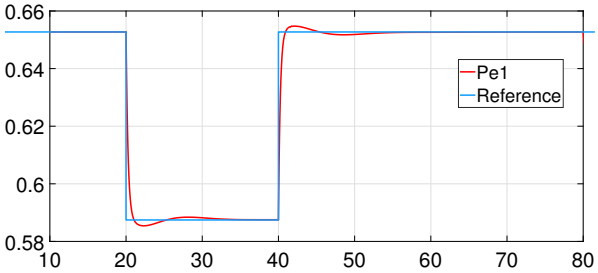

Figure 4.34: Step response for active power (p.u.) of PMSG1

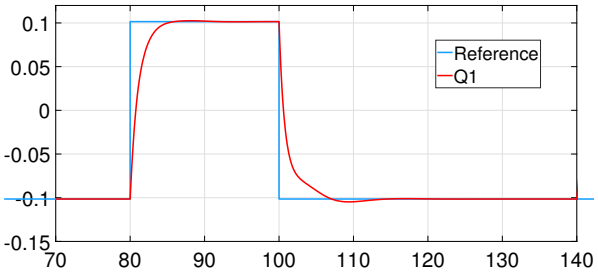

Figure 4.35: Step response for reactive power (p.u.) of PMSG1

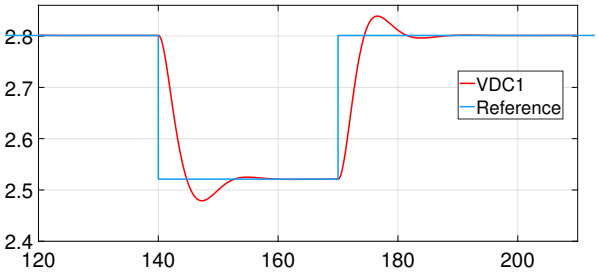

Figure 4.36: Step response for DC voltage (p.u.) of PMSG1

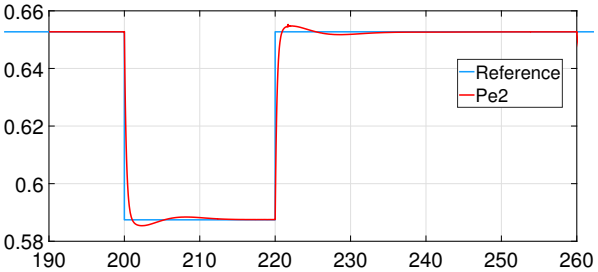

Figure 4.37: Step response for active power (p.u.) of PMSG2

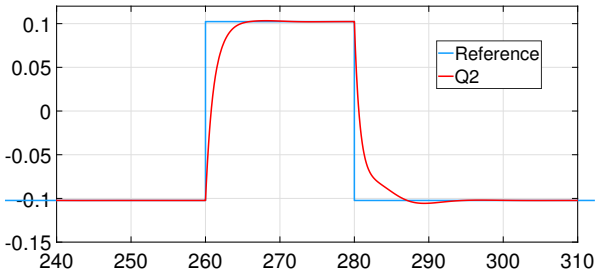

Figure 4.38: Step response for reactive power (p.u.) of PMSG2

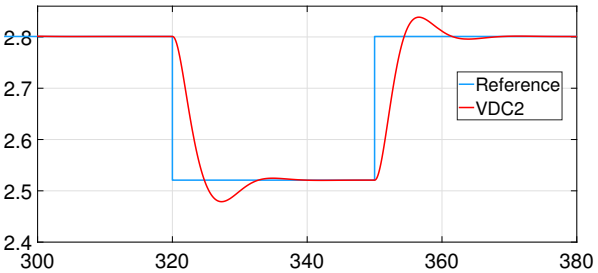

Figure 4.39: Step response for DC voltage (p.u.) of PMSG2

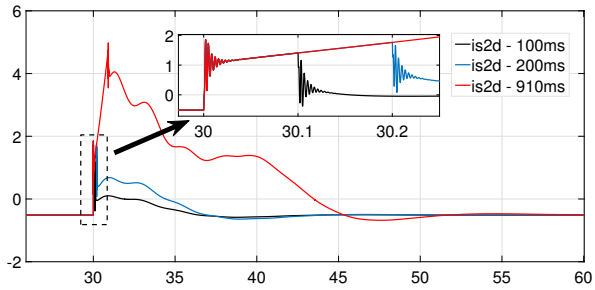

Figure 4.40: FRT - PMSG2 current i_{s2d} (p.u.) (DCBC)

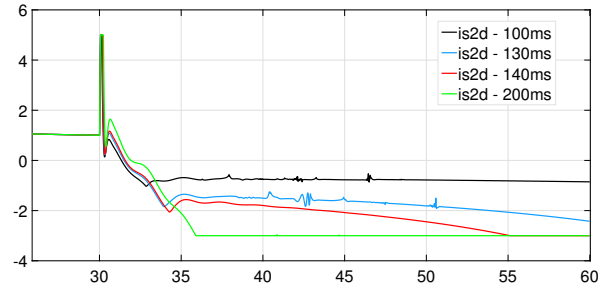

Figure 4.41: FRT - PMSG2 current i_{s2d} (p.u.) (vector control)

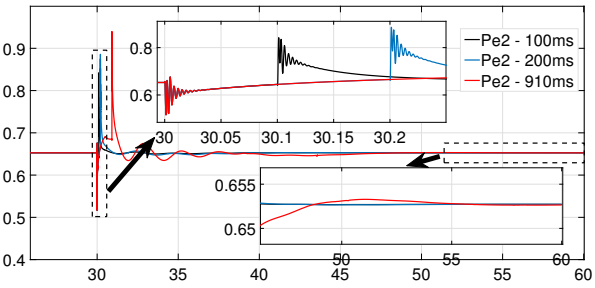

Figure 4.42: FRT - PMSG2 active power (p.u.) (DCBC)

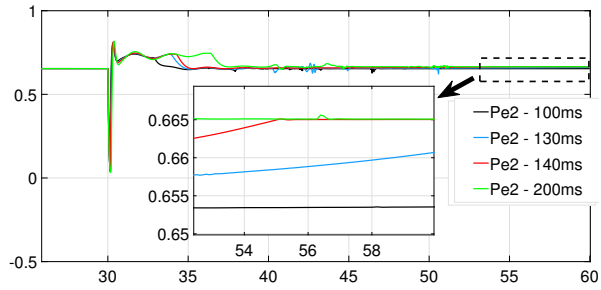

Figure 4.43: FRT - PMSG2 active power (p.u.) (vector control)

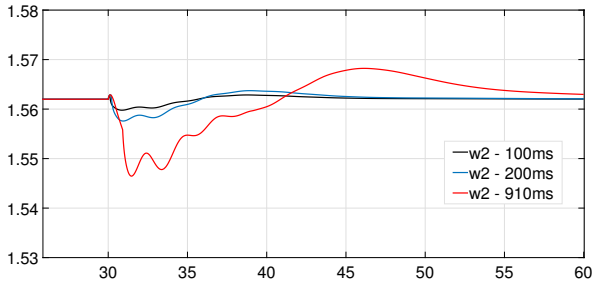

Figure 4.44: FRT - PMSG2 generator speed (p.u.) (DCBC)

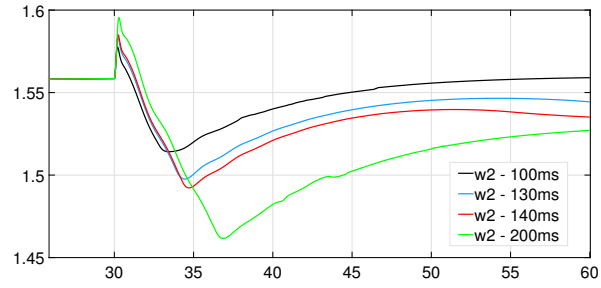

Figure 4.45: FRT - PMSG2 generator speed (p.u.) (vector control)

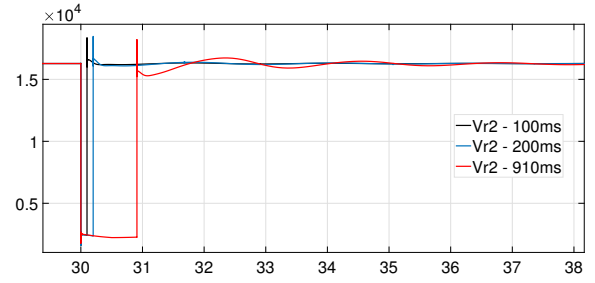

Figure 4.46: FRT - PMSG2 terminal voltage (V) (DCBC)

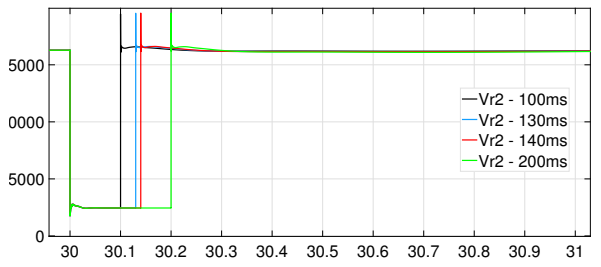

Figure 4.47: FRT - PMSG2 terminal voltage (V) (vector control)

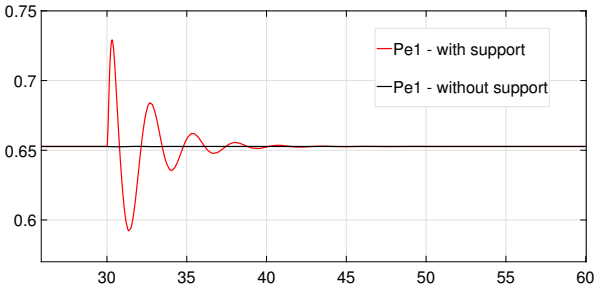

Figure 4.48: Frequency services - PMSG1 active power (p.u.)

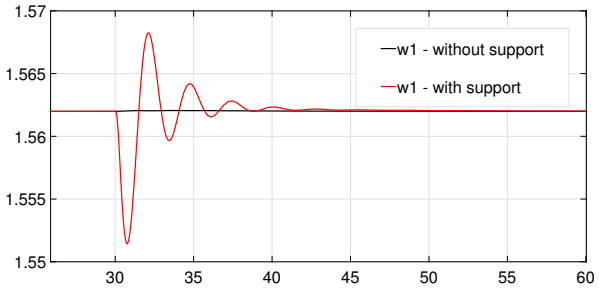

Figure 4.49: Frequency services - PMSG1 generator speed (p.u.)

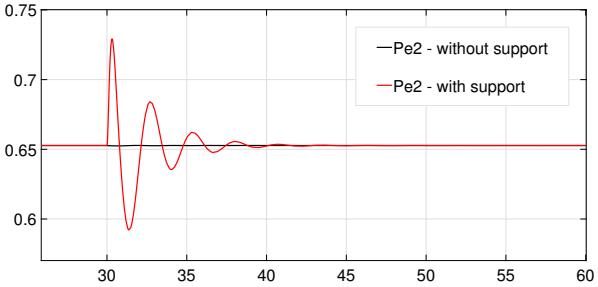

Figure 4.50: Frequency services - PMSG2 active power (p.u.)

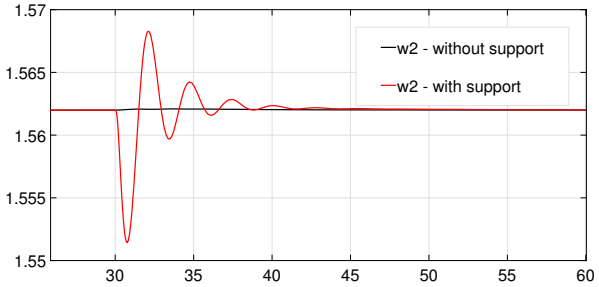

Figure 4.51: Frequency services - PMSG2 generator speed (p.u.)

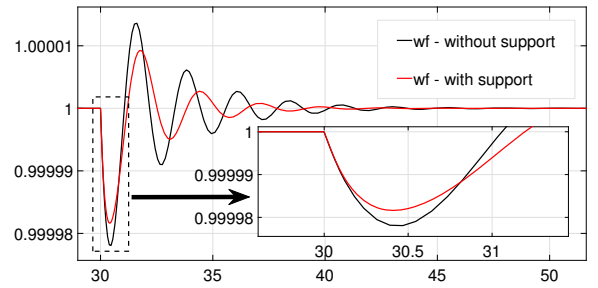

Figure 4.52: Frequency services - grid frequency (p.u.)

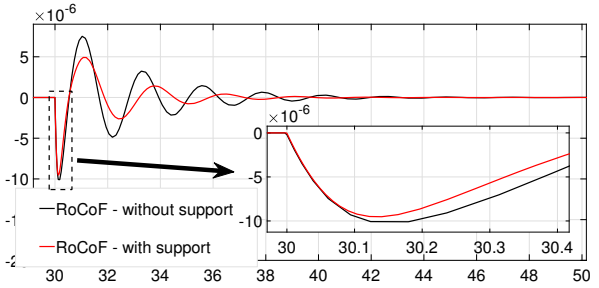

Figure 4.53: Frequency services - grid RoCoF (p.u.)

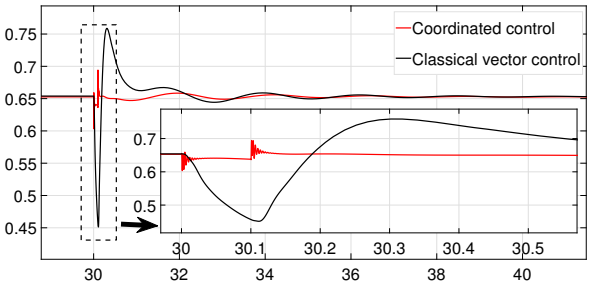

Figure 4.54: Q/V service - Active power (p.u.) of PMSG1

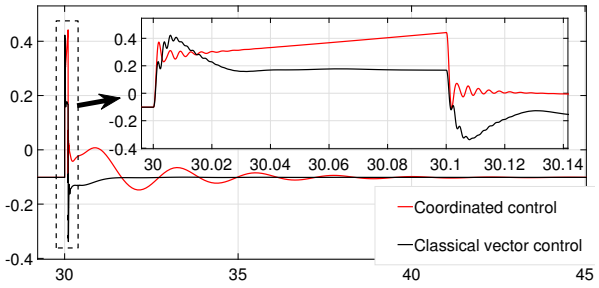

Figure 4.55: Q/V service - Reactive power (p.u.) of PMSG1

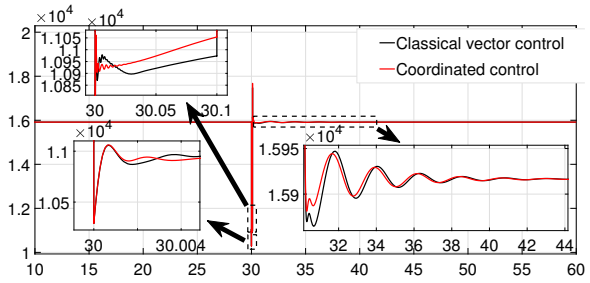

Figure 4.56: Q/V service - Terminal voltage (V) of PMSG1

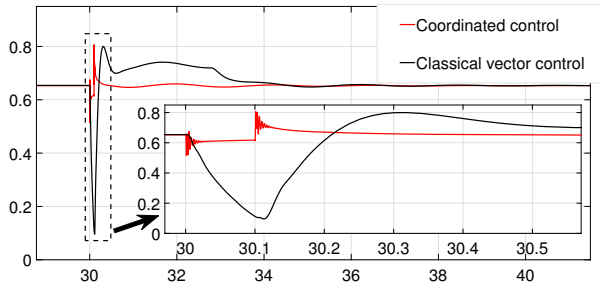

Figure 4.57: Q/V service - Active power (p.u.) of PMSG2

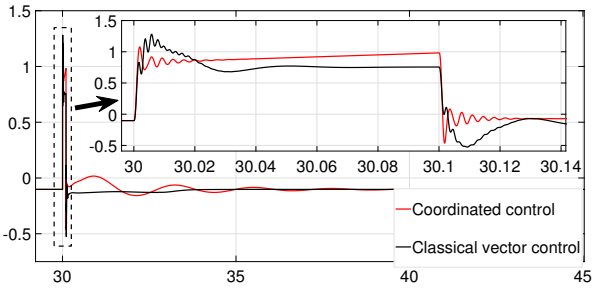

Figure 4.58: Q/V service - Reactive power (p.u.) of PMSG2

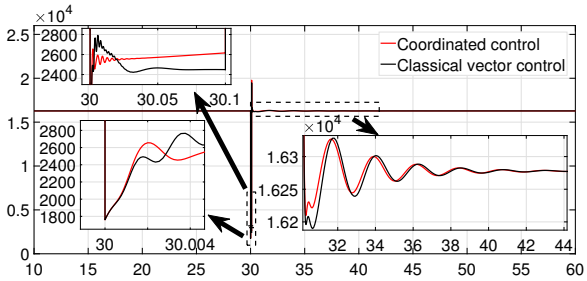

Figure 4.59: Q/V service - Terminal voltage (V) of PMSG2

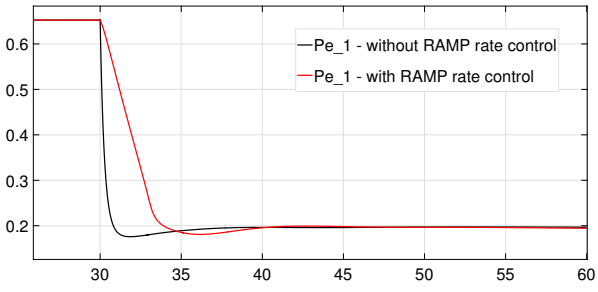

Figure 4.60: RAMP rate - test 1 - PMSG1 active power (p.u.)

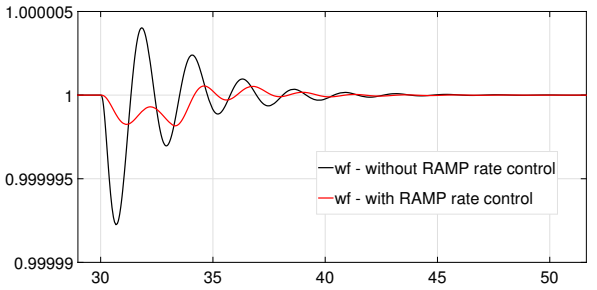

Figure 4.61: RAMP rate - test 1 - Grid frequency (p.u.)

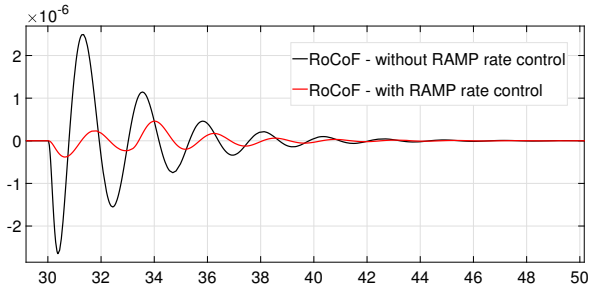

Figure 4.62: RAMP rate - test 1 - Grid RoCoF (p.u.)

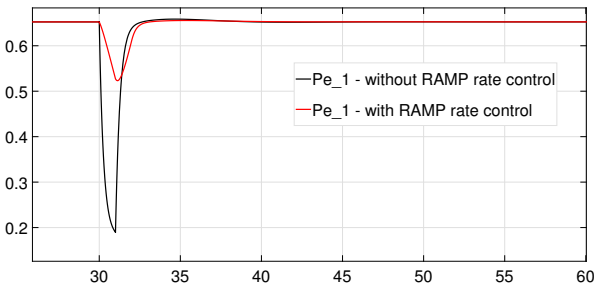

Figure 4.63: RAMP rate - test 2 - PMSG1 active power (p.u.)

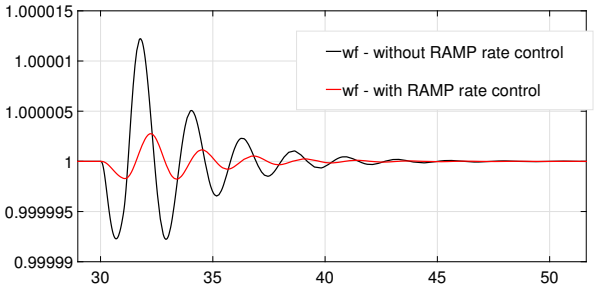

Figure 4.64: RAMP rate - test 2 - Grid frequency (p.u.)

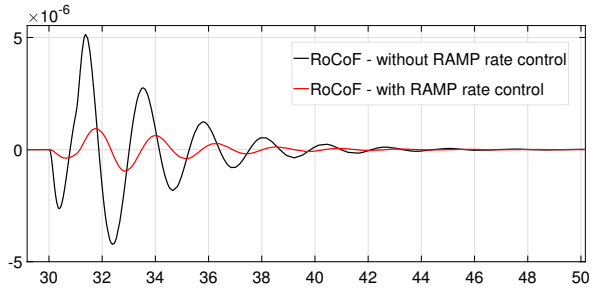

Figure 4.65: RAMP rate - test 2 - Grid RoCoF (p.u.)

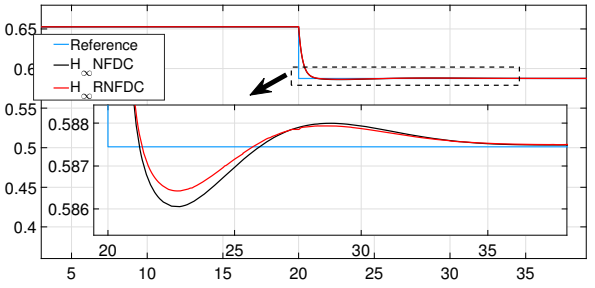

Figure 4.66: Scenario 6 - PMSG1 active power (p.u.)

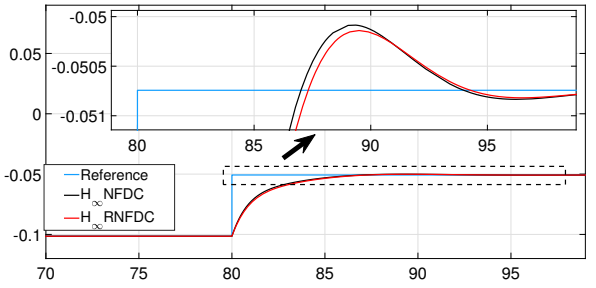

Figure 4.67: Scenario 6 - PMSG1 reactive power (p.u.)

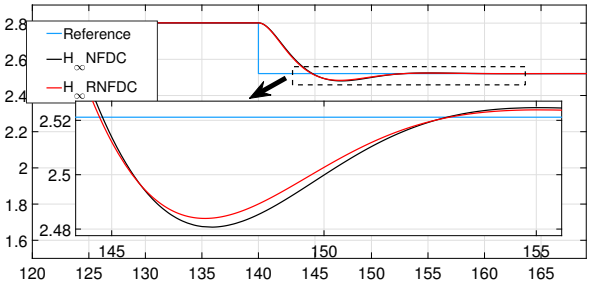

Figure 4.68: Scenario 6 - PMSG1 DC voltage (p.u.)

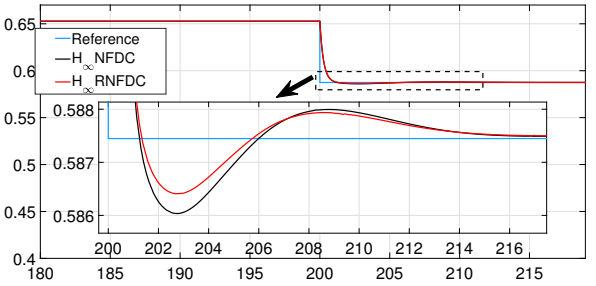

Figure 4.69: Scenario 6 - PMSG2 active power (p.u.)

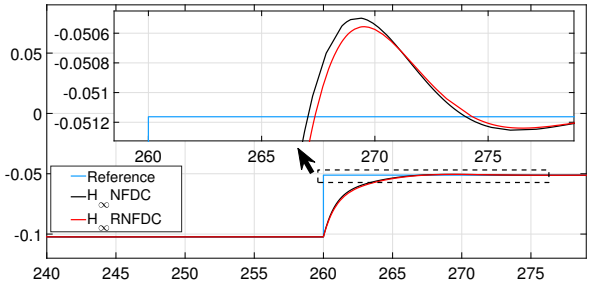

Figure 4.70: Scenario 6 - PMSG2 reactive power (p.u.)

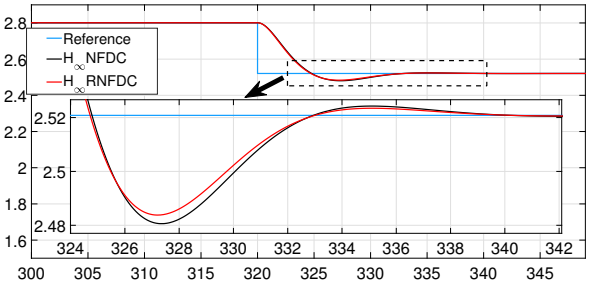

Figure 4.71: Scenario 6 - PMSG2 DC voltage (p.u.)

Bibliography

[1] "IEEE 14 Bus Power Flow Test Case", https://electricgrids.engr.tamu.edu/electric-grid-test-cases/ieee-14-bus-system/.

[2] Kamal, E., & Marinescu, B. (2019, September). Converter Nonlinear Fuzzy Control of PMSG-Based for Wind Energy System in Network Context. In 2019 IEEE PES Innovative Smart Grid Technologies Europe (ISGT-Europe) (pp. 1-5). IEEE.

[3] Bacha, S., Munteanu, I., & Bratcu, A. I. (2014). Power electronic converters modeling and control. Advanced textbooks in control and signal processing, 454, 454.

[4] Van, T. L., Nguyen, T. H., & Lee, D. C. (2015). Advanced pitch angle control based on fuzzy logic for variable-speed wind turbine systems. IEEE Transactions on Energy Conversion, 30(2), 578-587.

[5] Ackermann, T. (Ed.). (2012). Wind power in power systems. John Wiley & Sons.

[6] Marinescu, B., Kamal, E., & Ngo, H. T. (2021). A System Model-Based Approach for the Control of Power Park Modules for Grid Voltage and Frequency Services. arXiv preprint arXiv:2107.02000.

[7] Marinescu, B., Gomis-Bellmunt, O., Dörfler, F., Schulte, H., & Sigrist, L. (2021). Dynamic virtual power plant: A new concept for grid integration of renewable energy sources. arXiv preprint arXiv:2108.00153.

[8] Ngo, H. T., Kamal, E., Marinescu, B., & Xavier, F. (2020, November). Robust H_∞ Decentralized Control Design for HVDC Link Embedded in a Large-scale AC Grid. In 2020 Electrical Power and Energy Conference.

[9] Liserre, M., Blaabjerg, F., & Hansen, S. (2005). Design and control of an LCL-filter-based three-phase active rectifier. IEEE Transactions on industry applications, 41(5), 1281-1291.

[10] Fernández-Guillamón, A., Gómez-Lázaro, E., Muljadi, E., & Molina-García, Á. (2019). Power systems with high renewable energy sources: A review of inertia and frequency control strategies over time. Renewable and Sustainable Energy Reviews, 115, 109369.

[11] Jahangiri, P., & Aliprantis, D. C. (2013). Distributed Volt/VAr control by PV inverters. IEEE Transactions on power systems, 28(3), 3429-3439.

[12] Duan, G. R., & Yu, H. H. (2013). LMIs in control systems: analysis, design and applications. CRC press.

[13] Boyd, S., El Ghaoui, L., Feron, E., & Balakrishnan, V. (1994). Linear matrix inequalities in system and control theory. Society for industrial and applied mathematics.

[14] ApS, M. (2019). Mosek optimization toolbox for matlab. User's Guide and Reference Manual, Version, 4.

[15] Jahangiri, P., & Aliprantis, D. C. (2013). Distributed Volt/VAr control by PV inverters. IEEE Transactions on power systems, 28(3), 3429-3439.

[16] Tanaka, K., & Wang, H. O. (2004). Fuzzy control systems design and analysis: a linear matrix inequality approach. John Wiley & Sons.

Chapter 5

STATCOM application with EMT simulation

In this chapter EMT implementation and simulation is done for the proposed advanced MIMO control to demonstrate the applicability of new approaches for industrial-level application. A grid converter run in STATCOM mode is considered.

The power system objectives of the considered STATCOM system is to provide sufficient reactive power to the Point of Common Coupling (PCC) (i.e., an amount equal to some specific grid loads at PCC) in order to regulate the grid voltage. At the same time, the STATCOM regulates its output active power at zero to avoid frequency distortion. The validation tests are done for both of conventional cascade control and proposed advanced LMI-based H_∞ control to provides a practical look at their benefits and drawbacks.

The content of this chapter includes: modelling of VSC grid-connected converter in abc frame and in dq frame, the control strategies of VSC grid-connected converter (including classical vector control and advanced MIMO control), and finally the simulation validation (EMT simulation) and comparison between the two control methodologies.

5.1 EMT model of VSC grid-connected converter

In order to connect AC and DC systems using high-power electrical components like IGBTs, VSCs are used. The ability of VSCs to self-commutate, or to generate AC voltages without the aid of an AC system, makes it possible for them to control active and reactive power independently and quickly, as well as to provide black start services. As a result, VSC is quickly being used in transmission systems ([1], for example, HVDC and Flexible AC Transmission System (FACTS)) converter-based generators [2] (e.g., wind energy systems).

Particularly, extensive research is done on the popular VSC-based FACTS applications like STATCOM [3], which are preferred to outdated technologies like Static Var Compensator (SVC). Thyristor-Controlled Reactor (TCR) and thyristor-Switched Capacitor (TSC) are used by a VSC to contribute AC voltage service through the dynamic reactive power management of Var absorption and production, respectively. The same outcome is achieved by a STATCOM employing a SVC to synthesize a voltage waveform with changing magnitude with respect to the system voltage. Additionally, Pulse Width Modulation (PWM) is used to control STATCOM, which enables faster reaction and significantly enhances power quality [3].

Numerous studies have been done recently to improve the power quality supplied by VSCs. These studies include cascade control (also known as classical vector control [4]) and advanced MIMO control [5], [6]. For the two-loop cascade vector control strategy, feed-forward decoupling terms are used to separate the two d-axis current and q-axis current [4]. This is less effective than more sophisticated MIMO control (e.g., Linear–Quadratic Regulator (LQR) control [7] or optimal H_∞ disturbance rejection methods [6]). The new MIMO control methodology offers significantly higher performance and stability margin, as demonstrated in these studies (for example, in our prior study [5]).

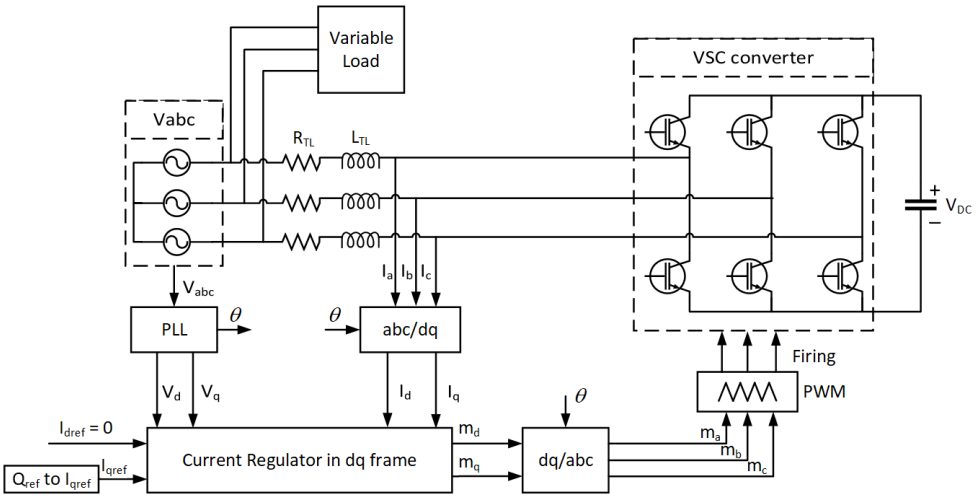

Figure 5.1: VSC grid-connected reactive power control - Simple STATCOM

The EMT model of the VSC grid-connected converter for STATCOM application is presented, as detailed in this section. A 3-phase 2-level VSC is utilized in this application to compensate for reactive power in the load. The EMT STATCOM model will be modeled in two versions, without and with an LCL filter.

5.1.1 Simple STATCOM without LCL filter

Fig. 5.1 depicts the VSC grid-connected converter model, a simple version of STATCOM without an LCL filter. It is made up of a three-phase two-level VSC that is linked to the grid V_{abc} through a transmission line (a R-L line equivalence is used). The PCC is also coupled to a changeable load. The PLL generates the phase angle θ of grid voltage, which is then utilised to derive dq frame currents I_{dq} from three-phase currents I_{abc}. The phase angle θ is also utilised to convert the control signal in the dq frame m_{dq} to the control signal in the abc frame m_{abc}, which provides the firing signal that controls the converter.

For this simple STATCOM model, the LCL filter is omitted to reduce the complexity of the system in terms of control designing and testing. However, for this EMT, without the LCL filter, the output voltage will have high Total Harmonic Distortion (THD), which will require a strong grid connection point at PCC and/or active filter. The next subsection will provide a full model of STATCOM with suitable LCL filter.

5.1.2 Full STATCOM with LCL filter

The STATCOM model in subsection 5.1.1 is a simple version since it doesnot contain the LCL filter, which is an important part of any grid-connected VSC converter. Now, consider the STATCOM in Fig. 5.1 with a full LCL filter as in Fig. 5.2. Apart from the LCL filter, the rest of the system is totally the same as in the simple version of STATCOM. The LCL filter is a 3-phase filter, each phase consists of 2 series inductors ($L1$ and $L2$) and a ground-connected capacitor C_f. The two inductors also have small parasited resistors $R1$ and $R2$, and the capacitor has a passive damping resistor R_f to damp the high oscillation mode generated by the LCL filter itself.

Another extended version of STATCOM is also investigated here. As seen in Fig. 5.3, the VSC converter in STATCOM model is now a three-phase three-level VSC instead of three-phase two-level VSC. This Modular Multilevel Converter (MMC) Neutral Point Clamped (NPC) topology has 1 more level of voltage, thus reduce the THD of the output terminal voltage. This characteristic is demonstrated in the simulation validation test.

5.1.3 System parameters for the two EMT STATCOM models

Table 5.1 is the data for the two STATCOM models, including the grid voltage V_{grid}, DC voltage V_{DC}, the converter characteristics and the value of the LCL filter. The VSC converter is running with fundamental frequency $50Hz$

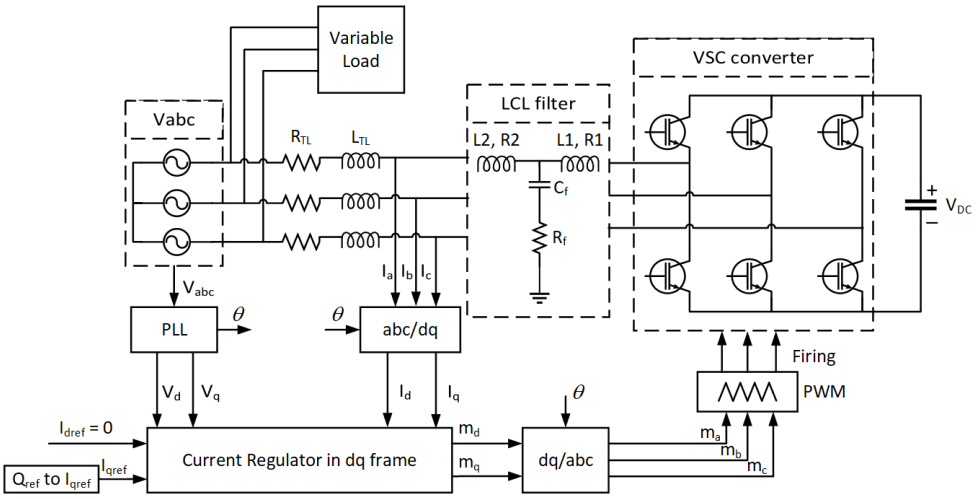

Figure 5.2: VSC grid-connected reactive power control with LCL filter - STATCOM

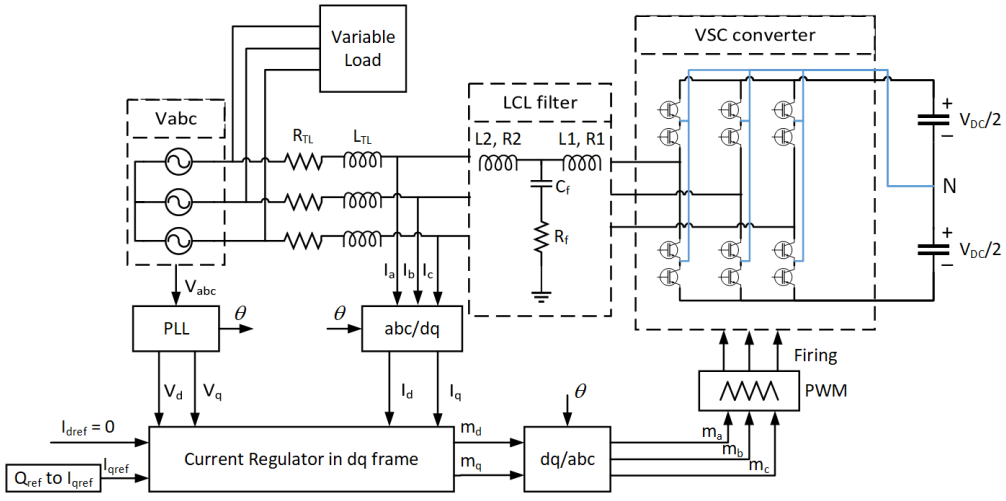

Figure 5.3: Three-level VSC grid-connected reactive power control with LCL filter - STATCOM

Variable	Detailed information	value	unit
V_{grid}	RMS phase-phase voltage of AC grid	400	V
V_{DC}	DC voltage value of VSC	1000	V
f_s	Switching frequency of VSC	5000	Hz
f	Voltage frequency of the AC system	50	Hz
T_s	Sample time for EMT simulation	10	μs
$L1$	Converter-side inductor of LCL filter	$3.1831e^{-4}$	H
$R1$	Converter-side resistor of LCL filter	0.1	Ω
$L2$	Grid-side inductor of LCL filter	$6.1115e^{-5}$	H
$R2$	Grid-side resistor of LCL filter	0.0038	Ω
C_f	Capacitor of LCL filter	$9.9472e^{-5}$	F
R_f	Damping resistor of LCL filter	0.2393	Ω
R_{TL}	R value of transmission line	0.02	Ω
L_{TL}	L value of transmission line	0.01	H

Table 5.1: The data for EMT VSC grid-connected model in Simscape

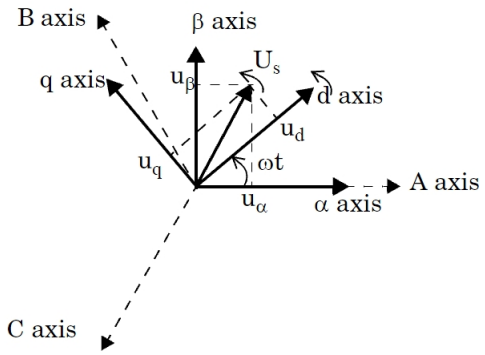

Figure 5.4: abc and dq frame in Park transformation

and switching frequency at 5000Hz, i.e., the time constant is $1/5000s = 200\mu s$. The EMT Simscape model is running with discrete mode with sample time at 10μs.

5.1.4 System modelling in abc and dq frames and control objectives

Naturally, the desired reference of VSC terminal voltages V_{VSCabc} in abc frame are in sine-wave form, i.e., the reference are two-order transfer function $L\{\sin(at)\} = \frac{a}{s^2+a^2}$. According to the internal model principle [9], the controller has to contain two-order dynamic $s^2 + a^2$ in order to track the reference. This requires a very complicated control structure, mathematically and computationally. To avoid this, a Park transform can be used and the targeted control output will be the voltages in dq frame which are rotating with the same speed $\theta = \omega t$ as of voltage in abc frame [4] as in Fig. 5.4.

With or without LCL filter (i.e., grid-connected VSC system as in Fig. 5.2 or Fig. 5.1), the transmission line (and LCL filter, if any) can be considered as an inductor L with parasite resistor R. Thus, the system equation in abc frame is (5.1).

$$\frac{dI_{abc}}{dt} = \frac{1}{L}\left(-RI_{abc} - V_{abc} + V_{VSCabc}\right) \tag{5.1}$$

where

$$\begin{cases} I_{abc} = \begin{bmatrix} i_a & i_b & i_c \end{bmatrix}^T \\ V_{abc} = \begin{bmatrix} V_a & V_b & V_c \end{bmatrix}^T \\ V_{VSCabc} = \begin{bmatrix} V_{VSCa} & V_{VSCb} & V_{VSCc} \end{bmatrix}^T \end{cases}$$

Using the inverse Park transform from abc frame to dq frame ($\theta = \omega t$):

$$\begin{cases} I_{abc} = T(\theta) I_{dq0} \\ V_{abc} = T(\theta) V_{dq0} \\ V_{VSCabc} = T(\theta) V_{VSCdq0} \end{cases} \tag{5.2}$$

where

$$\begin{cases} I_{dq0} = \begin{bmatrix} i_d & i_q & i_0 \end{bmatrix}^T \\ V_{abc} = \begin{bmatrix} V_d & V_q & V_0 \end{bmatrix}^T \\ V_{VSCdq0} = \begin{bmatrix} V_{VSCd} & V_{VSCq} & V_{VSC0} \end{bmatrix}^T \end{cases}$$

with the transform matrix

$$T = T(\theta) = \begin{bmatrix} \cos\theta & -\sin\theta & 1 \\ \cos\left(\theta - \frac{2\pi}{3}\right) & -\sin\left(\theta - \frac{2\pi}{3}\right) & 1 \\ \cos\left(\theta + \frac{2\pi}{3}\right) & -\sin\left(\theta + \frac{2\pi}{3}\right) & 1 \end{bmatrix} \tag{5.3}$$

quation (5.1) can be written as:

$$\frac{d[T(\theta) I_{dq0}]}{dt} = \frac{1}{L}\left(-RT(\theta) I_{dq0} - T(\theta) V_{dq0} + T(\theta) V_{VSCdq0}\right) \tag{5.4}$$

We have:

$$\frac{d[T I_{dq0}]}{dt} = \frac{dT}{dt} I_{dq0} + T\frac{dI_{dq0}}{dt}$$

Thus, (5.4) becomes:

$$T^{-1}(\theta)\frac{d[T(\theta)]}{dt} I_{dq0} + \frac{dI_{dq0}}{dt} = \frac{1}{L}\left(-RI_{dq0} - V_{dq0} + V_{VSCdq0}\right) \tag{5.5}$$

Besides:

$$T^{-1}(\theta) = \frac{2}{3}\begin{bmatrix} \cos\theta & \cos\left(\theta - \frac{2\pi}{3}\right) & \cos\left(\theta + \frac{2\pi}{3}\right) \\ -\sin\theta & -\sin\left(\theta - \frac{2\pi}{3}\right) & -\sin\left(\theta + \frac{2\pi}{3}\right) \\ \frac{1}{2} & \frac{1}{2} & \frac{1}{2} \end{bmatrix}$$

and:

$$\frac{dT(\theta)}{dt} = \begin{bmatrix} -\dot{\theta}\sin\theta & -\dot{\theta}\cos\theta & 1 \\ -\dot{\theta}\sin\left(\theta - \frac{2\pi}{3}\right) & -\dot{\theta}\cos\left(\theta - \frac{2\pi}{3}\right) & 1 \\ -\dot{\theta}\sin\left(\theta + \frac{2\pi}{3}\right) & -\dot{\theta}\cos\left(\theta + \frac{2\pi}{3}\right) & 1 \end{bmatrix}$$

Thus:

$$T^{-1}(\theta)\frac{d[T(\theta)]}{dt} = X_{T(\theta)} = \begin{bmatrix} 0 & -\dot{\theta} & 0 \\ \dot{\theta} & 0 & 0 \\ 0 & 0 & 0 \end{bmatrix} \tag{5.6}$$

The system equation (5.5) is now:

$$X_{T(\theta)} I_{dq0} + \frac{dI_{dq0}}{dt} = \frac{1}{L}\left(-RI_{dq0} - V_{dq0} + V_{VSCdq0}\right) \tag{5.7}$$

Consider that the system is three-phase balanced, i.e., $V_a + V_b + V_c = 0$. Hence, in qd frame, we have $V_0 = 0$ and $i_0 = 0$. Based on averaged model [13], the terminal voltages V_{VSCdq0} are (where $m_0 = 0$ since $V_0 = 0$):

$$V_{VSCdq0} = \frac{V_{DC}}{2}\begin{bmatrix} m_d & m_q & m_0 \end{bmatrix}^T \tag{5.8}$$

By using the PLL with d-axis aligned with a-axis (Fig. 5.4), voltage is imposed with $V_q = 0$. Therefore, the output powers at PCC in dq frame:

$$\begin{cases} P = \frac{3}{2}\left(V_d i_d + V_q i_q\right) = \frac{3}{2} V_d i_d \\ Q = \frac{3}{2}\left(-V_d i_q + V_q i_d\right) = -\frac{3}{2} V_d i_q \end{cases} \tag{5.9}$$

Based on the reference of the powers, the current's reference signals are:

$$\begin{cases} I_{dref} = \frac{2}{3}\frac{P_{ref}}{V_d} \\ I_{qref} = -\frac{2}{3}\frac{Q_{ref}}{V_d} \end{cases} \tag{5.10}$$

For the control objectives, to act as a STATCOM, the active power is kept at zero $P_{dref} = 0$ and reactive power is at the same amount of reactive load $Q_{qref} = -Q_{load}$. Thus, current control objectives are:

$$\begin{cases} I_{dref} = 0 \\ I_{qref} = \frac{2}{3}\frac{Q_{load}}{V_d} \end{cases} \tag{5.11}$$

5.2 Control strategies of VSC grid-connected converter

5.2.1 MIMO control synthesis with disturbance rejection

A MIMO control structure is used based on state-space method, and taking into account of grid voltage and frequency variation. The nonlinear system (5.7) is linearized at desired operating point, next the controller is syhthesized based on this linearized model. According to the designer's requirements (such as pole placement, $Hinfty$ optimization, and/or minimum gain), the LMI conditions can be formulated and modified. In order to meet the needs of control design, the proposed control in this chapter is built using pole placement and $Hinfty$ optimization, but other LMI conditions can be easily added to the overall condition.

Firstly, consider the desired operating point:

$$\begin{bmatrix} i_d^* \\ i_q^* \end{bmatrix} = \begin{bmatrix} i_{d0} \\ i_{q0} \end{bmatrix}; \begin{bmatrix} m_d^* \\ m_q^* \end{bmatrix} = \begin{bmatrix} m_{d0} \\ m_{q0} \end{bmatrix} \tag{5.12}$$

To improve transient behavior and performance, *disturbance rejection* will be enforced in control synthesis in order to minimize the effect of frequency and grid voltage variations.

The linear model version of original model (5.7) is (where $\omega_0 = 100\pi$ is the nominal frequency):

$$\begin{cases} \frac{d\Delta i_d}{dt} = -\frac{R}{L}\Delta i_d + \omega_0\left(\frac{\dot{\theta}}{\omega_0}\Delta i_q + i_q\frac{\Delta\dot{\theta}}{\omega_0} + \frac{-\Delta V_d}{\omega_0 L}\right) + \frac{V_{DC}}{2L}\Delta m_d \\ \frac{d\Delta i_q}{dt} = -\frac{R}{L}\Delta i_q - \omega_0\left(\frac{\dot{\theta}}{\omega_0}\Delta i_d + i_d\frac{\Delta\dot{\theta}}{\omega_0} + \frac{\Delta V_q}{\omega_0 L}\right) + \frac{V_{DC}}{2L}\Delta m_q \end{cases} \tag{5.13}$$

The model (5.13) can be equivalently written in state-space form:

$$\begin{cases} \dot{X} = AX + B_1 U + B_2 W \\ Y = X \end{cases} \tag{5.14}$$

Where state X, control signal U and disturbance W are:

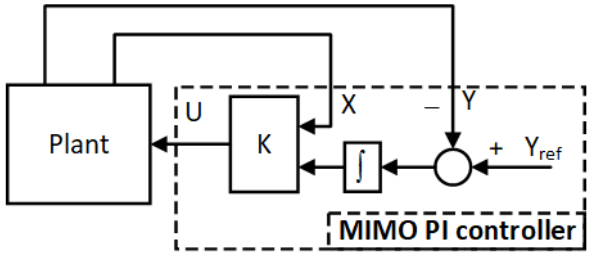

Figure 5.5: The MIMO PI controller implementation

$$
\begin{aligned}
X &= \begin{bmatrix} \Delta i_d \\ \Delta i_q \end{bmatrix} = \begin{bmatrix} i_d \\ i_q \end{bmatrix} - \begin{bmatrix} i_{d0} \\ i_{q0} \end{bmatrix}; \\
U &= \begin{bmatrix} \Delta m_d \\ \Delta m_q \end{bmatrix} = \begin{bmatrix} m_d \\ m_q \end{bmatrix} - \begin{bmatrix} m_{d0} \\ m_{q0} \end{bmatrix}; \\
W &= \begin{bmatrix} \frac{\dot{\theta}}{\omega_0}\Delta i_q + i_q\frac{\Delta\dot{\theta}}{\omega_0} + \frac{-\Delta V_d}{\omega_0 L} \\ \frac{\theta}{\omega_0}\Delta i_d + i_d\frac{\Delta\dot{\theta}}{\omega_0} + \frac{\Delta V_q}{\omega_0 L} \end{bmatrix}
\end{aligned}
$$

and state-space matrices are:

$$
A = \begin{bmatrix} -\frac{R}{L} & 0 \\ 0 & -\frac{R}{L} \end{bmatrix}; B_1 = \begin{bmatrix} \frac{V_{DC}}{2L} & 0 \\ 0 & \frac{V_{DC}}{2L} \end{bmatrix}; B_2 = \begin{bmatrix} \omega_0 & 0 \\ 0 & -\omega_0 \end{bmatrix}
$$

The main goal is to ensure the outputs asymptotically track the references Y_{ref}:

$$
e = -Y + Y_{ref} = -X + Y_{ref} \to 0
$$

where:

$$
Y_{ref} = \begin{bmatrix} i_{dref} & i_{qref} \end{bmatrix}^T
$$

Consider the augmented system:

$$
\begin{cases} \dot{\bar{X}} = \bar{A}\bar{X} + \bar{B}_1\bar{U} + \bar{B}_2\bar{W} \\ \bar{Y} = e = \bar{C}\bar{X} \end{cases} \tag{5.15}
$$

where:

$$
\bar{X} = \begin{bmatrix} \dot{X} \\ e \end{bmatrix}; \bar{U} = \dot{U}; \bar{W} = \dot{W}
$$

and the augmented matrices are:

$$
\bar{A} = \begin{bmatrix} A & 0 \\ -I & 0 \end{bmatrix}; \bar{B}_1 = \begin{bmatrix} B_1 \\ 0 \end{bmatrix}; \bar{B}_2 = \begin{bmatrix} B_2 \\ 0 \end{bmatrix}; \bar{C} = \begin{bmatrix} 0 \\ I \end{bmatrix}^T
$$

The state-feedback controller of augmented system (5.15) is $\bar{U} = K\bar{X}$. The MIMO controller of system (5.14) are calculated as:

$$
\begin{cases} U = \begin{bmatrix} \Delta m_d \\ \Delta m_q \end{bmatrix} = K \begin{bmatrix} X \\ \int e dt \end{bmatrix} \\ \begin{bmatrix} m_d \\ m_q \end{bmatrix} = U + \begin{bmatrix} m_{d0} \\ m_{q0} \end{bmatrix} \end{cases} \tag{5.16}
$$

The MIMO controller (5.16) can be seen as in Fig. 5.5, where the plant is the original system in dq frame (5.7).

Figure 5.6: The general LMI region $D_{(L,M)}$ (left) and strip region (right)

5.2.2 Pole-placement LMI-based techniques

To have a fare comparison with classical cascade vector control (see subsubsection 1.2.2.2 in chapter 1), the MIMO control gain should be generated such that the time-constant of the resulting closed-loop is close to the one of vector control.

Firstly, we define the LMI region as [10]:

$$D_{(L,M)} = \left\{ s \,|\, s \in C, L + sM + \bar{s}M^T < 0 \right\} \tag{5.17}$$

where L is a symmetric matrix and M is a square matrix.

As illustrated in Fig. 5.6, the LMI region $D_{(L,M)}$ is a convex set and is symmetric about the real axis [10].

To ensure the close-loop time constant $\tau_{closed-loop}$ is in a range near to vector control's time constant, i.e.:

$$-\frac{1}{\delta_2} < \tau_{closed-loop} < -\frac{1}{\delta_1}$$

Or, equivalently, the closed-loop poles satisfy:

$$\delta_2 < real(s) < \delta_1$$

This is the special case of general LMI region $D_{(L,M)}$ where:

$$L = \begin{bmatrix} -2\delta_2 & 0 \\ 0 & 2\delta_1 \end{bmatrix}; M = \begin{bmatrix} 1 & 0 \\ 0 & -1 \end{bmatrix} \tag{5.18}$$

5.2.3 LMI-based H_∞ MIMO control with pole placement condition

As discussed, the LMI-based control has to be designed such that the output time constants are comparable with those of vector control. For this purpose, we introduce the H_∞ problem 8 and its theorem 8 as follows.

Problem 8 *For the system* (5.15)*, the H_∞ problem is to establish a state feedback control law $\bar{U} = K\bar{X}$ satisfying:*

$$\|G(s)\|_\infty \leq \gamma \tag{5.19}$$

hold with positive scalar γ, where $G(s) = \dfrac{\bar{Y}(s)}{\bar{W}(s)}$.

Theorem 8 *The problem 8 has a solution iff there exist a matrix W_P and a symmetric positive definite matrix X_P , by the mean of LMI technique, satisfying:*

$$\underset{X_P, W_P}{minimize} \;\; \gamma$$

such that

$$\begin{cases} \begin{bmatrix} \Psi & \bar{B}_2 & \left(\bar{C}X_p\right)^T \\ \bar{B}_2^T & -\gamma I & 0 \\ \bar{C}X_p & 0 & -\gamma I \end{bmatrix} < 0 \\ L \otimes X_P + M \otimes \Psi_1 + M^T \otimes \Psi_1^T < 0 \\ \Psi = \Psi_1 + \Psi_1^T; \Psi_1 = \bar{A}X_P + \bar{B}_1 W_P \end{cases}$$

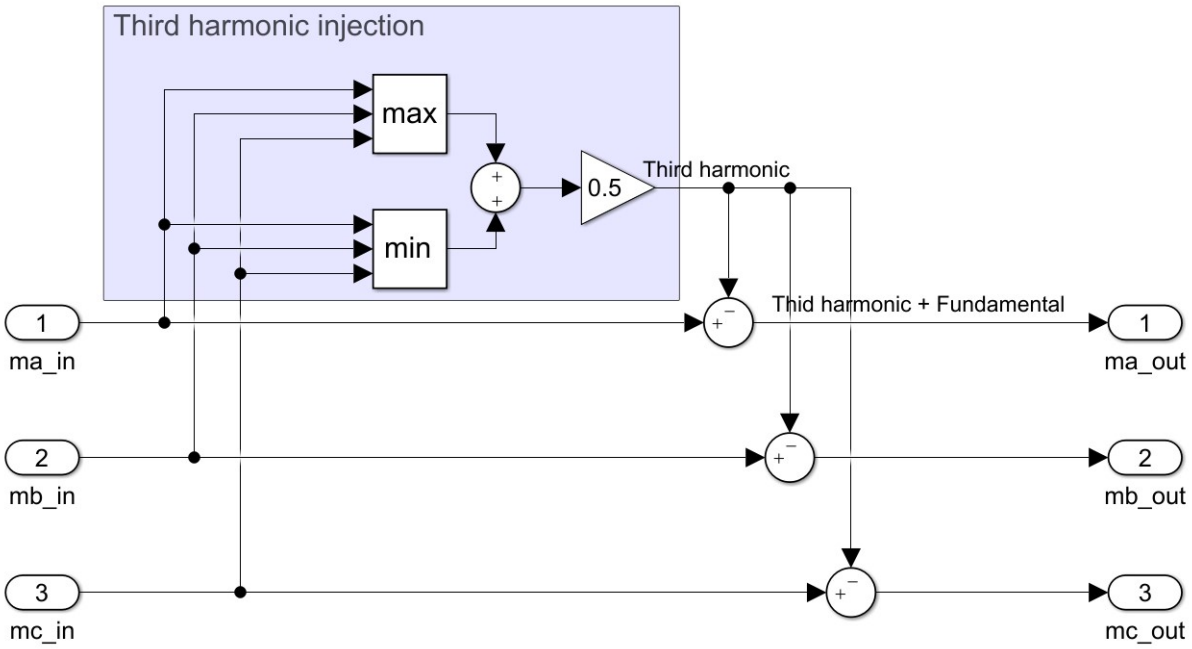

Figure 5.7: The third harmonic injection structure

with $\otimes$ is Kronecker product.
The matrix gain K is calculated as:

$$K = W_P X_P^{-1} \tag{5.20}$$

Proof 8 *The proof for the first LMI condition of the theorem 8 can be seen in [10] in general linear system and in [5], [6] for VSC-based systems.*

For the second LMI condition, i.e., the LMI condition for pole-placement mentioned in subsection 5.2.2, the proof can be seen in [10].

5.2.4 Third harmonic injection for AC voltage peak value enhancement

The major setback of PWM control method is that the maximum peak fundamental VSC terminal AC voltage is limited at $\frac{\sqrt{3}}{2\sqrt{2}}V_{DC}$ [14], corresponding to the input control maximum value of 1. This limitation will in turn affect the capacity of converter, in this case, the difficulty for increasing the converter output voltage. For this, there are two options to increase the output voltage [14]:

- Increase the output voltage by increasing DC voltage, which means higher cost for VSC converter system.
- Increase the output voltage by allowing over-modulation, i.e., control input is larger than 1. This will gradually transform PWM control into square wave modulation, i.e., introducing more undesired higher-order harmonics.

To tackle this problem, a third harmonic is injected into the reference of the PWM controller [14]. This helps to increase the maximum control input value while keeping the reference signal of PWM smaller than 1, i.e., allowing control input is larger than 1 while reducing the maximum reference signal. As proven in [14], the maximum value of input control using third harmonic injection is $\frac{2}{\sqrt{3}}\frac{\sqrt{3}}{2\sqrt{2}}V_{DC} = \frac{1}{\sqrt{2}}V_{DC}$ (around 15% increase).

A simple solution for third harmonic injection is to include a one-sixth Third Harmonic Injection (THJ) into the fundamental reference PWM waveforms, using a simple structure as in Fig. 5.7. As seen in Fig. 5.8, the

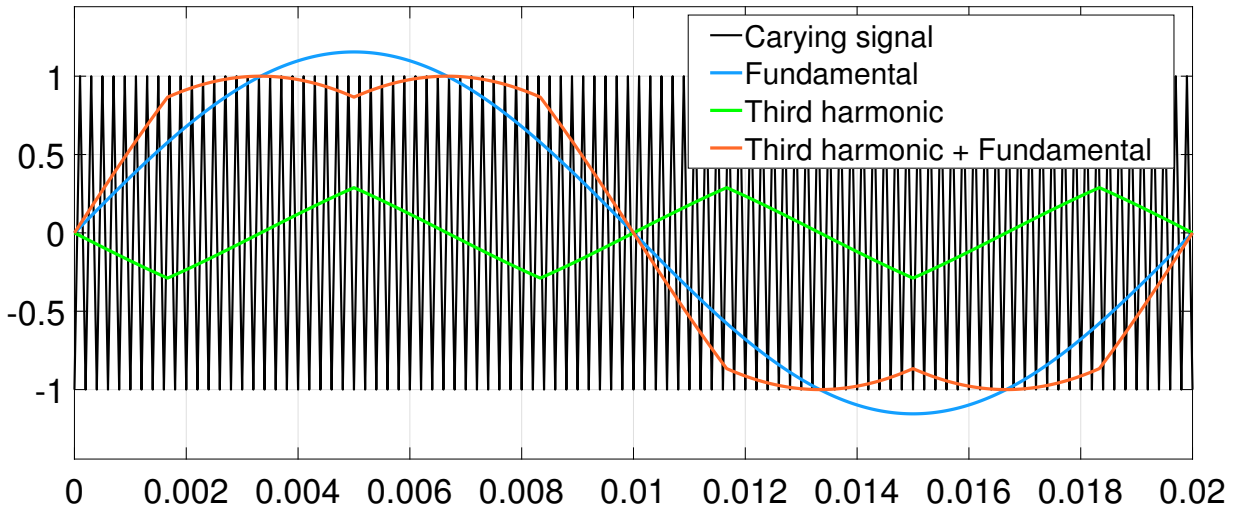

Figure 5.8: The PWM generation signals with third harmonic injection technique

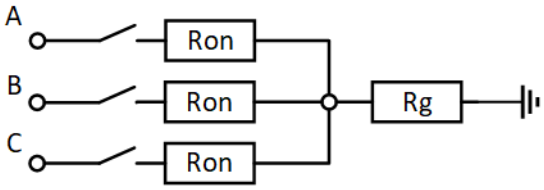

Figure 5.9: Three-phase fault implementation for the STATCOM

fundamental reference signal before using THJ technique (i.e., "Fundamental" signal in Fig. 5.8) is larger than 1, i.e., the PWM control introduces more undesired harmonics to the output voltage. However, with the THJ technique, the fundamental reference signal now is not larger than 1 (i.e., "Third harmonic + Fundamental" signal in Fig. 5.8), thus the output voltage has better quality, i.e., smaller THD.

5.3 Simulation and results

In this section, the proposed control method is validated using simple STATCOM model (Fig. 5.1) and full STATCOM model (Fig. 5.2). The results are also compared with those obtained with classical cascade vector control. The two controllers are design with the time-constant of 20ms.

The validation using the simple STATCOM model is done according to 3 scenarios: step response on current control, the load changing its value and a faulty event in the middle of the transmission line R-L (short-circuit using the three-phase fault implementation as in Fig. 5.9):

- Scenario 1 - step response: two steps are applied on the voltage reference, at t = 1s (from 47.5A to 56A) and at t = 3 (from 56A to 34.5A). As seen in Fig. 5.11, better responses for the output current phase A at the VSC terminal are obtained using proposed H_∞ LMI control compared to vector control. In addition, this trend is much clear for the RMS value of the current phase A as shown in Fig. 5.12. Indeed, the static error is around twice smaller that the one obtained with the vector control, and the transient time of propose control is also much smaller, at least 5 time smaller.

- Scenario 2 - Load changing: for this case, a second load (three-phase R-C branch with $R = 2\Omega$, $C = 0.02F$) is connected to the grid side at t = 1s. As shown in Figs. 5.13 and 5.14, the currents obtained with the proposed control have faster transient with smaller static error (2 times) compared to those obtained when

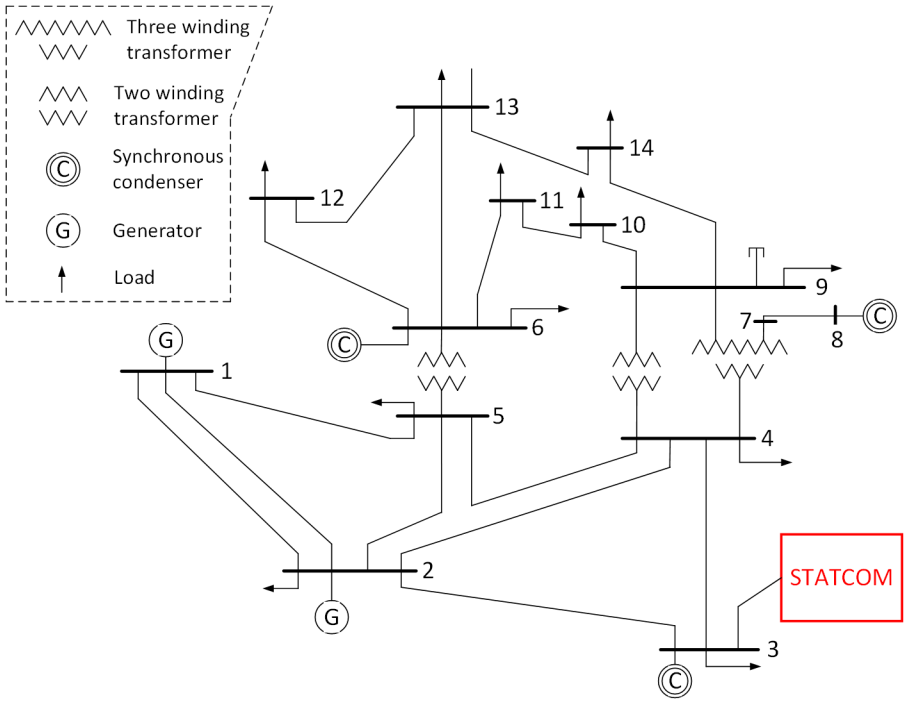

Figure 5.10: The modified IEEE 14-bus with an integrated STATCOM

using the vector control. The static error of reactive power injected to the grid using propose control is also smaller as shown in Fig. 5.15.

- Scenario 3 - short-circuit: a short circuit in the middle of transmission line R-L is simulated t = 1s. As shown in Figs. 5.17 and 5.18 for abc frame, the H_∞ LMI control provide a better current behavior with trasient time 5 times shorter and undershoot/overshoot 5 times smaller compared to the ones obtained using vector control. The trend is exactly the same for dq frame as shown in Fig. 5.16.

For the validation using full STATCOM model, the performance and stability of the model using proposed control and vector control are pretty much similar to the simple version, thus only short-circuit event and THD test are conducted:

- Scenario 4 - short-circuit: for the short-circuit, at the beginning and at the end of the faulty event, the responses of the current are much better compared to the ones obtained with classical vector control. As shown in Figs. 5.19 and 5.20 for abc frame, the transient of current using proposed control is much shorter (5 times shorter) and overshoot/undershoot is less than half of the current behavior using vector control. The same trend is shown for dq frame, as show in Fig.

- Scenario 5 - THD test: the interest is on the THD of the AC voltage output of LCL filter, which is tested with and without the third harmonic injection method with structure as in Fig. 5.7. As in Figs. 5.20. 5.22 and 5.23, for proposed control, the THD in case of using third harmonic injection method is much smaller, around two-third of the AC voltage obtained without such harmonic injection.

Finally, the last test is also a THD test with the two-level and three-level STATCOMs (Figs. 5.2 and 5.3, respectively) connected to the IEEE 14 bus benchmark (Fig. 5.10):

- Scenario 6 - THD test in IEEE 14-bus benchmark: The two two-level and three-level topologies as in Figs. 5.2 and 5.3, respectively, using the third harmonic injection method with structure as in Fig. 5.7, are integrated into IEEE 14-bus benchmark (Fig. 5.10, with the two STATCOMs is connected to bus 3). The controllers of the two STATCOMs (two two-level and three-level converters) are also tuned with the same gains using proposed H_∞ MIMO control. As shown in Figs. 5.24 and 5.25, the three-level topology provides a better output voltage, with much lower THD, 6.5% compared to 13.2% of the two-level topology.

5.4 Conclusion

As proven and discussed in this chapter, the proposed advanced control is applicable for converter-based application. In this case, for STATCOM application, it is superior to the classical vector control, validated using EMT model of a simple STATCOM and a full STATCOM with LCL filter. This superior characteristic is due to the disturbance rejection using $H_{\inf}$ optimization to minimize the effect of grid frequency and grid voltage variations.

In addition, the MMC topologies (e.g., two and three levels) as well as the THJ technique for PWM are also discussed and demonstrated. With the use of THJ and higher level topology, the THD is reduced vastly, thus the quality of the output of VSC application is enhanced.

The process of applying advanced MIMO control for EMT model, here is for converter-based application, is detailed into different steps. This step-by-step instruction is a suitable guide for implementing the advanced control in VSC-based industrial-level application.

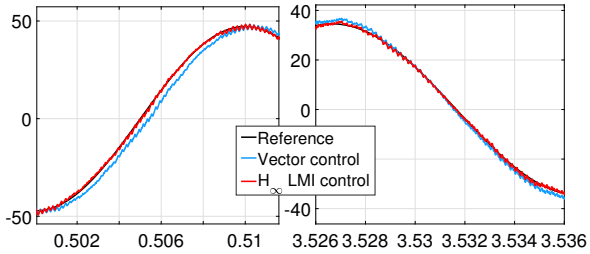

Figure 5.11: Scenario 1 - step response: current phase A (A)

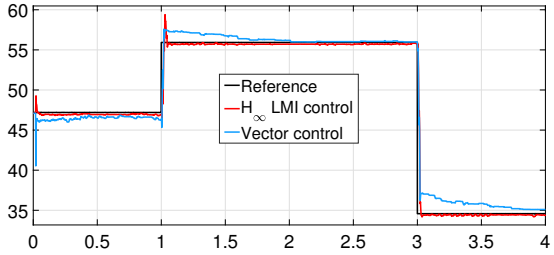

Figure 5.12: Scenario 1 - step response: current phase A in RMS (A)

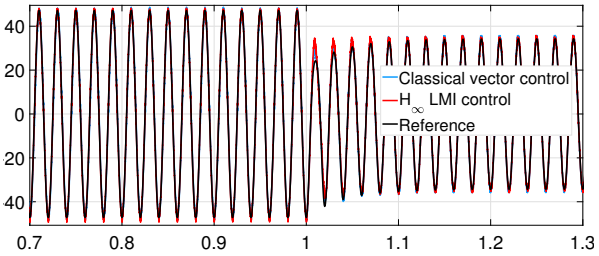

Figure 5.13: Scenario 2 - Load changing: current phase A (A)

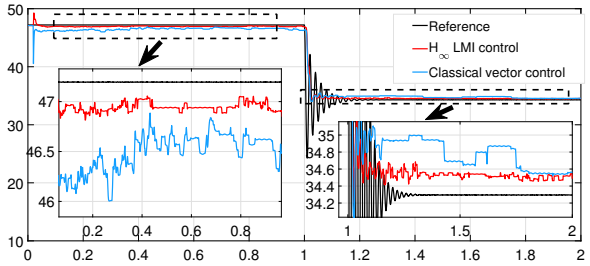

Figure 5.14: Scenario 2 - Load changing: current phase A in RMS (A)

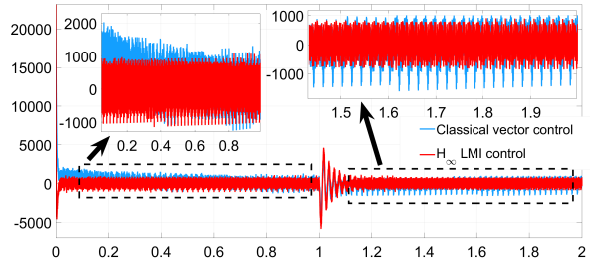

Figure 5.15: Scenario 2 - Load changing: Reactive power to the grid (Var)

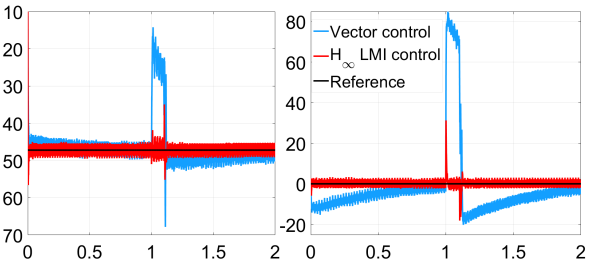

Figure 5.16: Scenario 3 - short-circuit: current in dq frame (A)

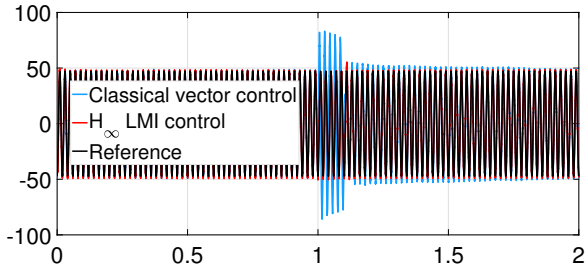

Figure 5.17: Scenario 3 - short-circuit: current phase A (A)

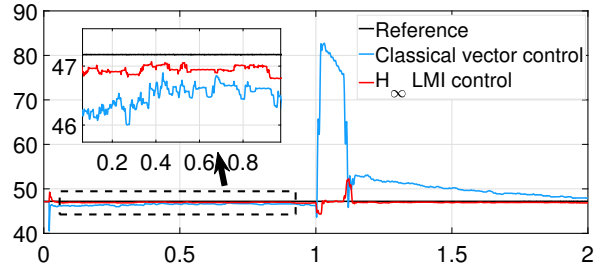

Figure 5.18: Scenario 3 - short-circuit: current phase A in RMS (A)

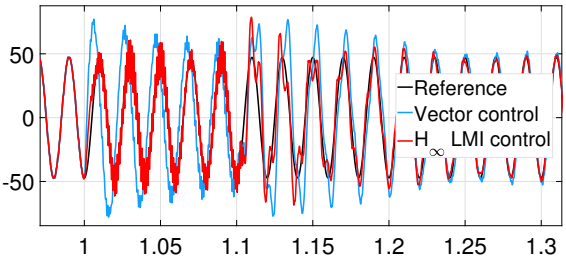

Figure 5.19: Scenario 4 - short-circuit: current phase A (A)

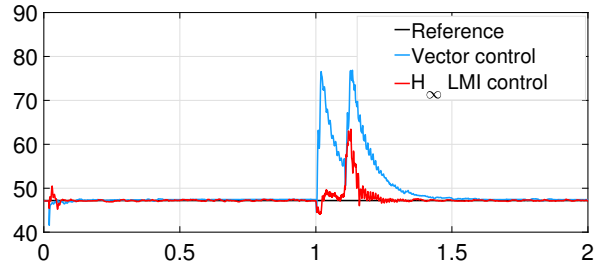

Figure 5.20: Scenario 4 - short-circuit: current phase A in RMS (A)

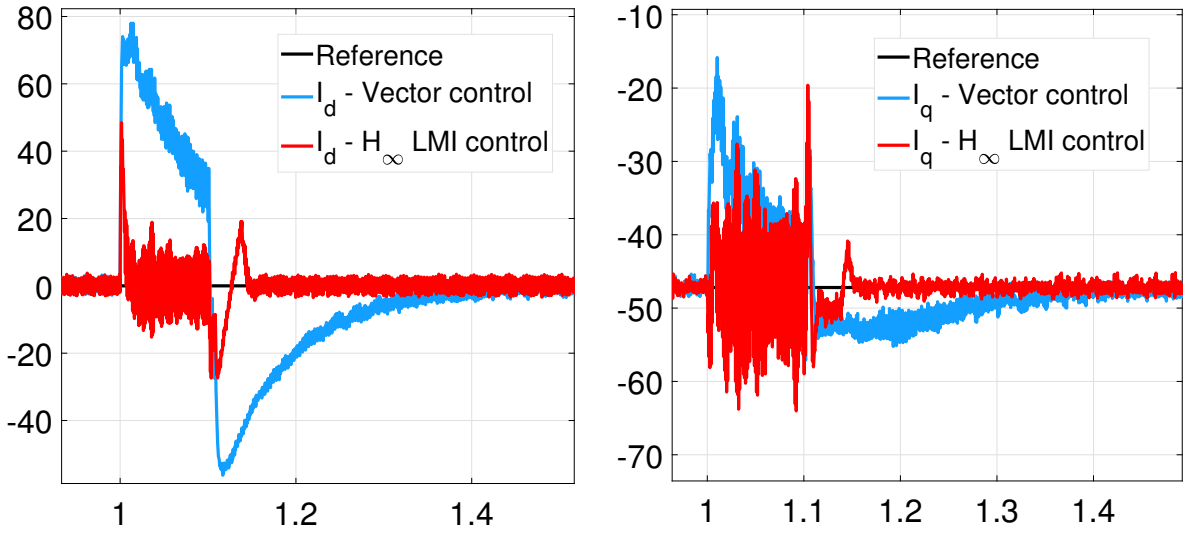

Figure 5.21: Scenario 4 - short-circuit: current in dq frame (A)

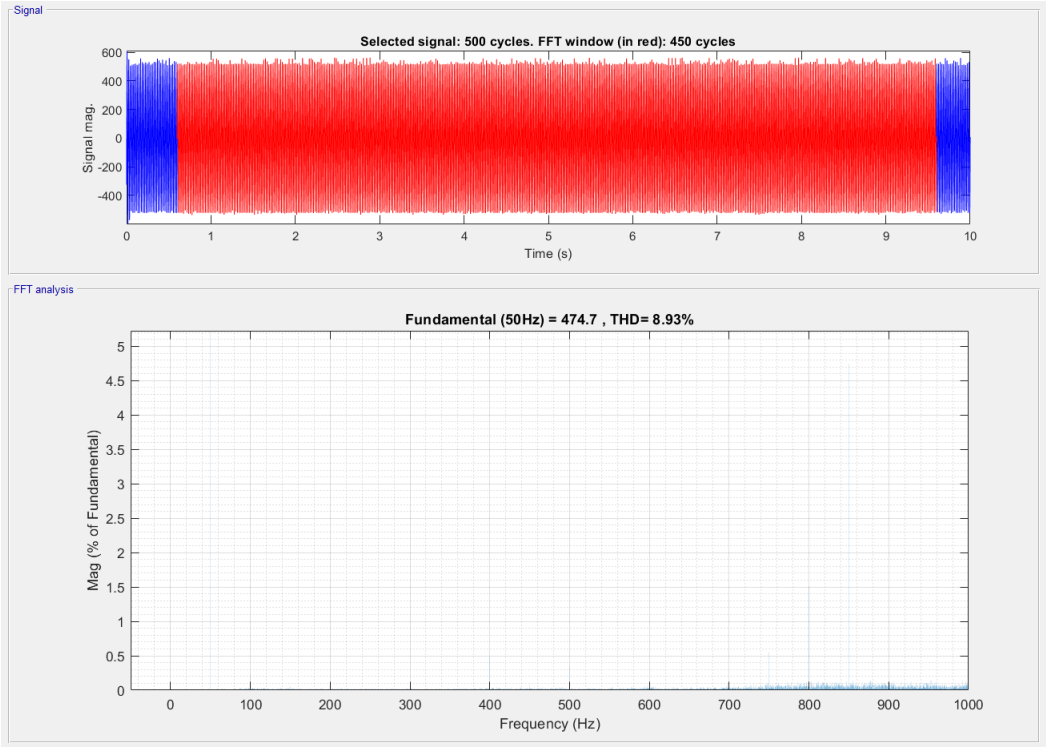

Figure 5.22: THD of AC voltage output of LCL filter with third harmonic injection

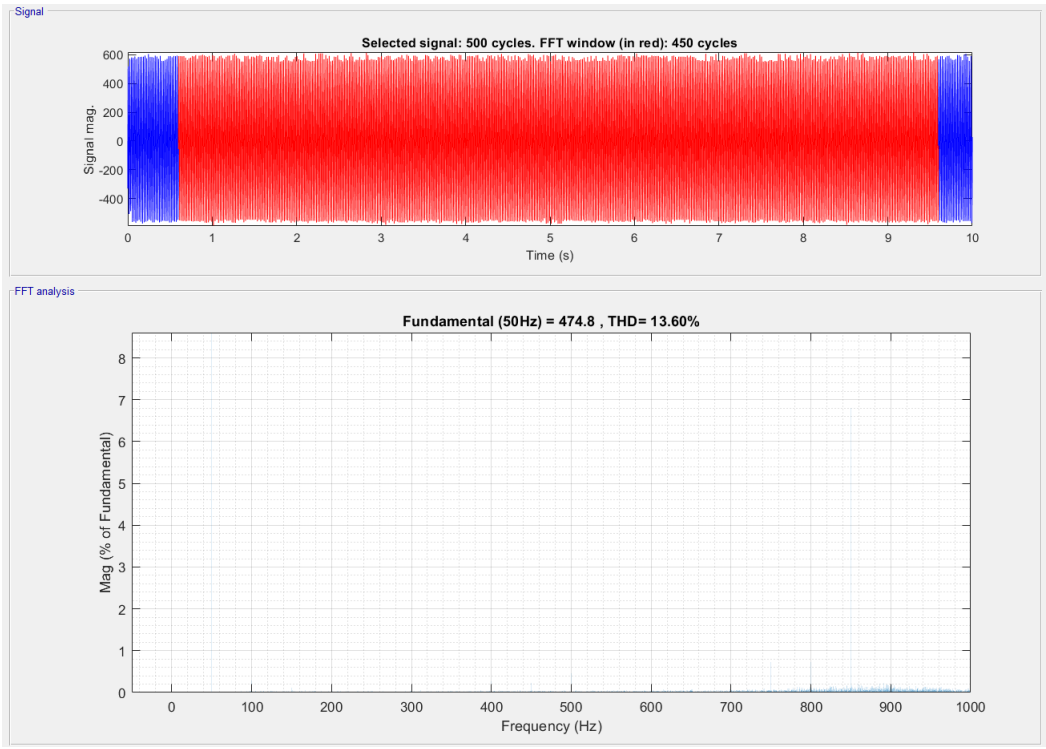

Figure 5.23: THD of AC voltage output of LCL filter without third harmonic injection

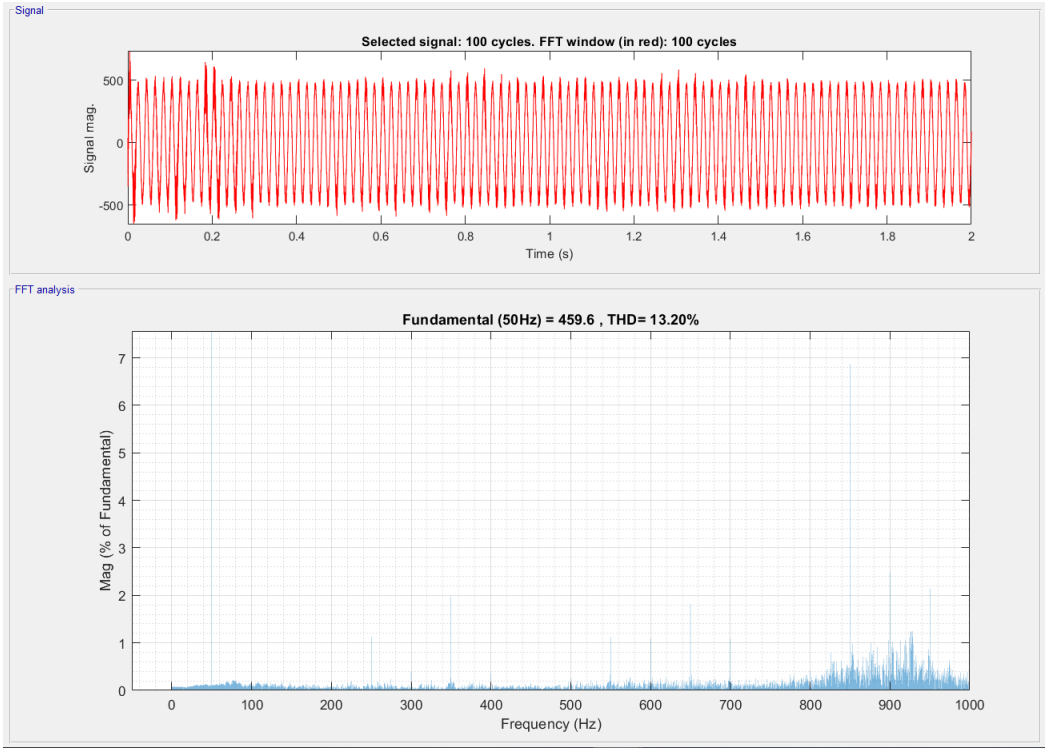

Figure 5.24: THD of AC voltage output of two-level VSC

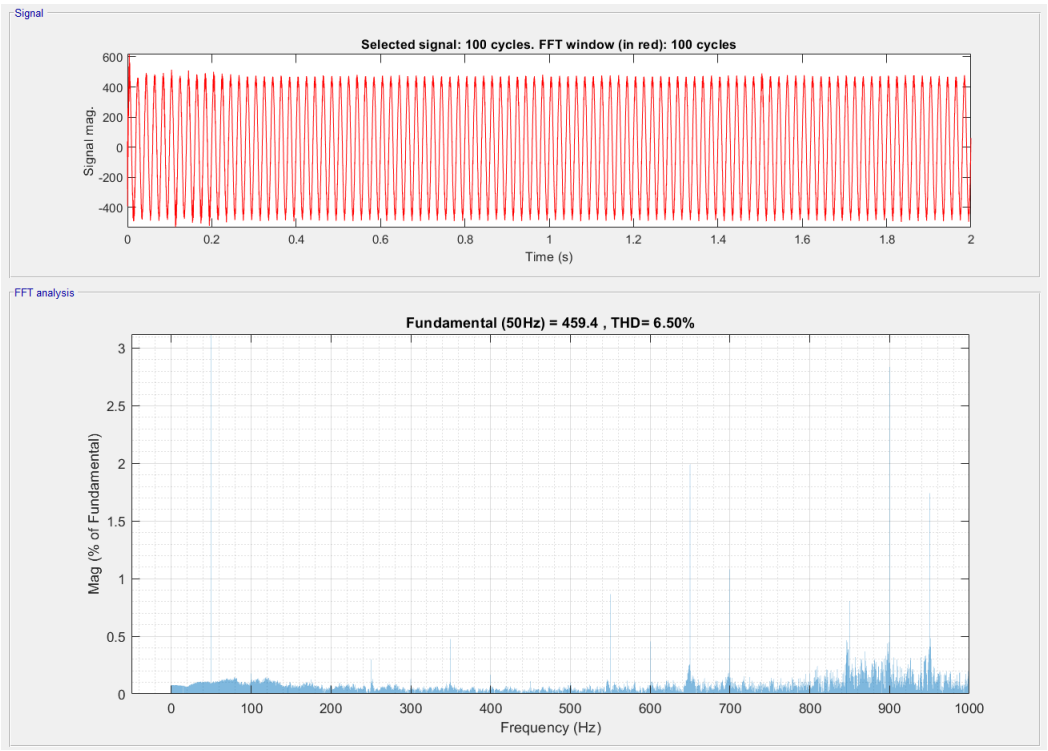

Figure 5.25: THD of AC voltage output of three-level VSC

Bibliography

[1] ENTSOE, TYNDP 2018 (2019, October), Technologies for Transmission System.

[2] Vormedal, P. K. M. (2010). Voltage Source Converter Technology for Offshore Grids. Norwegian University of Science and technology, Trondheim, Master thesis.

[3] Bahrman, M. P., Johansson, J. G., & Nilsson, B. A. (2003, July). Voltage source converter transmission technologies: the right fit for the application. In 2003 IEEE Power Engineering Society General Meeting (IEEE Cat. No. 03CH37491) (Vol. 3, pp. 1840-1847). IEEE.

[4] Bacha, S., Munteanu, I., & Bratcu, A. I. (2014). Power electronic converters modeling and control. Advanced textbooks in control and signal processing, 454(454).

[5] Marinescu, B., Kamal, E., & Ngo, H. T. (2021). A System Model-Based Approach for the Control of Power Park Modules for Grid Voltage and Frequency Services. arXiv preprint arXiv:2107.02000.

[6] Ngo, H. T., Kamal, E., Marinescu, B., & Xavier, F. (2020, November). Robust H_∞ Decentralized Control Design for HVDC Link Embedded in a Large-scale AC Grid. In 2020 Electrical Power and Energy Conference.

[7] Olalla, C., Leyva, R., El Aroudi, A., & Queinnec, I. (2009). Robust LQR control for PWM converters: An LMI approach. IEEE Transactions on industrial electronics, 56(7), 2548-2558.

[8] Singh, B., Saha, R., Chandra, A., & Al-Haddad, K. (2009). Static synchronous compensators (STATCOM): a review. IET Power Electronics, 2(4), 297-324.

[9] Richard C.. Dorf, & Bishop, R. H. (2008). Modern control systems. Pearson Prentice Hall.

[10] Duan, G. R., & Yu, H. H. (2013). LMIs in control systems: analysis, design and applications. CRC press.

[11] Lofberg, J. (2004, September). YALMIP: A toolbox for modeling and optimization in MATLAB. In 2004 IEEE international conference on robotics and automation (IEEE Cat. No. 04CH37508) (pp. 284-289). IEEE.

[12] ApS, M. (2019). Mosek optimization toolbox for matlab. User's Guide and Reference Manual, Version, 4.

[13] Bacha, S., Munteanu, I., & Bratcu, A. I. (2014). Power electronic converters modeling and control. Advanced textbooks in control and signal processing, 454(454).

[14] Bruckner, T., & Holmes, D. G. (2003, June). Optimal pulse width modulation for three-level inverters. In IEEE 34th Annual Conference on Power Electronics Specialist, 2003. PESC'03. (Vol. 1, pp. 165-170). IEEE.

Conclusion and possible future works

This thesis revised the control of modern power grid actuators by considering a combined local (generator) and global (grid) set of specifications.

From the application point of view, this allowed improvement of the participation of the RES generators to grid ancillary services and operation of such generators in new conceptual schemes as the Dynamic Virtual Power Plant one.

From the control point of view, a robust global model-based approach have been proposed with both centralized and decentralized implementations.

More specifically:

- a general GAS-oriented control structure which can provide primary GAS, as well as the ability to integrate the secondary grid frequency and voltage services into the control structure have been introduced.
- the principles of overlapping control have been exploited to provide a decentralized implementation of the above control of converter-based power system control.
- advanced notions and methods of robust control were used to improve the control at important points: handle nonlinearities and a wide range of operation points (which is a key point in operation of a DVPP), uncertainties of the models, strong variations of the structure of the control and of the set of available actuators (which is a key point for resilience and plug-and-play facilities of the DVPP). These methods include: linear robust control (H_∞/H_2), nonlinear fuzzy techniques, LMI methodologies for the synthesis of the gains of the controllers.

The following applications have been treated:

- Control of a VSC-HVDC system for local and grid specifications. It is based on an (overlapping) centralized control, in which advanced MIMO optimal H_∞/H_2 control techniques as well as nonlinear fuzzy technique are applied. In addition, the strong coupling between two converters is overcome via robust disturbance rejection.
- The PMSG wind energy control system was developed using GAS-oriented coordinated control structure in both centralized and decentralized approaches. The ancillary services consist of primary frequency services (inertia response, frequency response and power RAMP rate) and voltage services (Q/V support). The new proposed control structures are made up of various control levels/loops based on the natural dynamics of the system, in a coordinated structure, in order to improve performances and robustness. The very fast loop is used to provide local services (active/reactive power control, DC voltage control, and grid inertia/RoCoF support), the fast loop is for MPPT, frequency response, and AC voltage services, and a slow loop is for secondary control - both in frequency and voltage services. Additionally, other GAS according to grid code ENTSO-E such as FRT and adequate CCT are provided.
- A STATCOM control system with the validation in EMT to provide a guideline for applying the proposed control methodologies on real hardware. The proposed advanced control methods such as MIMO optimal H_∞ as well as converter-related problem handling such as THJ and VSC topologies (i.e., two and three

level VSC) have been studied in all implementation details. With these step-by-step guidelines, this thesis provided a concise and effective way to exploit the benefits of advanced control in improving performance and stability of grid connected power converter systems.

Extensions of this work are expected both at methodological as well as application levels:

- The first and foremost future work is to implement the proposed control for two possible applications of STATCOM and PMSG wind energy systems, with real hardware connected to grid via a HiL platform. The works will use the proposed advanced control, in both centralized and decentralized approaches, with the coordinated ancillary service-oriented structure.
- From the methodological point of view, the RoCoF support can be improved via advanced control.
- The proposed control strategy can also be applied to other RES systems, like the PV systems, along with a suitable MPPT and reserved mechanism to fulfill the need of ancillary services.
- The actual methodology can be extended to grid forming control for the aforementioned applications, i.e., STATCOM and RES energy systems as well as to be able to provide black start in GAS. This control structure will also help to tackle weak grids, where AC voltage support is strongly demanded.

Appendix A

Appendix for softwares and implementation techniques

A.1 Linearization with MATLAB/Simulink

MATLAB (an abbreviation of "MATrix LABoratory") is a proprietary numerical computing environment and multi-paradigm programming language created by MathWorks in 1970s. MATLAB supports matrix manipulations, data analysis and graph plotting, rapid algorithm testing, and can interface with other programming languages (e.g., python or C/C++).

Simulink is a graphical programming environment developed in MATLAB environment for modeling, simulation, and analysis of multidomain dynamical systems. Its graphical user interface is mainly a graphical block diagramming tool with a set of block libraries, mostly customizable. It supports deep integration with MATLAB and MATLAB toolboxes. A Simulink model can be created using Simulink itself or using MATLAB functions. Simulink is frequently used in digital signal processing and automatic control for multidomain simulation and model-based design.

There are many way to linearize a system, analytically and/or numerically. Using MATLAB/Simulink and its built-in functions, a nonlinear model can be linearized rapidly even with some predefined initial conditions of the system. To linearize a system, an operating point must be defined and some necessary steps in model setting must be followed.

A.1.1 Operating point finding technique using Simulink

To be able to find an operating point of a system, the model is firstly built using Simulink. Next, there are some steps must be followed one by one in order to find an operating point:

1. Output and input definition: there are some different ways to define input and output of a Simulink model, but the best way is to use Inport and Outport blocks. This method of input-output definition is not only explicit but also reusable for controller testing and system analysis. An example is illustrated as in Fig. A.1.

2. Solver setting: continuous or discrete mode, depending on the model analysis and/or control design purpose. Solver types are variable-step for continuous linearized system and fixed-step for discrete linearized system. This setting can be found un Simulink model using Simulation/Model configuration parameters or hotkey Ctrl+E. In some recent MATLAB version, such as 2017B and later, this setting can be found by click on the text line in the lowest corner on the right in Simulink model (e.g., the text VariableStepAuto in Fig. A.1), then click on the gear symbol. This setting is as in Fig. A.2, with some minor interface graphic may vary depends on the MATLAB version.

3. Next, for MATLAB R2018B and older, the linearization analysis toolbox can be called in Simulink model by choosing Analysis/Control Design/Linear Analysis. For newer MATLAB versions, this can be called in Simulink model through Apps/Linearization Manager. The Linear Analysis Tool is illustrated as in Fig. A.3.

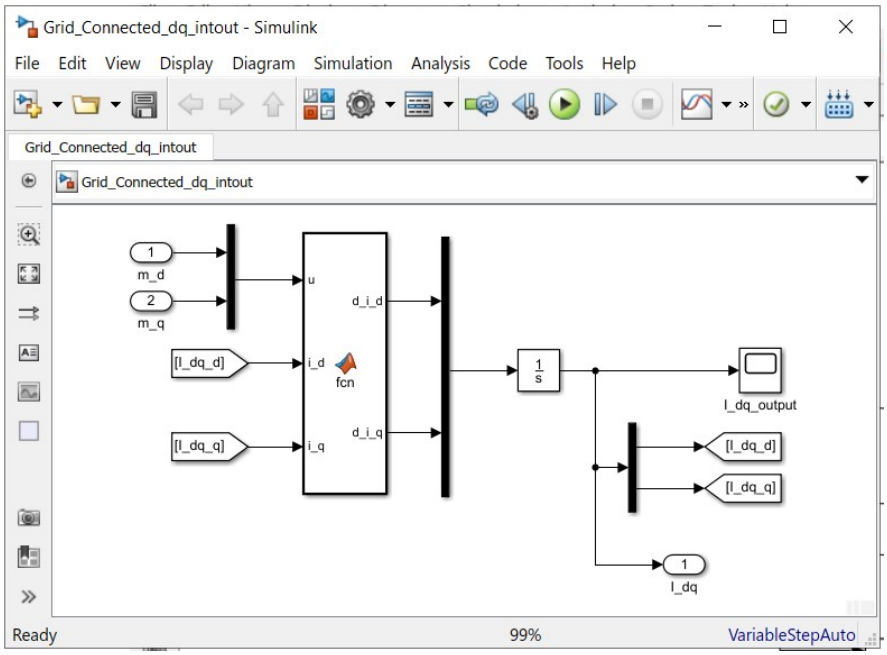

Figure A.1: A Simulink model with predefined input and output using inport and outport blocks

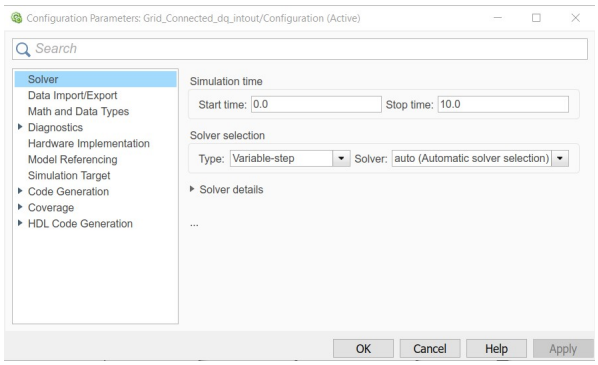

Figure A.2: Model setting for continuous system

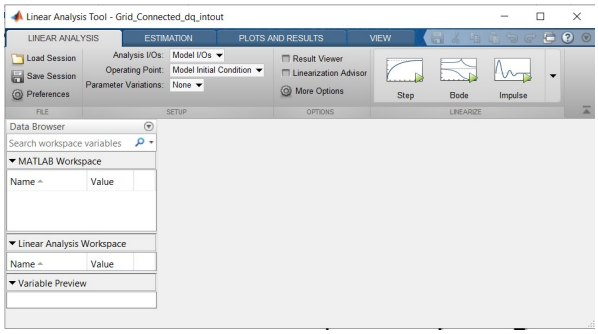

Figure A.3: Linearization analysis tool in MATLAB version R2018B

4. Linear Analysis Tool setting: in Linear Analysis/Analysis I/Os, choose Roor Level Inports and Outports (this is for predefined input-output).

5. To call the trim tool for finding the operating point, in Linear Analysis/Operating Point, choose Trim Model. The trim tool is as in Fig. A.4.

6. In trim tool, the initial conditions can be set for states, inputs and outputs of the model. For example, as in Fig. A.4, we are trying to find an operating point, all of the states are in steady state (tick on steady state box). The state 1 is known as 0 (tick on known box of state 1) and state 2 is known as -50 (tick on known box of state 2). There are also other options such as optimization method and constraint tolerance in Options tab.

7. Finally, click on Start trimming to run. The result as in Fig. A.5.

A.1.2 Linearization at a desired operating point

As of now, we have a desired operating point. This desired operating point is shown up in the Linear Analysis Workplace with the default name `op_trim1` as in Fig. A.6. Now, in Linear Analysis/Operating Point, be sure

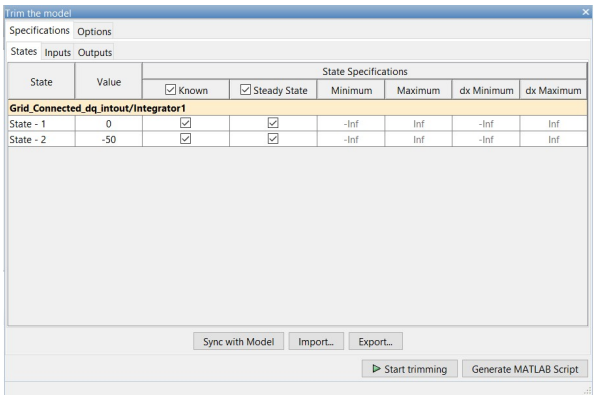

Figure A.4: Trim tool of linearization analysis toolbox

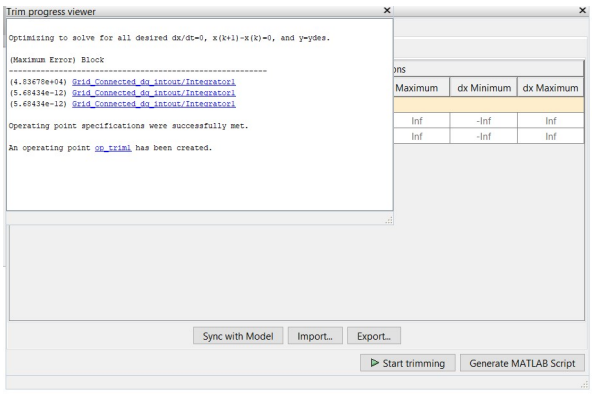

Figure A.5: Trim process viewer

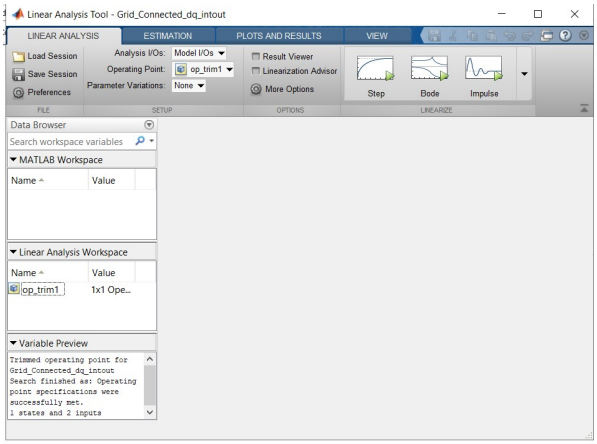

Figure A.6: Operating point `op_trim1` data in the Linear Analysis Workplace

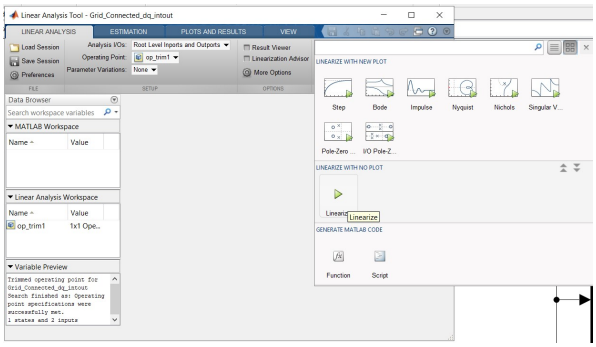

Figure A.7: Linearization without plot

to set it to `op_trim1` (normally it will automatically set). In Linear Analysis/Analysis I/Os, choose Roor Level Inports and Outports (this is for predefined input-output).

Now, to linearize the system with the desired operating point and with the predefined input-output, in Linear Analysis tab, under the Linearize part, choose Linearize with plot as in Fig. A.7. The matrices of linearized state-space system is now stored in linsys1 in the Linear Analysis Workplace as in Fig. A.8. To be able to manipulate the data, we need to click on and drag `op_trim1` and `linsys1` to the MATLAB Workplace.

The two elements we need to capture for control design or system analysis are operating point and linearized matrices. One crucial point is that we should not copy it manually (by click on it and copy the value of the vectors or matrices), because the value shown in the MATLAB workplace is with low precision (default is only 4 digit in display, while the precision of MATLAB in stored value is 16 digits of precision). Instead, the author of this thesis wrote a simple program in MATLAB to store these value with their own precision. For this, just need to run 2 files `Save_linsys1_to_m_file.m` and `Save_op_trim1_to_m_file.m`. The operating point including states, inputs (inputs may or may not inlcude disturbances) and outputs are in the file `Operating_state_file.m`, and the matrices of linearized system are in the file `linearized_system.m`. The programs are short but may need some time to understand. The reader can see them in the MATLAB codes Listings. A.1 and A.2.

```
1 [Matrix_a, Matrix_b, Matrix_c, Matrix_d] = ssdata(linsys1);
2
3 % Create and save variable 'Matrix_a','Matrix_b', 'Matrix_c', 'Matrix_d' from a workspace to
      a MATLAB script, linearized_system.m.
4 matlab.io.saveVariablesToScript('linearized_system.m',{'Matrix_a','Matrix_b', 'Matrix_c', '
    Matrix_d'});
```

Listing A.1: Extraction of matrices from `linsys1` data file

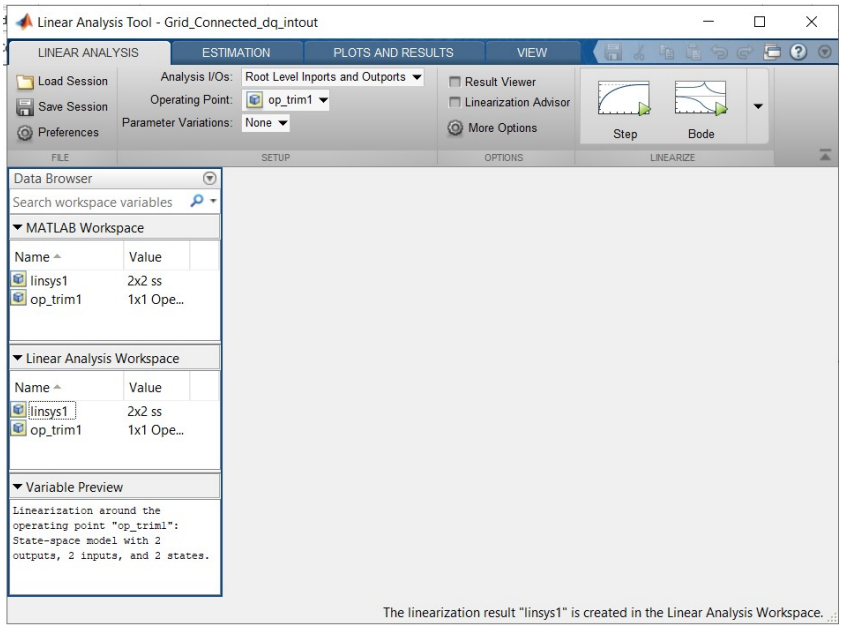

Figure A.8: Linearization data in MATLAB workplace

```
State_and_dx = get(op_trim1, 'States');
Operating_X = get(State_and_dx, 'x');
Operating_X = Operating_X';

U_and_W_input = get(op_trim1, 'Inputs');
Operating_U_and_W = get(U_and_W_input, 'u');
Operating_Beta = cell2mat((Operating_U_and_W(1:2,1))');
% Operating_W = (Operating_U_and_W(5,1))';

Output_Y = get(op_trim1, 'Outputs');
Operating_Y = get(Output_Y, 'y');
Operating_Y = Operating_Y';

% Create and save variable Operating_X from a workspace to a MATLAB script,
    Operating_state_file.m.
matlab.io.saveVariablesToScript('Operating_state_file',{'Operating_X', 'Operating_Beta', '
    Operating_Y'});
```

Listing A.2: Extraction of operating point from `op_trim1` data file

A.2 Linear matrix inequalities using YALMIP and MOSEK solver

For advanced and MIMO control techniques, LMI is an convenient and user-friendly way to produce the controller gain with multi-objective goals. However, the more constraints are added, the more complicated the LMI conditions are. This may lead to unsolvable LMI conditions, or a bad solution with unbalanced eigenvalues.

For LMI solving tools, just before 2006, MATLAB itself developed a set of built-in functions and solvers which can help to find a solution for any LMI problem. However, there are two problems with these built-in functions and solvers. The first one is these built-in functions are not user-friendly, especially in handling many different LMI conditions. The second problem is these solvers are far from optimal, which cause many numerical problems, including bad performance in solving LMI problems and unbalanced eigenvalues for closed-loop system. YALMIP and MOSEK appear to be the suitable answers for these two problems.

YALMIP was developed as a toolbox for MATLAB by Johan Löfberg when he was working at ETH Zurich, Switzerland [1]. As written in his paper [1], YALMIP was initially developed for Semidefinite Programming (SDP) and LMI, but then has evolved phenomenally throughout the years. YALMIP provides many functions to easily

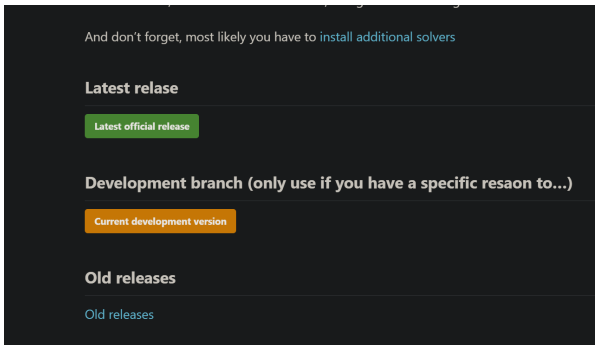

Figure A.9: YALMIP with different versions from its website

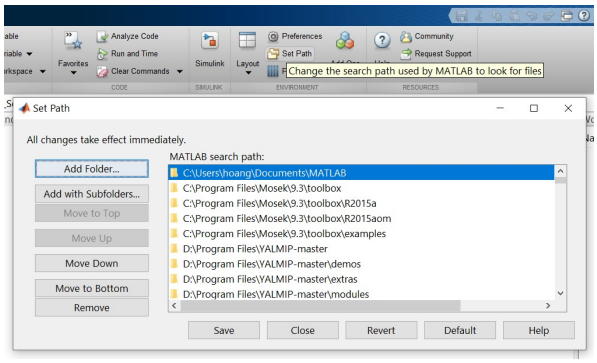

Figure A.10: MATLAB set path for YALMIP

handle matrix inequality as well as declare variables. It is also supporting most of the solvers in the fields of linear and nonlinear programming. YALMIP itself has built-in solvers but not so effective as other dedicated solvers.

MOSEK is a popular solver for linear, mixed-integer linear, quadratic, mixed-integer quadratic, quadratically constraint, conic and convex nonlinear mathematical optimization problems [2]. MOSEK is focusing on large-scale sparse problem solving, especially the interior-point optimizer for linear, conic quadratic (also known as Second-order cone programming) and SDP issues, which the software is popularly known that it is quite effective at solving. MOSEK supports many programming languages (C, C#, Java, MATLAB, Python and R) and most of modelling systems support MOSEK, e.g., MATLAB and GAMS.

A.2.1 LMI condition construction using YALMIP

A.2.1.1 YALMIP installation

YALMIP developer makes it very easy to download and install it. One just need to go to `https://yalmip.github.io/download/`, then get the latest version as in Fig. A.9. To install it in MATLAB, one first need to unzip the downloaded file into a suitable unchanged folder. Then, from MATLAB HOME tab, choose set path as in Fig. A.10, then choose Add with Subfolders and link to the folder of the YALMIP files. Then choose save and close the Set Path toolbox.

After the installation, one should run `yalmiptest` in MATLAB to check whether the installation is correct and there are suitable solvers for your core problems. Fig. A.11 shows a test results with MOSEK solver.

A.2.1.2 LMI manipulation with YALMIP

In general, there is a common step to manipulate a linear programming problem. As seen in Listing. A.3, here are the main steps:

1. Define variables: the variables are defined with sdpvar (line 6 in Listing. A.3). Note that square matrix is symmetric by default, so in order to declare a full square matrix variable, one has to use something like $x = sdpvar(3, 3, 'full')$.

2. Define constraints: this is where we set the conditions for our problems (line 9-12 in Listing. A.3). These conditions can be nonlinear or linear, ixed-integer linear, quadratic, mixed-integer quadratic, quadratically constraint, etc.

3. Define an objective: this is where we set our cost function, which we try to minimize its value (line 15 in Listing. A.3). For the case of maximization, just put the cost function equal to its negative value.

4. Set some options for YALMIP and solver: this is where to choose a suitable solver for the problem (line 18 in Listing. A.3). Also, depends on the solver and the problem, one has to set different options to be able to achieve the best results. Consult the solver user guide document for these settings.

5. Solve the problem: this is where to tell the solver to start to find the solution for the problems (line 21 in Listing. A.3).

6. Analyze error flags: this step is also important, since it is where to know whether the problems have solutions or not, and the solutions are good or bad (line 23-31 in Listing. A.3). For example, in case of control design, the resulting gain K may have eigenvalues with negative real parts, but there are some eigenvalues with very low damping (under 5%), so the controller is not good enough for the system.

```
% Clear YALMIPs internal database
% Each time sdpvar etc is called, internal database will grow larger
yalmip('clear')

% Step 1: Define variables for the LMI condtions
x_LMI = sdpvar(12,1);

% Step 2: Define constraints of LMI conditions
Constraints_LMI = [-2 <= sum(x_LMI) <= 20, x_LMI(1) == 1, 0 <= x_LMI(1) + x_LMI(2) <= 2];
for i = 1 : 9
  Constraints_LMI = [Constraints_LMI, 1+ x_LMI(i) + x_LMI(i+1) <= x_LMI(i+2) + x_LMI(i+3)];
end

% Step 3: Define an objective or cost function for the LMI conditions
Objective_LMI = x_LMI'*x_LMI+norm(x_LMI,1);

% Step 4: Choose solver and set options for Yalmip to work
options_LMI = sdpsettings('verbose',1,'solver','quadprog','quadprog.maxiter',100);

% Step 5: Solve the LMI problem using chosen solver
LMI_output = optimize(Constraints_LMI,Objective_LMI,options_LMI);

% Step 6: Analyze error flags to see if there are any problems
if LMI_output.problem == 0
 % Extract and display value
 solution_LMI = value(x_LMI)
else
 disp('Hmm, There are something wrong with this program!');
 disp('There is perhaps no solution or the solver cannot find a solution!');
 LMI_output.info
 yalmiperror(LMI_output.problem)
end
```

Listing A.3: LMI condition construction using YALMIP in MATLAB

A.2.2 LMI condition solving using MOSEK

A.2.2.1 MOSEK installation

To download MOSEK, go to its website `https://www.mosek.com/downloads/` and choose the suitable package for the current Operating System (OS). MOSEK support most of the popular OSs, including Linux (e.g., Red Hat and Ubuntu), MAC OS and Windows. Also, be careful to choose suitable MOSEK version for your OS version. The current stable version of MOSEK at the moment of writing this thesis is version 9. For the new ARM architecture of Apple Silicon M1 and M2, MOSEK released the beta 10 with native support.

For academic user, MOSEK license is free and can be obtained by requesting using an academic email. Go to MOSEK academic license website `https://www.mosek.com/products/academic-licenses/` and click on "Request Personal Academic License". The license is valid for 365 days and can be renewed unlimited times. MOSEK is also providing "Institutional Academic License" for a group of users in using MOSEK at the same time, through a License Server.

To activate MOSEK using the license file, put your license file in `/HOME/mosek/mosek.lic` for Linux/ MAC OS or in `\USERPROFILE\mosek\mosek.lic`. If that folder does not exist (mostly if you are installing MOSEK for the first time), then create the folder with the same name. To add MOSEK into MATLAB solver, we need to do the same process as of YALMIP, i.e., set path for MOSEK in MATLAB (add with Subfolders) as in Fig. A.12.

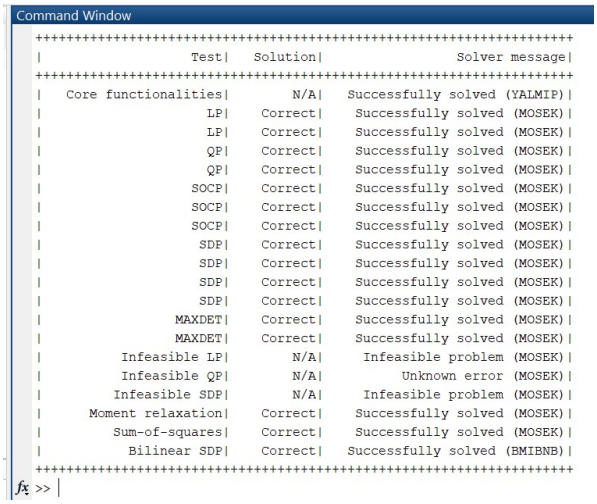

Figure A.11: YALMIP test in MATLAB with MOSEK solver

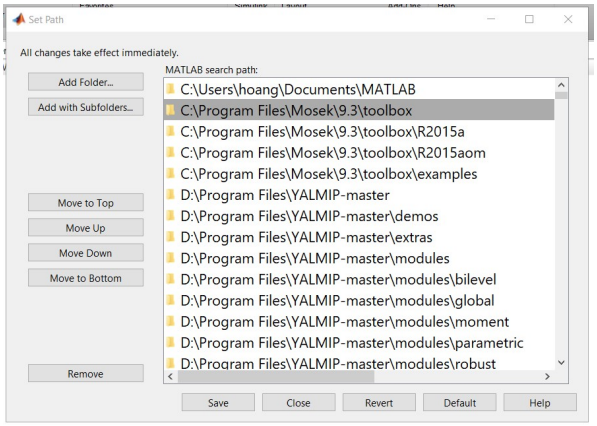

Figure A.12: Set path for MOSEK for MATLAB

A.2.2.2 LMI condition solving using MOSEK

To solve an LMI problem using MOSEK, the process is pretty similar to the one on Listing. A.3. However, in step 4 of choosing a solver, one have to change the solver to MOSEK with some options depending on the problem. The problem in Listing. A.3 is rewritten using MOSEK solver as in Listing. A.4.

```
% Clear YALMIPs internal database
% Each time sdpvar etc is called, internal database will grow larger
yalmip('clear')

% Step 1: Define variables for the LMI condtions
x_LMI = sdpvar(12,1);

% Step 2: Define constraints of LMI conditions
Constraints_LMI = [-2 <= sum(x_LMI) <= 20, x_LMI(1) == 1, 0 <= x_LMI(1) + x_LMI(2) <= 2];
for i = 1 : 9
  Constraints_LMI = [Constraints_LMI, 1+ x_LMI(i) + x_LMI(i+1) <= x_LMI(i+2) + x_LMI(i+3)];
end

% Step 3: Define an objective or cost function for the LMI conditions
Objective_LMI = x_LMI'*x_LMI+norm(x_LMI,1);

% Step 4: Choose solver and set options for Yalmip to work
% options_LMI = sdpsettings('verbose',1,'solver','quadprog','quadprog.maxiter',100);
options_LMI = sdpsettings('solver','mosek');

% Step 5: Solve the LMI problem using chosen solver
LMI_output = optimize(Constraints_LMI,Objective_LMI,options_LMI);

% Step 6: Analyze error flags to see if there are any problems
if LMI_output.problem == 0
 % Extract and display value
 solution_LMI = value(x_LMI)
else
 disp('Hmm, There are something wrong with this program!');
 disp('There is perhaps no solution or the solver cannot find a solution!');
 LMI_output.info
 yalmiperror(LMI_output.problem)
end
```

Listing A.4: LMI condition construction using YALMIP and MOSEK solver in MATLAB

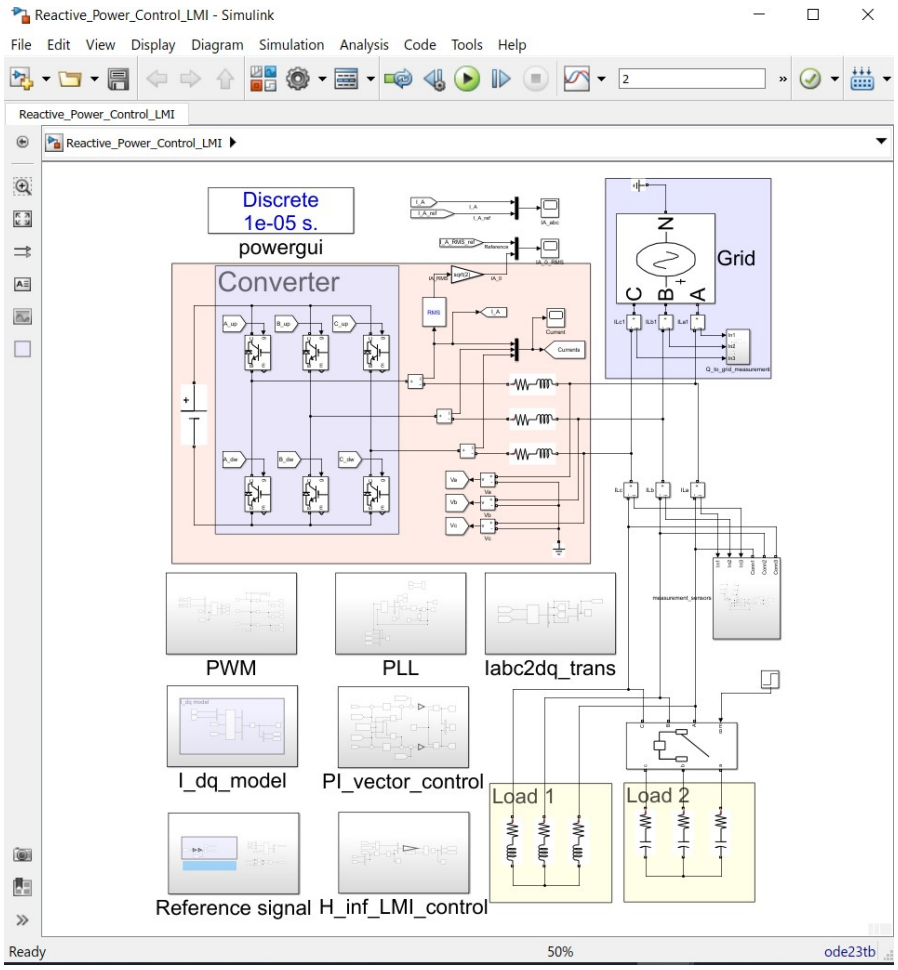

Figure A.13: VSC converter model using Simscape Specialized Power Systems

A.3 Power system simulation with MATLAB and OPAL

A.3.1 Power system simulation with MATLAB/Simscape electrical

Within the Simulink platform, Simscape enables you to quickly develop models of physical systems. Building physical component models using Simscape is based on physical connections, and these models seamlessly integrate with block diagrams and other modeling paradigms. By arranging basic components into a schematic, you may mimic systems like electric motors, bridge rectifiers, hydraulic actuators, and refrigeration systems. Simscape add-on products give users access to more sophisticated parts and analysis tools.

Simscape Specialized Power Systems is a part of Simscape products specialized in electrical system simulation, with a large library from generators and their regulators to power converters. More information can be found at their website: `https://www.mathworks.com/help/physmod/sps/specialized-power-systems.html`. In addition, there is a getting started with Specialized Power Systems guide, many related topics and lots of example for power system simulation and control in Mathwork website, all of that can be found here: `https://www.mathworks.com/help/physmod/sps/get-started-with-sps.html`.

To build a power system model using Simscape Specialized Power Systems, the process is identical to creating a model in Simulink. An example of VSC converter system model is as in Fig. A.13, where the converter is connected to the grid and its controller through Simulink connecting lines. Steps to build the model are:

1. First step is to create a Simulink model. Click on the Simulink icon in MATLAB working windows or write

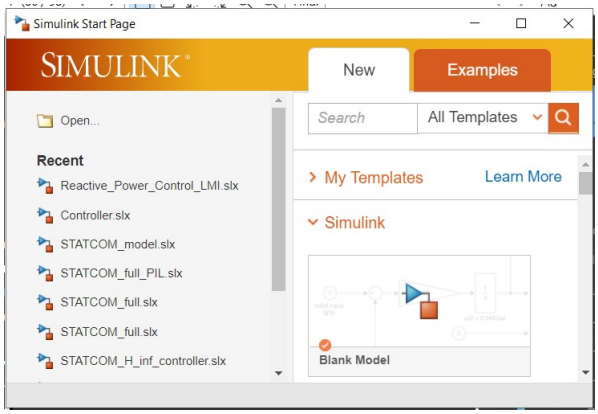

Figure A.14: Simulink Start Page

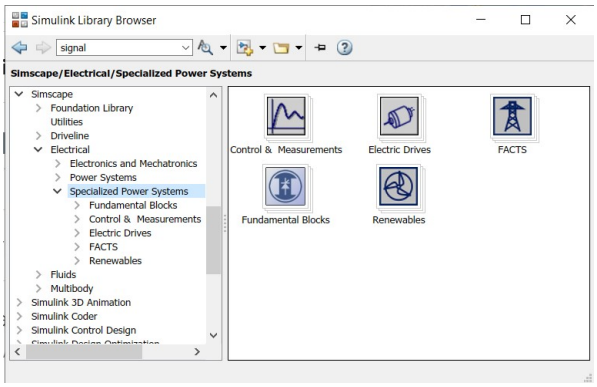

Figure A.15: Simulink library of Simscape Specialized Power Systems

$simulink$ in the MATLAB command window, then enter to call Simulink. In the $SimulinkStartPage$ (Fig. A.14), click on $BlankModel$ to create a new model.

2. In the Simulink model, click on $LibraryBrowser$ to open Simulink library, then choose $Simscape$, then $Electrical$, and then $SpecializedPowerSystems$ as in Fig. A.15. This folder contains all the libraries for power system simulation and control.

3. In this $SpecializedPowerSystems$ folder, choose all the blocks required for your simulation and drag them into the current model. Connect all the blocks as required.

A.3.2 Power system Simulink model simulation using OPAL RT-LAB

Simulink models may communicate in real time with the outside world thanks to OPAL RT-LAB, which is completely integrated with MATLAB/Simulink. Because of this, regardless of how complicated their applications are, developers can quickly design and validate them in real-time using RT-LAB. For the power systems, power electronics, aerospace, and automotive industries, RT-LAB's platform offers adaptable and scalable solutions.

To be able to import and run the Simulink model in OPAL RT-LAB, there are some steps to follow:

1. Grouping into subsystems: the top level of Simulink model have to be in the form of a set of different subsystems. This is also for the parallel computing, since each subsystem can be run on each core of the OPAL CPU.

2. Naming the subsystems: there are 3 naming rules, $SC\_anyName$ for subsystem contains user interface blocks (scopes, displays, manual switches, constants), the primary computation subsystem will be name as $SM\_anyName$, and each additional computation subsystem will be name as $SS\_anyName$

3. Adding OpComm blocks: all inputs of mentioned subsystems have to firstly go through an OpComm block as in Fig. .

4. Setting simulation parameters: there are some setting required for Simulink model, including fixed-step solver and sample time as in Fig. A.17.

5. Executing off-line: Make sure no errors are raised by running the model in Simulink. The model won't function in RT-LAB if Simulink cannot run it. We can try to build the model with RT-LAB once it is able to run in Simulink.

6. In OPAL RT LAB (as in Fig. A.18), create a new project and import the Simulink model, then process the step as in OPAL user guide for the simulation.

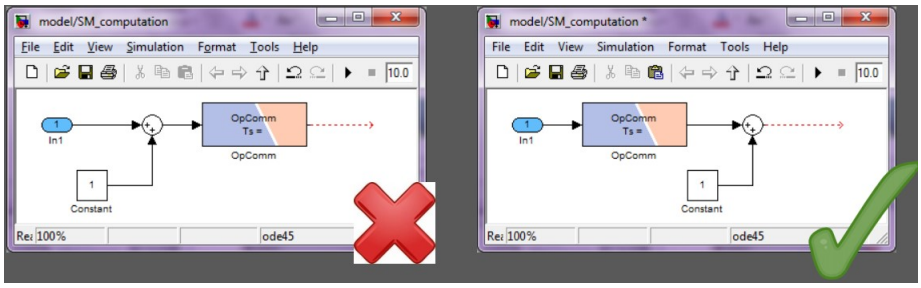

Figure A.16: OpComm position in Simulink model (left is wrong position, right is good position)

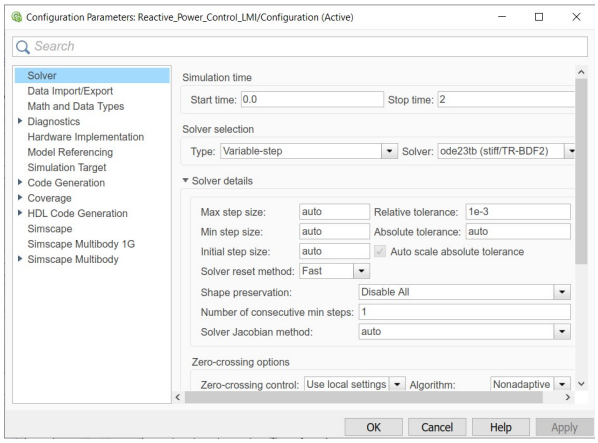

Figure A.17: Simulink model solver setting

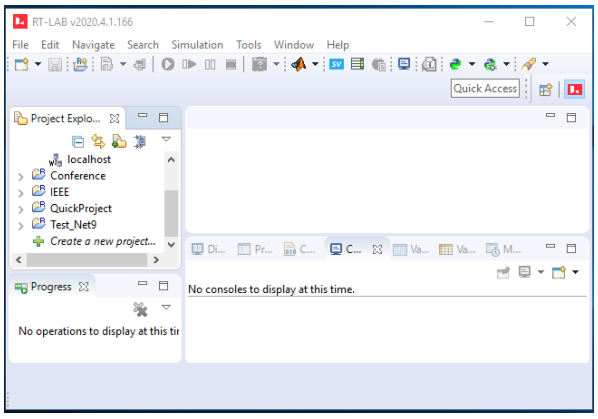

Figure A.18: OPAL RT LAB software

Bibliography

[1] Lofberg, J. (2004, September). YALMIP: A toolbox for modeling and optimization in MATLAB. In 2004 IEEE international conference on robotics and automation (IEEE Cat. No. 04CH37508) (pp. 284-289). IEEE.

[2] ApS, M. (2019). Mosek optimization toolbox for matlab. User's Guide and Reference Manual, Version, 4.

[3] Pena-Alzola, R., Liserre, M., Blaabjerg, F., Sebastián, R., Dannehl, J., & Fuchs, F. W. (2012). Analysis of the passive damping losses in LCL-filter-based grid converters. IEEE Transactions on Power Electronics, 28(6), 2642-2646.

[4] Rogers, G. (2012). Power system oscillations. Springer Science & Business Media.

Appendix B

Appendix for wind energy MPPT searching table

This appendix is to provide programs (in MATLAB) for wind energy MPPT searching table.

B.1 Maximum power point tracking data generation

```
clear all
close all
clc

% Input data for wind speed (m/s), pitch angle (deg)
pitch_angle_deg_resolution = 1; %0.1;
pitch_angle_deg_range = 0:pitch_angle_deg_resolution:20; %(deg)
pitch_angle_deg_index = size(pitch_angle_deg_range, 2);
i_pitch_angle_deg = 0;
wind_speed_range = 1:0.1:30;
no_wind_value = size(wind_speed_range, 2);
w_r_pu_range =0:(1e-3):5;
w_r_pu_index = size(w_r_pu_range,2);
Pm_pu_out_range = [];
Pm_pu_out_max_range = [];
w_r_pu_opt_range = [];
w_r_pu_opt = 0;
Pm_pu_out_del_range = [];
w_r_pu_del_range = [];
i = 0;
Searching_table_3D = [];



for pitch_angle_deg = pitch_angle_deg_range
    i_pitch_angle_deg = i_pitch_angle_deg + 1;
    for wind_speed = wind_speed_range

        for w_r_pu = w_r_pu_range
            Pm_pu_out = wind_power_func(w_r_pu, pitch_angle_deg, wind_speed);
            Pm_pu_out_range = [Pm_pu_out_range Pm_pu_out];
        end

        % find optimal value of w_r_pu and max Pm_pu
        [Pm_pu_out_max, opt_index] = max(Pm_pu_out_range);
        w_r_pu_opt = w_r_pu_range(opt_index);
        Pm_pu_out_max_range = [Pm_pu_out_max_range Pm_pu_out_max];
        w_r_pu_opt_range = [w_r_pu_opt_range w_r_pu_opt];

        % find deload point on the right of the optimal point
```

```
        deload = 0.1; % (10% power)
        i_del = opt_index - 1;
        for Pm_pu_out_del = Pm_pu_out_range(opt_index : w_r_pu_index)
            i_del = i_del + 1;
            if Pm_pu_out_del < (1-deload)*Pm_pu_out_max
                del_index = i_del;
                break
            end
        end
        w_r_pu_del = w_r_pu_range(del_index);
        Pm_pu_out_del_range = [Pm_pu_out_del_range Pm_pu_out_del];
        w_r_pu_del_range = [w_r_pu_del_range w_r_pu_del];


        % data for plot
        i = i+1;
        legend_plot = strcat(num2str(wind_speed,'%.2f'), ' (m/s)');
%         pitch_angle_deg_range_plot = pitch_angle_deg*ones(1, w_r_pu_index);
        hs_plot(i) = plot3(w_r_pu_range, pitch_angle_deg*ones(1, w_r_pu_index),
    Pm_pu_out_range, 'DisplayName', legend_plot);
        hold on

        Pm_pu_out_range = [];
        Pm_pu_out_max = 0;
        w_r_pu_opt = 0;
    end

    % table of optimal value and deload value of(pitch_angle_deg, wind_speed, Pm_pu_out,
    w_r_pu)
%     Searching_table_adding = [pitch_angle_deg*ones(1, size(wind_speed_range,2)); ...
%         wind_speed_range;  ...
%         Pm_pu_out_max_range; w_r_pu_opt_range; ...
%         Pm_pu_out_del_range; w_r_pu_del_range];
%     Searching_table = [Searching_table, Searching_table_adding];

    Searching_table_adding = [wind_speed_range;  ...
    Pm_pu_out_max_range; w_r_pu_opt_range; ...
    Pm_pu_out_del_range; w_r_pu_del_range];
    Searching_table_3D(:,:,i_pitch_angle_deg) = Searching_table_adding;

    del_legend = strcat('Deload point: ', num2str(deload*100, '%.1f'), ' %');
    opt_plot = plot3(w_r_pu_opt_range, pitch_angle_deg*ones(1, size(wind_speed_range,2)),
    Pm_pu_out_max_range,'r*', 'DisplayName','Optimal point');
    del_plot = plot3(w_r_pu_del_range, pitch_angle_deg*ones(1, size(wind_speed_range,2)),
    Pm_pu_out_del_range,'b*', 'DisplayName', del_legend);

    Pm_pu_out_max_range = [];
    Pm_pu_out_del_range = [];
    w_r_pu_opt_range = [];
    w_r_pu_del_range = [];

end

% set(gca,'FontSize',18); %set axes font size
set(gca,'FontSize',40); %set axes font size
pitch_angle_str = num2str(pitch_angle_deg,'%.2f');
title_str = strcat('Turbine Power Characteristics');
title(title_str);
hold on

legend([opt_plot, del_plot]);
xlabel('w_r (pu)');
ylabel('pitch angle (deg)');
zlabel('P_m (pu)');

hold off

function Pm_pu_out = wind_power_func(w_r_pu, pitch_angle_deg, wind_speed)
```

```
105
106 w_r_pu = min(1e6, max(1e-6, w_r_pu)); % rotor speed of generator
107 wind_speed = min(1e6, max(1e-6, wind_speed));
108
109
110 %% Parameters
111 wind_base = 12; % (m/s): wind speed base for pu
112 speed_nom = 1; % Base rotational speed (p.u. of base generator speed): here is 1 due to wind
        turbine speed = generator speed
113 lambda_nom = 8.1; %the nominal value (?_nom)
114 P_wind_base = 0.8; % Maximum power at base wind speed (pu of nominal mechanical power)
115 Pnom = 7.5e6; %Nominal mechanical output power (W)
116 Pelec_base = 7.5e6; %Base power of the electrical generator (VA)
117 %parameter for cp
118 c1_c6 = [0.51763          116          0.4            5           21     0.006795];
119 c1=c1_c6(1);c2=c1_c6(2);c3=c1_c6(3);c4=c1_c6(4);c5=c1_c6(5);c6=c1_c6(6);
120 cp_nom = 0.48;
121
122 %% Pwind_pu
123 wind_speed_pu = wind_speed/wind_base;
124 Pwind_pu = wind_speed_pu^3;
125
126 %% cp_pu
127 lambda_pu = w_r_pu/wind_speed_pu;
128 lambda = lambda_nom*lambda_pu;
129 lambda = min(inf, max(1e-6, lambda));
130
131 beta = pitch_angle_deg;
132 lambda_i = 1/(1/(lambda+0.08*beta)-0.035/(beta^3+1));
133 cp = c1*(c2/lambda_i-c3*beta-c4)*exp(-c5/lambda_i)+c6*lambda;
134
135 cp_pu = cp/cp_nom;
136
137 %% Pm_pu_out
138 Pm_pu = cp_pu*Pwind_pu;
139 Pm_pu_out = (P_wind_base*Pnom/Pelec_base)*Pm_pu;
140
141 %% Tm_pu_out
142 Tm_pu_out = Pm_pu_out/w_r_pu;
143
144 end
```

Listing B.1: Maximum power point tracking data generation program

Appendix C

Appendix for LMI control techniques

This appendix is to provide some LMI-related techniques and some important accompanied lemmas.

C.1 LMI lemma for convex problem

To establish some fuzzy LMI theorems, the lemma for convex problem is introduced.

Lemma 3 *With a finite number r, $r \in N^*$ and with a real set S defined as:*

$$S = \left\{ a_i \in R \middle| 0 \leq a_i \leq 1, \sum_{i=1}^{r} a_i = 1 \right\}$$

Consider P_i are symmetric matrices with real elements, the two LMI conditions (C.1) *and* (C.2) *are equivalent:*

$$\sum_{i=1}^{r} a_i P_i < 0; \forall a_i \in S \tag{C.1}$$

$$P_i < 0, \forall i = \overline{1, r} \tag{C.2}$$

Proof 9 *By using recursive technique, the introduced lemma can be proved as follow: with $r = 2$, the LMI* (C.1) *is equivalent to:*

$$a_1 P_1 + a_2 P_2 < 0 \tag{C.3}$$

Since $0 \leq a_i \leq 1$, choose $a_1 = 0$, we have:

$$a_2 P_2 < 0 \tag{C.4}$$

or, equivalent to:

$$P_2 < 0 \tag{C.5}$$

The same, choose $a_2 = 0$, we have:

$$P_1 < 0 \tag{C.6}$$

So LMI (C.1) *true leads to LMI* (C.2) *true.*
Now, assume that LMI (C.2) *true, we have:*

$$P_1 < 0, P_2 < 0 \tag{C.7}$$

Since $0 \leq a_i \leq 1$, this leads to:

$$a_1P_1 + a_2P_2 < 0 \tag{C.8}$$

Therefore, LMI (C.1) *and LMI* (C.2) *are equivalent with* $r = 2$.

Assuming that LMI (C.1) *and LMI* (C.2) *are equivalent with* $r = k, k \geq 2$, *i.e., the two following LMI conditions are equivalent:*

$$\sum_{i=1}^{k} a_iP_i < 0 \tag{C.9}$$

$$P_i < 0, \forall i = \overline{1,k} \tag{C.10}$$

We will prove that this is also true for $r = k + 1$.
For $r = k + 1$, *LMI* (C.1) *can be equivalently written as:*

$$a_1P_1 + a_2P_2 + ... + a_kP_k + a_{k+1}P_{k+1} < 0 \tag{C.11}$$

With $a_{k+1} = 0$, *the problem become as in the case of* $r = k$.
With $a_{k+1} > 0$, *this LMI can be written in another way:*

$$\begin{array}{l} a_1P_1 + a_2P_2 + ... \\ + (a_k + a_{k+1}) \left(\frac{a_k}{a_k+a_{k+1}} P_k + \frac{a_{k+1}}{a_k+a_{k+1}} P_{k+1} \right) < 0 \end{array} \tag{C.12}$$

Because LMI (C.1) *and LMI* (C.2) *are equivalent with* $r = k$, *and:*

$$\left\{ \begin{array}{l} a_1 + a_2 + ... + a_{k-1} + (a_k + a_{k+1}) = 1 \\ 0 \leq a_1 \leq 1, 0 \leq a_2 \leq 1, ..., 0 \leq (a_k + a_{k+1}) \leq 1 \end{array} \right. \tag{C.13}$$

the above LMI condition is equivalent to:

$$\left\{ \begin{array}{l} P_1 < 0 \\ P_2 < 0 \\ \vdots \\ P_{k-1} < 0 \\ \frac{a_k}{a_k+a_{k+1}} P_k + \frac{a_{k+1}}{a_k+a_{k+1}} P_{k+1} < 0 \end{array} \right. \tag{C.14}$$

Consider the last condition:

$$\frac{a_k}{a_k + a_{k+1}} P_k + \frac{a_{k+1}}{a_k + a_{k+1}} P_{k+1} < 0 \tag{C.15}$$

Since (C.11) *is true* $\forall a_i \in S$ *and*

$$\left\{ \begin{array}{l} \frac{a_k}{a_k+a_{k+1}} + \frac{a_{k+1}}{a_k+a_{k+1}} = 1 \\ 0 \leq \frac{a_k}{a_k+a_{k+1}} \leq 1, 0 \leq \frac{a_{k+1}}{a_k+a_{k+1}} \leq 1 \end{array} \right.$$

Apply the above lemma for $r = 2$, *the last condition* (C.15) *is true if and only if:*

$$\left\{ \begin{array}{l} P_k < 0 \\ P_{k+1} < 0 \end{array} \right. \tag{C.16}$$

Hence, the LMI condition (C.14) *is exactly equivalent to:*

$$P_1 < 0, P_2 < 0, \ldots, P_{k-1} < 0, P_k < 0, P_{k+1} < 0 \tag{C.17}$$

Therefore, the two LMI (C.1) *and LMI* (C.2) *are equivalent with* $r = k + 1, k \geq 2$.
In conclusion, the two LMI (C.1) *and LMI* (C.2) *are equivalent with all* $r \in N^*$.

Lemma 4 *Let* $X \in R^{m\times n}, Y \in R^{n\times m}, Q \in R^{m\times m}$, *then the two following LMIs are equivalent [1], [2]:*

(i) $Q + XFY + Y^T F^T X^T < 0, \forall F \in R^{n \times n},\ F^T F \leq I$

(ii) There exist $\delta > 0$ *such that:* $Q + \delta X X^T + \delta^{-1} Y^T Y < 0$

Proof 10 *The proof can be seen in, e.g., [1], section 2.1.3 Variable Elimination Lemma, Lemma 2.5.*

Bibliography

[1] Duan, G. R., & Yu, H. H. (2013). LMIs in control systems: analysis, design and applications. CRC press.

[2] Boyd, S., El Ghaoui, L., Feron, E., & Balakrishnan, V. (1994). Linear matrix inequalities in system and control theory. Society for industrial and applied mathematics.

Titre : Commande de l'électronique de puissance des futurs smart grids pour les services système

Mots clés : MIMO, commande optimale, VSC, CCHT, PMSG, STATCOM, services système

Résumé : Afin de fournir des services système et de gérer les intéractions entre convertisseurs, cette thèse a proposé une technique de commande coordonnée pour les systèmes de convertisseurs de puissance connectés au réseau, avec des implémentations centralisées et décentralisées. Les nouvelles structures de commande proposées sont divisées en différents niveaux de commande/boucles en fonction de la dynamique naturelle du système : la boucle très rapide est utilisée pour fournir des services locaux (puissance active/réactive, tension CC, et inertie du réseau / RoCoF support), la boucle rapide est pour MPPT, la réponse en fréquence et les services de tension CA, et la boucle lente est constituée par sert les commandes secondaires de la fréquence et de la tension. À cet égard, ce contrôle est une alternative à la commande vectorielle classique. De plus, des techniques de commande avancées comme H2/H-infini, des approches floues non linéaires et des techniques d'IMT, sont utilisées pour obtenir des performances optimales tout en maintenant une marge de stabilité (p. ex., FRT et CCT). Trois applications ont été traitées : commande décentralisée VSC-CCHT (non linéaire), commande décentralisé/centralisé du système éolien PMSG (non linéaire) raccordé au réseau et commande en tension (STATCOM) d'un convertisseur connecté au réseau. La mise en œuvre décentralisée renforce la résilience lors de la commande de plusieurs générateurs d'énergie renouvelable, comme dans le concept de centrale électrique virtuelle dynamique développé dans le projet H2020 RIA POSYTYF. Les résultats ont démontré que les structures de commande proposées sont plus performantes que la commande vectorielle classique en termes de stabilité et de performance. Cette thèse présente également une méthode de conception de système de commande conviviale sur la base des approches présentées, qui peut ensuite être appliquée aux applications au niveau industriel.

Title : Control of power electronics of future smart grids for ancillary services

Keywords : MIMO, Optimal control, VSC, HVDC, PMSG, STATCOM, ancillary services

Abstract : In order to provide ancillary services and handling coupling between converters, this thesis proposed a coordinated control technique for power converter systems connected to the grid, with both centralised and decentralised implementations. The new proposed control structures are divided into different control levels/loops based on the system's natural dynamics: the very fast loop is used to provide local services (active/reactive power, DC voltage, and grid inertia/ RoCoF support), the fast loop is for MPPT, frequency response, and AC voltage services, and the slow loop is for secondary frequency and voltage control. In this regard, such control is an alternative to traditional vector control. Furthermore, advanced control techniques including MIMO state-space, resilient and optimal H2/H-infinity control, nonlinear fuzzy approaches, and LMI techniques are used to obtain optimal performance while maintaining a stability margin (e.g., FRT and CCT). There are 3 applications: VSC-HVDC (nonlinear) decentralised control, grid-connected wind system PMSG (nonlinear) decentralized/centralized control, and a grid-connected STATCOM LMI-based pole-placement control. Decentralized implementation enhances resilience when controlling several renewable generators, such as in the Dynamic Virtual Power Plant concept developed in the H2020 RIA POSYTYF project. The results demonstrated that the proposed control structures outperform classical vector control in terms of stability and performance. This thesis also presents an engineering-friendly control system design method based on the presented approaches, which can then be applied to industrial-level applications.